DISSERTATION

VARIABILITY IN OBSERVED REMOTE MARINE AEROSOL POPULATIONS AND IMPLICATIONS FOR HAZE AND CLOUD FORMATION

Submitted by

Samuel A. Atwood

Department of Atmospheric Science

In partial fulfillment of the requirements

For the Degree of Doctor of Philosophy

Colorado State University

Fort Collins, Colorado

Spring 2020

Doctoral Committee:

Advisor: Sonia M. Kreidenweis

Susan C. van den Heever
Jeffrey R. Pierce
Daniel Cooley

ABSTRACT

VARIABILITY IN OBSERVED REMOTE MARINE AEROSOL POPULATIONS AND IMPLICATIONS FOR HAZE AND CLOUD FORMATION

In many oceanic regions of the planet, once pristine environments are known to have a high degree of sensitivity to changing aerosol populations and perturbations from anthropogenic emissions. However, difficulties in modeling and remote sensing efforts in remote marine regions have led to continued uncertainties in aerosol-cloud-climate interactions. Numerous properties of the aerosol and environment affect these interactions in complex and often non-linear ways. In this work, I examine the variability in observed remote marine aerosol properties and its implications for classifying aerosol impacts on cloud development and radiative transfer in the atmosphere.

The results from several field campaigns that measured aerosol and environmental properties relevant to these processes in marine and coastal regions are first presented. An unsupervised classification methodology was used to identify periods of impacts associated with distinct fine-mode aerosol population types and to quantify the observed range of variability associated with these types. A specific focus was placed on differentiating between internal variability in relevant properties within a given population type and external variability between the average values for each population type. The result was a set of aerosol population type models observed in marine regions that allowed for further investigation of the impact of different sources of variability on subsequent atmospheric processes.

Next presented are the results of several observationally driven sensitivity studies using the aerosol models. First, initial cloud properties were investigated using a cloud parcel model driven by the observed aerosol population types to examine relative sensitivity to updraft velocity, extensive aerosol properties including number concentration, and a range of intensive aerosol properties. It was found that the parameter space across which initial cloud property sensitivity to variability in the observed aerosol dataset was investigated could be simplified to incorporate relevant intensive aerosol properties into a single population type parameter. Previous work using simpler mono-modal aerosol populations had identified several regimes of sensitivity of initial cloud properties to updraft velocity and total particle number concentration. When driven by the more complex and atmospherically relevant marine population types additional sensitivity to population type was identified through portions of these two regimes, and a new regime was identified that was more sensitive to population type than either of the other parameters.

A Monte Carlo optical reconstruction model was then used to investigate sensitivity of atmospheric optical properties to observed variability in aerosol and environmental properties. As expected, aerosol dry mass concentrations were the largest contributors to overall sensitivity of extensive optical properties. However, in terms of intensive optical properties, the range of expected variability due to internal variability within a given population type was on the same order as impacts expected due to differences between population types. Specific aerosol population type models may therefore provide little advantage for further constraining expected optical property variability in this dataset. Additionally, the combined impacts of variability in environmental relative humidity (RH) and intensive aerosol properties within a nominally consistent population type could be quantified with coefficients of variation on the order of 0.3 in

this dataset—a value that was relatively constant and independent of total mass concentration, aerosol population type, and RH.

Overall, this work produced new representations of fine-mode aerosol types encountered in marine environments that were broadly consistent with those currently applied in remote sensing and climate modeling. However, the models presented here can account explicitly for the effects of ambient relative humidity, and thus may be useful for next-generation modeling that includes those effects. Future work focused on similar observationally-constrained model development for the marine and littoral coarse mode would be beneficial, as large particles are often significant fractions of optical depth in these regions.

ACKNOWLEDGEMENTS

Many people have provided motivation and assistance throughout my time at CSU and in the preparation of this dissertation. I would first like to thank my advisor, Sonia Kreidenweis, for being a constant source of inspiration, ideas, and support. I appreciate the many discussions we have had and her scientific insights and enthusiasm for our research. Many thanks also to my committee members Sue van den Heever, Jeff Pierce, and Dan Cooley, for their assistance and patience as I completed this work.

I would also like to thank Jeff Reid in particular for his mentorship and friendship throughout my time at CSU and while working on this dissertation. He has provided endless encouragement and support, and has helped me to refine my ideas on science, aerosol research, and where best to focus my efforts. Thanks also to the staff of the Naval Research Laboratory in Monterey for welcoming me and helping with much of this work throughout the many months in which I worked with them.

Thanks to the many individuals who participated in the 7SEAS experiments in Singapore and the Philippines. Jeff Reid, Haf Jonsson, Betsy Reid, and Walter Sessions assisted with measurements as part of the Vasco cruise. Liya Yu and her students, Nofel Lagrosas, and James Simpas provided considerable support as part of the 7SEAS experiments. I also gratefully thank Peng Xian for her assistance with NAAPS analyses and her support throughout my time working at NRL. Additional support for the 7SEAS experiments and analyses was provided by the NRL 6.1 Base Program via an Office of Naval Research (ONR) Global grant to the Manila Observatory, the Naval Research Enterprise Internship Program (NREIP), ONR under award number N00014-16-1-2040, and the Colorado State University Center for Geosciences/Atmospheric Research

(CG/AR). I am also grateful to the management and crew of the *Vasco*, the Manila Observatory, and the US State Department/Embassy in Manila for support of the SCS cruise.

Similarly, I would like to thank those who participated in the CalWater-2015 experiments in Bodega Bay and assisted with measurements and analysis. Paul DeMott and Sonia Kreidenweis provided considerable support in the planning of these experiments, as well as the analysis and preparation of this work. Markus Petters and his students operated the size-resolved CCN system, and Kathryn Moore operated the SMPS system and assisted with operation of the scanning-flow CCN system. Additional support and assistance in the operation of the research site was provided by Tom Hill, Ezra Levin, Christina McCluskey, Andy Martin, Gavin Cornwell, Nicholas Rothfuss, Hans Taylor, Yvonne Boose, Gregg Schill, Camille Sultana, and Kim Prather. Funding included support by ONR under award number N00014-16-1-2040, and the National Science Foundation under grant numbers 1450760, 1450690, and 1451347. Additional thanks to Jeff Reid and the Naval Research Laboratory, Monterey, for the loan of a CCN instrument during this experiment.

I would also like to thank and acknowledge everyone in the CSU Atmospheric Chemistry groups, and the Kreidenweis group in particular, for their support and friendship throughout the years. Thanks also to Sue van den Heever and Steve Saleeby for assistance with the cloud parcel model.

Finally, I would like to thank my parents and brothers, and my friends, especially Matt Garcia, for always being happy to explore this magical ol' world with me.

Parts of Chapters 2 (Atwood et al., 2017) and 3 (Atwood et al., 2019) in this dissertation have been published in peer-reviewed scientific journals, and are included here under Creative Commons Attribution 3.0 and 4.0 Licenses:

Atwood, S. A., Reid, J. S., Kreidenweis, S. M., Blake, D. R., Jonsson, H. H., Lagrosas, N. D., Xian, P., Reid, E. A., Sessions, W. R. and Simpas, J. B.: Size-resolved aerosol and cloud condensation nuclei (CCN) properties in the remote marine South China Sea – Part 1: Observations and source classification, Atmos Chem Phys, 17(2), 1105–1123, doi:10.5194/acp-17-1105-2017, 2017.

Atwood, S. A., Kreidenweis, S. M., DeMott, P. J., Petters, M. D., Cornwell, G. C., Martin, A. C. and Moore, K. A.: Classification of aerosol population type and cloud condensation nuclei properties in a coastal California littoral environment using an unsupervised cluster model, Atmospheric Chem. Phys., 19(10), 6931–6947, doi:10.5194/acp-19-6931-2019, 2019.

TABLE OF CONTENTS

1. INTRODUCTION

In remote oceanic regions of the planet, aerosol particles have long been established as an important factor in atmospheric processes. Suspended particles scatter and absorb incoming solar radiation, affecting the radiative energy budget and thereby altering the thermodynamic state of the atmosphere and potentially the ability of clouds to form (Charlson et al., 1992; Bates et al., 2006; Andersen and Cermak, 2015). Characteristically high relative humidity (RH) in marine air masses causes hygroscopic particles to grow by condensation of water vapor, changing the particles' size and indices of refraction, and further altering aerosol-radiation interactions. Often strong gradients in RH exacerbate uncertainties in attempts to quantify these effects, as unknowns in properties of both the environment and the aerosol produce relatively large potential differences in optical properties. In certain favorable remote marine regions in particular, aerosol affect the formation of extensive low-level fogs and long-lived stratocumulus cloud layers that reflect more incoming solar radiation out of the earth system as compared to the relatively dark ocean surface (Klein and Hartmann, 1993; Wood, 2012). As such clouds form, the aerosol available for condensation affects both the number and size of cloud droplets, along with additional non-linear impacts on further cloud development and lifetime (Twomey, 1974, 1977; Albrecht, 1989; Ackerman et al., 1993). Particle microphysical impacts on cloud droplet number concentration and size distribution have further influences on the onset and types of precipitation that form, ranging from drizzle to heavy precipitation (Rosenfeld et al., 2006, 2014b). Aerosol direct effects on radiative transfer and indirect effects on cloud reflectance and lifetime remain among the largest unknowns in estimates of global radiative forcings on climate and the global energy balance (IPCC, 2013; Rosenfeld et al., 2014a). Given the large fraction of global surface area covered by oceans, and the vulnerability of once-pristine ocean environments

to anthropogenic perturbations through continental outflow of pollution, shipping, and other factors, aerosol-modulated radiative transfer and cloud property impacts in remote marine regions have remained a topic of extensive study.

Many of the fundamental processes governing these aerosol-cloud-climate interactions have been well established theoretically via laboratory studies and some observational evidence (e.g. Andreae and Rosenfeld, 2008), but substantial uncertainty remains due to complex and non-linear relationships between particle characteristics and relevant processes, limitations on measurements and observations, and outstanding questions regarding the relative importance of various aspects of the system (Rosenfeld et al., 2014b). Application of such basic knowledge to the real atmosphere is complicated by the generally short lifetime of aerosol particles, numerous sources and sinks, variable transport pathways, and complex and variable nature of the particles themselves. Many of the "cleanest" airmasses that have been observed occur in remote marine regions, such that the "background" marine aerosol is generally conceptualized as comprised of relatively few particles as compared to terrestrial and littoral regions where higher concentrations from numerous sources are often observed. However, it is now clear that sea spray particles derived from the ocean surface do not consist solely of sea salt (Prather et al., 2013; Quinn et al., 2014), that nucleation of new particles can occur in the marine boundary layer (Petters et al., 2006; O'Dowd and Leeuw, 2007), and that aerosol that has been subjected to long-range transport can be mixed into the remote marine boundary layer and affect what are often considered nominally background marine air masses (Shank et al., 2012; Clarke et al., 2013). All of these processes will increase aerosol number concentrations and can modify aerosol size distributions from those expected for a "remote marine" region. In addition to impacts from the complexity of marine aerosol itself, cloud development in remote marine regions may be more

sensitive to changing aerosol properties—and have stronger non-linear impacts and forcings—as compared to regions with higher typical aerosol concentrations (Koren et al., 2014; Remer, 2014).

Remote marine regions in general therefore comprise a distinct regime within aerosol-cloud-climate sensitivity studies, with their own unique set of challenges and applications. Modeling efforts and remote sensing retrievals over ocean regions rely on sets of assumptions about both the aerosol populations in these regions and the impact they have on radiative transfer and cloud development. A wide range of parameters and assumptions nevertheless persists in numerous use cases (e.g. Kinne et al., 2006; Ghan et al., 2011, 2012; Khain et al., 2015), along with open questions as to how such models compare to observations of actual remote marine regions (Dubovik et al., 2002; Sayer et al., 2012a, 2012b, 2012c). As such, this dissertation focuses on efforts to utilize observationally-driven sensitivity studies of remote marine aerosol to better constrain expected variability in aerosol properties and their resulting impacts on aspects of radiative transfer and cloud development.

1.1. MARINE AEROSOL OBSERVATION AND MODELING CHALLENGES

In situ measurements of aerosols and their effects in marine regions present some unique observational challenges. Ship- and aircraft-based studies have been dedicated to the study of atmospheric processes in marine regions but are limited in both coverage and duration. Land-based measurements in littoral locations can allow for extended temporal sampling of marine air masses, but additional efforts are required to ensure they are representative of marine aerosol without biases due to terrestrial sources. Additional temporal and spatial coverage of ocean regions is provided by remote sensing, but such methods generally rely on a priori assumptions

and do not provide as much detailed information as in situ measurements. Further, passive remote sensing observations of the full atmospheric column often provide little or no information on the vertical distributions of aerosol, while active sensors such as lidars that probe aerosol throughout the column are subject to underlying assumptions about aerosol properties themselves and have additional spatial and temporal sampling limitations. Nevertheless, continued efforts are made to better refine aerosol measurements and understanding of remote marine aerosol populations and their three-dimensional distributions, and to provide quantitative observations to help with validation of models and remote sensing retrievals.

Estimates of the quantity and type of aerosol spread across vast ocean regions typically rely on remote sensing observations or atmospheric chemical transport models. Comparisons between remote sensing observations and in situ measurements are inherently dependent on the optical properties assumed in the remote sensing retrieval. Similarly, models often utilize data assimilation of optical remote sensing retrievals to constrain and improve the model aerosol values. Such efforts require linking aerosol optical properties to estimates of type and quantity. This is accomplished through the creation of aerosol population models that parameterize particle properties according to general types or species, thereby allowing retrieval algorithms to select from among multiple options. Various additional properties of the aerosol can then be calculated through known physical relationships. Aerosol population models are therefore based on observational efforts to quantify aerosol properties and variability according to classified types, and are representative of such aerosol types under specific scenarios or conditions.

With the advent of increased computing power, a large hierarchy of regional-to-global atmospheric models has been established that are used for a variety of purposes, from forecasts of weather and environmental conditions, to analysis of global chemical cycles and predictions

of global change. Most models that treat aerosol explicitly are linked to emissions databases and, at the very least, track the masses of individual aerosol species; some have schemes to predict both aerosol number and mass concentrations. However, for those that lack more detailed descriptions of aerosol microphysics, a priori information is needed to use predicted aerosol mass concentrations to estimate aerosol impacts on radiation, including aerosol optical depth and visibility, and on cloud microphysical properties, which require estimates of number concentration and cloud nucleating properties. As optical extinction impacts are proportional to aerosol humidified mass, consideration of aerosol hygroscopicity and environmental RH in addition to dry mass (among other controlling factors that include particle shape, size, chemical composition, and mixing state) is required for estimation of optical properties of the aerosol (Seinfeld and Pandis, 2012). Uncertainties and varying assumptions regarding RH-dependent humidified mass concentrations (i.e. in aerosol water contents as functions of humidity) complicate such parameterizations and lead to considerable variability in applied estimates of aerosol optical properties (e.g. Kinne et al., 2006). For the problem of using remote sensing observations to deduce aerosol mass concentrations, these challenges ultimately result in an under-constrained inverse problem, wherein multiple properties of the aerosol, environment, and column distribution can all be adjusted to arrive at values consistent with information retrieved from satellite observations (Dubovik and King, 2000).

Aerosol microphysical impacts on cloud development and precipitation can be similarly treated using underlying assumed aerosol population models. Cloud properties are more sensitive to aerosol particle number concentration than to total aerosol mass, again necessitating models that can link the two values through representations of the particle size distribution. Considerable advancements have been made in the treatment of aerosol microphysical impacts in atmospheric

models across a range of scales from individual cloud models to global circulation and climate models (e.g. Saleeby and van den Heever, 2013, and references therein). Nevertheless, numerous different sets of assumptions and aerosol models exist (Ghan et al., 2011; Khain et al., 2015).

In such use cases for information about aerosol population type, the underlying aerosol models that have been applied to estimate aerosol radiative and microphysical impacts generally represent attempts at optimized or "best-fit" representations. Of course, there is variability in the real atmosphere that such optimized representations cannot capture. Aerosol types do not change step-wise in moving from marine to terrestrial regions, for example, and the cleansed atmosphere after a precipitation event will require some time to re-establish the local ambient aerosol via sources and sinks. This distinction between internal variability within a given population type and external variability between the various types is crucial to understanding measurements of aerosol properties and assessing sensitivity of related phenomena to changes in the aerosol.

In general, systematic studies of the impacts of observed variability on predicted atmospheric phenomena of interest have not been undertaken. Among the studies that have investigated this issue, Clarke et al., (2002) compared in situ measurements of aerosol microphysical and optical properties from a variety of platforms in a remote marine region and found that variability in both time and space constituted an important component of the regional aerosol characterization. Doherty et al., (2005) found similar behavior in a dataset of in situ measurements of aerosol properties in a separate remote marine region, and performed additional analyses to show that variability in some individual aerosol optical properties could result in uncertainties in expected top-of-atmosphere radiative forcing at 550 nm that exceed ~30%. The authors of both studies highlighted the role of RH and associated humidified aerosol growth as a large and unresolved source of uncertainty in their results. Further, as part of instrument and platform inter-

comparisons, both found that differences between measurements of nominally similar air masses were larger than would be expected due to instrumentation uncertainty alone, and used these findings to underscore the difficulty in describing "typical" conditions due to the role of variability in aerosol and environmental properties.

Fundamental among these questions of aerosol sensitivity are the ways in which aerosol properties are parameterized. All aerosol models classify particle populations according to two categories of properties—intensive properties independent of the total amount of aerosol, such as size distribution, composition, mixing state, or mass extinction efficiency, and extensive properties that depend on how much aerosol is present including total particle number or mass concentration, extinction coefficient, and aerosol optical depth. Aerosol population models based on best-fit representations use intensive properties based on some average value and track changes to the extensive amount of aerosol present. Other aerosol models track changes to some combination of intensive and extensive properties, and may or may not have representations of typical internal variability within a given population type. In some cases, aerosol models are simply treated as average values encompassing the representative effects of RH and have no direct relationship to fluctuations in ambient humidity (e.g. MODIS; Remer et al., 2006; Levy et al., 2013). In all of these situations, some information about the aerosol and its impacts are lost—leaving open the question as to whether or not such information is useful. Such questions have been the subject of extensive work in aerosol sensitivity studies based around numerous aerosol intensive, extensive, and environmental properties, and applied to many optical and microphysical processes. Open questions nevertheless remain, and efforts to refine the parameter space where such information is useful can help with modeling, remote sensing, and physical understanding of the role aerosol particles play in marine environments.

1.2. SCIENTIFIC QUESTIONS AND GOALS

This dissertation will present and analyze marine aerosol observations with a specific focus on the role of variability in aerosol and environmental properties both within and between population types. The goal is to utilize such observationally driven findings to identify circumstances where more complex aerosol models that include detailed information about particle intensive properties and internal variability are useful, and where simpler models based primarily on extensive total particle number concentration or mass are sufficient.

I begin with the hypotheses that (1) analyses of observations of remote and littoral marine aerosol can be used to quantify internal and external variability among aerosol populations types, and (2) that these aerosol types and their variability can be utilized to test the relative importance of aerosol intensive properties, extensive properties, and key environmental properties such as RH on estimates of aerosol impacts on radiation and cloud microphysics. Related to the testing of these hypotheses are additional questions connected to the specific studies undertaken in this work:

1. Supervised or subjective methods to classify time periods associated with impacts from specific aerosol sources are potentially subject to bias and may therefore not provide accurate quantifications of variability in aerosol properties. Unsupervised aerosol classification methods have been successfully used in other studies to provide indications of typical values of aerosol properties associated with specific population types (e.g. Tunved et al., 2004; Charron et al., 2008; Salimi et al., 2014; Frossard et al., 2014). I propose that the use of unsupervised classification techniques can adequately classify observations into periods of impacts from distinct population types, and that doing so can provide measures of both

internal and external variability in aerosol population type sufficient for use in subsequent testing of aerosol impacts.

2. Quantifying observed variability in aerosol population types is necessarily associated with the circumstances under which the observations took place (e.g. time, location, and instrumentation utilized for the observations). I propose that examination of marine aerosol populations associated with different sets of observations, instrumentation, and methodologies can improve confidence in the representativeness of the variability results beyond the specific circumstances of one observational dataset.
3. The implications of variability in aerosol properties on initial cloud microphysical properties are associated with the relative role of aerosol intensive and extensive properties. I propose that using the results of a population type classification of marine aerosol can allow for the larger set of aerosol intensive properties (e.g. size distribution, composition, mixing state) to be adequately represented by a simpler population type parameter, and that such a representation will allow for more useful and straightforward analyses of the relative importance of key parameters on initial cloud properties.
4. Fine mode aerosol population models used in some remote sensing retrievals such as MODIS place relatively little importance on capturing a wide range of aerosol intensive properties, while still producing useful retrievals (Remer et al., 2006; Levy et al., 2013). I propose that observations of natural internal variability in aerosol and environmental properties within nominally consistent aerosol population types can be shown in some circumstances to produce fluctuations in optical properties on the same order as that from external variability arising from changes between population types, and that this may explain some of the success associated with relatively simple aerosol models in such retrievals.

1.3. ORGANIZATION

This dissertation presents the results of aerosol and meteorological measurements from two field campaigns, along with several modeling studies that assess the extent to which variability in the results is expected to be relevant to microphysical and optical processes in the atmosphere. It is organized into four primary chapters that address each set of science questions. Additional background, review, and motivation are given within each of the chapters.

Chapter 2 presents aerosol measurements made during a ship-based cruise in the South China Sea, a remote region that included observations of both background marine air masses and impacts by long-range transport of pollution and smoke from biomass burning. The measurements were parameterized, classified into distinct aerosol population types, and quantified in terms of variability in measurements. Chapter 3 describes a similar set of observations and their classification for a relatively clean littoral region along the central coast of California. The results are compared against those from the remote marine region. In Chapter 4, the identified aerosol population type models are used to drive a cloud parcel model and investigate the relevance of aerosol population type variability to initial cloud development in the remote marine region. Chapter 5 investigates the impact of variability in aerosol populations on atmospheric optical properties using an optical reconstruction model, again applying the population type models derived from the observations. Specific relevant conclusions are given in each chapter. A final discussion of general conclusions in regard to the science questions posed above and potential future work is presented in Chapter 6.

2. REMOTE MARINE AEROSOL MEASUREMENTS IN THE MARITIME CONTINENT

In the Southeast Asian Maritime Continent (MC) and South China Sea/East Sea (SCS), aerosol particles are expected to play an important role modulating cloud development, precipitation, and radiative properties that affect heat transfer through the atmosphere (Reid et al., 2013). Assessment of aerosol properties important to understanding such processes in remote marine segments of this region has proven difficult. Extensive cloud cover confounds remote sensing and leads to a clear sky bias in observations (Feng and Christopher, 2013; Reid et al., 2013). Aerosol monitoring has largely been confined to urban centers that are often dominated by local emissions, while in-situ sampling in remote areas has been limited in duration and scope (Irwin et al., 2011; Robinson et al., 2011; Lin et al., 2014; Reid et al., 2015). Airborne measurements have provided some representation of aerosol over wider regions and at various levels (Hewitt et al., 2010; Robinson et al., 2012), but additional questions regarding the representativeness of such point measurements across larger time scales remain. Similarly, the impact of various aerosol sources on surface properties and concentrations in remote marine regions, and their relationship to expected transport pathways and the few remotely sensed column measurements that exist is not well understood. Thus, over these remote ocean regions the aerosol optical and physical properties, their variability in time and space, and the processes controlling aerosol lifecycle have not been well constrained. This uncertainty in the aerosol environment itself comes in addition to uncertainty about its impacts on meteorological processes. Aerosol concentration has been found to relate to cloud development, cloud microphysics, and precipitation formation in the region (Yu et al., 2008; Yuan et al., 2011; Wang et al., 2013), while smoke may affect cloud droplet size distributions and the onset of precipitation, similar to

processes observed in other tropical regions impacted by biomass burning (Rosenfeld, 1999; Andreae et al., 2004). Improved knowledge of the aerosol environment and aerosol-cloud-climate relationships in the Southeast Asian region has therefore been identified as important regionally, and in regards to links with global climate and large-scale aerosol budgets (Reid et al., 2013).

During the May through October Southwestern Monsoon (SWM) season, burning throughout the MC typically reaches its greatest extent between August and early October as precipitation associated with the ITCZ shifts north into Indochina (Reid et al., 2012). The resulting heavy smoke mixes with urban, industrial, marine, and shipping emissions in an exceedingly complex aerosol mixture (Balasubramanian et al., 2003; Atwood et al., 2013; Reid et al., 2013). During this period, aerosol particles from surface sources are generally advected by low level mean winds throughout the SCS, where they are scavenged by precipitation or eventually removed in the monsoonal trough east of the Philippines (Reid et al., 2012, 2015; Wang et al., 2013; Xian et al., 2013). As a result, the region of the SCS and Sulu Sea to the north and east of Borneo has been predicted to be a receptor for much of these biomass burning and pollution emissions from the greater MC during periods when air masses enter more convective phases of the SWM (Reid et al., 2012; Xian et al., 2013).

Remote marine aerosol and its impact on atmospheric processes have been studied in a number of ocean regions (Hoppel et al., 1986; Russell et al., 1994; Jensen et al., 1996; Brechtel et al., 1998; Murphy et al., 1998; Bates et al., 2000; Petters et al., 2006; Quinn et al., 2006). These studies identified a background submicron marine aerosol that is composed of two distinct modes in the number distribution, due to processing by non-precipitating clouds (Hoppel et al., 1986, 1994; Hudson et al., 2015). Bates et al., (2000) linked the differences in the average size

distributions of background marine aerosol in two remote marine regions to regional meteorology, including differences in aerosol residence time and cloud processing. Increased wind speeds lead to increased flux of sea-salt particles into the atmosphere, contributing submicron particles as small as 40 nm in diameter (O'Dowd and Leeuw, 2007; Russell et al., 2010; de Leeuw et al., 2011; Bates et al., 2012; Modini et al., 2015). Non-seasalt-sulfate and organic matter from marine sources also comprise large fractions of the submicron aerosol mass loading in clean and background marine air masses (Murphy et al., 1998; Cavalli et al., 2004). As air masses from more terrestrial or anthropogenically-influenced regions advect over remote marine regions, submicron size distributions and chemical compositions often diverge from background conditions (Bates et al., 2000; Quinn et al., 2006). More recent studies have further quantified the role of various processes in shaping the marine aerosol population, including primary and secondary production, aging, and mixing with non-marine sources (Allan et al., 2009; Russell et al., 2010; de Leeuw et al., 2011; Bates et al., 2012; Prather et al., 2013; Frossard et al., 2014; Modini et al., 2015). In particular, the contribution of dissolved organic components in the sea surface micro layer to aerosol produced by bubble breaking has been noted, with increasing organic enrichment as size decreases (Russell et al., 2010; Bates et al., 2012; Prather et al., 2013; Quinn et al., 2014). Additional studies into the source dependent composition of marine aerosol have indicated non-marine sources can be important contributors to aerosol in marine regions. Shank et al., (2012) found evidence of biomass burning and combustion impacts on remote marine MBL aerosol, including in nominally clean marine conditions. These authors also noted the limited importance of organic components in particulate matter in a tropical Pacific location, as compared to other regions where organics were a more important fraction of the submicron aerosol. Frossard et al., (2014) found influences on aerosol organic matter from

shipping and mixing with non-marine sources in 63% of observations across five ocean regions. Modini et al., (2015) evaluated the contribution of primary marine aerosol to cloud condensation nuclei (CCN) number concentrations, and found that it accounted for less than 10% of CCN active at 0.9% supersaturation during low wind conditions, with increasing importance (up to 58% of CCN) at higher wind speeds and lower environmental supersaturations. Taken as a whole, recent understanding of marine aerosol indicates that the background marine aerosol and primary marine emissions can be complex and play an important role in cloud, radiative, and precipitation processes, and that other sources of aerosol contribute to number and mass concentrations, even in relatively clean and/or remote regions.

Two research cruises were conducted in the remote marine boundary layer (MBL) of the SCS and Sulu Sea during the 2011 and 2012 SWM seasons to perform in situ aerosol and meteorological measurements, and to investigate marine aerosol and its impacts on clouds, precipitation, and climate as it reflects the complex set of sources in the region (Reid et al., 2015, 2016). Here, we present observations of aerosol and CCN characteristics during the second cruise, along with their relationship to aerosol source type, air mass, and meteorological phenomena. These measurements represent the first in situ observations of size-resolved CCN properties in the area, and fill a gap in knowledge needed to assess aerosol-cloud-precipitation relationships in the data poor remote marine SCS region.

2.1. METHODS AND CRUISE DESCRIPTION

The SCS research cruises occurred during the month of September in both 2011 and 2012, and took place aboard the 35m, 186 ton *M/Y Vasco*, operated out of Manila by Cosmix Underwater Research Ltd. A thorough description of the vessel and instrumentation for the 2011 and 2012

cruises can be found in Reid et al. (2015) and Reid et al. (2016), respectively. Here we are concerned with the 2012 cruise, which departed Manila on 4 September from Navotas, Manila Bay, and returned on 29 September. The sampling strategy for these cruises involved moving between various anchorages in the SCS and Sulu Sea around the Palawan Archipelago. Sampling occurred throughout the cruise, but aerosol measurements were shut down or invalidated and removed from the dataset during periods when representative sampling could not be achieved (i.e. measured relative wind not from over the ship bow, leading to potential self-sampling; see Reid et al., (2016) for more details). Remaining periods of self-sampling of ship emissions were identified by anomalous size distributions and high particle number concentrations, and were removed from the data set before analysis. The size-resolved CCN system (Petters et al., 2009) that provided the bulk of the measurements reported here had a computer failure that, once fixed, limited reliable measurements to primarily the last two weeks of the cruise, hence we focus here on data from 14–26 September 2012. This period included several transits along the east side of Palawan Island, stationary measurements at an anchorage between Palawan and Borneo (7.86N, 116.94E), and two anchorages at Tubbataha Reef in the middle of the Sulu Sea (8.80N, 119.26E).

2.1.1. *Aerosol Measurements*

A DMT Passive Cavity Aerosol Spectrometer Probe (PCASP) X2 configured in an aviation pod with heated inlet was mounted at the *Vasco* top mast approximately 10 m above the water surface to provide optical measurements of dry particle size distributions between approximately 125 nm and 3 μm. Additional aerosol instrumentation was located in a forward locker, below and slightly behind the aerosol inlet. Sampled air was fed to the locker via a 3 cm diameter, 4 m long inlet located next to the PCASP. Although the inlet was not aspirated, several high flow rate

nephelometers sampling from the inlet ensured low residence time in the sample line. Further details and additional instrumentation are discussed in Reid et al. (2016). A size resolved CCN system sampled air from the inlet just inside the instrument locker with an approximately 2 m, 0.635 cm diameter copper tube. A URG cyclone with an approximate 1 μm 50% size cut was used to remove the largest particles from this CCN sampling line, including coarse mode sea-salt, to minimize wear and corrosion on downstream components. The sample was then dried using a Permapure poly-tube Nafion dryer with low pressure sheath air to RH values below 30%, as verified by occasional in line checks using a handheld Extech Hygro-Thermometer.

Approximately 1.1 liters per minute (lpm) were drawn through the size resolved CCN system, which was comprised of an x-ray neutralizer (TSI Model 3087) and a TSI 3080 Electrostatic Classifier with a long DMA column (TSI Model 3081) for quasi-mono-disperse particle sizing, preceded by a 0.071 cm orifice (0.69 μm 50% cutpoint diameter) impactor. The DMA was operated with a sheath flow rate of 5 lpm (liters per minute) and sample flow rate of 1.1 lpm. The sample flow was then split between a TSI 3782 Water Condensation Particle Counter (CPC) with a flow rate of 0.6 lpm, and a DMT Cloud Condensation Nuclei Counter (CCNc) with a flow rate of 0.5 lpm. Flow rates used to calculate number concentrations were calibrated using a Gilibrator (Models 800285 & 800286) system, with in-line measurements conducted prior to each CCNc supersaturation calibration session as noted below.

The size-resolved CCN system measured CN and CCN (activated particles at a CCNc set-point supersaturation) concentrations in each of 30 quasi-mono-disperse size bins between 17 nm and 500 nm. The CCNc was operated at five temperature gradient settings and calibrated using ammonium sulfate (following the methods described by Petters et al., 2009) to measure the corresponding maximum environmental supersaturation within the CCNc column. The scan of

all 30 size bins at each supersaturation took approximately 15 minutes, while a complete measurement over all 5 supersaturation settings took approximately two hours due to pauses between settings while column temperatures stabilized. The measured CN and CCN particle counts were inverted using the methodology of Petters et al. (2009). The inversion yielded the dry ambient aerosol size distribution over the measured range ($dN/d\log_{10}D_p$ for $17 \leq D_p \leq 500$ nm) and the equivalent distribution of CCN particles activated at each supersaturation ($dCCN/d\log_{10}D_p$). The activated fraction spectrum was then calculated as the fraction of total particles that formed droplets (CCN/CN) at each diameter. Each activated fraction spectrum was then fit using a three parameter fit similar to the approach of Rose et al. (2010). The diameter at which 50% of particles in the fit had activated (D_{50}) was used to calculate the associated hygroscopicity parameter, κ (Petters and Kreidenweis, 2007). Full calibration of the CCN system flow rates and supersaturations took two to five hours to complete, and was therefore conducted four times throughout the study on 15, 20, 27 and 29 September to limit measurement downtime. Each calibration session involved running a calibration scan at each CCNc temperature gradient setting (with two full scans conducted at each setting on 27 Sep) yielding a total of five calibrations per setting throughout the cruise. Calibrated supersaturation set-points and their respective standard deviations were 0.14% ± 0.01, 0.38% ± 0.01, 0.52% ± 0.01, 0.71% ± 0.02, and 0.85% ± 0.03, with no significant trend or calibration drift noted during the cruise. The measured range of 0.14% to 0.85% supersaturation was selected based on values that could both be reliably measured by the CCNc instrument and represented supersaturations expected in the region where aerosol effects may be relevant, ranging from marine stratocumulus with peak supersaturations often below 0.2% to highly convective clouds with supersaturations above 1% (Reutter et al., 2009; Ward et al., 2010; Tao et al., 2012).

As the SCS environment tended to have relatively few particles smaller than 50 nm, only the measurements at the 0.14% and 0.38% supersaturation settings had complete activation curves that spanned the measured particle diameter range. For the higher supersaturation settings, the D_{50} diameter tended to occur at small diameters with low CN and CCN concentrations, thereby increasing uncertainty in the associated κ values. As a result, κ values were only reported for the 0.14% and 0.38% supersaturation settings. In addition, rather than continuously running a full two-hour scan across all supersaturation settings, individual scans (approximately 15 minutes) were run more often for the 0.14% and 0.38% settings to take advantage of this outcome. The range of κ values measured for the particles active at supersaturations of 0.14% and 0.38% was typically between about 0.3 and 0.8, although the full range was between 0.2 and 1.1 (Figure 2.2e&f). The D_{50} diameters for these hygroscopicity values spanned approximately 96 to 150 nm (κ range: 0.8 – 0.2) for the 0.14% supersaturation setting, and 45 to 80 nm (κ range: 1.1 – 0.2) for the 0.38% setting. The hygroscopicity measurements were therefore more indicative of accumulation mode hygroscopicity during the 0.14% scans and Aitken mode hygroscopicity during those at 0.38%. Additionally, particles outside these size ranges were not well quantified by these measurements.

2.1.2. *Ancillary Measurements and Products*

Additional measurements of aerosol composition were used to validate identified source types impacting the measurements throughout the cruise. A series of $PM_{2.5}$ filters were collected by 5 lpm Minivol Tactical Air Samplers with sampling periods that varied between one and two and a half days, and were analyzed for elemental concentrations by gravimetric, XRF, and ion chromatography methods, and organic and black carbon concentrations by the thermal-optical methods (Reid et al., 2016). Trace gas concentrations were measured intermittently throughout

the cruise by whole-air gas samples for gas chromatography analysis, as discussed further in Reid et al. (2016).

A suite of weather monitoring instruments was located on a 3m bow mast to provide coincident meteorological measurements throughout the study. From this suite, wind speed and wind direction measurements from a Campbell sonic anemometer were used to identify gust front passage. An OTT Parsivel disdrometer was utilized to measure precipitation, from which only the rain rate measurements were used in this analysis.

Several remote sensing and model products were used to characterize the wider SCS atmospheric environment and to identify potential aerosol sources. MODIS visible and IR products were used to identify convection and squall line propagation across the SCS. The MODIS Collection 6 MOD08 Level 3 daily Aerosol Optical Depth products were utilized for AOD measurements in the region, though cloud cover obscured measurements throughout much of the study. MODIS active fire hotspot analysis and the FLAMBE smoke flux product from Terra and Aqua were used to identify the locations and times during which fires were burning in the MC (Giglio et al., 2003; Reid et al., 2009; Hyer et al., 2013). Simulations from the Navy NOGAPS model were used to represent surface and 700 hPa winds, interpolated to one-degree spatial resolution and averaged over the study period, to provide an estimate of typical aerosol transport pathways (Hogan and Rosmond, 1991; Xian et al., 2013). Finally, the Navy Aerosol Analysis and Prediction System (NAAPS) was used to predict smoke and sulfate aerosol mass concentrations at the surface along the *Vasco* ship track (Lynch et al., 2016).

The NOAA Hybrid Single Particle Lagrangian Integrated Trajectory (HYSPLIT) Version 4.9 model (Draxler et al., 1999; Draxler and Hess, 1997, 1998) was used to generate daily 72-hour

backtrajectories (spawned at 0Z, 8 AM local) from the *Vasco* location with arrival heights of 500m to indicate likely marine boundary layer transport patterns. The GDAS1, 1° x 1° HYSPLIT meteorological dataset was used to drive the model. Trajectory paths were found to be largely influenced by synoptic scale changes in the regional meteorological state of the atmosphere, with no substantial differences due to arrival time of day. Arrival heights between 100 m and 3000 m were examined. Trajectories with arrival heights below 1000 m were generally consistent and representative of boundary layer transport (Atwood et al., 2013; Xian et al., 2013), while higher heights tended to be increasingly influenced by free troposphere transport pathways with a more westerly component. As such, 500 m was selected to be representative of general shifts in synoptic scale boundary layer transport pathways, though more complex vertical interactions and mixing from aloft are a potential influence in the region (Atwood et al., 2013). Trajectory lengths of 72 hours were found to be sufficient to demonstrate general transport path differences between ocean dominated regions of the central portion of the SCS and more terrestrially influenced regions that passed closer to Borneo and Sumatra.

2.1.3. *Aerosol Population Type Classification*

The $dN/d\log_{10}D_p$ dry particle size distributions obtained every 15 minutes from the CCN system were first normalized by the particle number concentration summed over all bins. Each of these normalized size distributions was then parameterized by fitting a lognormal mixture distribution using an algorithm based on Hussein et al., (2005). This algorithm fit each distribution to one, two, or three lognormal modes, each defined by three lognormal distribution parameters (median diameter, geometric standard deviation, and fractional number concentration). Two modes were identified as the best fit for 690 of 731 data points in this dataset. In order to have a common point of comparison for classification purposes the two-mode fit was used for all data points,

yielding a parameterized Aitken and accumulation mode for each 15-minute data point. Data points for which the fitting algorithm selected an additional third mode are noted and discussed further in the clustering results section.

Parameters associated with each data point were then used to cluster the data points into groups based on similar observed aerosol properties. Cluster analyses have long been used to group observed aerosol size distributions into clusters of generally similar size distributions (Tunved et al., 2004), which can then be associated with various sources or atmospheric processes that shaped them (Charron et al., 2008; Beddows et al., 2009; Wegner et al., 2012). Similar cluster analyses have been utilized to classify aerosol types based on particle chemistry (Frossard et al., 2014), with Frossard et al., (2014) identifying clusters in marine aerosol observations associated with marine and non-marine aerosol types. As pointed out by those authors, the clustering approach can be superior to algorithms using simpler criteria to distinguish "clean" from "polluted" conditions, as more variables and a measure of similarity between data points are used to find the underlying population types. In this study normalized size distribution parameters were combined with total number concentration and particle composition information via hygroscopicity measurements to serve as input variables for the cluster analysis (parameters given in Table 2.1). As hygroscopicity data were available for at most one mode (during the 0.14% or 0.38% supersaturation scans), Aitken and accumulation mode hygroscopicities were treated as missing for data points without this information. In order to account for missing data and adjust all clustering variables to the same scale, each variable was first standardized to a mean of zero and standard deviation of one, with missing data points imputed to a value a zero (the mean value). As a result, the clustering distance function was insensitive to missing data, but still included information on hygroscopicity when available.

A hierarchical cluster analysis was first conducted using the *cluster.AgglomerativeClustering* class of the Python scikit-learn package (Pedregosa et al., 2011) using the Ward linkage to help ascertain the number of clusters that can be found in the dataset. Each step in this process involved merging two data points or clusters into a new cluster based on those points with the shortest distance between normalized input measurements (Karl Pearson distance function; Wilks, 2011). A dendrogram and associated measure of the distance between merged clusters for each subsequent clustering step was used to identify potential numbers of clusters appropriate for the dataset. The distance between merged clusters increases at steps that merge substantially different clusters (Wilks, 2011), in this case indicating 5, 8, 9, and 12 clusters as potentially appropriate for this data set.

A nonhierarchical K-Means cluster analysis was then conducted for each of these four potential cluster numbers using the scikit-learn *cluster.KMeans* class to refine the cluster members. The appropriate number of clusters was selected based on the K-Means result with the least number of clusters that maintained physically distinct and temporally consistent aerosol populations for the associated clusters. In particular, as the timestamp of a data point was not included in the cluster analysis, clusters with smaller numbers of data points were considered distinct if they all occurred during a narrow time frame that could be associated with a transient atmospheric phenomenon. The time frames of all clusters were then compared against other aerosol and meteorological observations to ensure they were physically meaningful. The result was a set of eight identified aerosol population types with associated time periods corresponding to the 15-minute CCN system data points. Finally, size distribution and hygroscopicity measurements were averaged for all time periods associated with each population type.

2.2. OVERVIEW OF STUDY

The daily positions of the *Vasco* during the two weeks in September 2012 that comprise this study are shown in Figure 2.1a, together with HYSPLIT 72-hour backtrajectories initiated within the MBL. Several extended periods at the same anchorage are noted by the range of dates spent at these locations. The daily fire hot spots are also indicated in this figure. Average NOGAPS surface winds in the boundary layer were from the southwest, often advecting air parcels from near Borneo, while lower free tropospheric winds, such as those at 700 hPa, were more westerly

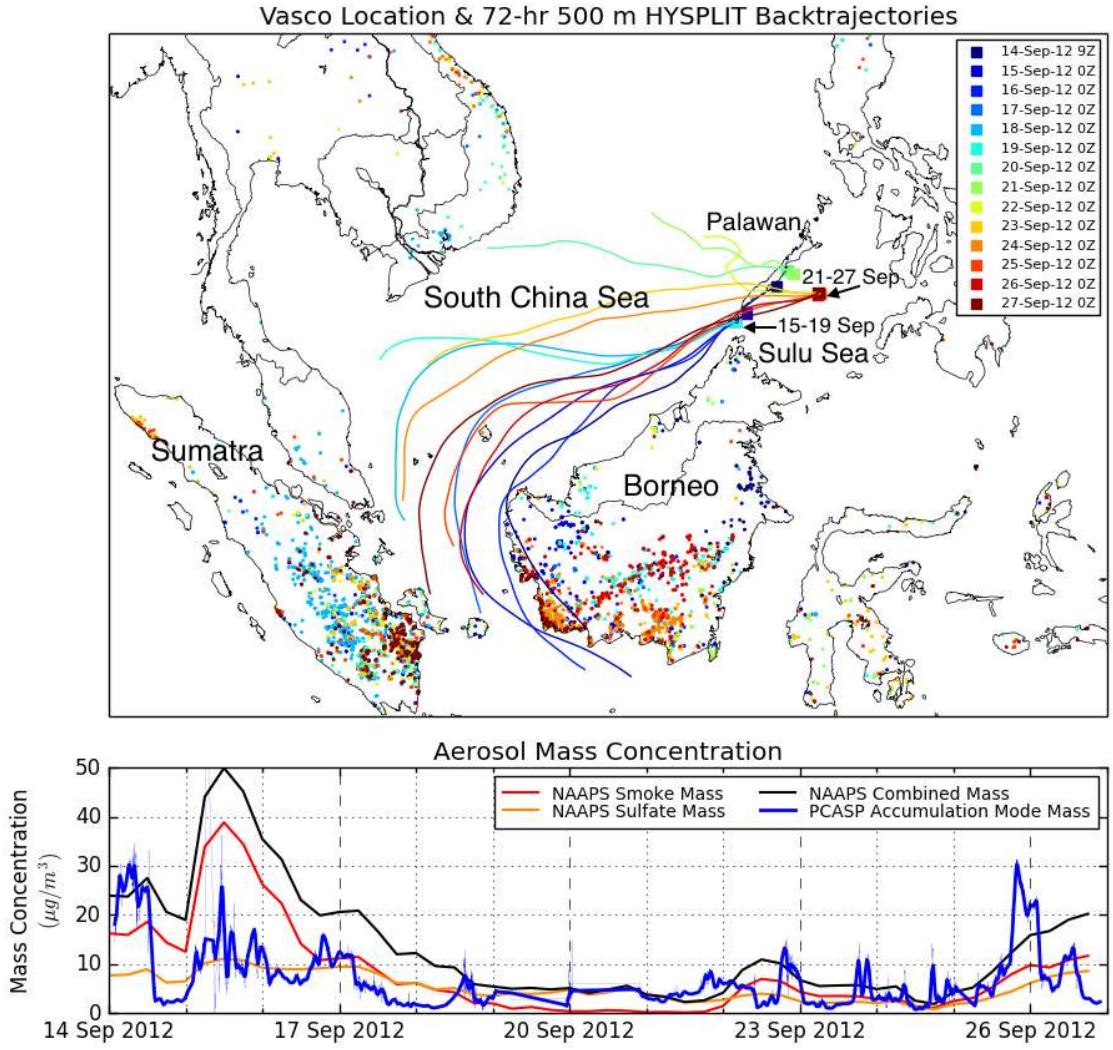

Figure 2.1 (a) *Vasco* cruise locations (squares) and 72-hour, 500 m HYSPLIT backtrajectories; MODIS fire detections (dots) from Terra and Aqua are included for each day (color coded) during the sampling period. (b) PCASP reconstructed accumulation mode (125nm – 800nm) mass concentration (assumed density 1.4 μg m^{-3}) and NAAPS estimated smoke and sulfate mass concentration along the *Vasco* ship-track.

due to the generally veering structure of the lower atmosphere in the SCS (Reid et al., 2016). Fires detected by MODIS occurred throughout much of Borneo and Southern Sumatra during the study, with surface-level trajectories near the start and near the end of the study period passing close to active fires, whereas those during the middle period remained primarily over open ocean. Results from the NAAPS model, along with limited satellite AOD measurements not obscured by clouds during this period, confirmed this general smoke transport pathway. Accumulation mode aerosol mass concentration estimates (Figure 2.1b) were initially generated from the PCASP measurements using a density of 1.4 μg m^{-3} (Levin et al., 2010), assumed to be representative of a combination of smoldering peat and agricultural fire emissions typical in the MC (Reid et al., 2012) that constituted the largest plumes observed during the study (Reid et al., 2016). Coincident model estimates generated by NAAPS along the ship track indicated generally similar results, with the highest mass concentrations occurring early and late in the measurement period, in general agreement with times during which backtrajectories passed over terrestrial sources and active fires. Air parcels advecting into the SCS and Sulu Sea during this period that originated from areas further to the north and west were cleaner than those from other sectors due to fewer emission sources and more precipitation along the trajectories. Changes in the observed particle concentrations also occurred on timescales shorter than these weekly large-scale variations, as shown in the aerosol observation timelines in Figure 2.2a–c. Many of these higher-frequency fluctuations were associated with squall line passages and heavy local precipitation, as discussed further below. The timeline of dN/dlogDp size distributions, as measured by the CCN system and shown in Figure 2.2a, indicated that most of the particle number concentration fell within the 17–500 nm measurement range, except possibly during the

highest-concentration periods. A more extensive comparison of model and satellite measurement in situ observations is discussed in Reid et al. (2016).

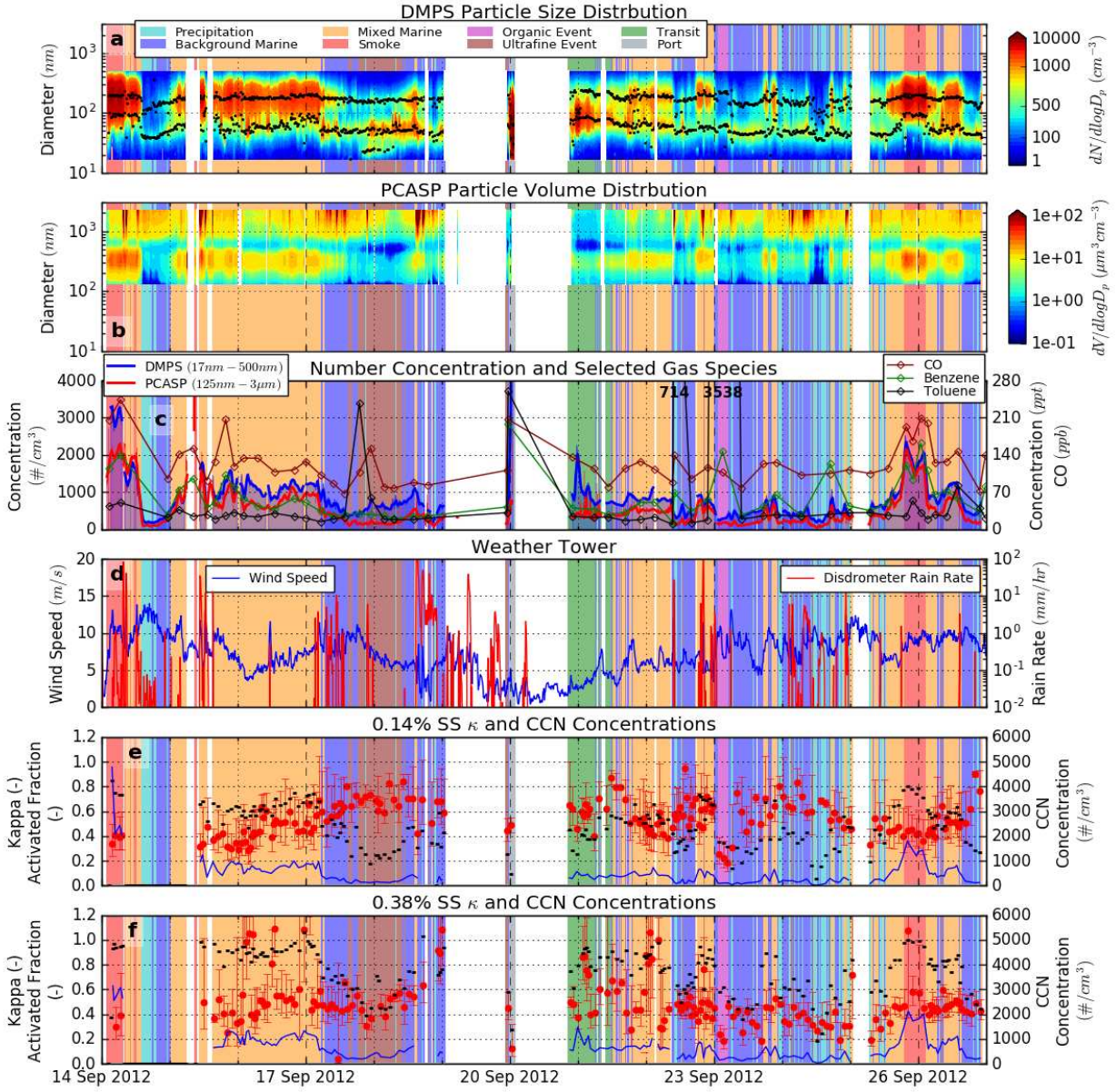

Figure 2.2 Timelines of measured and derived variables during *Vasco* 2012 cruise. In all figures, background colors correspond to aerosol type classification from the cluster analysis, as indicated in the legend in panel a. (a) $dN/dlogD_p$ spectra from the CCN system measurements with black dots at best-fit modal median diameters; (b) $dV/dlogD_p$ spectra derived from the PCASP measurements; (c) total number concentrations measured by the CCN system (blue; shaded below for contrast) and the PCASP (red), with 60 minute boxcar average smoothing; gas canister grab sample concentrations for carbon monoxide, benzene, and toluene are shown on the right axis with colored numbers indicating points above the upper scale extent; (d) wind speed and disdrometer rain rate from the *Vasco* weather tower. (e & f) κ parameter (red) and CCN concentrations (blue) for 0.14% and 0.38% supersaturation settings (corresponding approximately to accumulation and Aitken modes, respectively), with total activated particle number fractions ($CCN_{SS\%}$ / CN_{Total}) bars in black. Error bars on κ data points indicate the κ values associated with 25% / 75% activated fraction curve fits.

2.3. AEROSOL POPULATION TYPE CLASSIFICATION AND PROPERTIES

The cluster analysis was first conducted to investigate potential aerosol population types in the dataset, followed by physical interpretation of the results against cluster aerosol properties, coincident measurements, and meteorological conditions. The parameter values input to the cluster analysis are shown for each data point and variable in Figure 2.3, and colored by cluster number for the results of the eight-cluster K-Means analysis. The average value and intra-cluster standard deviation for each cluster parameter and cluster are given in Table 2.1. Normalized size distributions for each of these eight aerosol populations are shown in Figure 2.4; the average CN and CCN number concentrations and hygroscopicities are given in Table 2.2. Equivalent normalized volume distributions are shown in Figure 2.5. The cluster number associated with each measurement is similarly shown as the background color in Figure 2.2. The aerosol properties, meteorological conditions, and likely transport pathways associated with data points in each cluster were then used to provide a physical interpretation of the results and identify each population type on the basis of its likely sources as discussed below. Clusters 1-4 were the most commonly found (representing 85% of the total observations, Table 2.2), while clusters 5-8 represented special cases, generally of short duration, that could be identified by specific locations or sampling conditions.

Table 2.1 Aerosol population type parameters used for clustering and the resulting average values (standard deviations in grey parentheses) for each identified population.

Population Type	Total Number	Aitken Mode				Accumulation Mode			
	Concentration (# cm^{-3})	Median (nm)	Geometric Std Dev	Number Fraction	Kappa	Median (nm)	Geometric Std Dev	Number Fraction	Kappa
1: Back. Marine	510 (181)	50 (7)	1.45 (0.05)	0.57 (0.08)	0.46 (0.17)	162 (18)	1.55 (0.10)	0.42 (0.09)	0.65 (0.11)
2: Precipitation	361 (164)	42 (5)	1.40 (0.10)	0.50 (0.12)	0.34 (0.11)	115 (27)	1.91 (0.20)	0.51 (0.12)	0.54 (0.14)
3: Smoke	2280 (606)	89 (15)	1.53 (0.17)	0.20 (0.06)	0.56 (0.25)	199 (9)	1.55 (0.04)	0.81 (0.06)	0.40 (0.03)
4: Mixed Marine	975 (271)	62 (13)	1.54 (0.18)	0.32 (0.13)	0.54 (0.23)	184 (17)	1.61 (0.08)	0.68 (0.12)	0.48 (0.10)
5: Organic Event	277 (30)	61 (2)	1.45 (0.04)	0.66 (0.01)	0.21 (0.03)	221 (8)	1.48 (0.05)	0.34 (0.01)	0.22 (0.03)
6: Ultrafine Event	577 (158)	50 (6)	1.69 (0.16)	0.82 (0.08)	0.50 (0.10)	174 (19)	1.30 (0.07)	0.19 (0.06)	0.65 (0.09)
7: Transit	976 (384)	80 (6)	1.53 (0.12)	0.73 (0.11)	0.62 (0.16)	209 (42)	1.50 (0.21)	0.26 (0.11)	0.58 (0.08)
8: Port	4890 (2550)	42 (22)	1.62 (0.37)	0.49 (0.18)	0.13 (-)	87 (26)	1.57 (0.22)	0.53 (0.18)	0.49 (-)

Table 2.2 Average values (standard deviations in parentheses) for identified aerosol population types. Shown are number of CCN system data points classified as each type, total number concentrations for the PCASP (125 nm–3 µm) and CCN system (17–500 nm), CCN number concentrations and activated fractions for each CCNc supersaturation set point, and measured κ values for the accumulation mode (0.14% SS) and Aitken mode (0.38% SS) set points.

Population type	No. meas.	PCASP number		CCN system number		0.14 % SS CCN		act. frac.		κ		0.38 % SS CCN		act. frac.		κ	
	(No.)	(no. cm^{-3})		(no. cm^{-3})		(no. cm^{-3})		(–)		(–)		(no. cm^{-3})		(–)		(–)	
1: Back. marine	214	231	(111)	510	(181)	213	(101)	0.38	(0.09)	0.65	(0.11)	320	(148)	0.60	(0.12)	0.46	(0.17)
2: Precipitation	67	142	(79)	361	(164)	96	(58)	0.24	(0.11)	0.54	(0.14)	243	(135)	0.48	(0.15)	0.34	(0.11)
3: Smoke	44	1800	(273)	2280	(606)	1720	(388)	0.72	(0.04)	0.40	(0.03)	2340	(480)	0.93	(0.02)	0.56	(0.25)
4: Mixed marine	294	689	(295)	975	(271)	591	(201)	0.58	(0.08)	0.48	(0.10)	827	(270)	0.83	(0.07)	0.54	(0.23)
5: Organic event	11	151	(19)	277	(30)	88	(10)	0.31	(0.02)	0.22	(0.03)	144	(9)	0.53	(0.01)	0.21	(0.03)
6: Ultrafine event	59	163	(58)	577	(158)	138	(45)	0.25	(0.06)	0.65	(0.09)	361	(172)	0.56	(0.11)	0.50	(0.10)
7: Transit	36	311	(44)	976	(384)	363	(87)	0.37	(0.06)	0.58	(0.08)	772	(263)	0.81	(0.09)	0.62	(0.16)
8: Port	6	671	(210)	4890	(2550)	251	(–)*	0.09	(–)*	0.49	(–)*	1126	(–)*	0.26	(–)*	0.13	(–)*
All types	731	503	(455)	851	(677)	450	(388)	0.47	(0.16)	0.54	(0.14)	675	(516)	0.72	(0.17)	0.50	(0.21)

Population type	0.53 % SS CCN		act. frac.		0.71 % SS CCN		act. frac.		0.85 % SS CCN		act. frac.	
	(no. cm^{-3})		(–)		(no. cm^{-3})		(–)		(no. cm^{-3})		(–)	
1: Back. marine	416	(194)	0.74	(0.11)	444	(239)	0.81	(0.09)	480	(210)	0.87	(0.05)
2: Precipitation	352	(175)	0.65	(0.15)	265	(82)	0.71	(0.09)	228	(100)	0.79	(0.03)
3: Smoke	1990	(359)	0.97	(0.02)	2080	(396)	0.98	(0.05)	2150	(523)	0.99	(0.02)
4: Mixed marine	861	(247)	0.89	(0.10)	876	(244)	0.94	(0.06)	893	(271)	0.96	(0.05)
5: Organic event	182	(26)	0.72	(0.01)	268	(56)	0.89	(0.14)	257	(24)	0.93	(0.07)
6: Ultrafine event	373	(168)	0.65	(0.12)	439	(163)	0.72	(0.07)	473	(147)	0.79	(0.10)
7: Transit	832	(423)	0.87	(0.05)	877	(370)	0.90	(0.02)	878	(195)	0.95	(0.03)
8: Port	3936	(–)*	0.40	(–)*	1742	(289)	0.57	(0.22)	2080	(–)*	0.45	(–)*
All types	698	(555)	0.79	(0.15)	724	(512)	0.85	(0.13)	723	(502)	0.90	(0.10)

* Only one data point. Note that port measurements fluctuated as the *Vasco* entered port.

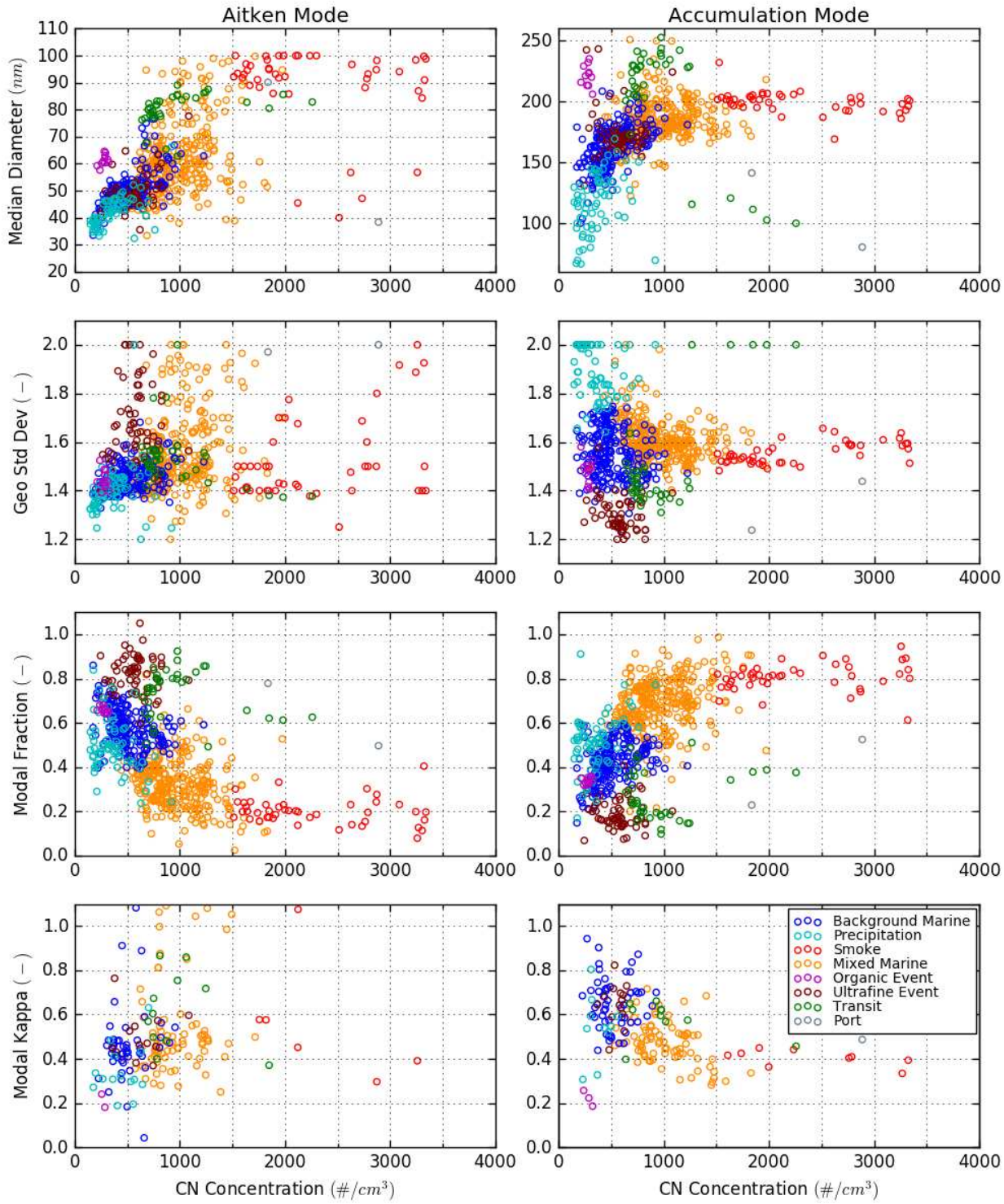

Figure 2.3 Parameterized variable values for Aitken and accumulation modes (median diameter, geometric standard deviation, modal fraction) at each of the 15 minute data points during the study, along with κ values for data points at CCNc superstation set points of 0.38% (Aitken mode) and 0.14% (accumulation mode). Each data point is colored according to the cluster type to which it was classified.

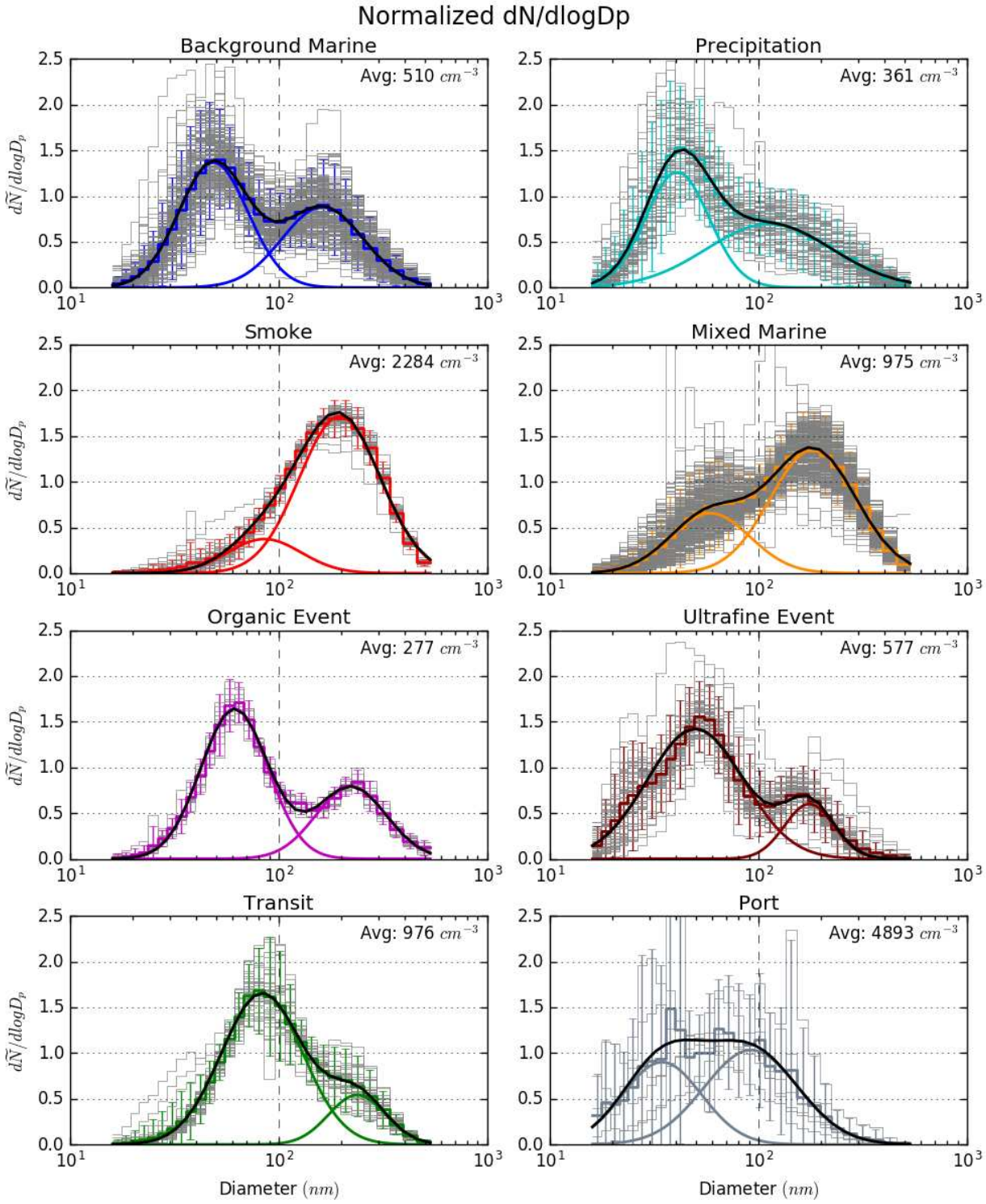

Figure 2.4 Normalized $dN/dlog_{10}D_p$ particle size distributions for each spectrum within identified aerosol population types (grey), the associated average bin values with error bars at 95% confidence interval (colored step lines; 1.96 * bin standard deviation), and best fit lognormal modes (colored curves) with bimodal fit (black). The average particle number concentrations of data points within each population type are listed.

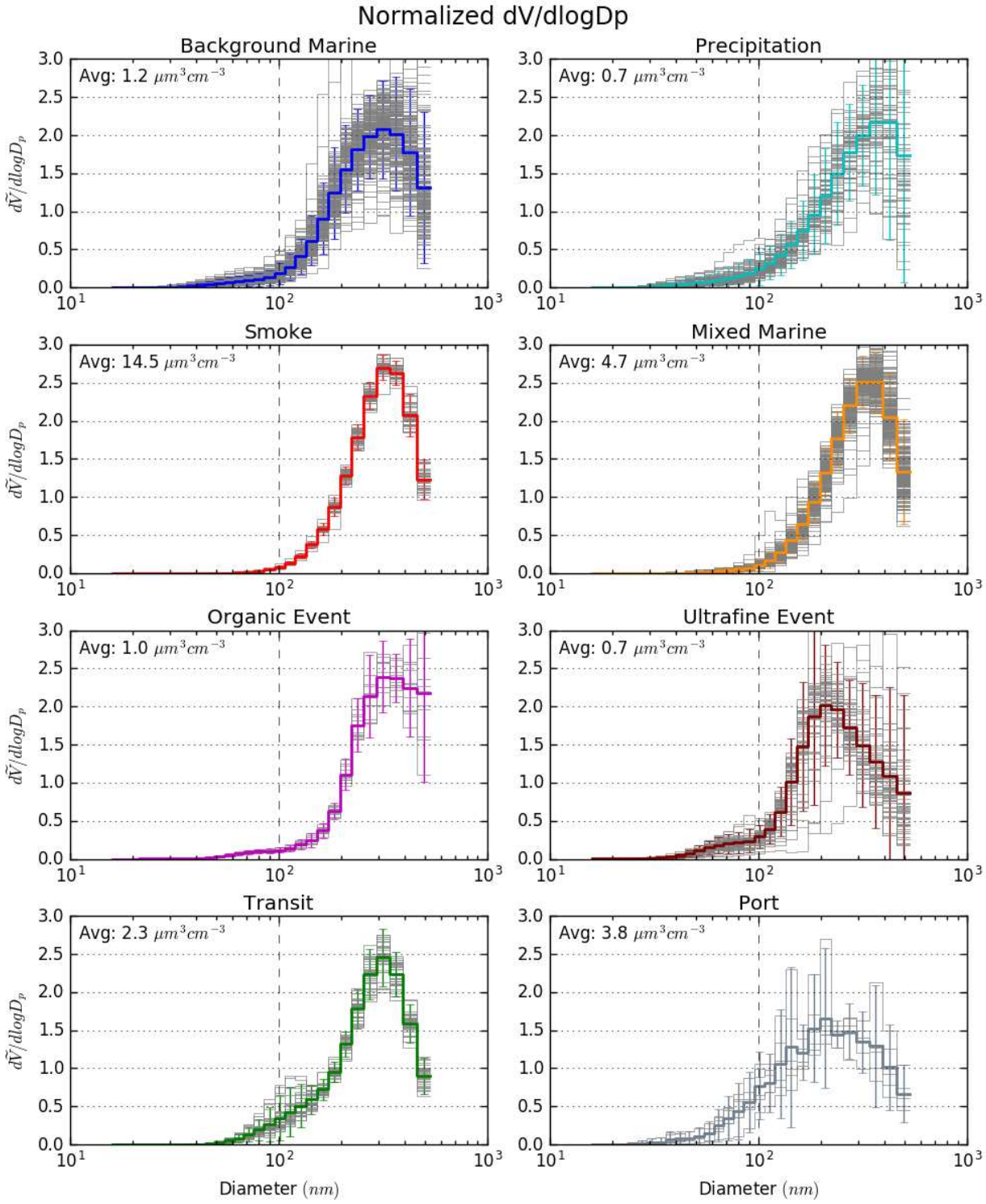

Figure 2.5 Normalized dV/dlog$_{10}$D$_p$ particle size distributions for each spectrum within identified aerosol population types (grey), the associated average bin values with error bars at 95% confidence interval (colored step lines; 1.96 * bin standard deviation). The average particle volume concentrations of data points within each population type are listed.

1. Background Marine: Data points associated with this cluster occurred throughout the study, typically following rain in the vicinity of the *Vasco* or transport from areas further removed from terrestrial regions. In addition, this type was observed following shortly after periods associated with each of the other identified clusters, often appearing as a transition between other types (Figure 2.2). The measured properties of this population type were similar to the background marine aerosol reported in many prior studies (Hoppel et al., 1994; Jensen et al., 1996; Brechtel et al., 1998; O'Dowd et al., 1997; Heintzenberg et al., 2004; Allan et al., 2009; Good et al., 2010). The population featured a bimodal size distribution with a Hoppel minimum near 90 nm. The inner quartile range (IQR: middle 50% of observations between the 25%–75% percentiles) of number concentrations ranged from 382 to 623 cm^{-3}, with on average 42% of the total number concentration residing in the accumulation mode as specified by the bimodal fit. Modal hygroscopicities were found to average 0.65 for the accumulation mode and 0.46 for the smaller Aitken mode, while activated fractions were generally moderate across the range of measured supersaturations as compared to other identified population types (Table 2.1). Each of these findings further reinforced the classification of this cluster as a typical background marine aerosol.
2. Precipitation: This distribution was found during periods immediately following extensive precipitation at or near the *Vasco* (Figure 2.2d). Air masses had been substantially scrubbed of particles and accumulation mode particles had been preferentially removed. While the number concentrations of large-mode particles were lower than those in the background marine periods, the number concentrations of smaller particles, particularly those below 40-50 nm, were comparable to the background marine type. The longest contiguous period of this type occurred on 14 Sept. immediately following the passage of a squall line observed in

the satellite visible and IR products (not shown) that left a clean air mass with fewer than 200 cm^{-3} measured in the 17-500 nm range in its wake. Number concentrations tended to be lower than the background marine type with an IQR from 227 to 441 cm^{-3}. Hygroscopicities were similarly lower than the background marine population with κ values of 0.54 and 0.34 for the accumulation and Aitken modes, respectively. Total CCN concentrations across all supersaturations were found to be lower than in background marine air masses due to the combination of fewer total particles, generally smaller particle sizes, and lower hygroscopicities.

3. Smoke: Data points associated with this aerosol type occurred primarily in two events on 14 Sept. and 25-26 Sept., during which backtrajectories were at their furthest south, near burning regions in Borneo (Figure 2.1a). Normalized size distributions indicated that particles were largely concentrated in a single accumulation mode with a tail of smaller particles. This type was associated with the highest total particle number and estimated submicron mass concentrations observed during the cruise, with the exception of measurements taken in the urban plume of Puerto Princesa. The standard deviations in the normalized size distribution parameters for the dominant accumulation mode in this population (Figure 2.4, Table 2.1) were small, even while number concentration varied widely (IQR 1802 to 2780 cm^{-3}; 81% accumulation modal fraction). Accumulation mode hygroscopicities were lower than either the background marine or precipitation types, with average κ values of 0.40. Aitken mode hygroscopicities showed the opposite behavior from the first two population types with higher κ values of 0.54, though the measured uncertainties (Figure 2.2 e&f) and standard deviations were considerably higher than for the accumulation mode (0.25 and 0.03, respectively). Interestingly, activated fractions were highest among all

population types across the full range of measured supersaturations, owing to the large number fraction of particles in the accumulation mode, while CCN concentrations were the highest of all types (except those measured in port) due primarily to the larger total particle number concentration in these smoke plumes.

Accumulation mode lognormal median diameters around 200 nm with a tail of smaller particles, elevated concentrations of carbon monoxide and benzene, as well as potassium in filter samples during this period (Reid et al., 2016; Figure 2.2c) were all consistent with expectations for aged biomass burning smoke (Yokelson et al., 2008; Akagi et al., 2011; Reid et al., 2015; Sakamoto et al., 2015). Additional examination and attribution of this event to biomass burning in Sumatra and Borneo is discussed further in Reid et al., (2016). Finally, while smoke is considered the dominant aerosol source during these periods, anthropogenic pollution may still have been co-emitted along the transport path and contributed to measured results.

4. Mixed Marine: This population was characterized by periods during which the background marine type mixed with other sources of aerosol. Most of the data points associated with this type had transport pathways and biomass burning sources similar to those for the smoke population type, but with number concentrations and size distribution parameters between those of the background marine and smoke types (IQR 782 to 1160 cm^{-3}; 68% accumulation modal fraction), indicating there was insufficient smoke for it to dominate the properties of the marine background. Accumulation and Aitken mode hygroscopicities of 0.48 and 0.54, along with activated fractions and CCN concentrations, were similarly indicative of mixing between smoke and background marine sources.

   While periods of smoke mixing with a background marine air mass appeared to constitute the

majority of data points in this cluster, several other periods point to other phenomena of interest being included in this type, perhaps indicating this cluster was relatively more complex than other population types. Short lived intrusions (two to five hours) of accumulation mode particles were regularly observed in both the CCN system and PCASP datasets (e.g. 18-23Z on 22, 23, and 24 Sep) after which the size distributions quickly returned to background marine conditions. These excursions were largely constrained to the pre-dawn hours (sunrise occurs around 22Z) when the boundary layer was thinnest, and when precipitation was occurring in the vicinity of the *Vasco*. Several prior studies have shown that smoke and anthropogenic pollution aerosol within the wider MC region can be lofted into and transported in the lower free troposphere (Tosca et al., 2011; Robinson et al., 2012; Zender et al., 2012; Campbell et al., 2013; Atwood et al., 2013). The influence of a free tropospheric aerosol layer as a source of MBL aerosol and CCN has been identified in other remote oceanic regions as well (Clarke et al., 2013). One possible explanation for these events (and possibly for the observed organic and ultrafine events that were characterized by increases in gas phase VOCs as noted in the next clusters) is therefore that aerosol may have been mixed down into the MBL from a layer aloft, perhaps on the edge of rain shafts. Alternatively, they may also be due to intermittent plumes of aerosol that survived stochastic precipitation removal events along a boundary layer transport pathway or human terrestrial activities in the pre-dawn hours. In addition, air masses influenced by anthropogenic pollution may have been included in this cluster as well, but without sufficiently different impacts on aerosol parameters to result in a distinct cluster.

5. Organic Event: An approximately four-hour period starting at 1Z on 23 Sept. had measured particle concentrations between 200 and 325 cm^{-3}, but with significantly ($p<0.001$) larger

median diameters than either the precipitation or background marine types (Figure 2.3). Both Aitken and accumulation mode particles had among the lowest hygroscopicities measured during the cruise, with κ values around 0.2. During this event measured concentrations of numerous VOCs were much higher than in gas canisters collected approximately 6 hours before and after it, with no associated increase in carbon monoxide (Reid et al., 2016; Figure 2.2c). The particles had lower hygroscopicities and larger sizes than the background marine particles observed just before this event. While the source of this event is uncertain, Robinson et al. (2012) found occasional organic aerosol above the boundary layer they attributed to biogenic Secondary Organic Aerosol (SOA) formation during an airborne campaign in the outflow regions of Borneo, while Irwin et al. (2011) reported κ values between 0.05 and 0.37 in a terrestrial, biogenically dominated MC environment. Such a source would be consistent with the observed population, perhaps due to growth of a background marine population by condensation of organics, although we lack the ancillary data needed to establish this.

6. Ultrafine Event: This cluster was associated with an approximately 20-hour period on 17-18 Sept. that included the highest concentration of particles below about 30 nm observed throughout the study (Figure 2.2a), and coincided with a period of elevated VOC measurements at the start of this event (Figure 2.2c). A filter during this period showed very low potassium concentrations, while benzene was among the lowest values measured during the study, indicating that biomass burning was not the likely source for this event. Anthropogenic, shipping, and marine and terrestrial biogenic emissions are known sources of such compounds; isoprene, a common biogenic VOC, was not observed during this event, and a brief period of elevated dimethyl sulfide, associated with marine emissions from

phytoplankton, was observed shortly before—but not during—this event (Reid et al., 2016). A tri-modal best-fit was indicated by the Hussein, et al. (2005) algorithm for a number of these data points (Figure 2.2a and Figure 2.6). The period had an overall IQR of 482 to 661 cm^{-3}, with generally higher ultrafine number concentrations than other periods with similar total concentrations. The accumulation mode was similar in both size and hygroscopicity ($\kappa = 0.65$) to the accumulation mode of the background marine type, while the smaller Aitken mode showed larger modal fractions and overall number concentrations, and slightly higher hygroscopicities ($\kappa = 0.50$) as compared to the background marine measurements. However, we note that the 0.38% supersaturation hygroscopicity measurement would likely not have been sensitive to these below 30 nm particles, and therefore was likely not representative of this smallest third mode. Additionally, while total number concentration was slightly higher than the background marine population, measured CCN concentrations and activated fractions were generally lower, indicating many of the additional particles would not be expected to influence CCN concentrations until higher environmental supersaturations were reached. While not enough information is available to verify the nature of differences between ultrafine particles in these types, the results are consistent with an influx of smaller particles and VOCs into a background marine air mass, and were sufficiently distinct to be identified as a coherent period by the unsupervised K-Means analysis.

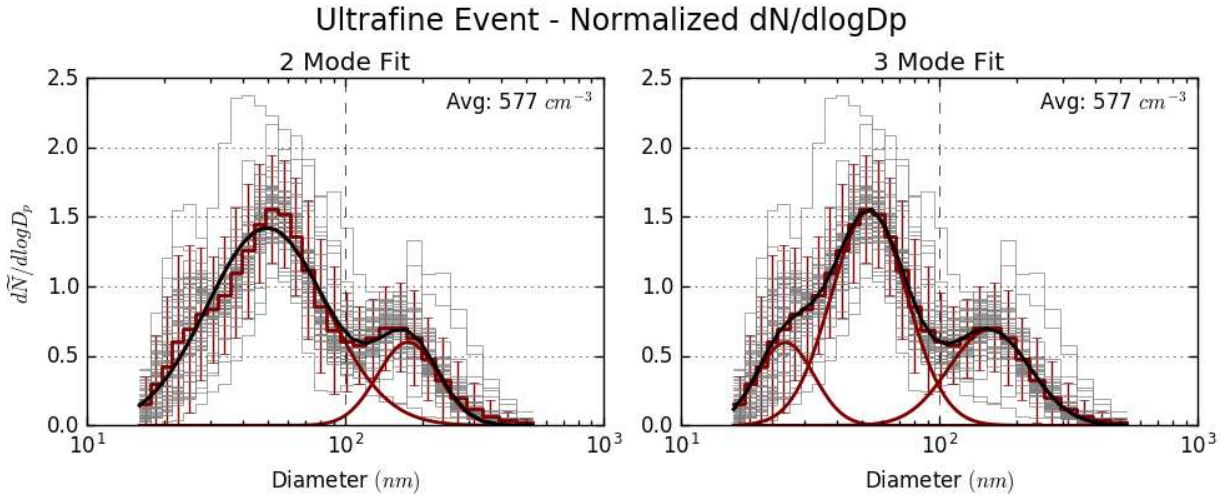

Figure 2.6 The best fit of the Normalized dN/dlogD$_p$ particle size distributions for the Ultrafine Event population type using two lognormal modes (left) and three lognormal modes (right). A three-mode fit was indicated by the Hussein et al., (2005) algorithm for this population type, however for clustering purposes the two mode fit was used. Shown in these plots are the particle size distribution spectrum for each data point within the population (grey), the associated average bin values with error bars at 95% confidence interval (colored step lines; 1.96 * bin standard deviation), and best fit lognormal modes (colored curves) with multi-modal fit (black). The average particle number concentrations of data points within each population type are listed.

7. Transit: This type was associated with measurements taken during a transit away from the port of Puerto Princesa, a city with a population of over 200,000. During this period light, westerly winds advected anthropogenic pollution out over the Sulu Sea and along the path of the *Vasco*, allowing for sampling of the urban plume as it diluted and mixed with aerosol from other sources. Size distributions were dominated by an Aitken mode with a number median diameter around 80-90 nm, unique in measurements from this study, mixed with an accumulation mode with a smaller modal fraction than other types. The population had an IQR of 738 to 1029 cm^{-3}, while the generally decreasing number concentrations were consistent with an urban plume diluting and mixing with other aerosol populations. Modal hygroscopicity values of 0.58 and 0.62 for the accumulation and Aitken modes, respectively, were closer than those most of the other population types and consistent with high levels of sulfate aerosol in typical urban plumes.

8. Port: This type was assigned to the measurements taken during a short period in the port of Puerto Princesa. Local anthropogenic emissions were dominant during this period, with number concentrations that fluctuated between 4000 and 10,000 cm^{-3}. Ultrafine particles (D_p < 100 nm) dominated number concentrations during this period, although large number concentrations of accumulation mode particles with diameters between 100 and 300 nm were also observed. As measurements were fluctuating rapidly and only one CCN scan at each supersaturation setting could be completed before instrumentation was shut down, hygroscopicity results were inconclusive and uncertain. This type is considered separate from the other types as it was not measured in a remote marine area away from the immediate influence of a nearby terrestrial source.

Finally, throughout the study coarse mode particles with diameters larger than about 800 nm were consistently observed in the PCASP volume distributions (Figure 2.2b). Concentrations of particles in this size range increased with increasing wind speed (Figure 2.7), consistent with generation of sea spray aerosol due to bubble breaking and wave action (O'Dowd and Leeuw, 2007). While the total number concentration of coarse particles is small compared to typical CCN concentrations (Figure 2.2e, f), in the cleanest conditions measured they represented non-trivial fractions of CCN active at 0.14% and 0.38% supersaturations. The large diameter of these particles makes them likely to activate at very low supersaturations, and they are present in more than sufficient number concentration to impact the microphysical structure and processes in stratocumulus clouds by serving as "giant CCN" (Feingold et al., 1999).

No significant relationship between wind speed and fine mode aerosol population type was noted. However, particles in the coarse mode range are not measured or accounted for in the cluster analysis (CCN system range: 17-500 nm), while submicron aerosol was often dominated

by aerosol from other sources. Modini et al., (2015) utilized a dedicated size distribution fitting analysis that included size resolved observations of particles above 500 nm to examine primary submicron marine aerosol production. They found a primary mode with a median diameter around 200 nm and tail that extended to sizes well above 500 nm, with number concentrations of 12 +/- 2 cm^{-3} during a period of low wind speeds that increased to 71 +/- 2 cm^{-3} as winds increased. Concentrations differences of around 50-60 cm^{-3} due to wind speed changes may not have resulted in large enough changes to concentrations or size distributions to alter the clustering of the observed population types, which often included number concentrations that were larger by an order of magnitude or more.

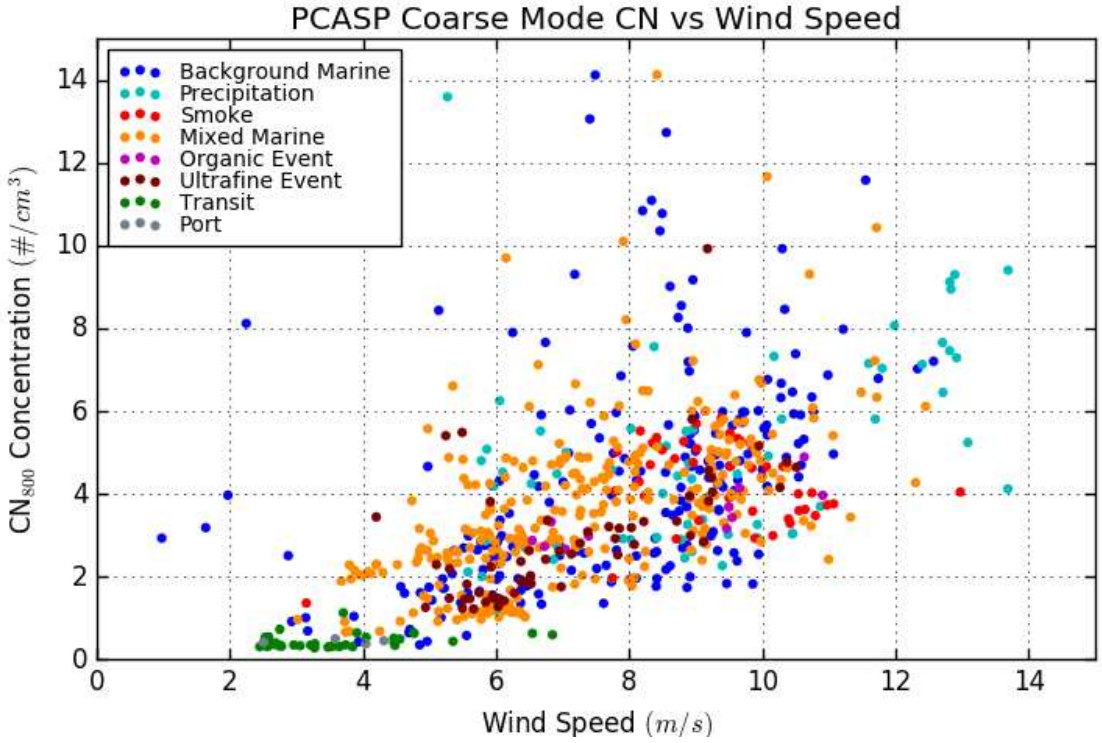

Figure 2.7 Number concentrations of coarse mode particles (D_p > 800 nm) measured by the PCASP as functions of local surface wind speed measured by the onboard *Vasco* weather station. Each point was averaged over the same approximately 15-minute time period as for the CCN system measurements, and is colored by the aerosol type as described in the text.

2.3.1. *SCS Aerosol Environment*

Based on this classification of the SCS remote marine boundary layer aerosol environment, a conceptual picture emerges as to the nature and sources of particles encountered during the *Vasco* 2012 cruise. A bimodal marine aerosol background was present with number concentrations usually between about 300 and 700 cm^{-3} and a Hoppel minimum around 90 nm. Primary emissions via sea spray supply submicron particles consisting of a mixture of sea salt and organic components, with emitted particle diameters as small as 40 nm (Clarke et al., 2006; Keene et al., 2007; O'Dowd and Leeuw, 2007; Prather et al., 2013; Quinn et al., 2014). However, even in remote marine environments transported anthropogenic and combustion aerosol may still be an important or even dominant source of small particles (Shank et al., 2012). The background marine population identified in this study is therefore considered a background state across the remote SCS that is likely comprised of a mixture of primary marine emissions along with particles derived from anthropogenic, biomass burning, and terrestrial and marine biogenic sources throughout the region (Frossard et al., 2014). Departures from the typical range of background marine characteristics and number concentrations occurred under large influxes of aerosol from other sources, such as smoke from biomass burning regions, anthropogenic pollution from population centers or shipping, or when convection and precipitation removed much of the ambient particulate matter and created relatively clean air masses.

During the SWM when large amounts of biomass burning aerosol were being advected into the SCS, a population of aged, accumulation mode smoke particles was periodically injected into the MBL where it mixed with existing particles. When total particle concentrations were above roughly 1500 cm^{-3} (Figure 2.3), the smoke particles dominated the background marine particles and had characteristic size distribution parameters and hygroscopicities that remained roughly

constant regardless of further increases in the concentration of biomass burning particles. In situations when smoke concentrations were insufficient to dominate the background marine aerosol population, smoke mixed with the background marine population, yielding size distribution and hygroscopicity parameters in between the two types. While the background marine type was earlier noted to be impacted to some extent by background anthropogenic or terrestrial aerosol similar to impacts noted for the mixed marine type, the later was characterized by mixing with a separate, distinct aerosol population, but at levels that were insufficient to dominate the background aerosol properties.

Precipitation removal of particles that had been advected into the region or ventilation by cleaner air masses when transport pathways changed returned the environment near the surface to its background marine state. However, when extensive precipitation occurred, accumulation mode particles were removed by wet deposition to a greater extent than Aitken mode particles, leading to lower overall surface number concentrations that were dominated by smaller particles, as evidenced by the emergence of a distinct precipitation population type from the cluster analysis. Based on the two *Vasco* cruises, the cleanest periods were encountered in cold pools following the passage of squall lines with number concentrations as low as 100 to 150 cm^{-3}. During these periods, increased number concentrations of coarse mode aerosol were regularly observed (Figure 2.7; $CN_{>800}$: 5.5 ± 2.1 cm^{-3}), that constituted a potentially important additional source of total CCN not measured by the CCN system (0.14% SS: 44 ± 25 cm^{-3}; 0.38% SS: 70 ± 36 cm^{-3}), particularly at low supersaturations where they would be expected to activate first.

In addition to these findings, several observed phenomena during the 2012 study were similar to those from the 2011 cruise (Reid et al., 2015). In particular, rapid changes in aerosol properties and source type were noted in the wake of squall lines that left clean air masses in their wake,

while longer period fluctuations on the order of days occurred as impacts from anthropogenic and smoke transport mixed with cleaner background marine and precipitation impacted air masses. As both studies were conducted in the remote marine SCS during the biomass burning season and saw similar meteorological phenomena modulating the aerosol populations, the more detailed aerosol property results of the 2012 cruise may be representative of the general nature of changes in SCS remote marine aerosol during the SWM season. Future work in the region to compare surface properties with model results and satellite retrievals will be ultimately required to fully validate these findings.

While the cluster analysis assigned each data point to a single cluster, in reality these first four clusters could be better described as a spectrum due to the variable impacts of mixing or meteorological processes, rather than as distinct or mutually exclusive population types. As is evident in Figure 2.3, overlap between these four clusters occurred in the parameter space for all nine of the measured variables used in the cluster model.

Deviations from this general picture arose when influxes of other aerosol types occurred. The additional population types each mapped out generally distinct areas in one or more of the parameters, leading to their identification by the cluster model. That such clusters corresponded to temporally distinct periods with physical and meteorological relevance ultimately justified the use of the cluster model to classify aerosol population types and assign rough population boundaries to the parameter space.

While the spectrum of mixing between population types is relevant to the identification of impacts from various sources, additional consideration of these aerosol types against measurements in other regions is also warranted. Fresh sea spray particles, dominated by sodium

chloride (κ = 1.28), are expected to have the highest κ values, although co-emitted organic species and replacement of chlorine by uptake of acidic gases can potentially reduce hygroscopicities. Additionally, the increasing organic fractions at smaller sizes reported in sea spray aerosol (Keene et al., 2007; Prather et al., 2013; Quinn et al., 2014; Forestieri et al., 2016) lead to decreased hygroscopicities as particle size decreases. Reported hygroscopicities for aerosol in marine regions vary, with Good et al., (2010) reporting CCN-derived κ values above 1 for some background or marine dominated MBL air masses, consistent with pure sodium chloride dominated sea salt κ values. Prather et al., (2013) generated aerosol using sea water with varying organic concentrations and associated marine biological activity, and reported CCN activation diameters at 0.2% supersaturation that correspond to κ values above 1 during periods of low organic concentration, that then dropped to κ values as low as 0.1 as organic concentration was increased. In addition, they found more organic enrichment and lower associated hygroscopicities in smaller particles. Quinn et al., (2014) explored the relationship between organic aerosol content, particle size, and particle hygroscopicity in primary marine aerosol generated in several ocean regions. They found a similar enrichment of average aerosol organic volume fraction with decreasing particle size (40 nm dry diameter: 0.8 organic volume fraction; to 100 nm: 0.4 fraction) that corresponded with decreased hygroscopicities (40 nm: κ=0.4; 100 nm: κ=0.8), and was consistent in various ocean regions and largely independent of biological activity as indicated by chlorophyll-a levels. Such findings are consistent with the lower Aitken mode hygroscopicities found in the background marine populations observed in this dataset, as well as the additional decreases in hygroscopicity noted in the precipitation population that had been further scrubbed of larger accumulation mode particles. Our findings of background and precipitation impacted marine aerosol κ values generally between 0.2 and 0.6

for the Aitken mode and 0.4 and 1.0 for the accumulation mode are therefore consistent with reported hygroscopicities of background marine aerosol that had been enriched by organic components. The presence of organics explains the noted lower hygroscopicities, as compared to what would be expected from pure sea salt aerosol, in population types that were otherwise expected to be dominated by background marine aerosol.

Aged biomass burning aerosol have often been found to have κ values below 0.2 (Andreae and Rosenfeld, 2008; Petters et al., 2009; Engelhart et al., 2012)—below the smoke population type average of approximately 0.4 in the accumulation mode during this study. However, high concentrations of both SO_2 and sulfate aerosol (ammonium sulfate, $\kappa = 0.61$) from numerous sources have been observed in the MC (Robinson et al., 2011; Reid et al., 2013). During this study, multi-day filter samples showed average sulfate concentrations between approximately 0.8 and 3 $\mu g/m^3$ at the *Vasco*, potentially increasing during periods of smoke impacts due to burning of sulfur rich peat in the region (Reid et al., 2016). The potential peat source or mixing with other sources of sulfate may explain the higher than typical κ values observed for aged biomass burning aerosol in the MC.

2.4. CCN PARAMETERIZATION

In order to further evaluate changes in CCN activity associated with different aerosol population types in the SCS dataset, reconstruction of expected CCN concentrations across a range of supersaturations was performed and the results parameterized. The eight size distribution and hygroscopicity properties for the parameterized Aitken and accumulation modes (Table 2.1) were used to predict the CCN concentration for a given supersaturation via κ-Köhler theory (Petters and Kreidenweis, 2007). Accordingly, the fraction of particles expected to activate for a

given parameterized distribution can be estimated by integrating the normalized modal size distribution above a supersaturation and hygroscopicity dependent critical particle size, which is then multiplied by total number concentration to give the expected CCN concentration at that environmental supersaturation.

The water vapor saturation ratio, S, for a given particle can be predicted by,

$$S(D) = \frac{D^3 - D_d^3}{D^3 - D_d^3(1-\kappa)} exp\left(\frac{4\sigma_{s/a} M_w}{RT\rho_w D}\right) \tag{2.1}$$

where D is the droplet wet diameter, D_d is the dry diameter, $\sigma_{s/a}$ is the surface tension, M_w is the molecular weight of water, R is the universal gas constant, T is the temperature, ρ_w is the density of water, and κ is the particle hygroscopicity parameter. For the purposes of this reconstruction, modes were assumed to be internally mixed with the measured average hygroscopicity used for all particles within that mode. The critical supersaturation, s_c (where $s_c = S_c - 1$) at which particle activation occurs is found at the maximum saturation ratio of this κ-Köhler curve, which was calculated iteratively here using the SciPy *optimize.minimize* Nelder-Mead simplex solver in Python. Assuming typical values for Eq. 1 variables (Petters and Kreidenweis, 2007), activation of a given particle is therefore primarily a function of D_d, S, and κ.

In the case of the SCS dataset, integration of the size distribution was then approximated by summing size bins in the normalized modal size distribution by,

$$AF = \sum_i^N \frac{m_i}{2} - \frac{m_i}{2} erf\left(\frac{\ln\left(D_{c_i}/\mu_{g_i}\right)}{\sqrt{2}\ln\sigma_{g_i}}\right) \tag{2.2}$$

where AF is the activated fraction, N is the number of parameterized aerosol modes for each mode i, m is the modal number fraction, μ_g is the median diameter, σ_g is the geometric standard deviation, D_c is the critical diameter, and erf is the error function. The critical diameter can then be estimated as the particle dry diameter associated with a critical supersaturation equal to the desired environmental supersaturation, solved iteratively using Eqn 2.1.

As there is no analytic solution to Eqn 2.2 in which activated fraction can be solved as a function of supersaturation and population parameters, it was instead calculated at a large number of points between 0.01% and 10% supersaturation for each SCS average population type. A lognormal cumulative mixture distribution was then fit to the results to parameterize CCN properties for each population type as,

$$AF_{pop}(ss) = \sum_{i}^{FN} \frac{c_i}{2} + \frac{c_i}{2} erf\left(\frac{\ln(ss/a_i)}{\sqrt{2}\ln b_i}\right) \tag{2.3}$$

where AF_{pop} is the activated fraction for an SCS average population type, ss is the environmental supersaturation expressed as a percentage ($ss = (S-1) * 100\%$), FN is the total number of fit modes for each mode i, and a, b, and c are the fit parameters for each lognormal mode. CCN concentration as a function of supersaturation can then be estimated by,

$$CCN_{pop}(ss) = CN * AF_{pop}(ss) \tag{2.4}$$

where CCN and CN are the respective number concentrations. The resulting parameterized activation spectra are given in Table 2.3 and shown as lines in Figure 2.8 for each of the identified SCS average population types.

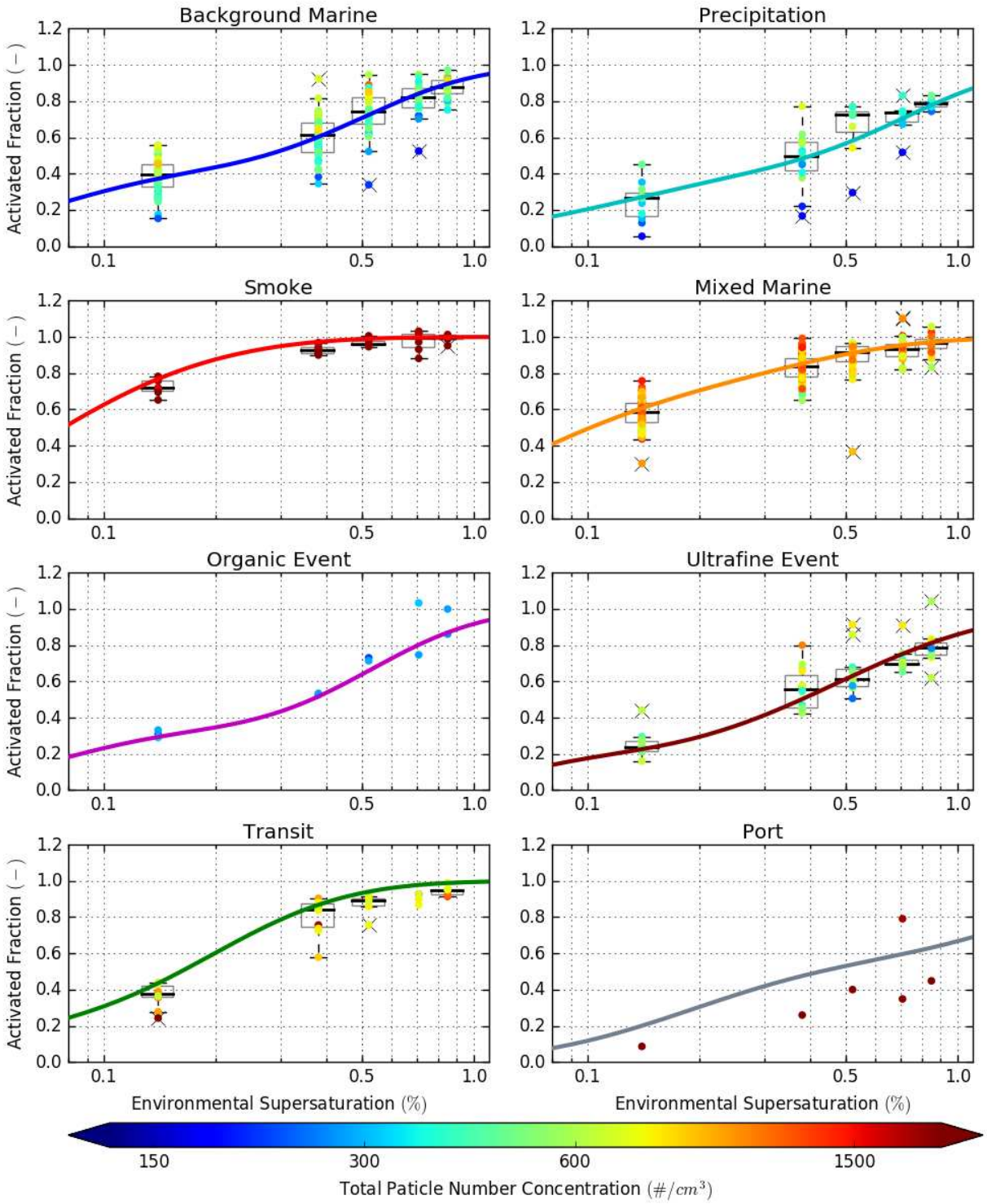

Figure 2.8 Parameterized activated fraction curves for each of the SCS average population types as a function of environmental supersaturation. Measured activated fractions from the CCN system are shown as circles colored according to the total particle number concentration at that data point. Box and whisker plots (with caps at most 1.5 times the inner-quartile range; outliers beyond this are marked by x symbols) are included for scenarios with at least five valid measurement points.

Table 2.3 Best-fit activation spectra parameters for each SCS aerosol population type using Eqn 2.3.

Population Type	Mode 1			Mode 2		
	a	b	c	a	b	c
1: Back. Marine	0.5072	1.7718	0.5691	0.0701	1.9555	0.4309
2: Precipitation	0.7673	1.6934	0.4790	0.1329	2.8288	0.5210
3: Smoke	0.0669	1.9623	0.8352	0.1974	1.8388	0.1648
4: Mixed Marine	0.3540	1.9371	0.3115	0.0685	2.0320	0.6885
5: Organic Event	0.5297	1.7389	0.6645	0.0750	1.7884	0.3355
6: Ultrafine Event	0.4699	2.2188	0.8226	0.0627	1.5040	0.1774
7: Transit	0.0421	1.5992	0.1858	0.1961	1.9577	0.8142
8: Port	1.5970	1.8957	0.4215	0.1903	2.1796	0.5788

2.4.1. *Comparison of Parameterized and Observed CCN Concentrations*

The parameterized CCN activation spectra were first compared against observed CCN concentrations from the CCN system. Each CCN scan was first integrated across all bin sizes to generate a reconstructed CCN concentration, which was then divided by the average CN concentration during that scan to provide a measured fraction of particles that had activated. This value for each CCN scan was plotted as circles in Figure 2.8 at the scan supersaturation set point by classified population type. Activated fraction data points were colored by average CN concentration for the scan. Box and whisker plots were included for scenarios in which there were at least five valid measurements.

Parameterized activation spectra showed general agreement with observations, with most curves falling within the inner-quartile range of measured values. Further investigation of closure between CCN concentrations from the parameterization estimates and measured values was conducted using measured total number concentration and identified population type for each data point (Figure 2.9). A linear best-fit line comparing the two values had a slope of 1.01 and R-squared value of 0.98, again indicating parameterized values were generally consistent with

observations and similar comparisons reported from other CCN closure studies (e.g. Bougiatioti et al., 2009; Kammermann et al., 2010).

The largest deviations tended to occur at low supersaturations and total number concentrations where overprediction of CCN concentration occurred, particularly in the background marine and precipitation types (Figure 2.9). Similar behavior has been noted in other CCN closure studies (e.g. McFiggans et al., 2006; Kammermann et al., 2010) and was also noted at a littoral marine site discussed further in Chapter 3. Kammermann et al., (2010) reviewed a number of studies that compared such predicted CCN concentrations against observed values and found biases were often largest at supersaturations below 0.3%, where predictions deviated from observations by factors ranging from 0.6 to 3.3, though with most studies finding overprediction occurred. They attributed the increasing bias at decreasing supersaturations to increased uncertainty in the critical activation diameter and associated CCN number prediction, though they also noted that

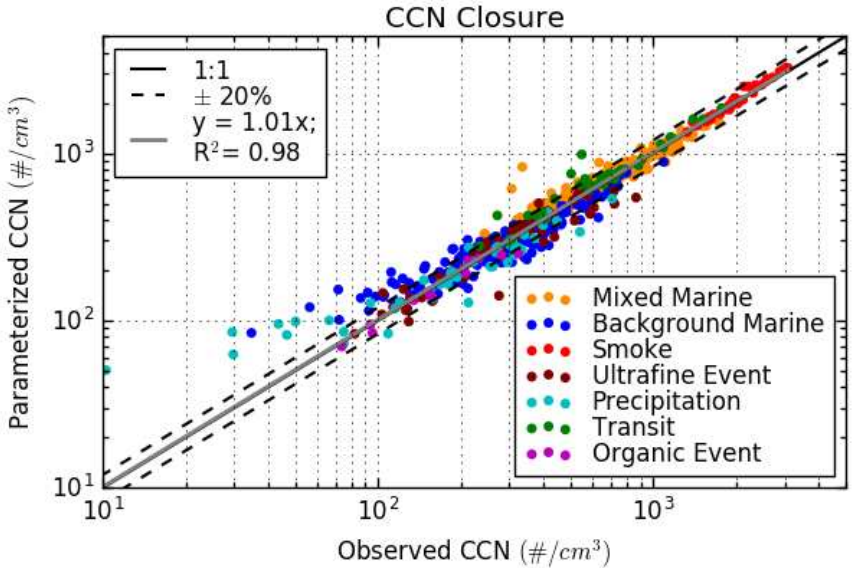

Figure 2.9 CCN closure comparing predicted concentrations from the parameterization using average population type activation spectra and observed total number concentration against observed values for all measured supersaturations. Linear best-fit slope is shown in grey with the associated R-squared value. One to one lines and lines at ± 20% are shown.

this discrepancy between predicted and observed CCN concentrations has not been fully resolved.

Uncertainty in the critical activation diameter may similarly explain the CCN overprediction bias in the SCS dataset. However, activation spectra for background marine and precipitation types in Figure 2.8 showed a similar overprediction for data points with the lowest measured number concentrations—though this was noted across the range of measured supersaturations rather than just at low values. As noted in the previous sections, the lowest number concentrations tended to occur in the wake of squall line passage where extensive precipitation scrubbing and wet deposition would be expected. In the SCS dataset, as precipitation scrubbing was associated with both preferential removal of larger particles and lower overall number concentrations, this bias could potentially also be explained by varying degrees of wet deposition and primary marine production of particles. Such a phenomena would tend to skew size distributions to smaller sizes as compared to the average population type, thereby suppressing activation spectra and CCN concentrations across all supersaturations. Median diameter parameters in Figure 2.3 for both the Aitken and accumulation modes also show a tendency to decrease as total number concentration decreases. An additional dependence of the parameterized size distribution and activation spectra on the degree of precipitation scrubbing in background marine and precipitation impacted air masses may therefore explain some of this noted overprediction in marine aerosol types in this dataset. Additional measurements in the wake of squall lines or other heavy precipitation events could potentially allow for better discrimination between background marine and precipitation impacted types, and could allow for further testing of this hypothesis.

Nevertheless, the CCN parameterizations for the identified population types were consistent with the behavior reported in other CCN closure studies, and were considered to be generally representative of CCN properties in the SCS dataset.

2.5. SUMMARY

Ship based measurements of aerosol size distributions and CCN properties conducted as part of the first extensive, in situ aerosol measurement campaign in remote marine regions of the South China Sea/East Sea during the important Southwestern Monsoon and biomass burning season were reported. Analysis of approximately two weeks of measurements found aerosol characteristics consistent with those from a previous pilot study in the region during the same season, indicating that descriptions of aerosol population types and the associated meteorological and transport phenomena that modulate changes and mixing between these populations may be representative of the wider remote marine SCS during the SWM season.

Eight aerosol population types were identified in the dataset that were associated with various impacts from background marine particles, smoke, and anthropogenic sources, as well as precipitation impacts and shorter-lived events linked to influxes of VOCs or ultrafine particles. Efforts to measure or model the impact of aerosol on cloud development or atmospheric optical properties often rely on proper characterization of aerosol microphysics associated with impacts from various aerosol sources. As such, we provided population type average values and observed variabilities for aerosol size distribution, hygroscopicity, and parameterized activated fraction across a range of environmental supersaturations. Reutter et al., (2009) identified specific regimes of cloud development where aerosol number concentration was important using a cloud parcel model, while Ward et al., (2010) found such results may be further complicated by aerosol

size and hygroscopic properties. Inclusion of both population type average properties and the range that they vary across into such a model may help constrain when various properties of the aerosol are relevant to cloud development in the SCS. Additionally, differences in aerosol population type are expected to be relevant to studies of radiative transfer, optical propagation through the atmosphere, and satellite retrievals in sub-saturated marine environments where differences in particle number concentration, size, hygroscopicity, index of refraction, and relative humidity all affect the interaction of radiation with particles in complex ways. Investigation of such potential impacts on cloud development and optical properties are explored further in chapters 4 and 5, respectively.

Lastly, while specific observed aerosol population types were identified in this dataset, additional open questions remain regarding the relative importance of various sources and transport pathways of aerosol into remote MBL air masses and their impact on aerosol populations. Since the surface-based observations provide only a portion of the observations needed to construct a true aerosol budget for the MBL, the degree to which MBL aerosol may be impacted by mixing down from a reservoir aloft was not clear. Future airborne aerosol campaigns in the region may be useful to shed light on this important topic.

3. LITTORAL ZONE AEROSOL MEASUREMENTS AT BODEGA BAY

Atmospheric rivers (ARs) are tropical moisture advection phenomena that can account for large fractions of the wintertime precipitation in California (Ralph et al., 2004; Dettinger et al., 2011). The winter-spring 2015 CalWater-2015 study (Ralph et al., 2015), and coordinated U.S. Department of Energy Atmospheric Radiation Measurement (ARM) Climate Research Facility Cloud-Aerosol-Precipitation Experiment (ACAPEX) (Leung, 2016) that included aircraft- and ship-based observations in the same region, were designed to probe the atmospheric conditions in and around ARs, and to provide new observations of the characteristics of regional aerosols that may interact with these atmospheric moisture features and thereby influence the downwind formation of precipitation. As part of the CalWater-2015 study, ground-based aerosol observations were conducted at the Bodega Bay Marine Laboratory (BML), a coastal California site that is suitable for observation of aerosols in landfalling marine air masses, and in mixtures of marine and continental air.

In marine regions impacted by continental outflow, aerosol chemical and microphysical properties, including particle number concentrations and size distributions, are often moderated by impacts from terrestrial sources (Nair et al., 2013; Wex et al., 2016; Zhao et al., 2016; Phillips et al., 2018). For example, freshly emitted sea spray aerosol particles comprise a mixture of salts with generally high hygroscopicities ($\kappa \sim 0.6–1.2$), and co-emitted organic species with lower hygroscopicities ($\kappa \sim 0–0.3$) (Prather et al., 2013; Quinn et al., 2014)—classified using the κ hygroscopicity parameter (Petters and Kreidenweis, 2007). Bulk hygroscopicity values above 1 are infrequently observed, but have been reported for some background and precipitation impacted marine aerosol populations (Good et al., 2010; Prather et al., 2013). As the aerosol

ages, chlorine replacement by uptake of acidic gases can reduce the hygroscopicity of the salts (Finlayson-Pitts and Pitts, 1999; Song and Carmichael, 1999). Aging and organic components result in reported κ values in the range of 0.4 to 0.7 for more pristine or background marine aerosol populations (Keene et al., 2007; Bates et al., 2012; Prather et al., 2013; Quinn et al., 2014; Zhang et al., 2014; Forestieri et al., 2016; Atwood et al., 2017; Royalty et al., 2017; Phillips et al., 2018). In contrast, average hygroscopicities for continental aerosol populations are often in the range of 0.1 to 0.3 due to heavy influence of organic and insoluble material, although individual inorganic sulfates and nitrate salts have higher values in the same range as many remote marine aerosol populations (Andreae and Rosenfeld, 2008). The cloud-droplet-nucleating activity of particles in coastal regions therefore depends on the composition, size distribution, and degree of aging of the marine particles, along with the characteristics of particles from non-marine sources that become mixed with the marine aerosol. Thus, observation and analysis of the coastal California aerosol environment will support efforts to better understand implications of aerosol properties on precipitation and cloud development in the region, including aerosol influences on how precipitation develops in landfalling ARs in this region.

In this study, observations from 23 January 2015–5 March 2015 at the BML ground site were used to evaluate the nature and variability of surface (marine boundary layer, MBL) aerosol populations. Observations were classified into periods of similar aerosol and meteorological characteristics using an unsupervised cluster model (Atwood et al., 2017) to derive distinct littoral aerosol population types and link them to source regions. The clusters were assessed with respect to their aerosol characteristics, particularly the contributions of each population type to cloud condensation nuclei (CCN) concentrations that influence the microphysical properties of liquid-phase clouds and the evolution of precipitation in mixed-phase clouds (e.g., Rosenfeld et

al., 2008). In prior work analyzing ground-, ship-, and aircraft-based meteorological and microphysical observations from the CalWater-2015 and ACAPEX field experiments, Leung (2016) discusses an AR event that was first observed and sampled from aircraft platforms off the coast of California on 5 February 2015, during the observational period analyzed here. The AR made landfall near BML on the morning of 6 February, and the AR-associated front, producing heavy precipitation along its trajectory, reached the Central Valley and Sierra Nevada in the afternoon. We thus also contrast the aerosol cluster types identified at BML during AR and marine aerosol dominated events to observations outside those periods.

3.1. METHODS AND SITE DESCRIPTION

Measurements occurred at Bodega Bay Marine Laboratory (BML; 38.32° N, 123.07° W) and took place between January and March 2015. Data utilized in this study were gathered between 23 January and 5 March, when relevant instruments were operational. All aerosol measurements used here were made from within the Colorado State University/National Park Service mobile lab, located approximately 200 m from the coast, and approximately 150 m north of the main BML lab building. Air was sampled through several ½" stainless steel tube inlets routed through the roof of the mobile lab to a height of approximately 5 m above the ground, before the flow was split and sent to various instruments described further below. A map and additional description of the site and instrumentation are provided in Martin et al., (2017).

3.1.1. *Meteorological Data*

Local meteorological measurements were obtained from a 10 m surface met tower located approximately 100 m north of the mobile lab, and operated as part of a NOAA/ESRL observation network (White et al., 2013). Air mass source regions were defined using 24-hour

backtrajectories that were initiated every three hours during the study period and computed using the HYSPLIT version 4.9 Lagrangian parcel model (Draxler and Hess, 1997, 1998; Draxler et al., 1999; Stein et al., 2015) with the 40 km x 40 km Edas40 meteorological dataset. All trajectories were generated with 100 m arrival heights at BML to characterize transport in the MBL.

3.1.2. *Aerosol Size Distribution Measurements*

Aerosol size distribution measurements made during CalWater-2015 at BML are described in detail in Martin et al., (2017). This study used size distribution measurements for particle diameters between 14 and 730 nm from a TSI 3080 SMPS using a 0.3 L min^{-1} sample flow rate and 3.0 L min^{-1} sheath flow rate. SMPS scans were conducted approximately every 5 minutes and were subsequently averaged to approximately 15-minute time periods to match additional coincident measurements.

The presence of large numbers of particles smaller than approximately 30 nm in diameter was intermittently observed in the size distribution measurements. These particles were likely from a combination of local sources that included vehicle and other activity at BML, local camp and brush fires, and emissions from the nearby town of Bodega Bay, located to the east of the site. This nucleation mode was generally superimposed on more stable aerosol populations, and thus rather than removing the entire observation during these events, we removed only the contamination mode, as described below.

The best-fit modal parameterization for each size distribution spectrum was first assessed using the lognormal mixture distribution fitting algorithm based on Hussein et al., (2005) and described in Chapter 1. The algorithm selects between one and three modes to best represent the

number size distribution based on empirical rules and maximum-likelihood fitting criteria, and defines each mode by three parameters (median diameter, geometric standard deviation, and fractional number concentration). Within each of the size spectra, a fitted mode was identified as local contamination if the following criteria were met:

- The combined fit's distribution was identified to have more than one mode
- The median diameter of the smallest fitted mode was at or below 20 nm
- The smallest fitted mode constituted less than 50% of the total fitted number concentration at 50 nm (indicating only a small contribution to total particle count at larger sizes)
- The smallest fitted mode did not persist continuously for more than three hours

In the case that an observed size distribution spectrum passed all these criteria, the smallest mode was classified as a contamination mode likely associated with local sources as described above and therefore not representative of the regional aerosol. These modes were removed from the size distributions and total number concentrations while retaining the remaining fitted modes. This was accomplished by multiplying the observed $dN/d\log_{10}D_p$ value by one minus the contamination mode's number fraction of the total distribution for each size bin. An example of the removal is shown in Figure 3.1, with an observed distribution without a local contamination mode shown in (a). Approximately one hour later, a distinct small mode was observed with a median diameter less than 14 nm and nearly no contribution to particle concentration at diameters above 20 nm (b), while total number concentration showed a rapid increase (not shown). This mode was no longer present approximately 1.5 hours later. Therefore, the observation passed all four criteria to be considered local contamination and was removed from

the reported size distribution and total number concentration to give the final corrected distribution (c).

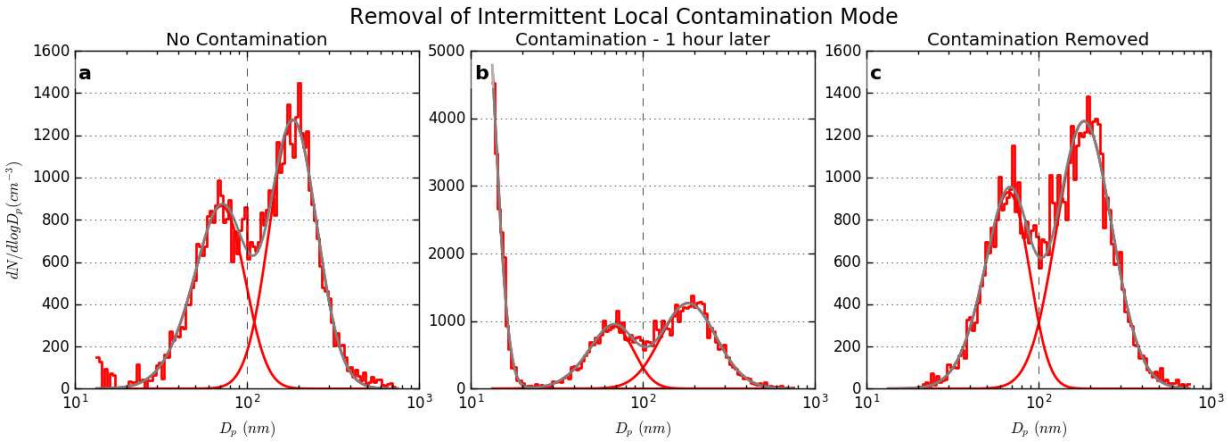

Figure 3.1 Example removal of intermittent local contamination mode. (a) An observed size distribution with limited impacts from the smallest nucleation mode particles. (b) An observation approximately 1 hour later with contamination from small particles that are not representative of the regional aerosol. (c) The same size distribution as in (b), but with the smallest contamination mode identified and removed as described in the text.

A raw timeline of particle number concentration and size distribution is shown in Figure 3.2 (a&b), with corrected number concentrations and size distributions after removal of the contamination modes shown in (a&c). Both the generally short duration and small particle size of the identified contamination modes are evident in these figures. Narrow peaks in the light blue line in (a) show that the correction to number concentration occurred over generally short time periods, while the predominant differences in the corrected size distribution of (c) were for the smallest particle sizes. Relatively little change in the overall nature of the shape of the overall distributions resulted from this correction, but it allowed for markedly improved performance of the cluster model.

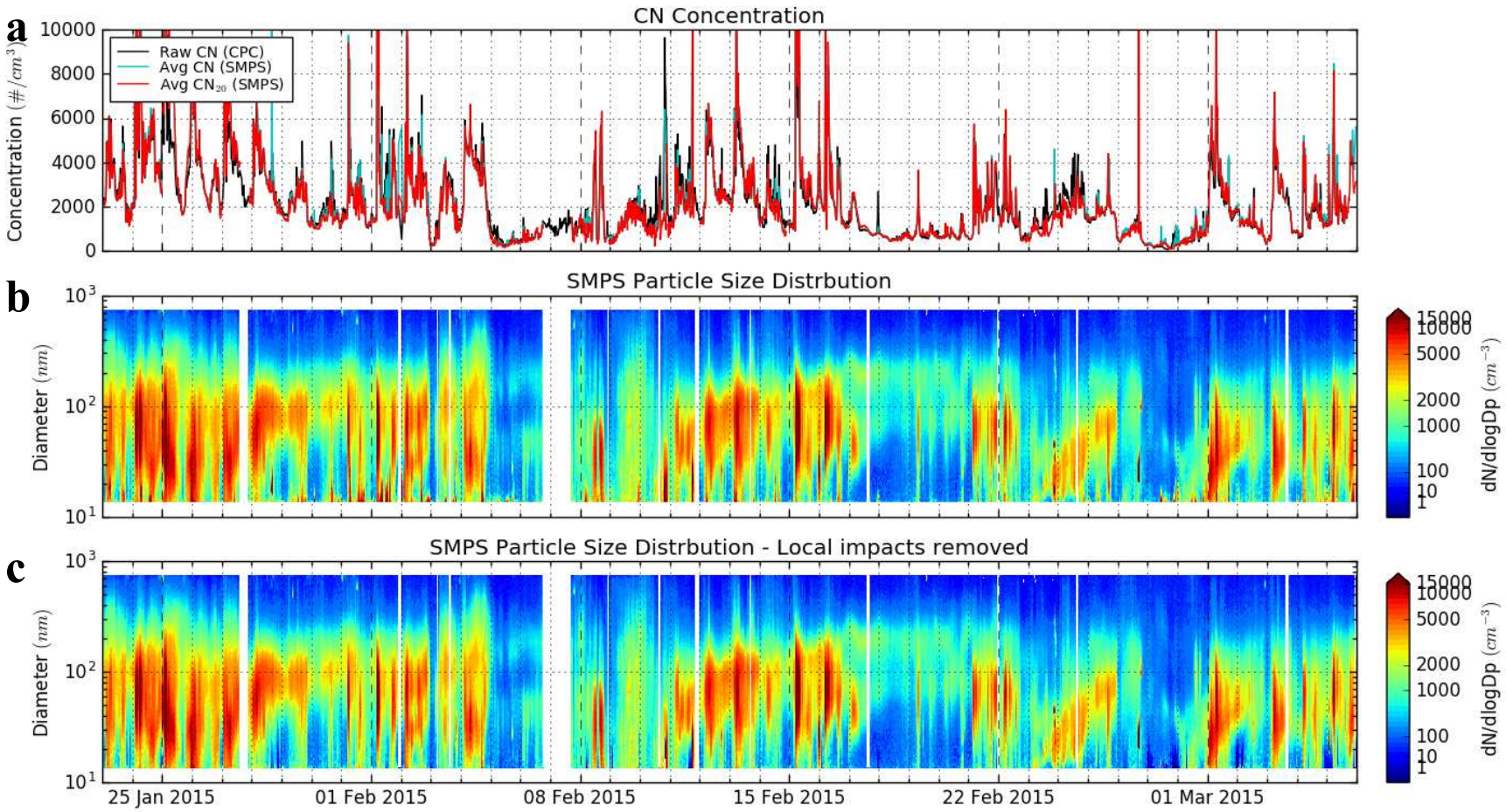

Figure 3.2 (a) Study timeline with CN concentrations from the bulk CPC (black), reconstructed CN from the SMPS (light blue), and reconstructed CN corrected for intermittent local contamination modes (red). SMPS particle size distributions are shown (b) before and (c) after correction to remove contamination.

Further criteria for identification of contamination periods and modes in the number size distribution were considered, including analysis of signal-to-noise or similar measures of relative smoothness of potential contamination modes. However, such metrics were not always consistent in their identification of such small contamination modes due to competing factors from measurement noise and physical variability. Ultimately, the criteria listed above were found to be sufficiently capable of removing small contamination modes such that the cluster model was able utilize these data points without skewing the results, and so were used for the purposes of this analysis.

3.1.3. *Size Resolved CCN Measurements*

A size-resolved CCN system (srCCN) similar to that described in Chapter 2 was utilized to provide size-resolved CCN concentration and hygroscopicity measurements. As described further in Martin et al. (2017) and Petters et al. (2019), a DMT cloud condensation nuclei counter (CCN-100) coupled with a TSI 3080 SMPS was used to scan across a range of particle diameters (12-540 nm at water supersaturation of s = 0.1%, 0.19%, 0.28%, 0.44%, 0.58%, 0.67%). An apparent hygroscopicity parameter κ (Petters and Kreidenweis, 2007) was calculated from these scans as described in Petters and Petters, (2016).

3.1.4. *Scanning Flow CCN Measurements*

Additional measurements of CCN activity across a range of environmental supersaturations were conducted at higher temporal resolution than the SCS dataset using a separate measurement system. A scanning flow CCN system (sfCCN) was used to measure total CCN number concentration as supersaturation was ramped between approximately 0.08% and 1.1% supersaturation. The system used a DMT CCN-100 instrument that had been modified by connecting a voltage modulated proportional flow valve to the bottom of the column to control

flow (Suda et al., 2014). The flow rate through the CCN column was increased from 0.2 to 1.2 lpm over 5 minutes while holding the temperature gradient constant, thereby scanning peak column supersaturation as a function of flow rate and column temperature gradient (Moore and Nenes, 2009). A TSI 3010 Condensation Particle Counter (CPC) was placed in parallel to the CCN to measure total particle number concentration (CN). CCN and CN concentrations were recorded at a frequency of one hertz. Each approximately 5-minute scan was repeated three times, after which the temperature gradient was changed between gradients of 4 and 8 K (dT4 and dT8, respectively) in order to scan a different range of supersaturations. As the column temperatures took approximately 3 minutes to stabilize, the first scan of each three-repetition set was not analyzed. Scans at a temperature gradient setting were then combined with scans at the other dT setting before and after to yield rolling average data points approximately every 15 minutes, and each consisting of data the spanned approximately 40 minutes of measurements (Figure 3.3).

Example sfCCN concentrations (Figure 3.4a) and activated fraction spectra (Figure 3.4b) are shown for the same time stamp as the size distribution data in Figure 3.1. The range of CN concentrations as measured by the parallel CPC during this period are shown via the red background bar. During the contamination period approximately one hour later the effect of the small mode noted in Figure 3.1b was seen via increased CN concentrations (reaching as high as 5000 cm^{-3}; Figure 3.4c) and decreased activated fractions above approximately 0.1% supersaturation (Figure 3.4d). Observed CCN concentrations remained relatively constant indicating the additional particles were too small to activate below 1.1% supersaturation. After removal of this small contamination mode the corrected CN concentrations and activation

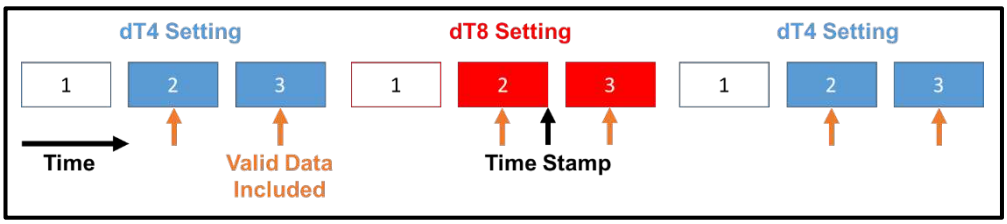

Figure 3.3 Example generation of an averaged sfCCN data point. Of the nine 5 minute scans, the six solid boxes were included. The combined data formed a single data point placed at a time stamp shown.

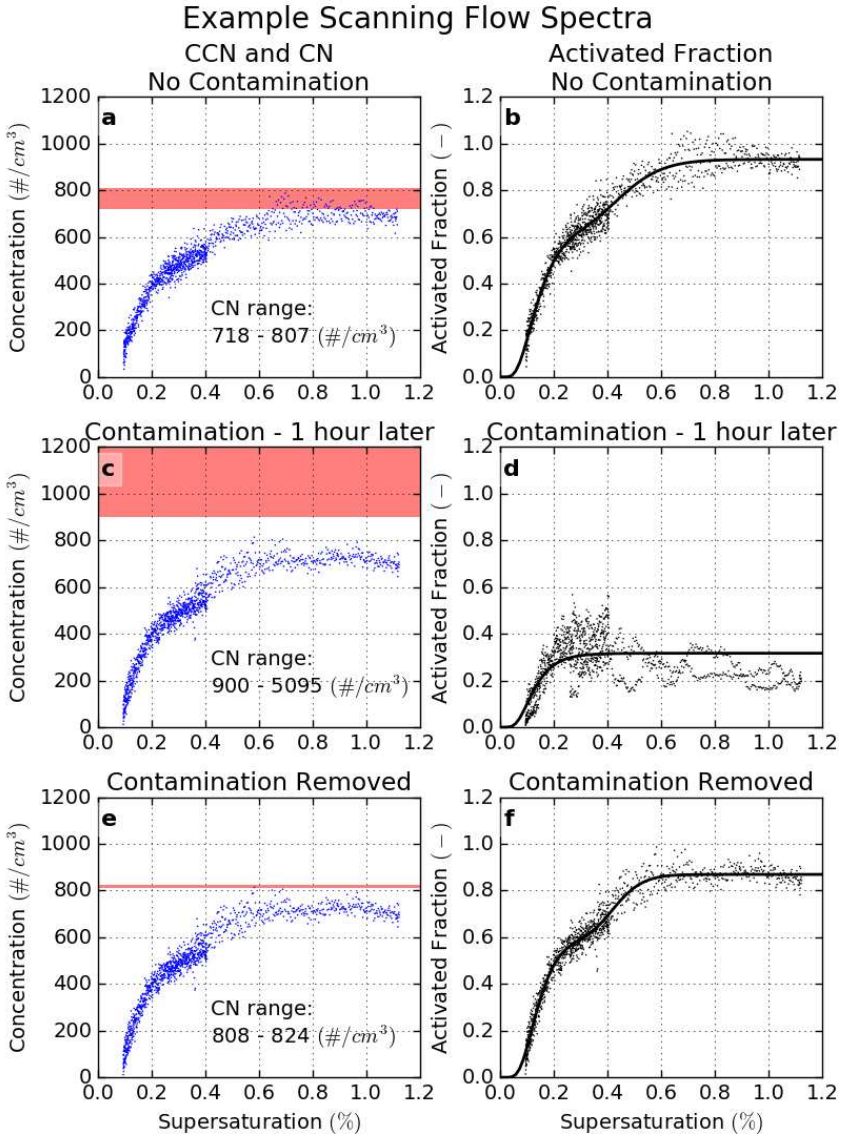

Figure 3.4 Example spectra measured by the sfCCN system for the same time period as in Figure 1. (a) One second CCN (blue) and the range of CN (red) concentration measurements for a single scan. (b) Activated fractions for measured points in (a) along with a best-fit activated fraction spectrum curve (black line). (c) & (d) As in (a) and (b), but for a scan approximately one hour later that was contaminated by an intermittent local ultrafine mode; CN were observed as high as 5000 cm^{-3}. (e) and (f) The same spectra as in (c) and (d), but after correction to remove the contamination mode; corrected CN concentrations are now similar to the range in (a).

spectrum (Figure 3.4e and Figure 3.4f, respectively) were similar in characteristics to the earlier non-contaminated period.

3.1.5. *Activated Fraction Spectra Parameterization*

Parameterizations of activated fraction spectra are presented using several methodologies. The parameterizations of Paramonov et al., (2015) for various locations in the EUCAARI network, discussed further for comparison in the following sections, used a two parameter fit of the form $AF = a \times \ln(S_{eff}) + b$, where S_{eff} is the effective environmental supersaturation. However, this parameterization did not adequately reflect the differences between spectra in the BML dataset. In order to provide a more accurate parameterization of observed BML activation spectra, a lognormal cumulative mixture distribution function of the same form used in Section 2.4 was fitted to the results as,

$$AF(ss)_{pop} = \sum_{i}^{FN} \frac{c_i}{2} + \frac{c_i}{2} erf\left(\frac{\ln(ss/a_i)}{\sqrt{2}\ln b_i}\right) \tag{3.1}$$

where AF is the parameterized activated fraction for the population, ss is the environmental supersaturation expressed as a percentage ($ss = (S - 1) * 100\%$), FN is the total number of fit modes for each mode i, and a, b, and c are the fit parameters for each lognormal mode. As most cluster average size distributions were bimodal with only a small fraction of the total number in an additional third identified mode, a bimodal activation spectrum parameterization was used for all population types here.

3.1.6. *CCN Calibrations*

Calibration of the scanning flow CCN column supersaturation for a given flow rate at each temperature gradient setting was conducted following the methodology described in Suda et al.,

(2012). Briefly, a monodisperse ammonium sulfate aerosol was generated by atomizing an ammonium sulfate solution and size selecting using a TSI 3080 Differential Mobility Analyzer (DMA) set to a fixed voltage. Concentrations of CN and CCN were measured as flow rate changed. The flow rate at which 50% of particles had activated (Q_{50}) was calculated by fitting a sigmoid curve to the activation plots for a range of DMA column voltages. Given a κ hygroscopicity parameter of 0.61 (Petters and Kreidenweis, 2007) for the ammonium sulfate particles and the parameters of the DMA, calibration curves for column supersaturation as a function of flow rate and temperature gradient were calculated (Figure 3.5). Calibration of the srCCN was similarly conducted following the methodology described in Suda et al., (2012).

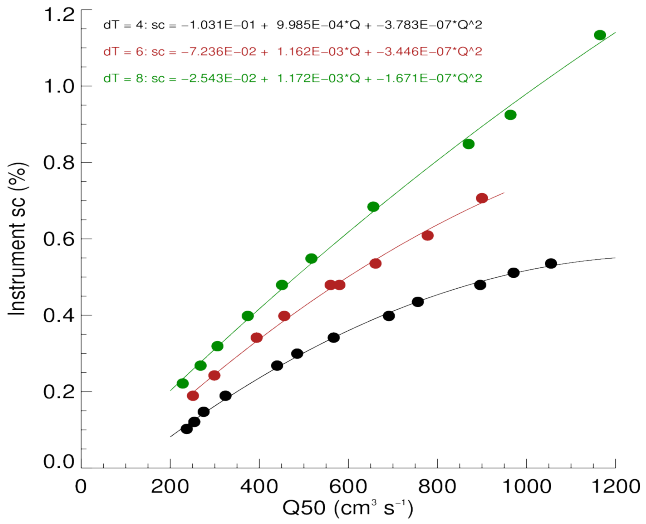

Figure 3.5 Critical supersaturation calibration curves for dT4, dT6, and dT8 sfCCN temperature gradient settings.

As residence time in the sfCCN varied with total flow rate, timestamps were empirically adjusted to align the data with the parallel CPC. The calibrated CPC timestamp adjustment was made as a function of flow by measuring the time delay between narrow peaks of particles introduced at specific flow rates (Figure 3.6). A filter was placed upstream of the split between instruments and then briefly removed, thereby allowing ambient particles to be sampled by both instruments.

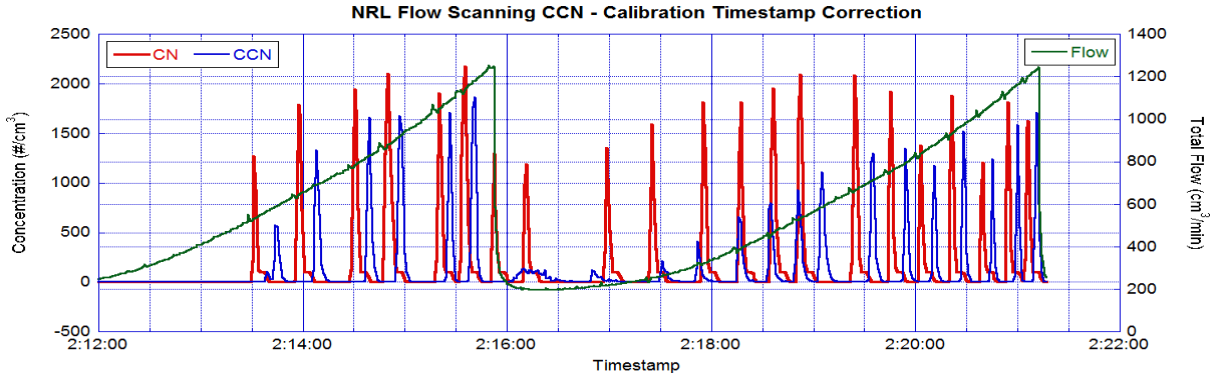

Figure 3.6 Timestamp correction during calibration to account for variable residence time in the sfCCN system as flow changed. Lag between peaks in the CN (red) and CCN (blue) concentrations were dependent of the flow (green) through the sfCCN system.

The time lag between measurements was then determined for a number of flow rates for both measurement and calibration samples. A calibration curve was fit to the aligned time stamps (Figure 3.7) and used to adjust the timestamp of the CPC data points. An example scan with and without the timestamp adjustment is shown in Figure 3.8. Alignment between CN and CCN peaks was improved by the time stamp adjustment, with corresponding reduction in noise in the calculated activated fraction.

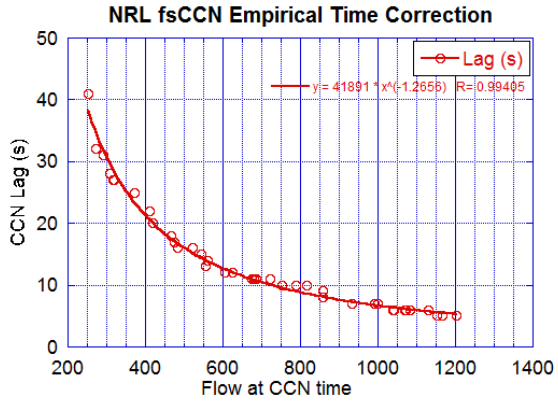

Figure 3.7 Equivalent CPC time correction function for the sfCCN system.

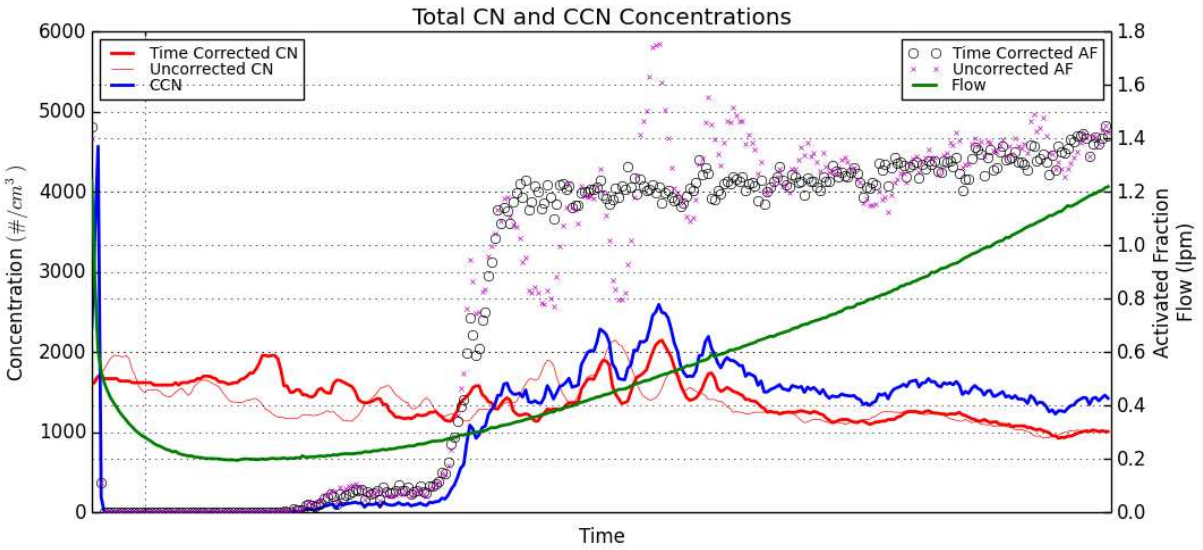

Figure 3.8 Example sfCCN scan (roughly five minutes in length). CCN concentration is shown in blue, with CN concentration without timestamp correction (thin red) and with the correction (thick red), with the coincident flow through the CCNc column. Concentration peaks show better alignment and noise is reduced for the timestamp corrected activated fraction (black circles) as compared to the uncorrected equivalent (purple Xs).

3.2. CLASSIFICATION OF AEROSOL POPULATION TYPE

Classification of aerosol population types impacting BML was conducted using an unsupervised K-means cluster analysis. Such clustering methods utilize properties of the aerosol and environment to identify periods of potentially similar impacts and aerosol population types (Wilks, 2011). Cluster analyses have been used to classify aerosol particle size distributions (Tunved et al., 2004), associate them with various environmental and atmospheric processes (Charron et al., 2008; Beddows et al., 2009; Wegner et al., 2012), and conduct aerosol source apportionment studies (Salimi et al., 2014). Information on aerosol chemistry or composition has also been used for clustering purposes (Frossard et al., 2014), and has been integrated with size distribution measurements and atmospheric transport data to produce cluster results based on multiple types of observations (Charron et al., 2008; Atwood et al., 2017).

The K-means clustering methodology involved selection of specific variables that partially defined the state of the aerosol and meteorological environment at the sampling site. The degree

of similarity of the state of the environment between any two data points (i.e. specific times) was estimated by the use of a distance function that grouped data points into clusters that had broadly similar values among the input variables. Here, we utilized the *cluster.KMeans* class of the Python scikit-learn package (Pedregosa et al., 2011) to perform the analysis. Selection of the appropriate number of clusters for the K-Means analysis followed a similar methodology to that described in Atwood et al., (2017), and was based on both an initial hierarchical clustering and the use of internal validity measures (Wilks, 2011). First, a hierarchical agglomerative cluster analysis was created using the *cluster.AgglomerativeClustering* class of scikit-learn to merge the two data points or clusters with the smallest value of the distance function together into a single cluster in subsequent steps until only one cluster remained. A dendrogram was then used to identify potential numbers of clusters at agglomeration steps that had the largest increase in distance between merged clusters. Various internal validity measures of clusters in the ensuing K-Means clustering (Beddows et al., 2009; Baarsch and Celebi, 2012) were then used to further assess appropriate numbers of clusters. The final selection of appropriate cluster numbers was based on each of these measures, along with verification that the results maintained physically distinct and temporally coherent clusters, in order to select the appropriate number of K-means clusters.

3.2.1. *Cluster Variables*

A total of 67 clustering variables were used to describe each time stamp in this analysis, which included measurements of aerosol microphysical properties and meteorological parameters at BML. Aerosol property variables included the normalized size distribution (normalized to an integrated value of 1 cm^{-3} by dividing by the total particle number concentration), after correction for local contamination. Values of the normalized number size distributions

($dN/d\log_{10}Dp$) were discretized into 20 logarithmically spaced bins, with each mean bin value then serving as a separate variable in the clustering distance function (e.g. Charron et al., 2008). Similarly, activated fraction spectra (the fraction of particles activated at supersaturation S) for each time stamp were divided into 20 linearly spaced bins distributed between 0% and 1.1% supersaturation to incorporate CCN properties into the analysis. Total particle number concentration was included as a separate cluster variable.

Meteorological parameters at BML included the local 10m observed wind velocity as perpendicular u and v component variables (2 variables). Additionally, HYSPLIT backtrajectories were assigned to data points closest in time to each trajectory. The backtrajectory was converted to separate variables for the distance function by determining the distance from the receptor, initial bearing, and altitude, every three hours backwards along the trajectory for 24 hours, yielding a total of 24 trajectory clustering variables for each time stamp.

3.2.2. *Distance Function*

As variables of different scale were used in the cluster modelling, the Karl Pearson distance function (Wilks, 2011) was used, wherein each variable is first standardized to ensure they have equal weight on the distance function. However, as the 67 clustering variables were grouped into five categories of measurements (number size distribution, activation spectrum, total particle number concentration, wind speed, and backtrajectory), a further modification to the weighting (described below) was used to reduce the impact of differing numbers of variables in these categories on the distance function. The resulting distance between any two data points i and j was given by the function:

$$d_{i,j} = \left[\sum_{k=1}^{K} \boldsymbol{w_k}\left(\boldsymbol{x_{i,k}} - \boldsymbol{x_{j,k}}\right)^2\right]^{\frac{1}{2}} \tag{3.2}$$

where $d_{i,j}$ gives the distance between two data point vectors, x_i and x_j, in a K-dimensional space (i.e. K nominally independently measured or observed, orthogonal variables at each time stamp), for each variable, k, with weight, w_k, calculated for each variable by:

$$\boldsymbol{w_k} = \frac{v_k}{s_k} \tag{3.3}$$

where s_k is the variance of the variable k, and v_k is the further relative weight used for each variable.

Only data points with valid measurements for number size distribution and activated fraction were used in the clustering analysis, leaving approximately 94% of data points (3357 of a total of 3583) utilized. Of the remaining data, two data points had partially invalid activation spectra and were kept in the analysis. The partial spectra had invalid data points imputed to the variable mean to minimize their impact on the distance function.

The size distribution and activated fraction variable categories, each of which had 20 variables, were given relative weights, v_k, of 1/20 such that their total relative weights summed to 1. As these variables were of primary importance to aerosol population microphysical properties, the other variable groups were decreased in relative importance. The backtrajectory and wind vector categories were each assigned a relative weight of 0.5, and the total particle number concentration variable assigned a relative weight of 0.1. As cluster analysis is by its nature an exploratory data analysis technique, these relative weight values were reached by varying their

values and assessing the physical interpretability of the results (discussed further in the next section).

3.2.3. *Number of Clusters*

Hierarchical clustering and internal validity measures indicated two, six, eight, and twelve clusters were potentially appropriate for the K-means analysis. Clusters associated with periods of marine aerosol impacts (discussed further in the next section) became temporally coherent (i.e. data points assigned to specific clusters tended to occur near each other rather than randomly distributed throughout the study period) and physically meaningful (i.e. could be related to physical phenomena such as land/sea-breeze shifts) after the number of clusters was increased to eight.

In the case of the twelve-cluster analysis, several of the clusters were composed of few or even a single data point, indicating the model had begun to separate outliers into distinct clusters. In addition, several of the temporally consistent clusters were split, indicating that too many clusters had been selected. All potential cluster numbers between seven and eleven were then investigated to determine if physically or temporally coherent population types emerged to a greater degree than the eight-cluster model. The eight-cluster option had been initially identified as potentially appropriate based on the internal validity measures and hierarchical clustering, while other numbers of clusters did not improve results based on the criteria of temporally coherent clusters and physically meaningful interpretation of the cluster results. As such, the eight-cluster model was selected as the most appropriate unsupervised classification result.

3.3. AEROSOL POPULATION TYPE CLASSIFICATION RESULTS AND DISCUSSION

Three of the eight identified clusters were defined as "marine" population types, as backtrajectory data showed evidence of transport pathways primarily over ocean areas. These marine types, denoted as clusters M1–M3, tended to have lower average number concentrations (below approximately 1500 cm^{-3}), while the terrestrial clusters (T1–T5) had typical averages between approximately 2000 and 4000 cm^{-3} and were associated with transport from more terrestrial source regions. The exception to this was cluster T5, which had number concentrations of roughly 1500 cm^{-3}, more oceanic transport pathways, and size distributions with the largest median diameters among the "terrestrial" clusters. Table 3.1 provides the cluster-averaged number concentrations, wind velocities, HYSPLIT accumulated precipitation along the 24-hour trajectory, hygroscopicity parameters from the srCCN system, and the percentage of all measurements associated with each of the eight identified clusters. Multi-modal lognormal number size distributions were fit to the average of all spectra associated with each cluster. Fit parameters and best-fit CCN-spectrum activated fraction parameters for each cluster are provided in Table 3.2.

Figure 3.9 presents the study timelines of measured (a) aerosol, and (b) meteorological variables, and the (c) corrected and (d) normalized aerosol size distributions. The fitted modal diameters are superimposed on the normalized number size distributions, revealing periods of stability in the size distributions as well as periods that are highly variable. Time periods associated with each cluster are shown as colors in the background of the panels.

Changes between identified cluster types often tracked diurnal changes in wind direction associated with the land/sea-breeze cycle (Figure 3.9b; e.g., 28–30 Jan). Several periods occurred during the study during which this diurnal cycle collapsed and BML was ventilated with air

masses from marine regions for several days at a time (starting on 4 Feb, 17 Feb, and 26 Feb). Clusters M1, M2, and M3 were selected by the model more consistently during these extended periods and confirmed their characterization as marine aerosol population types.

Normalized size distributions for the eight clusters are shown in grey in Figure 3.10, along with the average total corrected particle number concentrations and the total number of data points included in each cluster. Clusters with terrestrial and/or anthropogenic influence were ordered by increasing median diameter of the mode with the largest number fraction. HYSPLIT backtrajectories and wind rose plots for each data point included in each cluster are shown in Figure 3.11. Measured activation spectra from the sfCCN system for each cluster data point are shown as grey density contours in Figure 3.12 along with colored best-fit lines.

Table 3.1 Aerosol and meteorological parameters for each of the cluster time periods with the total number and percentage of observations in each cluster. Cluster mean values are given for total particle number concentration, κ hygroscopicity parameter from the srCCN system, HYSPLIT 24-hour accumulated precipitation along the trajectory, and local wind velocity observations.

BML	Percentage of	Total Number	κ	Wind Velocity		Trajectory 24-hr
Cluster	Observations	Concentration	Mean	u	v	Accum Precip
	% (total N)	(# cm^{-3}) (std dev)	(-) (std dev)	(m/s)	(m/s)	(mm) (std dev)
M1	5% (169)	592 (435)	0.49 (0.23)	6.76	-4.22	0.31 (0.73)
M2	9% (308)	774 (462)	0.30 (0.10)	2.77	1.16	0.07 (0.30)
M3	10% (345)	1547 (1177)	0.46 (0.22)	-2.63	5.70	1.02 (1.76)
T1	9% (304)	1975 (2166)	0.25 (0.17)	0.25	4.12	0.51 (1.21)
T2	17% (566)	3189 (2055)	0.18 (0.07)	-1.90	2.70	0.16 (0.70)
T3	16% (545)	3816 (3447)	0.15 (0.06)	-0.70	2.25	0.03 (0.21)
T4	20% (659)	2306 (1166)	0.17 (0.06)	0.46	2.49	0.01 (0.04)
T5	14% (461)	1459 (600)	0.20 (0.07)	2.72	0.67	0.00 (0.00)

Table 3.2 Cluster best-fit number size distribution and activated fraction parameters are shown, with activated fraction parameters a, b, and c pertaining to the fit model equation given in the supplemental information. Clusters with "M" and "T" names refer to marine and terrestrial aerosol population types, respectively.

BML	Avg Size Dist - Mode 1			Avg Size Dist - Mode 2			Avg Size Dist - Mode 3			Activation Specrum Fit			Activation Specrum Fit		
Cluster	Median	Geometric	Number	Median	Geometric	Number	Median	Geometric	Number	Mode 1			Mode 2		
	(nm)	Std Dev	Fraction	(nm)	Std Dev	Fraction	(nm)	Std Dev	Fraction	a	b	c	a	b	c
M1	45	1.77	0.69	189	1.54	0.28	561	1.22	0.03	0.12	1.34	0.09	0.38	2.72	0.71
M2	21	1.46	0.07	67	1.47	0.39	185	1.45	0.54	0.1399	1.5613	0.60	0.4331	1.4379	0.30
M3	40	1.99	0.69	182	1.59	0.32	--	--	--	0.1246	1.299	0.09	0.266	2.8918	0.68
T1	28	1.78	0.9	144	1.51	0.10	--	--	--	0.1619	2.0963	0.09	1.528	3	0.57
T2	39	2	0.88	170	1.49	0.12	--	--	--	0.4686	1.2076	0.02	0.5111	2.8612	0.63
T3	59	1.8	0.95	211	1.42	0.04	--	--	--	0.4567	1.2878	0.08	0.63	2.6407	0.70
T4	12	1.72	0.1	76	2	0.90	--	--	--	0.38	2.3426	0.70	0.4228	1.2607	0.08
T5	15	1.53	0.06	94	1.85	0.94	--	--	--	0.28	2.16	0.75	0.42	1.28	0.15

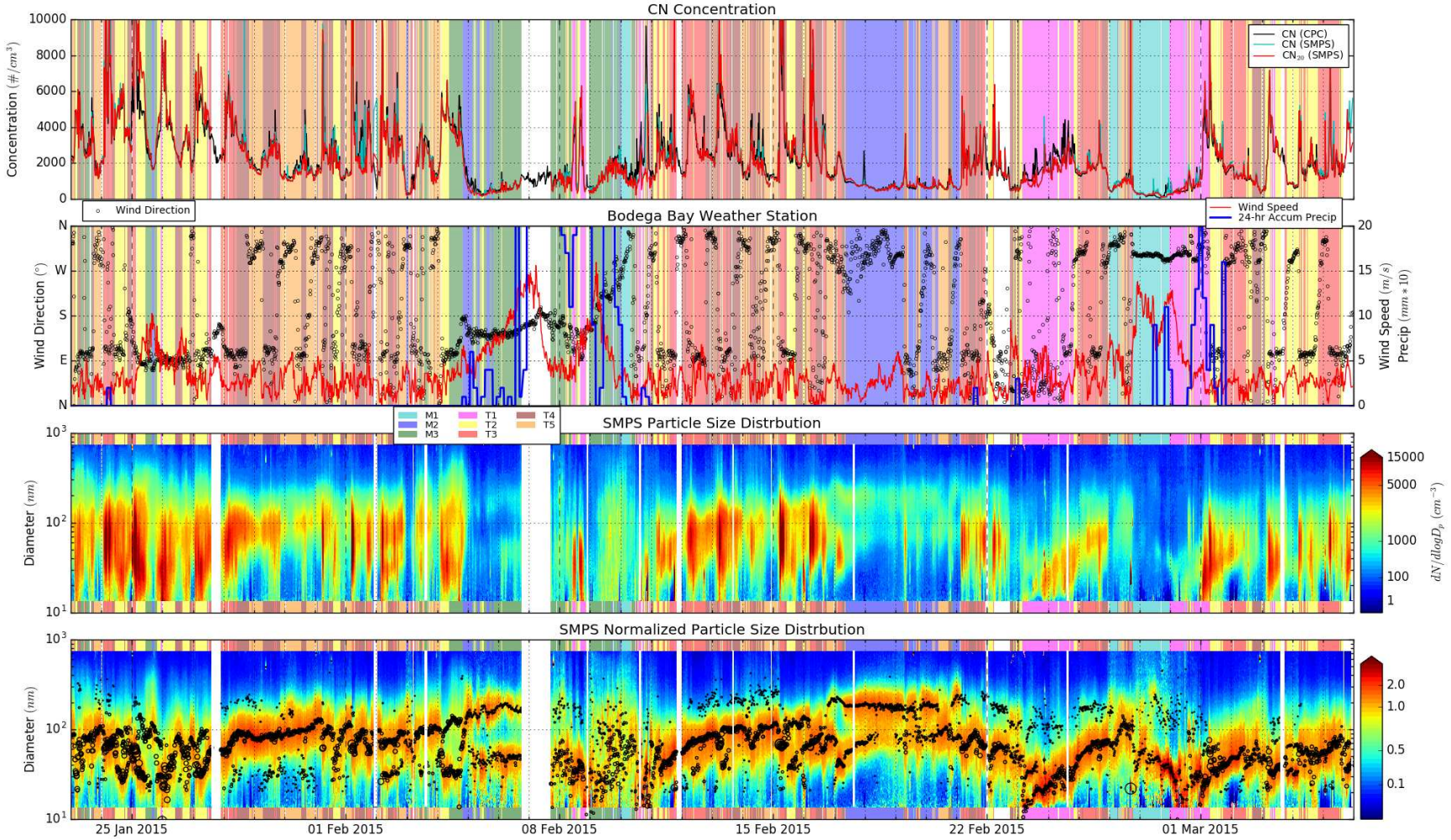

Figure 3.9 Timelines of study data; all times shown are UTC. (a) Total particle number concentration at BML measured by the CPC (black), reconstructed from SMPS size distributions (blue), and after correction for removal of local sources (red). (b) BML weather station measurements of wind direction (black circles) and wind speed (red lines), with HYSPLIT 24-hour accumulated precipitation along the airmass trajectory (blue). (c) SMPS size distribution as $dN/dlog_{10}D_p$. and (d) normalized size distributions with best fit median diameters (black circles) with the size of the circle proportional to the number of particles in the mode. Colored backgrounds in each panel are shown for time periods classified as each cluster type for the 8-cluster K-means classification.

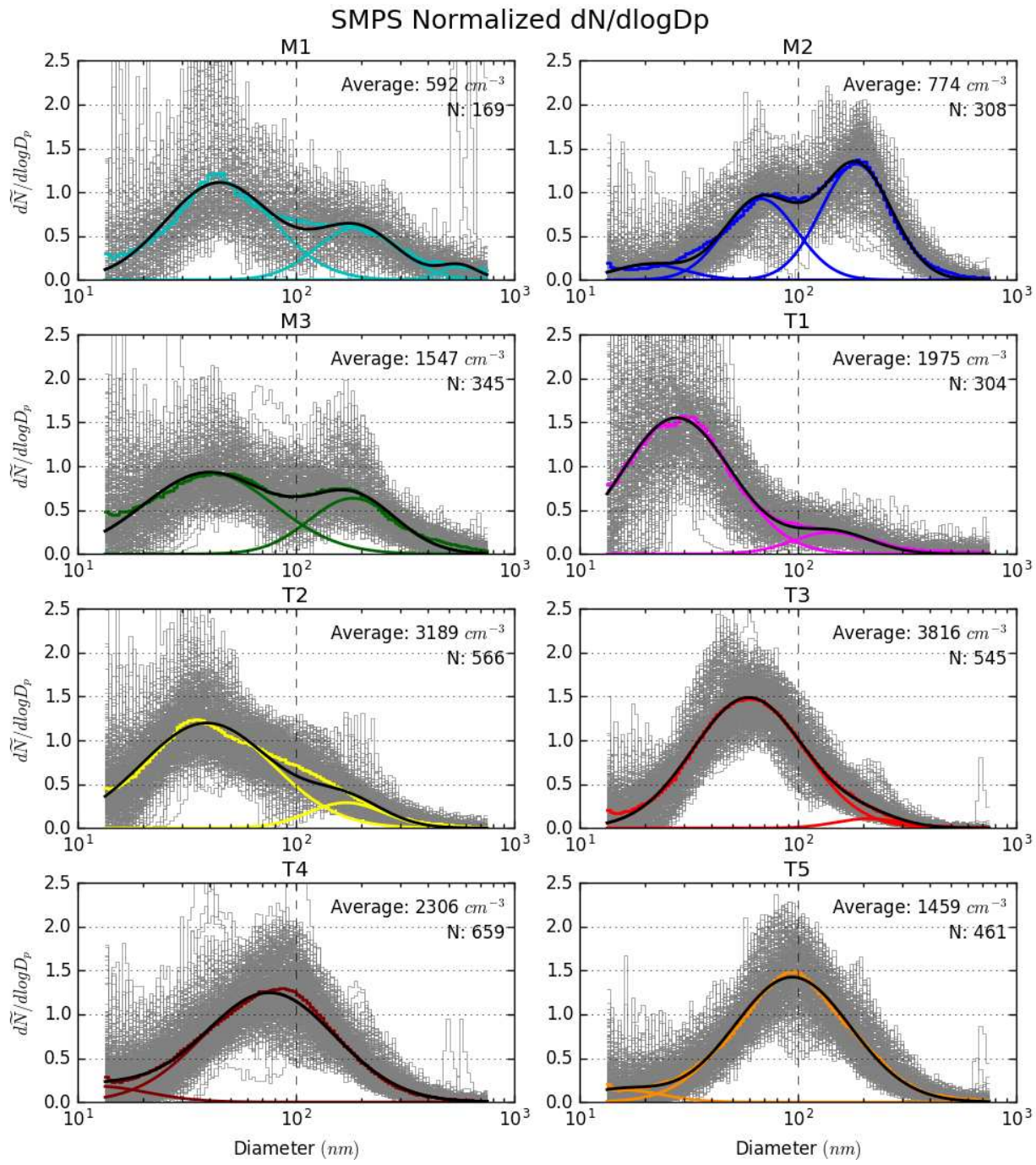

Figure 3.10 Normalized size distribution for each cluster from the 8 cluster K-means classification. Colored step lines show the average distribution, with best-fit multimodal lognormal fit in black and each mode as colored curves. Observed spectra for each data point in the cluster are shown in grey. Average cluster total particle number concentration and number of data points in each cluster are shown.

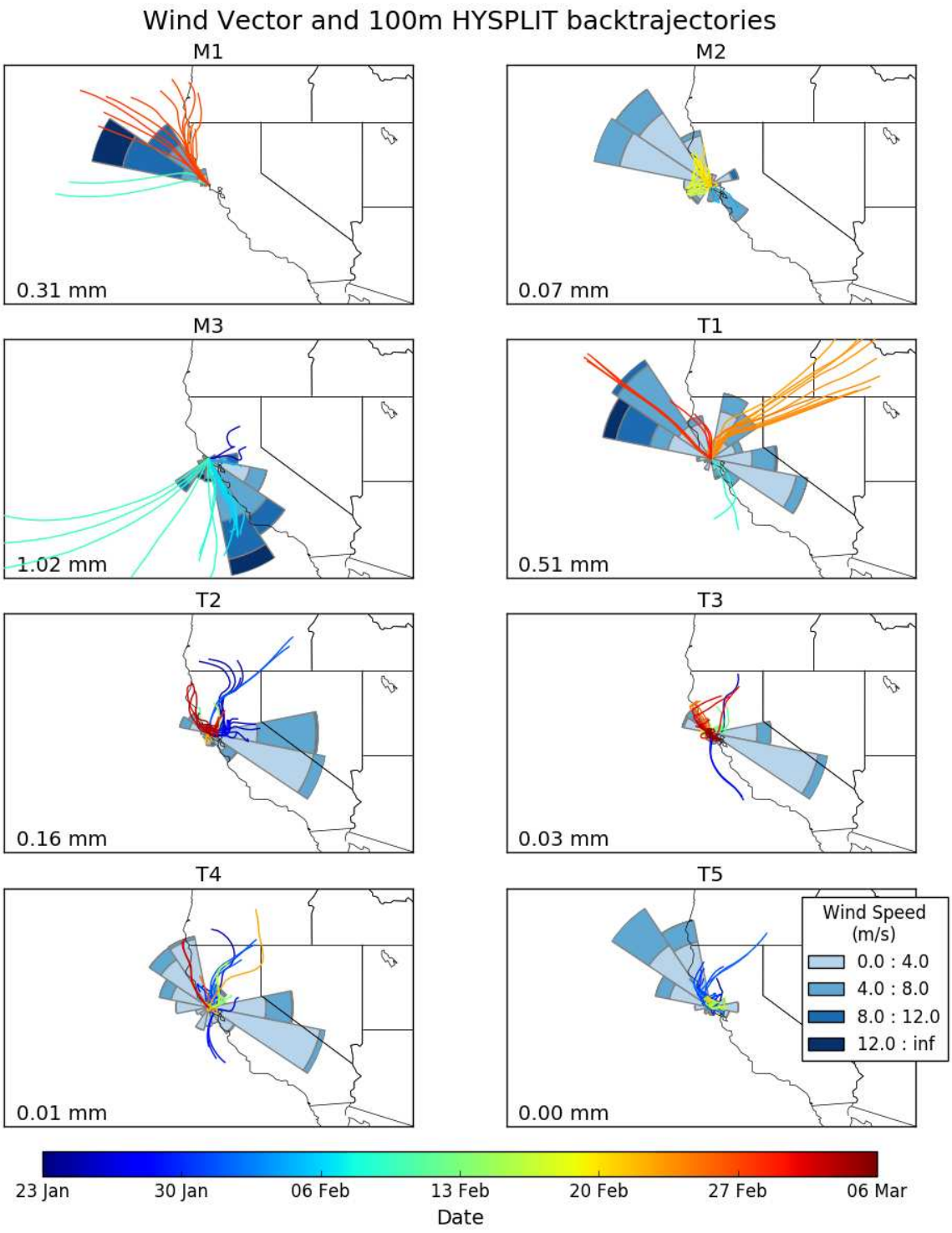

Figure 3.11 Meteorological overview for each cluster from the 8 cluster K-means classification. HYSPLIT 24-hr backtrajectories are shown for each time stamp associated with the cluster and colored by the date of arrival at the receptor. Wind rose plots are shown for all BML local 10m wind direction and velocity measurements for each time stamp associated with the cluster. Mean values for 24-hour accumulated precipitation along the trajectory are included in the lower left for each cluster.

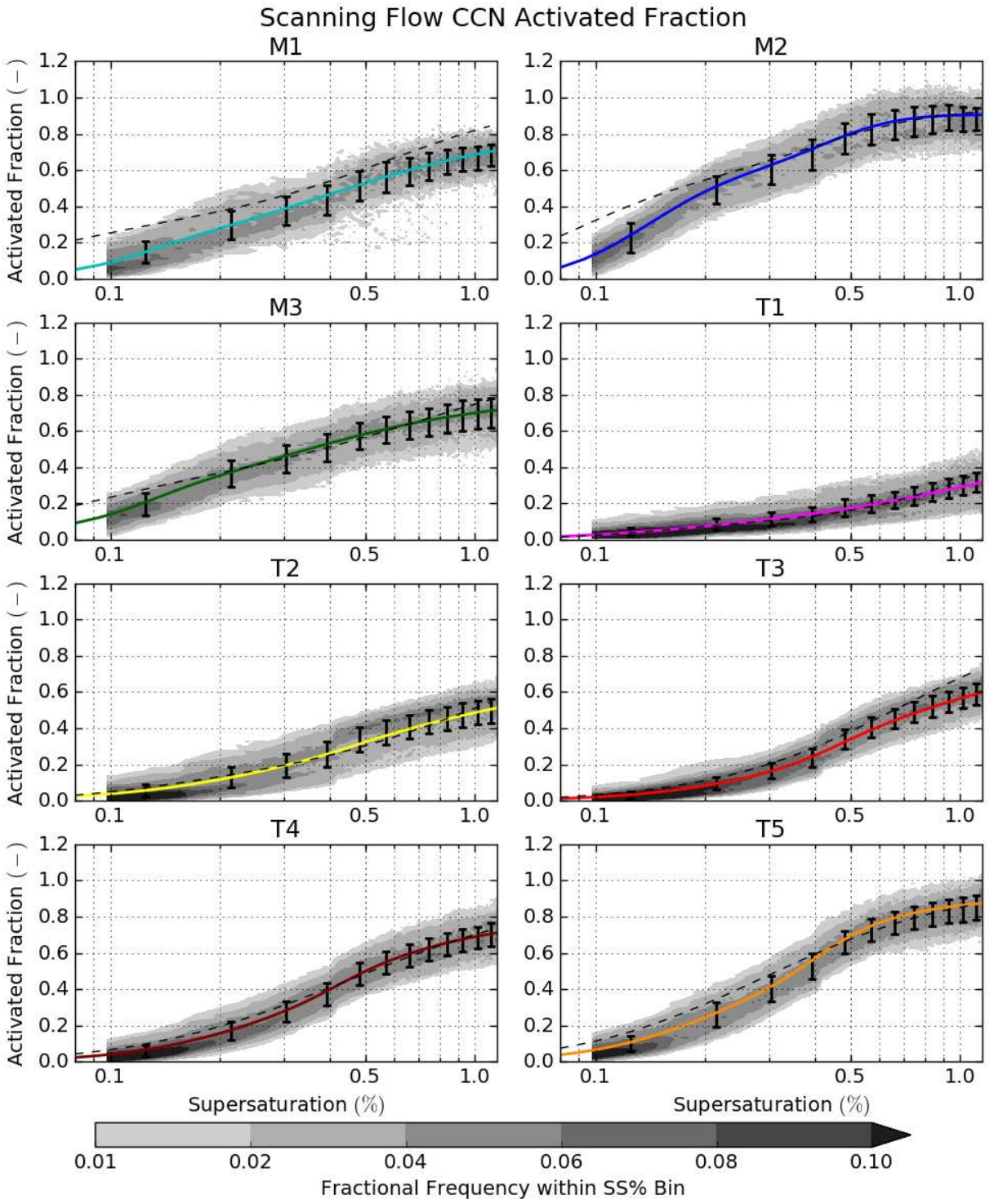

Figure 3.12 Activated fraction spectra for each cluster from the 8 cluster K-means analysis. Best-fit bimodal lognormal cumulative distribution functions are shown in colors for each cluster, with black error bars plotted at +/- 1 standard deviation of the mean for data split into 10 linear-spaced supersaturation bins with roughly equal numbers of data points. Grey contours show relative density of valid cluster data points in each supersaturation bin. Dashed black lines show the reconstructed activated fraction spectra based on average measured size distribution parameters and median measured kappa hygroscopicity parameter.

3.3.1. *Marine Population Types*

Further analysis of the marine clusters showed generally distinct meteorological conditions associated with each. Cluster M1 primarily occurred toward the end of the study period, during a period of high velocity winds from the northwest. Backtrajectories agreed with local winds and showed generally faster transport velocities. This cluster dominated during 26 and 27 February, a period during which the cleanest air masses and lowest number concentrations of the study were observed, reaching as low as 50 cm^{-3} during the height of the event. The normalized size distributions indicated that the Aitken mode dominated the number distribution (Figure 3.10), and also suggested the presence of a somewhat larger mode (particles larger than ~400 nm) that may have been associated with generation of sea spray by the higher wind velocities. Backtrajectories indicated that airmasses had passed over the ocean to the northwest of BML, while 24-hour accumulated precipitation along the trajectories (Table 3.1) indicated rainfall had occurred in the days prior to the airmass' arrival at BML. Each of these findings was consistent with classification of the M1 cluster as a precipitation scrubbed, clean marine aerosol population.

The marine cluster with the next highest number concentration was M2, with 78% of its total occurrences between 17 and 21 February. The wind rose for this cluster indicated a primarily northwesterly wind, similar to cluster M1 but with much slower velocities, and backtrajectories with oceanic transport pathways. While HYSPLIT does not always simulate sub-synoptic scale transport with high fidelity, this pattern may be indicative of slower transport of air from a marine region just off the coast, as opposed to the direct fast-transport path from more distant ocean regions seen in the M1 type. As observed for M1, the best-fit average normalized particle size distribution (Figure 3.10) was primarily bimodal, consistent with many reports of cloud-processed background marine aerosol populations (Hoppel et al., 1986; Bates et al., 2000; Wex

et al., 2016; Atwood et al., 2017; Royalty et al., 2017; Phillips et al., 2018), though with a larger accumulation mode number fraction than the M1 type. Minimal rainfall along the transport pathway was evident in the HYSPLIT accumulated precipitation estimates, indicating no recent precipitation scrubbing and suggesting that more cloud processing without rainout led to larger numbers of particles in the accumulation mode compared with M1. In contrast to M1, for which a third fitted mode was found above 400 nm, the third mode in M2 occurred at very small particle sizes (diameters less than 30 nm).

The final marine cluster, M3, shared similarities with the other marine types, including a bimodal normalized size distribution with a minimum near 110 nm and indications of oceanic source regions in local winds and backtrajectories. However, the average total number concentration was nearly double that of the other marine types. The primary period during which this cluster occurred was during 4-9 February, bracketing the time before, during, and after landfall of the AR that impacted the BML region during CalWater-2015. This cluster is therefore interesting as it may be indicative of a unique population type associated with AR meteorological conditions. Some caution is warranted, however, as instrument downtime lead to a gap in the aerosol size distribution dataset during late 6 February through 7 February, during a high-wind and precipitation period that marked the landfall of the AR, and thus some key data that could be used to guide the clustering during this event were missing. When confined to the 5-8 February period noted by Leung (2016) when the AR made landfall at BML, average number concentration was 749 cm^{-3} for time periods associated with the M3 cluster (excluding the data gap on 6-7 February), and 1052 cm^{-3} for the entire 5-8 February AR period (including the intermittent periods classified as terrestrial or anthropogenic aerosol).

Backtrajectories for the M3 cluster indicated source regions from just off the coast of the San Francisco Bay area prior to reaching BML, while HYSPLIT accumulated precipitation along the trajectory was the highest of any cluster. Flows associated with AR landfall at the coast can be complex (Neiman et al., 2013), however, emissions from this urban area could potentially have mixed with the relatively low particle number counts that would be expected in a precipitation scrubbed AR air mass as it made landfall, accounting for the elevated (> 1000 cm^{-3}) total number (CN) concentrations that persisted for much of the AR, including during the high-wind and heavy precipitation period (Figure 3.9b) when SMPS and CCN data were not available. However, local generation of fine-mode sea spray aerosol could also be a factor during high winds.

3.3.2. *Terrestrial Population Types*

During periods dominated by diurnal shifts in aerosol and meteorological observations, and for short-duration periods during times associated primarily with marine clusters, the cluster model identified clusters that corresponded to terrestrially influenced populations. In the case of the multi-day events dominated by the M1 and M2 types, these short duration periods were often identified as either T4 or T5, clusters that were notable for having largely monomodal normalized size distributions with median diameters around 100 nm. Occurrences of these cluster types were often associated with a spike in number concentration and changes to either wind direction or wind velocity. Thus, the cluster model was able to identify and separate short duration periods of impacts from terrestrial sources during multi-day marine aerosol conditions at BML.

Several longer periods (28-31 January and 13-16 February) were observed during which populations T4 and T5 regularly alternated in tandem with the diurnal land/sea-breeze shift.

Similar diurnal-shift behavior, but between clusters T2 and T3, occurred during 25–28 January and 1–5 March. During these diurnal shifts between various terrestrial clusters, the cluster with the larger median diameter was typically associated with the sea-breeze and transport from oceanic regions, while the smaller diameter cluster was associated with the land-breeze and transport from terrestrial regions. As aging of terrestrial aerosol typically leads to an increase in the median diameter of the aerosol modes, these four clusters may therefore be indicative of various degrees of aging of regional terrestrial aerosol during "sea-breeze resampling" at BML (Martin et al., 2017). Resampling occurs when terrestrial and marine aerosol populations mix and flow across the coastal boundary at low levels, leading to a region of mixed aerosol populations wherein the larger number concentrations associated with terrestrial types dominate the observed number concentrations in the resulting littoral zone airmass. When this diurnal cycle collapsed and BML was subjected to extended periods of sea-breezes and ventilation by air masses almost exclusively from ocean regions, the cluster model selected marine cluster types, indicative of marine airmasses that had not experienced much mixing with terrestrial air masses.

The terrestrial type T1 featured a dominant mode of particles with median diameters around 30 nm, indicating relatively little aging of the particles had occurred. Both low-level winds and backtrajectories during this cluster type indicated transport pathways from many directions (Figure 3.11), though with the highest wind speeds of the terrestrial clusters, consistent with less time between the aerosol source and observation at BML. This cluster occurred primarily during two periods, 23–24 February and 28 February–1 March. During these times, normalized size distributions and modal median diameter fits shown in Figure 3.9 indicated that the size distributions associated with the T1 cluster grew over the course of several days into distributions with larger median diameters, which were then classified as other terrestrial cluster

types. The T1 cluster may therefore identify a freshly emitted population type or a recent new particle formation event.

3.3.3. *CCN and Activated Fraction Spectra Characteristics*

The best-fit activated fraction spectra, as functions of water supersaturation, are shown for all valid data points in each of the clusters in Figure 3.13(a). As a general comparison against other reported values for aerosol activation spectra, Figure 3.13 also shows the parameterized spectra reported by Paramonov et al. (2015) for a range of measurement locations from the European EUCAARI Network (grey background) and an overall typical average value (black line). The EUCAARI activation spectra were drawn from a range of marine, littoral, and continental sites, and were impacted by both marine and terrestrial airmasses, subject to a variety of emissions. The BML spectra spanned much of the range reported for the EUCAARI network, with the M2 cluster slightly above this range at intermediate superaturations. Activated fraction spectra are

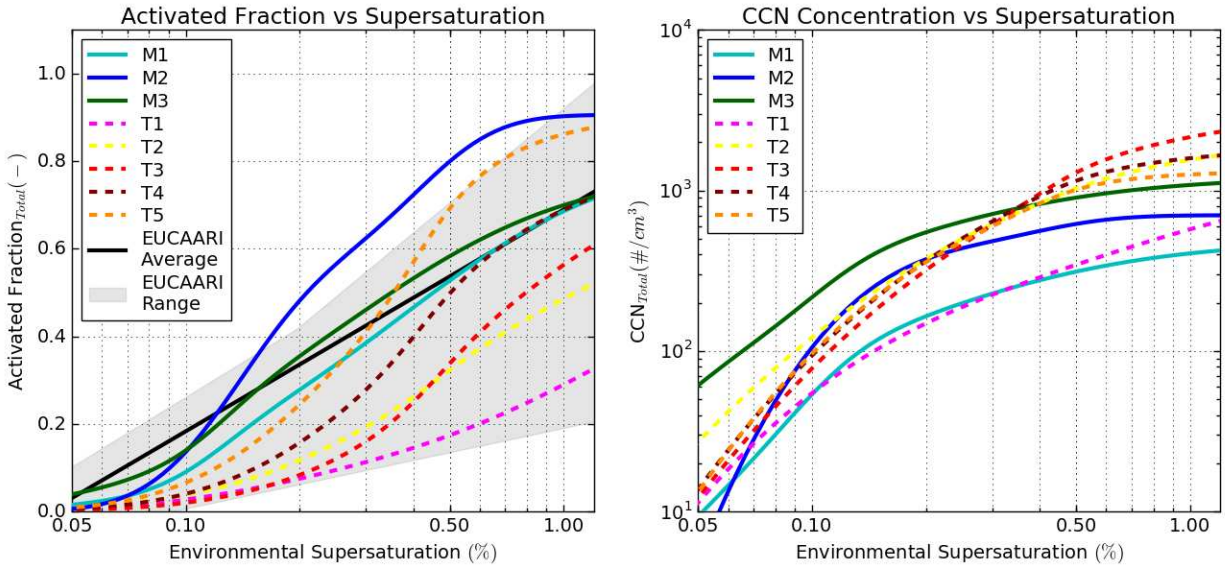

Figure 3.13 (a) Best-fit activated fraction spectra for each cluster in the 8 cluster K-means analysis, with marine aerosol population types plotted as solid lines, and terrestrial clusters types as dotted lines. Cluster average spectra are compared against the maximum and minimum values (grey shading) and overall average (black line) reported by Paramonov et al., (2015) from a range of sampling locations in the European EUCAARI network. (b) Parameterized mean CCN concentrations across the same range of supersaturation values for each cluster in the 8 cluster K-means analysis.

independent of total number concentration, thus the effect of particle size on activation is evident for the BML cases, with clusters with larger size modes having higher activated fractions across the range of measured supersaturations. These results show the wide range of activated fraction spectra at BML associated with differences in aerosol population type, and the corresponding complexity of the population characteristics at this site.

In the CalWater-2015 dataset, marine population types all reached activated fractions of about 0.2 at supersaturations around 0.1% to 0.15%, while the terrestrial types did not reach equivalent fractions until supersaturations between approximately 0.18% and 0.6% were reached. Terrestrial population types with smaller median diameters tended to have less fractional activation across the full range of measured supersaturations, leading to activated fractions at 1.0% supersaturation that varied from approximately 0.3 to 0.85. However, due to the generally higher total particle number concentrations, and despite lower activated fractions of the terrestrial populations, differences in CCN concentrations between marine and terrestrial types (Figure 3.13b) were smaller than the differences in the activated fraction spectra. Only at supersaturations above approximately 0.5% did the CCN concentration for the terrestrial types (except T1, associated with many fresh, small particles) consistently exceed those of the marine types (Figure 3.13b). Between approximately 0.1% and 0.4%, CCN concentrations were often similar between the marine and terrestrial types.

3.3.4. *Comparison of Reconstructed and Directly-measured CCN Spectra*

Average values for observations of the hygroscopicity parameter κ from the srCCN system are given for each cluster in Table 3.1. Mean κ values for the three marine population types were higher than for any of the terrestrial clusters, with the κ for the marine populations found to be significantly different ($p < 0.05$) from those for any of the terrestrial clusters.

Mean measured κ values of 0.49 and 0.46 for the M1 and M3 population types, respectively, were within the range of mean κ values (0.30 to 0.54) for marine aerosol dominated periods in a coastal outflow marine region presented by Phillips et al., (2018). Mean values for terrestrial population types T1–T5 varied between 0.15 and 0.25, and were consistent with the 0.20 value for Aitken mode continental outflow aerosol reported by Phillips et al. (2018). However, we note that κ values measured in this study and used in the closure calculations were derived from supersaturated CCN measurements, whereas Phillips et al. (2018) reported κ from humidified growth factors at 80% RH. Prior work has shown that κ is not always consistent across this large of a span of RH (Irwin et al., 2010; Whitehead et al., 2014), thus contributing to uncertainty in such comparisons. The hygroscopicity for the final marine M2 type was 0.30, near the lower end of typical values for marine aerosol in regions of continental outflow, but still above those of the terrestrial population types. As the M2 cluster was also the only marine population type with no indication of recent precipitation scrubbing of the airmass prior to arrival at BML (Figure 3.9b), some combination of influences from cloud processing, marine, and terrestrial or anthropogenic sources may result in the observed hygroscopicity values between those of the other population types.

The cluster-average hygroscopicities from Table 3.1 were combined with the average cluster size distributions from Table 3.2 to create a reconstructed activated fraction spectrum for each cluster. These reconstructions are compared with the direct-measured CCN spectra in Figure 3.12 and Table 3.2. Generally, the reconstructed spectra are within one standard deviation of the directly measured spectra from the sfCCN system. However, as was noted in the SCS dataset, the reconstruction tends to overpredict activated fraction, in particular for the marine clusters and at low supersaturations and low CCN number concentrations. Such overprediction of CCN

concentrations based on reconstructions using hygroscopicity and size distributions has been noted before (e.g. McFiggans et al., 2006; Kammermann et al., 2010). Kammermann et al., (2010) had proposed this as being due to uncertainty in the critical activation diameter. At larger particle diameters measurement uncertainty increases due to imprecise particle size cuts, losses in inlets and tubing, and inversion uncertainties, along with generally lower number concentrations than at smaller particle diameters, leading to higher expected uncertainty in CCN predictions and reconstructions when the critical activation diameter is in this range of particle sizes. At low supersaturations where BML data showed an overprediction bias the critical activation diameter would be above 150 nm. The marine types that had the largest biases at low supersaturations also tended to have larger fractions of particles at these large sizes. This would be expected to add to uncertainty in ways similar to those noted by Kammermann et al., (2010) and potentially explain the larger discrepancies in CCN prediction at lower supersaturations in the marine aerosol types.

Further investigation of the closure between predicted and observed CCN concentration was conducted using two prediction models. Hygroscopicity derived predictions using cluster average κ and normalized size distribution values were generated and compared against all observed CCN concentrations by the sfCCN system in Figure 3.14a. Similarly, the predicted CCN concentration using cluster average activated fraction spectra were compared against observations in Figure 3.14b. Both models predicted the activated fraction using the cluster type identified during the observation, which was then multiplied by the observed total number concentration at the observation time. The hygroscopicity and size model showed overprediction compared to both observations and the activated fraction model (Figure 3.14c), with best-fit slopes of 1.08 and 1.09 respectively. The activated fraction model predictions did improve on the

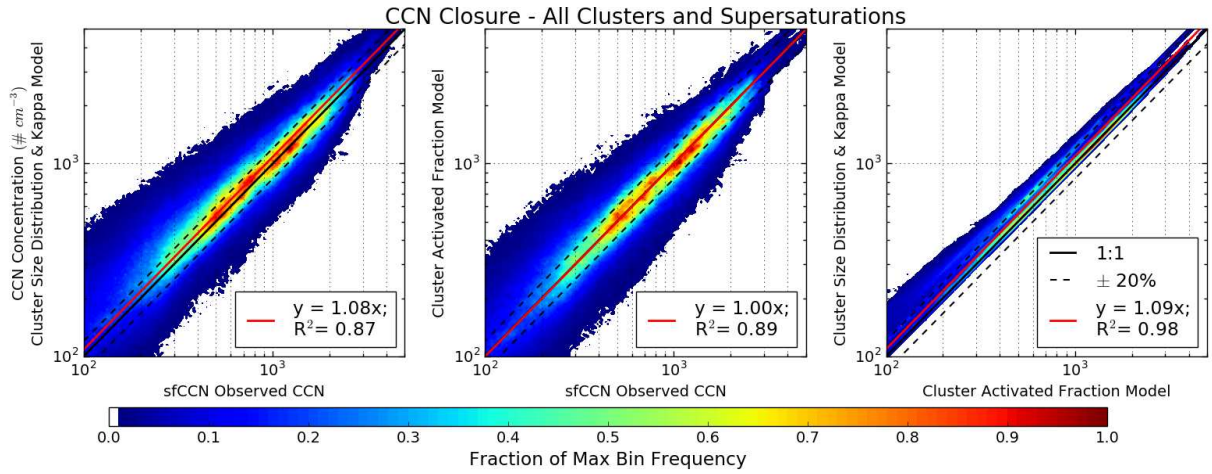

Figure 3.14 CCN closure comparing predicted and measured CCN number concentrations for (a) the predicted concentration based on the size distribution and κ reconstruction against observed concentrations, (b) the predicted concentration based on the best-fit activated fraction reconstruction against observed concentrations, and (c) the comparison between the two reconstruction methods. All cluster types and supersaturations across the full range of observed values are shown. Linear best-fit slope is shown in red with the associated R-squared values. One to one lines and lines at ± 20% are shown. Colors represent the data point density as a fraction of the maximum density in each plot.

hygroscopicity model, with a slope of 1.00 and R^2 values increasing from 0.87 to 0.89, though this is in part due to the model being based on a direct fit of the observed data. Nevertheless, the degree of closure between model predictions and observed CCN concentrations is similar to closures previously reported in field studies (e.g. Bougiatioti et al., 2009; Kammermann et al., 2010).

Interestingly, the M1 and M3 population types that were thought to be associated with more recent precipitation scrubbing of the airmass had somewhat larger overprediction biases of the type noted by Kammermann et al. (2010) at lower number concentrations when using the size distribution and hygroscopicity model as compared to the M2 background marine type (Figure 3.15). Such behavior was also noted in the SCS precipitation type. This could provide some indication that wet deposition may have played some role in the noted overpredictions as a result of precipitation scrubbing shifting the size distribution to smaller sizes (and with potentially lower hygroscopicities than modal averages due to further organic enrichment at smaller sizes)

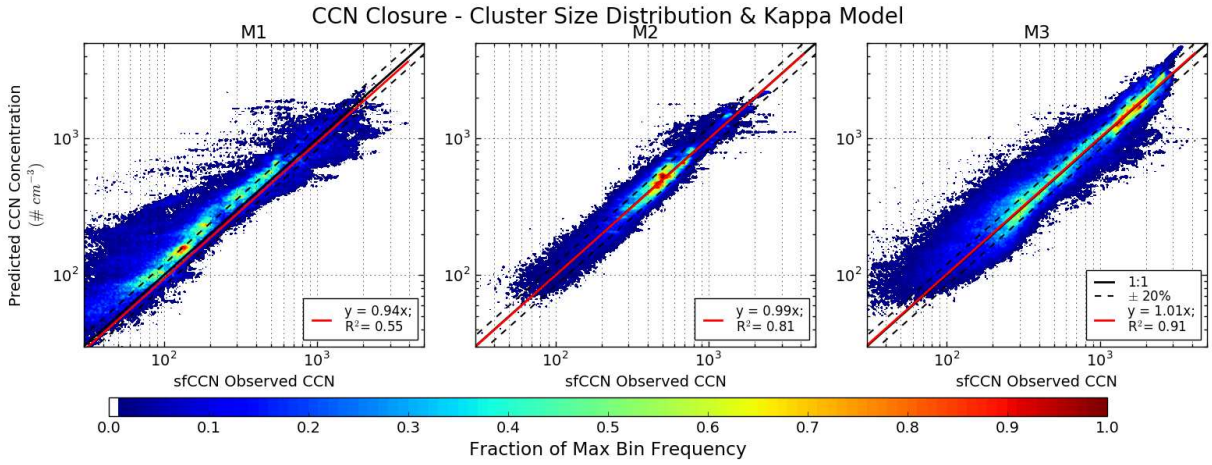

Figure 3.15 CCN closure as in Figure 3.14a, comparing the predicted concentration based on the size distribution and κ reconstruction against observed concentrations for the marine population types.

as compared to the population average. However, similar overprediction was also noted at lower concentrations in the terrestrial types, so such an explanation would nevertheless leave some part of the bias unresolved in this dataset.

3.3.5. *Validation of Clustering Methodology During Marine Aerosol Dominated Periods*

In order to validate that the ability of the clustering model to improve characterization of distinct aerosol population types, further analysis of the cluster results was performed for three multi-day time periods that were associated with marine aerosol dominated air masses impacting BML. As noted in section 3.3.1, these marine dominated periods were the precipitation scrubbed clean marine event (25 Feb 23:00 UTC – 28 Feb 12:00 UTC), the cloud-processed background marine event that involved ventilation of BML from oceanic regions (17 Feb 09:00 UTC – 21 Feb 03:00 UTC), and the atmospheric river (5 Feb 13:00 UTC – 9 Feb 08:00 UTC).

Normalized size distributions for all data from each of the event time periods were generated and are shown in the left column of Figure 3.16, all showing typical bimodal size distributions expected of cloud processed marine aerosol populations. The data points for these time periods were then segregated into only those corresponding to the marine cluster identified with each

event (center column), and all data points from other cluster types that were excluded from that cluster (right column). In all three cases, noise in the range of distributions associated only with the cluster periods was reduced and average particle number concentration decreased. The data excluded from the marine clusters included some distributions that were largely monomodal and similar to the aged terrestrial distributions discussed in the previous section. Local wind vectors shown in Figure 3.17 showed that the marine cluster data points were more generally associated with northwesterly winds from ocean regions, while the excluded data points occurred during periods of more easterly winds from inland regions.

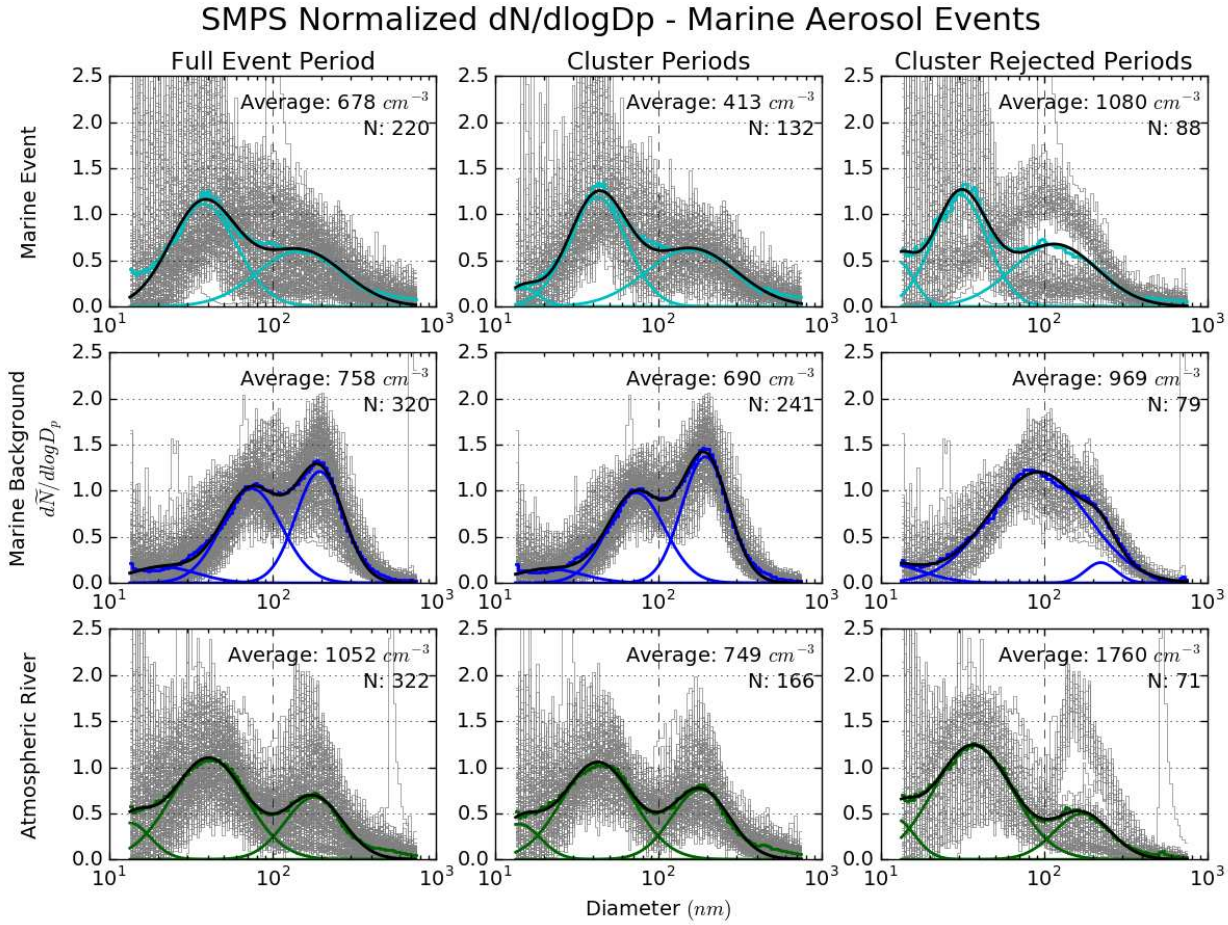

Figure 3.16 Normalized size distribution comparison for the three marine aerosol events (rows), averaged by the entire event time period (left column), only those times associated with the marine cluster associated with the event (center column), and those times that were excluded from the marine cluster (right column).

The consequences to predicted CCN characteristics of removing non-marine data points are obvious in the resulting activated fraction spectra shown in Figure 3.18. For the marine event associated with cluster M1 (top row), averaging all time points (left column) resulted in two distinct activated fraction curves, with the lower curve resulting from the inclusion of a period with small particles that had low activated fractions. Excluded data (right column) removed not only those data points, but also screened time periods with higher activated fractions that belonged to a different population type from M1. The resulting activated fraction spectrum associated with this event for only cluster periods (center column) had considerably smaller standard deviations in the result. Similar results were seen in the analysis of the M3 cluster event,

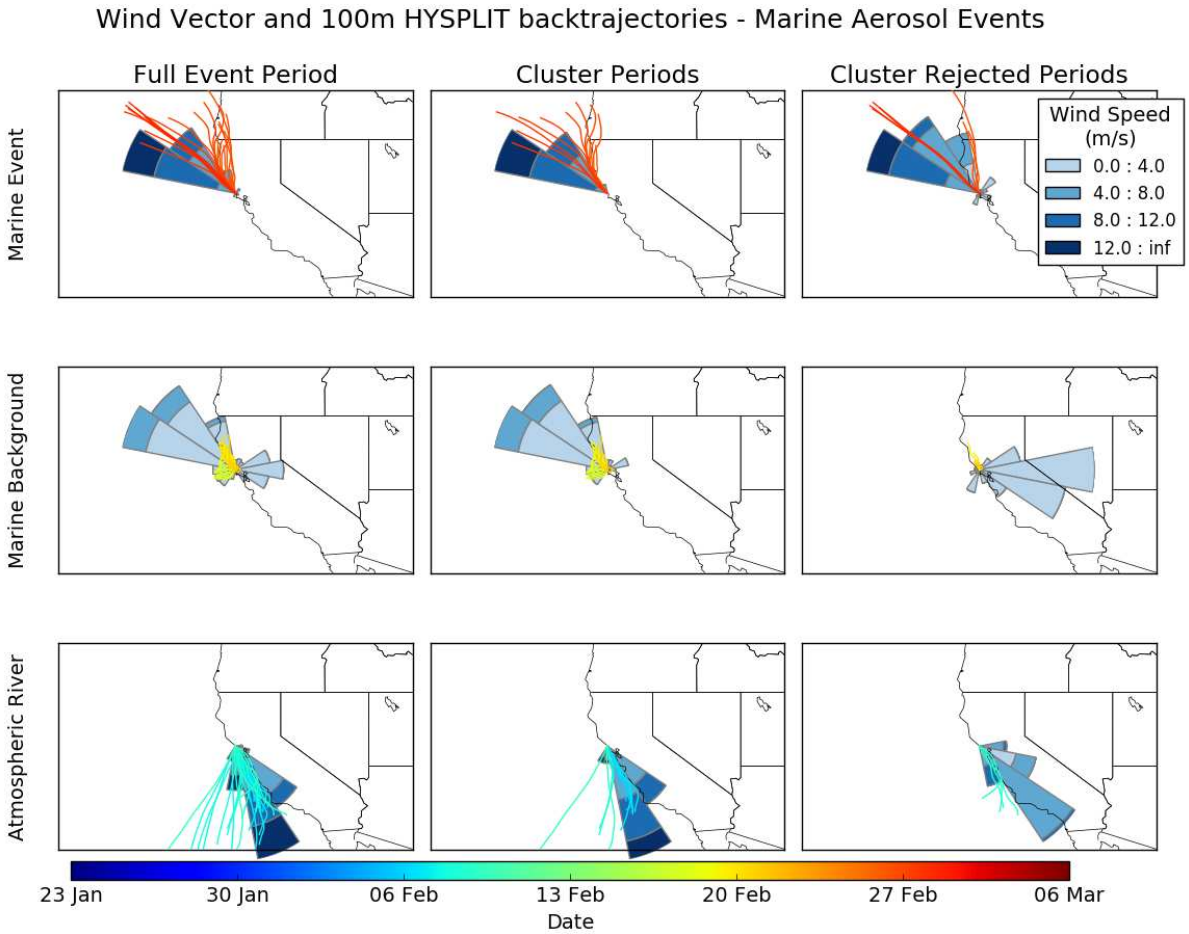

Figure 3.17 Meteorological comparison for the three marine aerosol events as in Figure 3.16.

with lower activated fractions associated with the terrestrial or anthropogenic contamination periods being effectively removed in the clustering activated fraction spectrum. While the M2 marine background event did not see as large of a change between time-averaging and cluster-averaging, the standard deviations were smaller in the clustering results, indicating increased precision in the activated fraction parameterization. Additionally, the excluded data points were themselves generally consistent and had low standard deviations, indicating that that a single separate population with distinct microphysical properties was likely intermittently observed during this event.

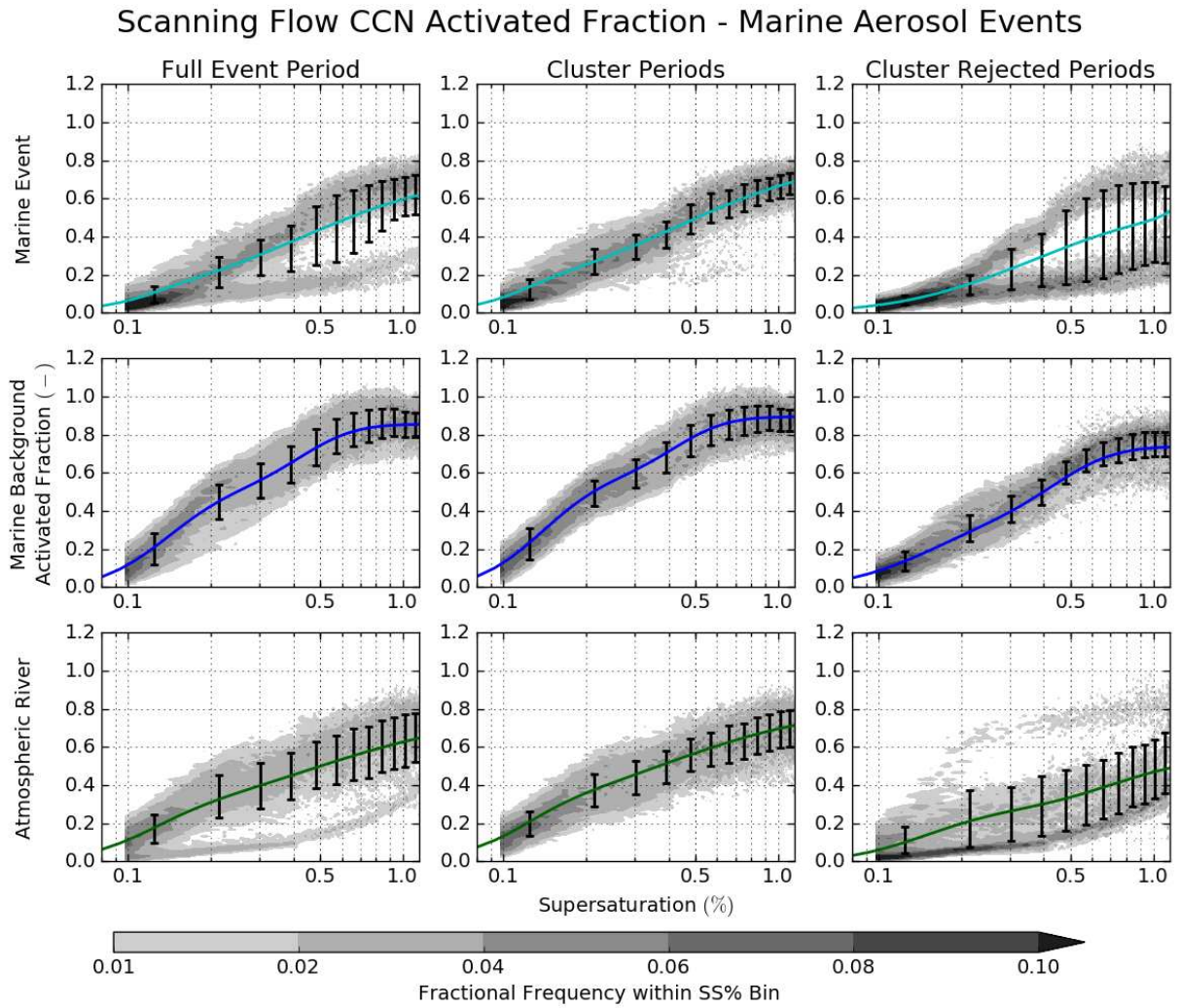

Figure 3.18 Activated fraction spectra comparison for the three marine aerosol events as in Figure 3.16.

As a result, it was concluded that the clustering methodology using both properties of the aerosol and meteorological values was able to successfully segregate time periods associated with various aerosol population impacts. Additionally, it was able to provide improved identification of aerosol population types with less noise in the resulting parameterizations.

3.4. COMPARISON OF MARINE AEROSOL POPULATIONS

The microphysical properties of the three marine aerosol population types identified in the previous section were compared to the results of the SCS dataset. Comparison of the activated fraction spectra for the average population types, shown in Figure 3.19, indicated the marine background types were found to be generally consistent between the datasets. The SCS parameterization fell within the inner quartile range of the BB observations across most of the observed supersaturation range, with a slight difference below about 0.1%. The precipitation impacted marine and atmospheric river types of the BB dataset were likewise similar to the SCS precipitation impacted clean marine type, here with slight differences above about 0.7% due primarily to fewer ultrafine particles in the remote SCS region. In both datasets, a background

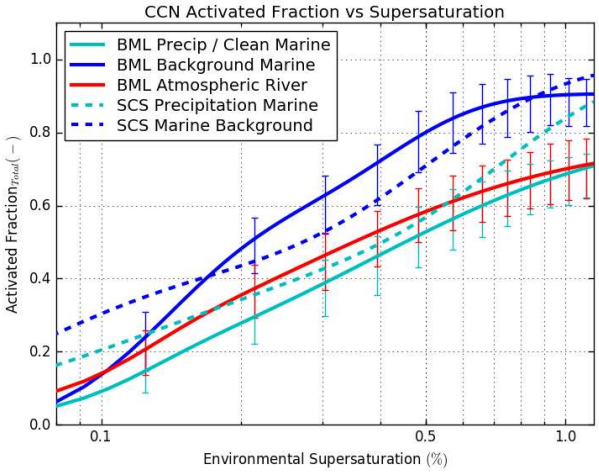

Figure 3.19 Best-fit parameterized activated fraction spectra for marine aerosol population types from the Bodega Bay (solid) and South China Sea (dashed) datasets. Error bars show the inner quartile regions of all observed data points associated with each population type from the Bodega Bay dataset.

marine population was observed that had slightly higher CCN activity across the full range of supersaturations as compared to periods when precipitation scrubbed this background population.

In order to place the microphysical properties of the marine aerosol in context against other observed population types, the marine aerosol types are shown together with other identified types for each dataset in Figure 3.20. It is notable that the activated fraction spectra of the marine types were found to be of moderate CCN activity across the observed supersaturation range. In the case of the BB dataset, the smaller and less aged types from terrestrial sources led to lower activated fraction spectra as compared to the marine types, while in the SCS dataset an influx of aged terrestrial aerosol that had grown well into the accumulation mode range resulted in higher activated fractions than the marine types.

These observations from relatively distinct marine impacted regions point to several conclusions regarding marine aerosol populations. First, marine aerosol that has not been mixed with or

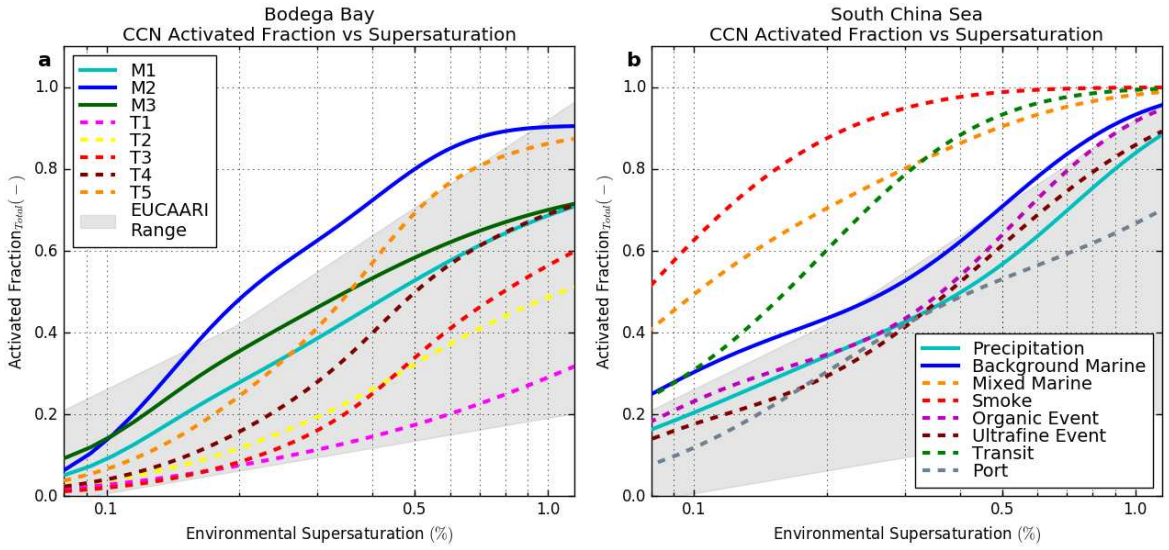

Figure 3.20 Activated fraction spectra for identified population types from (a) the Bodega Bay dataset and (b) the South China Sea dataset. Marine aerosol population types are shown as solid lines, while terrestrial types are show as dashed lines. The range of reported average observed activated fraction from the EUCAARI network is again shown for comparison.

impacted by other sources tended to be fairly similar between the two regions, with precipitation serving to slightly reduce activated fractions due to relative decreases in the accumulation mode particle number fraction. Second, when impacts from other sources of aerosol occurred, the activated fraction could vary from considerably below to above the typical marine aerosol ranges. This was largely due to particle size, with the degree of aging potentially strongly controlling the CCN activity of the aerosol population. Lastly, while these general conclusions hold for the average parameterized population types described in this chapter, questions as to the effect of variability within population types, and the effect of variability between population types remain. In particular, the scenarios under which the differences in these microphysical properties are important, as opposed to mere differences in particle number concentration, will be addressed in subsequent chapters.

3.5. SUMMARY

The unsupervised cluster model analysis successfully identified distinct aerosol population types in the littoral zone aerosol at BML during CalWater-2015. The time periods selected by each cluster tended to be both temporally and physically coherent. Clusters also tended to be grouped into periods with physically meaningful microphysical properties that could be associated with meteorological processes and expected sources and transport pathways. For example, the clustering methodology identified regular diurnal swings in aerosol properties associated with land/sea-breeze changes and assigned two distinct, terrestrially-influenced aerosol types during these periods. Overall, the clustering results for the CalWater-2015 dataset produced a reliable set of aerosol population types, and appropriately screened intermittent periods of impacts from various other sources as an outcome of the classification. Both marine and terrestrially influenced aerosol population types were identified by the unsupervised cluster model. Several

marine events that persisted for days were identified as distinct in character from each other—differing in the degree of cloud processing and precipitation removal prior to arrival at the measurement site, and in the extent to which high winds contributed larger sea spray particles. About 10% of the observations were associated with a terrestrial population with a large fraction of small particles, indicating it was affected by relatively fresh emissions and/or new particle formation.

A primary motivation for CalWater-2015 was improving characterization of the regional aerosol and how it might affect the formation of precipitation. The CCN activation spectra observed at BML spanned a full range reported in the literature, from clean marine to strongly terrestrially influenced in character. However, differences in total aerosol number concentrations associated with the marine and terrestrial types partially offset the differences in activated fraction over a range of measured supersaturations, such that the variability in CCN concentrations between some marine and terrestrial aerosol types at some supersaturations was less than expected from the differences in the averaged total aerosol particle concentrations.

In this littoral region sea-breeze resampling and complex mixing between marine, terrestrial, and free-tropospheric air masses lead to complex aerosol populations. Determination of which aerosol types can become incorporated into AR events and thereby affect cloud and precipitation over California depends strongly on the individual nature of the flow regimes and potential aerosol source regions that they tap into. Nevertheless, the observational data set had cases for which marine and terrestrial CCN concentrations were comparable at supersaturations below approximately 0.4%, and thus changes in aerosol types would result in little change to initial drop populations in the resulting stratus cloud, except at very low supersaturations. Thus, mixed-phase microphysical processes occurring in those clouds might also be expected to be similar

whether marine or terrestrial aerosols served as the nuclei for the supercooled droplets. In contrast, for clouds forming at higher maximum supersaturations, terrestrial aerosol populations are expected to yield higher drop concentrations than marine types, with the exception of a terrestrial population characterized by primarily small, recently emitted or newly formed particles. Thus the droplet size distributions formed on terrestrial vs. marine types, for liquid clouds formed in stronger updrafts or at higher cooling rates that reach such higher supersaturations, should be distinctly different.

At the BML observational site, apparent aerosol types changed over much shorter time scales than a multi-day classification based on prevailing meteorological conditions would suggest, consistent with complex flows in coastal zones. Inclusion of both meteorological and aerosol properties into the schemes used in unsupervised cluster models therefore yielded improvements in classification of aerosol and air mass types observed at the surface, and successfully identified changes at time resolutions on the order of hours. Further work into classification of aerosol populations in complex or highly variable regions may therefore benefit from inclusion of a wider range of measurements or observed properties into clustering methods.

4. SENSITIVITY OF INITIAL CLOUD PROPERTIES TO OBSERVED MARINE AEROSOL POPULATION TYPES

The nature of available CCN supporting cloud formation has been shown to have a direct effect not only on initial cloud formation, but on cloud dynamics and the evolution of cloud features including precipitation, cold pools, anvils, and processes such as convective invigoration (Rosenfeld et al., 2008; Fan et al., 2016), which in turn impact radiative transfer and climate (Twomey, 1974, 1977; Albrecht, 1989; Ackerman et al., 1993). In marine environments, noted aerosol impacts include those on low level warm-phase clouds including fogs and stratocumulus layers, through to deep convective mixed-phase cloud systems where impacts become increasingly complicated as numerous processes combine to modulate cloud development (Wood, 2012; Rosenfeld et al., 2014b). Important to this aerosol-cloud relationship is the process by which particles activate as cloud condensation nuclei (CCN) and grow via condensation into cloud droplets. In shallow warm-phase clouds enhanced CCN concentrations produce more droplets of smaller sizes, which tends to reduce precipitation efficiency and increase cloud fraction, lifetime, and reflectivity to incoming solar radiation (Ramanathan et al., 2001; Lu et al., 2007; Xue et al., 2008; Andersen and Cermak, 2015). In deeper mixed-phase clouds sensitivity to CCN becomes more complex, with non-linearities and dependencies on other meteorological parameters increasing in addition to impacts from warm-phase processes (Khain et al., 2008; van den Heever et al., 2010; Storer and van den Heever, 2012; Li et al., 2013; Sheffield et al., 2015).

The initial cloud droplet number concentration (CDNC) that forms near cloud base is of fundamental importance to the aerosol-cloud relationship, and is commonly used to assess initial sensitivity of a forming cloud to changes in aerosol properties before the impact of more complex processes begin to affect cloud development (Rosenfeld et al., 2014b). Generally,

CDNC is most sensitive to the aerosol particle number concentration (CN) and updraft velocity near cloud base (w) (Feingold, 2003; Feingold et al., 2003; Rosenfeld et al., 2014b; Fan et al., 2016). Enhanced CN concentrations lead to formation of more and smaller droplets, while higher supersaturations generated with increasing w tend to activate a larger fraction of particles and result in higher initial CDNC values (Andreae and Rosenfeld, 2008; Fan et al., 2016). However, these relationships are non-linear and do not apply across the full range of atmospherically relevant values for w and CN. Using a parcel model with a simple mono-modal aerosol population to estimate CDNC across a range of values for these parameters, Reutter et al. (2009) identified several regimes of CDNC sensitivity defined roughly by the ratio of updraft velocity to total particle number concentration. Briefly, an aerosol-limited regime was characterized by high w/CN ratios ($\gtrsim 10^{-3}$ m s^{-1} cm^3), large peak parcel supersaturations ($\gtrsim$ 0.5 %), and large activated fractions ($\gtrsim$ 90 %), where CDNC was roughly proportional to CN and independent of w. At the other extreme, an updraft-limited regime was characterized by low w/CN ratios ($\lesssim 10^{-4}$ m s^{-1} cm^3), low peak parcel supersaturations ($\lesssim$ 0.2 %), and small activated fractions ($\lesssim$ 20 %), where CDNC was roughly proportional to w and independent of CN. At w/CN ratios between 10^{-3} and 10^{-4} m s^{-1} cm^3 a transitional regime was noted where CDNC was non-linearly dependent on both CN and w.

Similar to CDNC, the spectral shape of the initial cloud droplet distribution can be sensitive to differences in aerosol properties and can alter cloud development and radiative properties. Liu and Daum (2002) found that the droplet relative dispersion (ε)—the ratio of the standard deviation to the mean diameter of the droplet size distribution—near cloud base increased as CN concentrations rose in observations of marine clouds, and that this change affected cloud radiative properties in ways that may partially offset radiative impacts associated with changes in

CDNC. A theoretical basis for this dispersion effect formulated by Liu et al. (2006) showed ε increasing with CN and decreasing with *w*, with similar behaviors reported in various parcel model studies (Yum and Hudson, 2005; Peng et al., 2007) and observations (Peng and Lohmann, 2003; Rotstayn and Liu, 2003; Pandithurai et al., 2012). However, as with CDNC this general relationship applied only to an aerosol-limited regime. Conflicting observations and model results have reported ε unchanged or decreasing with CN in some scenarios, particularly in conditions of higher pollution loading (and therefore likely higher CN concentration) or when additional cloud dynamics processes are considered, as well as a more complex and non-linear relationship between ε and updraft velocity (Lu and Seinfeld, 2006; Lu et al., 2007; Martins and Dias, 2009; Ma et al., 2010; Berg et al., 2011; Hudson et al., 2012). Such descriptions are further complicated by the complex behavior of the droplet spectral width (i.e., the standard deviation of the droplet distribution not normalized by the mean diameter), which may not relate to CN or *w* in the same manner as ε (Lu et al., 2007; Hudson et al., 2012; Hudson and Noble, 2014; Liu et al., 2014). Nevertheless, initial cloud droplet relative dispersion has been shown to be highly relevant for parameterization of droplet spectral shape impacts on cloud radiative properties (Liu and Daum, 2002; Rotstayn and Liu, 2003) and dynamical evolution of clouds (Lu and Seinfeld, 2006).

Following from these uncertainties, Chen et al. (2016) investigated the behavior of ε at peak supersaturation across the *w*/CN regimes described by Reutter et al. (2009) using a similar parcel model and simple mono-modal aerosol population. They found similar regime dependencies in ε as were found for CDNC, with ε increasing with CN in the aerosol-limited regime, peaking in the transitional regime, and decreasing with CN in the updraft-limited regime. Similarly, ε increased with *w* in the updraft-limited regime, peaked in the transitional regime, and decreased

with *w* in the aerosol-limited regime. The results clarified some of the contrasting behavior in the initial droplet dispersion effect of ε noted in earlier works, and importantly, showed that sensitivity of ε could be described according to regimes defined in much the same way as for CDNC.

The complexity of the aerosol-cloud relationship, however, means that the CN and *w* parameters are insufficient to fully account for observed initial cloud droplet properties including CDNC and ε, or the resulting differences in cloud dynamics, precipitation, and optical properties that occur as clouds evolve. Changes to CDNC and ε alter the cloud droplet effective radius, and hence the reflectivity of the cloud to incoming solar radiation. The efficiency of the collision-coalescence process by which drops grow to sizes sufficient to form precipitation is similarly related to the distribution of droplet sizes, meaning changes to number and distribution of droplets can impact both precipitation and cloud lifetime (Andreae et al., 2004; Freud et al., 2011; Freud and Rosenfeld, 2012). Consequently, the optical impacts, known as aerosol indirect effects (AIE), remain among the largest sources of uncertainty in estimates of Earth's energy budget and climate forcings (IPCC, 2013; Rosenfeld et al., 2014a), and complicate efforts to include AIE into regional and global atmospheric models. Estimating impacts to the onset, type, and amount of precipitation in both warm-phase and deep convective cloud systems are complicated by both limited observations of these relationships across wide regions and variability in the ways such processes are represented in models (Fan et al., 2016). A number of parameterizations of cloud droplet nucleation have been proposed and are used in various cloud-scale (Khain et al., 2015) to large-scale (Ghan et al., 2011) models, but reconciling these predictions against observations remains a challenge (Rosenfeld et al., 2014b; Fan et al., 2016). As a result, the relative importance of additional factors related to both the aerosol population and environment on CCN

properties and cloud droplet activation has been the subject of extensive study (Feingold, 2003; Kreidenweis et al., 2003; Ervens et al., 2005; Dusek et al., 2006; McFiggans et al., 2006; Cubison et al., 2008; Quinn et al., 2008; Andreae and Rosenfeld, 2008; Reutter et al., 2009; Ward et al., 2010; Partridge et al., 2011; West et al., 2014; Chen et al., 2016; Sanchez et al., 2016).

Confounding these efforts is the complexity and resource intensive nature of such investigations using models, which often necessitates the use of idealized or simplified aerosol representations to limit the parameter space that various models must be run across. At the same time, aerosol population models and the microphysical impacts of aerosol particles in models have grown more complex (e.g. Saleeby and van den Heever, 2013, and references therein). Processes such as emission and evolution of multi-modal aerosol populations, competition among separate populations for activation into cloud droplets, removal processes (e.g. wet and dry deposition), hydrometeor evaporation and regeneration, and modification of an aerosol population are now included in various models run across different scales (Ghan et al., 2011; Khain et al., 2015). While CN concentration is critically important for CDNC and droplet distribution, this value will change as a population evolves. Consequently, some models that lack more advanced aerosol microphysical representations will track dry aerosol mass (under the assumption that mass conservation is required and is the most important constraint) and use source or population type specific aerosol models to estimate particle number concentration and to parameterize droplet properties from the varying mass concentrations. A question therefore emerges as to when differences between aerosol models or population types are relevant to initial CDNC and ε, and under what circumstances simpler representations based solely on CN and w would be sufficient to adequately parametrize initial droplet properties.

Globally, the aerosol-limited regime is thought to prevail, with the updraft-limited regime encountered only in more polluted air masses (Rosenfeld et al., 2014b), implying a primary dependence of CDNC on total number concentration. However, in remote marine regions in particular, where cleaner conditions and lower particle number concentrations are expected, sensitivity of the initial droplet distribution to other parameters of the aerosol distribution (e.g., composition and multi-modality) increases (Partridge et al., 2011; Koren et al., 2014; Remer, 2014). The remote marine SCS dataset—which captured both generally clean conditions and periods of higher CN concentrations associated with impacts from populations with substantially different intensive aerosol properties as compared to background marine conditions—therefore represents a potentially useful observationally-based dataset to examine initial cloud droplet property sensitivity to aerosol population differences.

4.1. METHODS

4.1.1. *Cloud Parcel Model*

Initial cloud droplet properties were investigated using a Lagrangian cloud parcel model (Heymsfield and Sabin, 1989; Feingold and Heymsfield, 1992) modified to utilize the κ hygroscopicity parameter (Petters and Kreidenweis, 2007) for computing droplet supersaturations (e.g. Eidhammer et al., 2009), and translated into the Python language for integration with data and aerosol models from the SCS dataset. The parcel model physics follow typical cloud parcel models—briefly, a simulated air parcel is lifted adiabatically leading to cooling and supersaturation of water vapor, which then condenses on modeled aerosol particles allowing growth of some fraction of particles to cloud droplet sizes. The multi-modal aerosol models from the SCS dataset were used as inputs to define both size distribution and hygroscopicity parameters. Aerosol distributions were discretized into 200 logarithmically

spaced bins with distribution edges sized to capture 99.9% of both the number and volume distributions, which were then grown by condensation to new sizes for each bin with each model step—that is, the mean size of the particles in each bin evolved with time. Similar model studies have found 200 bins to be generally sufficient to produce stable cloud droplet properties around the level of maximum supersaturation (where ε is evaluated in this work; e.g. Chen, 2018). In the case of model runs with externally-mixed aerosol modes, 200 bins were used for each mode; the modes were then grown and tracked independently, but with communication through the computed changes in the vapor phase. Following prior published studies, simulations were initialized at a temperature of 285.2 K, a pressure of 950 hPa, and a relative humidity of 95%, with all particle sizes and water contents initialized to their equilibrium sizes at 95% RH, using κ-Köhler theory. Updraft velocity was fixed throughout each simulation, with model time step defined by 1.0 m/w (Saleeby and Cotton, 2004). Droplet condensational growth expressions (Pruppacher and Klett, 2010) were solved using a Python implementation of the variable-coefficient ordinary differential equation (VODE) solver (Brown et al., 1989). As described further below, simulations were stopped once they reached a liquid water content of 0.8 g kg^{-1}, with additional testing using alternative conditions as explained further in section 4.2.2. Other model setup parameters investigated in more depth are described in the following sections. Additional information on the droplet growth rate governing equations used for this parcel model can be found in Appendix A, with additional implementation information found in Saleeby and Cotton (2004) (henceforth SC04).

Setup of the parcel model was focused on maintaining consistency with previous studies to allow for comparison of relevant findings against the impact of different aerosol population types on initial cloud droplet properties. However, a number of other physical processes not being

accounted for in these results are relevant to cloud evolution. Among these, droplet collision and coalescence, sedimentation, and dry air entrainment are important in shaping the cloud droplet size distribution as the cloud evolves, but were not considered here. Additionally, evolution of the underlying aerosol population within a cloud via scavenging, regeneration, physical or chemical changes, and radiative effects (e.g. Saleeby and van den Heever, 2013 for additional discussion), and the impact of ice nucleation in mixed phase clouds, are the subjects of extensive study, but were beyond the scope of this work. The presence of giant CCN may affect cloud development and could potentially change model results, even for the initial drop distribution, in some circumstances (Feingold et al., 1999), but are not examined here. The results presented in this chapter are therefore indicative of aerosol-induced changes relevant to the initial stages of cloud formation, to the initial expected cloud droplet number concentration and relative dispersion of the drop distribution, and to cloud properties associated with these parameters.

4.1.2. *Cloud Property Sensitivity*

Feingold (2003) evaluated the sensitivity of cloud top droplet effective radius to changes in various aerosol and environmental parameters using a parcel model, and suggested the use of a relative sensitivity parameter for comparison of the relative importance of various parcel input parameters. Such methods have since been extended to evaluation of the relative importance of various parcel model input parameters on a number of cloud properties (e.g. McFiggans et al., 2006; Reutter et al., 2009; Ward et al., 2010), where the relative sensitivity, S, of some cloud property parameter, ϕ, to a change in some parcel input variable, X_i, while other input parameters are held constant, was defined as the ratio of a differential change in the logarithms of the model variables as:

$$S_{\phi}(X_i) = \frac{\partial \ln \phi}{\partial \ln X_i} \tag{4.1}$$

Relative sensitivity values near zero therefore indicate that changes in X_i have little impact on the value of ϕ, with values further from zero indicating increased relative importance of X_i on ϕ. In the case where $S_{\phi}(X_i)$ is roughly constant over a large range of values for X_i, relative sensitivity can be estimated by a linear best fit. However, in cases where relative sensitivity is not constant across the parameter space and linear best fits are therefore not sufficient, parameter relative sensitivity can be estimated as a function of some set of model input parameters, **X**, as:

$$S_{\phi}(X_i|\mathbf{X}) = \frac{\partial \ln \phi}{\partial \ln X_i} \approx \frac{\Delta\phi/\phi}{\Delta X_i/X_i} \tag{4.2}$$

In such a case, for example, a relative sensitivity of 0.2 (-0.4) would indicate that a 50% increase in X_i was associated with a 10% increase (20% decrease) in ϕ. Given that CDNC and ε are generally not constant over the range of atmospherically relevant values for parameters of interest, and that various parcel model properties can be obtained for fixed differences in input parameters, we use this form of relative sensitivity estimates in the following sections and provide results for S_{CDNC} and S_{ε} across a range of atmospherically relevant values for **X**.

Reutter et al. (2009) used the ratio of the CDNC relative sensitivities for CN and *w*, i.e. $S_{CDNC}(w)/S_{CDNC}(CN)$, to establish boundaries between the aerosol-limited, transition, and updraft-limited regimes. Relative sensitivity ratios of 4:1 and 1:4 were found to be roughly consistent with *w*/CN ratios of 10^{-3} and 10^{-4} m s^{-1} cm^3, respectively, which were therefore used as effective boundaries between the regimes. Relative sensitivity ratios, ξ, used here for similar comparisons between two model input parameters X_a and X_b are in the form:

$$\xi_{\phi}(X_a, X_b|\mathbf{X}) = \left|\frac{S_{\phi}(X_a|\mathbf{X})}{S_{\phi}(X_b|\mathbf{X})}\right| \tag{4.3}$$

where $|\mathbf{X}$ is included where helpful to clarify that the sensitivities for various parameters may be evaluated for different sets and values of input parameters.

4.1.3. *Population Type Sensitivity*

Sensitivity studies using cloud parcel models often quantify a property such as CDNC as a function of a limited set of various aerosol and environmental input parameters relevant to the scenario of interest, with all other parameters (contained in **X**) fixed at some realistic value. Relative sensitivity and relative sensitivity ratios are then used to yield information about the relative importance of the various input parameters on cloud properties. However, under real atmospheric conditions aerosol parameters are often not fully independent, meaning investigating changes to a single parameter can span more of the vast parameter space than necessary to examine physically relevant differences associated with changing population types. In addition, identified sensitivities may not be associated with realistic aerosol populations. In this study, we aim to correct this misinterpretation of the true variability in the atmosphere using observational constraints as described below.

In the SCS dataset, a particular emphasis was placed on classifying differences between observed population types as a whole as opposed to differences in individual aerosol parameters. Parcel model cloud property output based on this dataset could therefore be represented as a function of population type as opposed to individual aerosol parameters, thereby allowing for more efficient and physically relevant investigation of the impact of different population types on cloud properties. As a result, SCS cloud properties modeled here are generally evaluated as a function

of particle number concentration, updraft velocity, and the set of relevant aerosol intensive parameters, $\boldsymbol{\gamma}$, associated with given population types, i.e. $\phi(CN, w, \boldsymbol{\gamma})$.

The population type as classified in the SCS dataset is a discrete, un-ordered parameter, whereas application of relative sensitivity calculations as formulated in Eqns 4.1 and 4.2 requires variables that can be measured on a continuous ratio-scale. In order to evaluate the sensitivity of cloud properties to differences in population type in a similar manner, an equivalent scale was created wherein the largest possible difference between population types in the SCS (from a microphysical perspective) was given a value of 1 (i.e., a maximum of 100% difference in intensive aerosol properties is possible due to changing population type). As there is no order to various population types, the difference between the two is simply defined here as positive one for the direction which increases the associated cloud property value, in order to maintain a methodology consistent with other calculations. Relative sensitivity of a cloud property to the maximum expected difference arising from changes to intensive properties of the population type model is therefore evaluated as:

$$S_{\phi}^{*}(\boldsymbol{\gamma}_{max}) \approx \frac{|\phi(\boldsymbol{\gamma}_A) - \phi(\boldsymbol{\gamma}_B)| \Big/ min\{\phi(\boldsymbol{\gamma}_A), \phi(\boldsymbol{\gamma}_B)\}}{1} \tag{4.4}$$

where S^* indicates the relative sensitivity is only valid for comparisons between two population types, A and B, that have the largest microphysical difference in intensive aerosol parameters, $\boldsymbol{\gamma}_{max}$, among available population type models, and min yields the minimum value.

Additionally, the relative sensitivity for other parameters must be evaluated for single population types, which are not necessarily the same, e.g. $S_{\phi}(X_i|\boldsymbol{\gamma}_A) \neq S_{\phi}(X_i|\boldsymbol{\gamma}_B)$. As a result, we use the

average value of the relative sensitivity, $\overline{S_\phi^*}(X_i) = mean\{S_\phi^*(X_i|\boldsymbol{\gamma}_A), S_\phi^*(X_i|\boldsymbol{\gamma}_B)\}$, to approximate the relative sensitivity ratio, ξ_ϕ^*, as:

$$\xi_\phi^*(\boldsymbol{\gamma}_{max}, X_i) \approx \frac{S_\phi^*(\boldsymbol{\gamma}_{max})}{\overline{S_\phi^*}(X_i)} \tag{4.5}$$

As $S_\phi^*(\boldsymbol{\gamma}_{max})$ is associated with a nominal 100% difference in population type, $\xi_\phi^*(\boldsymbol{\gamma}_{max}, X_i) * 100\%$ therefore gives the effective percentage change in X_i needed to generate the equivalent change in ϕ as would be expected from the largest change in population type. A value of $\xi_{CDNC}^*(\boldsymbol{\gamma}_{max}, CN|\mathbf{X}) = 0.5$, for example, implies that a 50% increase in CN concentration would produce the same change in CDNC as the maximum change in population type for a given set of input parameters, **X**. Other discrete, unordered parameters, such as sensitivity to mixing state, are evaluated here using this same methodology.

4.2. RESULTS

Parcel model sensitivity cases were conducted using 37 logarithmically distributed CN concentrations between 10^1 and 10^5 cm^{-3} and 34 logarithmically distributed w values between 0.01 and ~40 m/s for each scenario of interest. It should be noted that observations did not span this full range of CN concentrations for individual population types and therefore not all results are relevant to observed scenarios. They were examined here to allow for interpretation of the results against the regime classifications of Reutter et al. (2009) and Chen et al. (2016), hereafter R09 and C16, respectively. In the SCS dataset the largest microphysical difference in CCN activation properties among population types—seen most readily in the cumulative CCN spectrum as a function of critical supersaturation—was generally between the precipitation and smoke type models (Figure 4.1). As such, population type sensitivity tests were conducted using

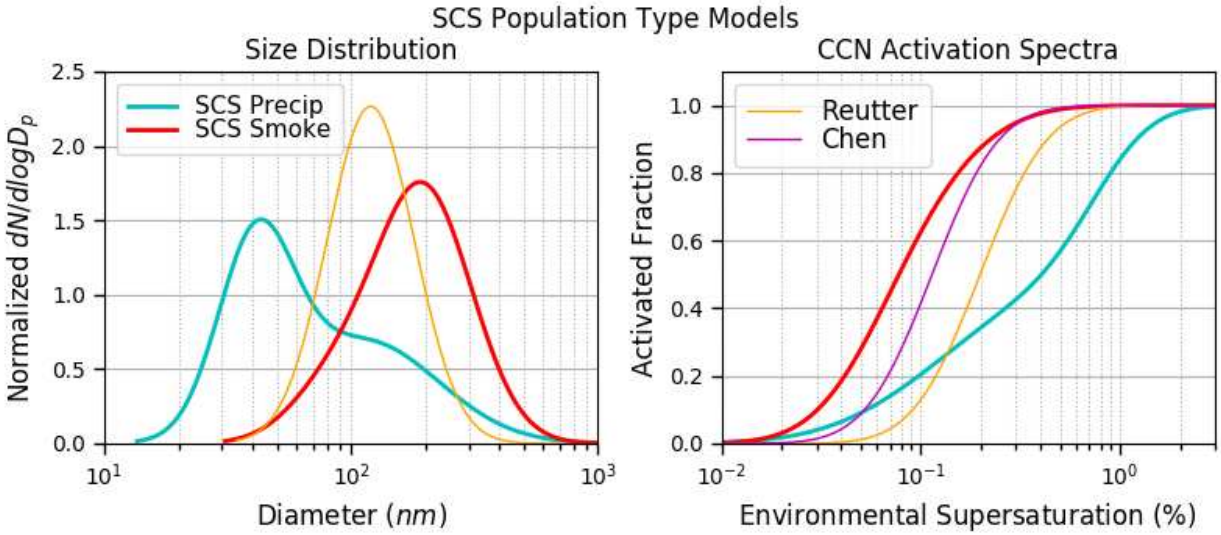

Figure 4.1 Normalized size distribution and CCN activation spectra for the SCS population types used in this study and the monomodal types used in the Reutter et al. (2009) and Chen et al. (2016) studies. Differences in the activation spectra among SCS population types were generally largest between the precipitation and smoke types.

these two population types. In order to validate the model and compare against the regime classifications, parcel model runs using the simpler mono-modal aerosol population types used in the R09 and C16 studies were conducted as well. We note that while the SCS smoke type appears somewhat mono-modal, it was in fact defined by two modes and was skewed as compared to a simpler lognormal distribution. Intensive aerosol parameters for each modeled aerosol population type are given in Table 4.1.

The computed initial CDNC values for these population types are shown in Figure 4.2. The results for the Reutter inputs (orange isopleths) showed generally similar values and behaviors to

Table 4.1 Intensive aerosol parameters for each population type used in the parcel model. Reutter and Chen types are from the parameters used in the R09 and C16 studies, respectively.

	Mode 1				Mode 2			
	Median	Geo	Number	κ	Median	Geo	Number	κ
Population Type	(nm)	Std Dev	Fraction	(-)	(nm)	Std Dev	Fraction	(-)
SCS Precipitation	41	1.42	0.48	0.34	113	2.00	0.52	0.54
SCS Smoke	85	1.50	0.16	0.56	196	1.57	0.84	0.40
Reutter	120	1.50	1.00	0.20	-	-	-	-
Chen	120	1.50	1.00	0.61	-	-	-	-

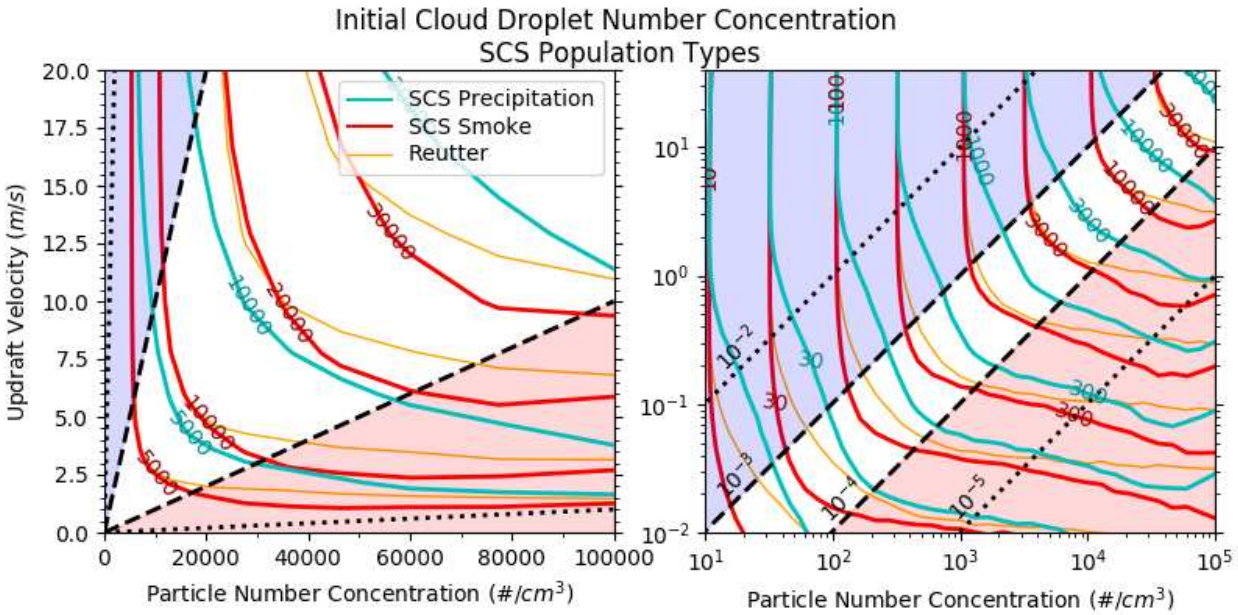

Figure 4.2 Initial CDNC isopleths for each of the SCS population types on linear (left) and logarithmic (right) scales. The R09 population type is included for comparison (orange). The R09 transitional regime is the region between the dashed lines (white background) at 10^{-3} and 10^{-4} m s^{-1} cm^3, with the aerosol-limited regime (blue) and the updraft-limited regime (red) beyond these lines. Additional dotted lines at 10^{-2} and 10^{-5} are shown for reference.

those reported in R09 and followed their proposed CDNC regimes, including concentrations primarily dependent on CN in the aerosol-limited regime (blue background) and *w* in the updraft-limited regime (red background). In the case of the multi-modal SCS population type models, greater complexity in the isopleths was noted, potentially confounding some of the R09 regime relationships associated with a simpler mono-modal aerosol population. In the red updraft-limited regime, isopleths for the SCS types indicated additional dependence on CN concentration as compared to the Reutter model across much of the regime's parameter-space. In the aerosol-limited regime the precipitation type showed greater sensitivity to *w* as compared to the Reutter model (while the smoke type showed less) at *w*/CN ratios below about 10^{-2} m s^{-1} cm^3. Further, sensitivity to population type was noted across all regimes, specifically in this region below roughly 10^{-2} m s^{-1} cm^3.

CDNC sensitivities to both CN and *w* are shown in Figure 4.3 for each of the SCS and Reutter population type models. Isopleth lines for S and ξ were first smoothed by 2-D Gaussian kernel filters due to noise arising from parcel non-linear behavior and numerical errors. Relative sensitivity tests for the Reutter population type showed the regime sensitivity as described by

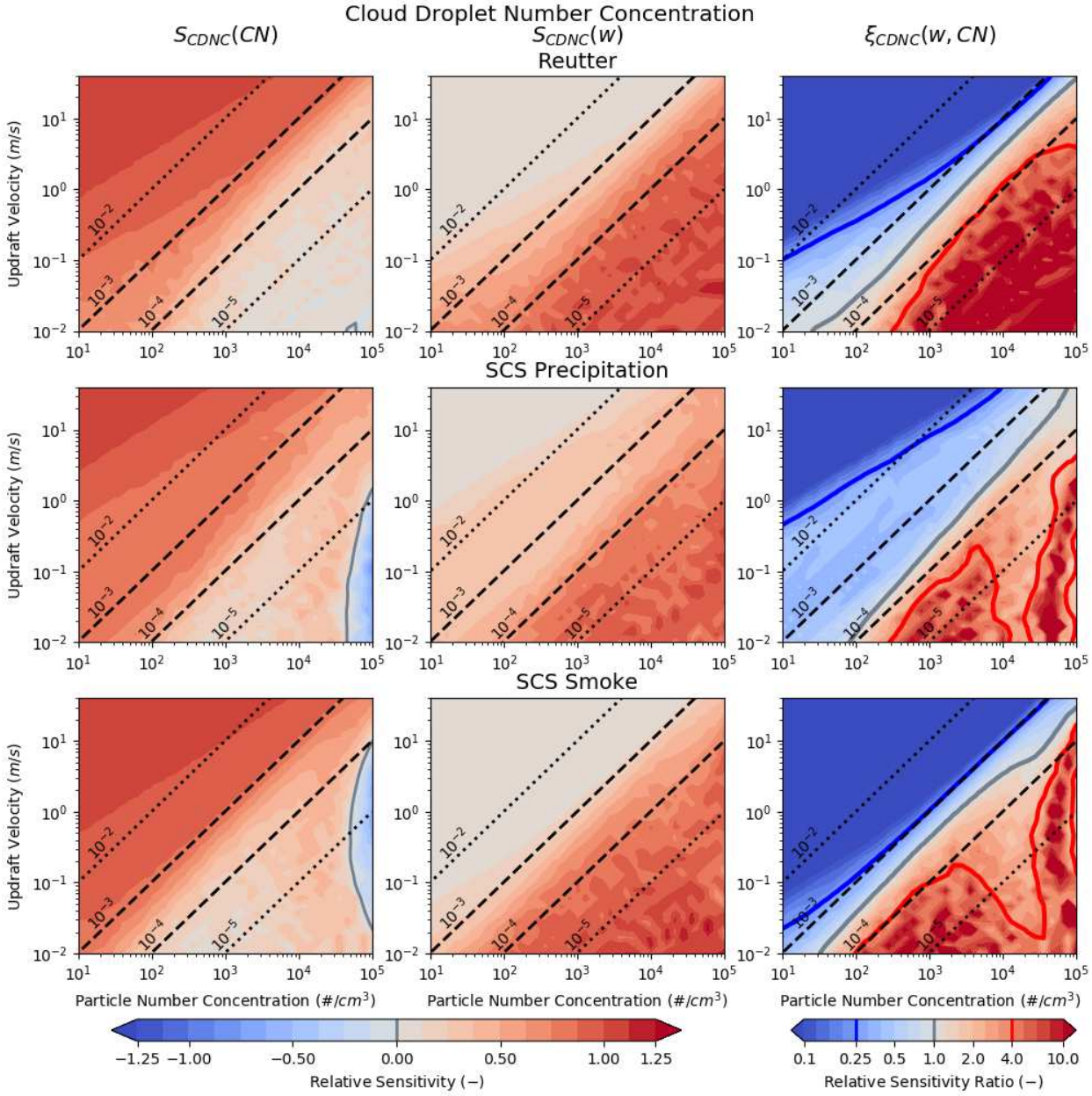

Figure 4.3 Initial CDNC relative sensitivity to particle number concentration and updraft velocity for the SCS and Reutter population types. Isopleths for relative sensitivity ratios, $\xi_{CDNC}(w, CN)$, are shown at 1:4 (blue), 1:1 (grey) and 4:1 (red).

R09, including $\xi_{CDNC}(w, CN)$ relative sensitivity ratios of 1/4 and 4 (thick blue and red lines) that roughly corresponded to w/CN ratios of 10^{-3} and 10^{-4} m s^{-1} cm^3, respectively. The more complex multimodal types of the SCS dataset, however, yielded additional sensitivity to CN in the updraft-limited regime, particularly for number concentrations above roughly 3×10^3 cm^{-3}. The nominal transitional regime between the red and blue lines of constant $\xi_{CDNC}(w, CN)$ was also wider for the precipitation type and narrower (in some portions of the parameter space) for the smoke type, further indicating sensitivity to population type. Additionally for SCS types, at high number concentrations sensitivity to increasing CN shifted to negative values associated with decreases in modeled CDNC. This behavior was characterized as a "supersaturation-quenched" sub-regime by R09, where supersaturation generated by updrafts was consumed by the large number of particles before many reached sizes large enough to activate. This sub-regime was larger and occurred at lower CN concentrations in the multi-modal SCS population types.

Results for relative dispersion calculated at peak parcel supersaturation are shown for each population type in Figure 4.4, along with associated relative sensitivities in Figure 4.5. The Chen

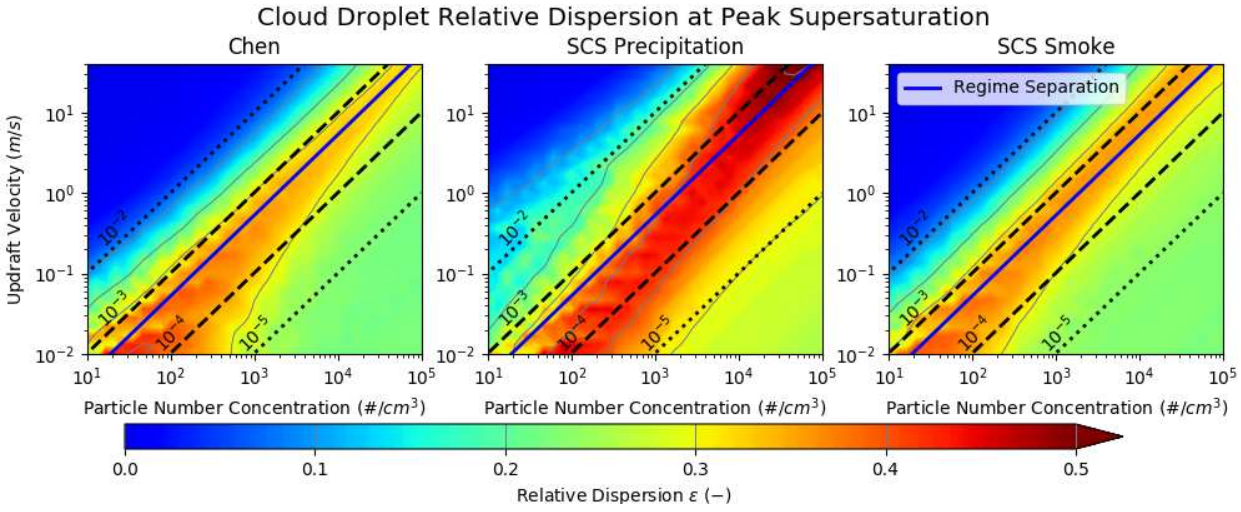

Figure 4.4 Initial cloud droplet relative dispersion at modeled peak supersaturation for the SCS and Chen population types. The C16 parametrized regime separation equation is included (blue line).

population type model, used here rather than the Reutter type to allow for comparison to C16, again yielded values consistent with the reported results. As part of their results C16 also presented a parameterized regime separation equation, $w = 5.298 \times 10^{-4} * CN$, which represented the best-fit of maxima in the value of ε and is plotted for reference as the blue line in the figure. The region above the line was therefore associated with the aerosol-limited regime

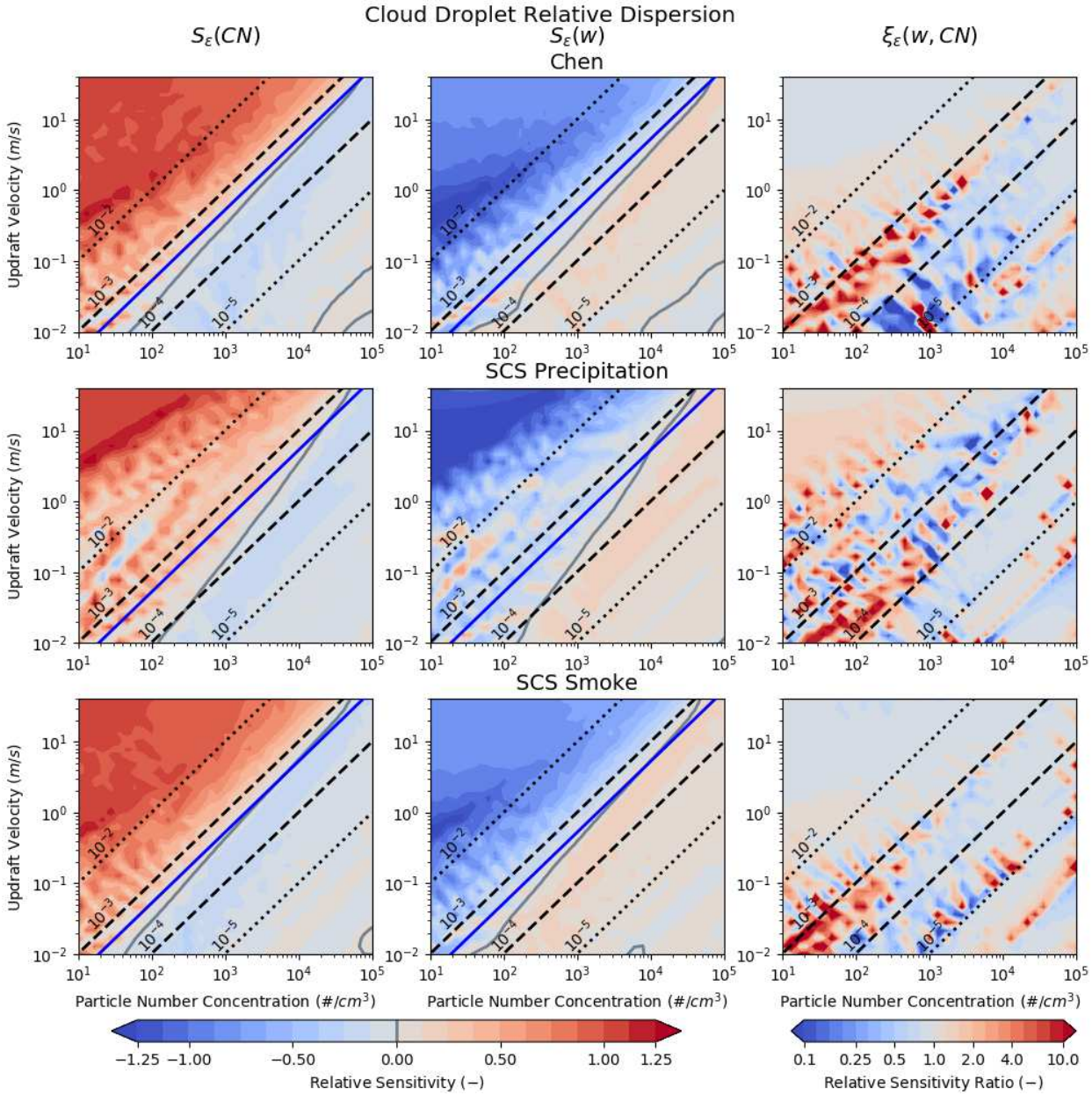

Figure 4.5 Relative sensitivity of cloud droplet relative dispersion at peak parcel supersaturation to particle number concentration and updraft velocity for the SCS and Chen population types. The C16 parametrized regime separation equation is included (blue line).

where ε generally increased with CN and decreased with *w*, and below the line with the updraft-limited regime where ε generally decreased with CN and increased with *w*. Relative sensitivities for both $S_\varepsilon(CN)$ and $S_\varepsilon(w)$ reflect this behavior well, though zero value isopleths for relative sensitivities—reflecting the point at which sensitivity tended to flip—were somewhat below this parameterization at lower values of CN and *w*. Relative sensitivity to both parameters was also considerably higher in the aerosol-limited regime. However, this is largely due to the low values of ε and high droplet mean diameters in this regime, which can lead to some issues with the use of relative dispersion over the standard deviation of the droplet distribution in these scenarios (Hudson and Noble, 2014; Liu et al., 2014). Relative sensitivity ratios were noisy and yielded little information as $S_\varepsilon(CN)$ and $S_\varepsilon(w)$ were themselves noisy due to model numerical errors and non-linearities, but were roughly equal in magnitude over much of the CN-*w* parameter-space for all three assumed aerosol types.

Results for the SCS types therefore demonstrated much the same behavior in ε as the simpler mono-modal population type. Maxima in relative dispersion tended to fall roughly within the R09 transitional-regime and were decently well characterized by C16 regime separation line. Differences associated with population type were primarily in the magnitude of ε, though some small differences in the shape of its isopleths occurred.

4.2.1. *Population Type*

The relative sensitivity of initial CDNC to the maximum expected change in population type model in the SCS dataset, $S^*_{CDNC}(\boldsymbol{\gamma}_{max})$, is shown in Figure 4.6. Relative sensitivity was highest where both CN and *w* values were lowest, with a peak along w/CN ratios of 10^{-3} m s^{-1} cm^3. The highest sensitivity to population type models from the SCS dataset would therefore be expected

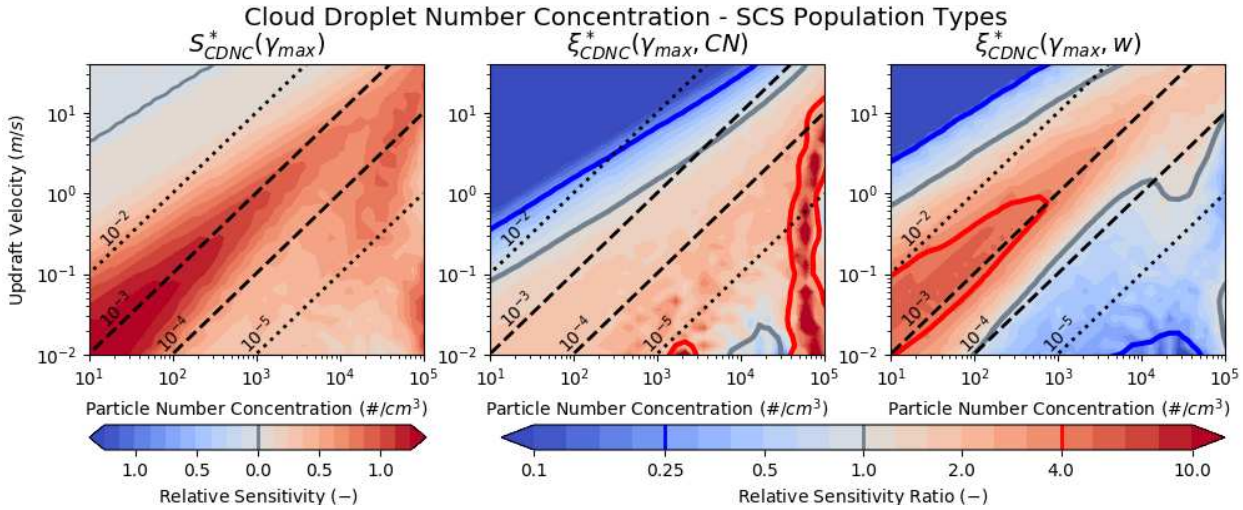

Figure 4.6 Initial CDNC relative sensitivity to aerosol population type in the SCS dataset. Relative sensitivity ratios for population type against particle number concentration and updraft velocity.

in the cleanest conditions (observed number concentrations were generally between ~10^2 and ~10^4 cm^{-3}) for fogs and weakly forced stratocumulus where updraft velocities are typically less than about 1 m s^{-1} (Wood, 2012). However, the cleanest conditions were also predominately associated with the precipitation type. Given that CN concentrations around 1000 cm^{-3} were associated with impacts from a number of different population types and source impacts, realistic conditions where population type might be relevant could therefore be expected at concentrations around 10^3 cm^{-3} and updraft velocities around 1 m s^{-1}. This region of the CN-*w* parameter-space is associated with marine stratocumulus cloud development, but also has relevance to clouds with somewhat deeper convection such as tropical cumulus congestus (e.g. Sheffield et al., 2015).

Some additional sensitivity was noted at high CN concentrations above roughly 10^4 cm^{-3} as differences in the onset of the supersaturation-quenched regime between population types became apparent, though such concentrations are above what would typically be expected in the remote marine SCS environment. Relative sensitivity ratios comparing population type against

both CN and *w* in Figure 4.6 also showed relatively wide regions of CDNC sensitivity to more than one factor (the region between the thick blue and red lines). The allowance for multiple multi-modal aerosol population type models therefore resulted in a region of CDNC sensitivity to more than one parameter that was considerably wider than the limits of the R09 transitional regime, and in fact included most of the R09 updraft-limited regime.

Cloud droplet relative dispersion showed generally less sensitivity to population type than did CDNC (Figure 4.7). As with the other parameters, $S_\varepsilon^*(\boldsymbol{\gamma}_{max})$ was highest above *w*/CN ratios of 10^{-2} where droplet median diameters are high and ε is near zero, and considerably lower throughout the rest of the parameter space. However, sensitivity to population type was higher than the sensitivity to either CN or *w* throughout most of CN-*w* parameter-space. The exception was at generally low values for CN and *w* along the 10^{-3} *w*/CN ratio line where sensitivity of ε to both CN and *w* was higher than to population type. In the SCS dataset ε would therefore be

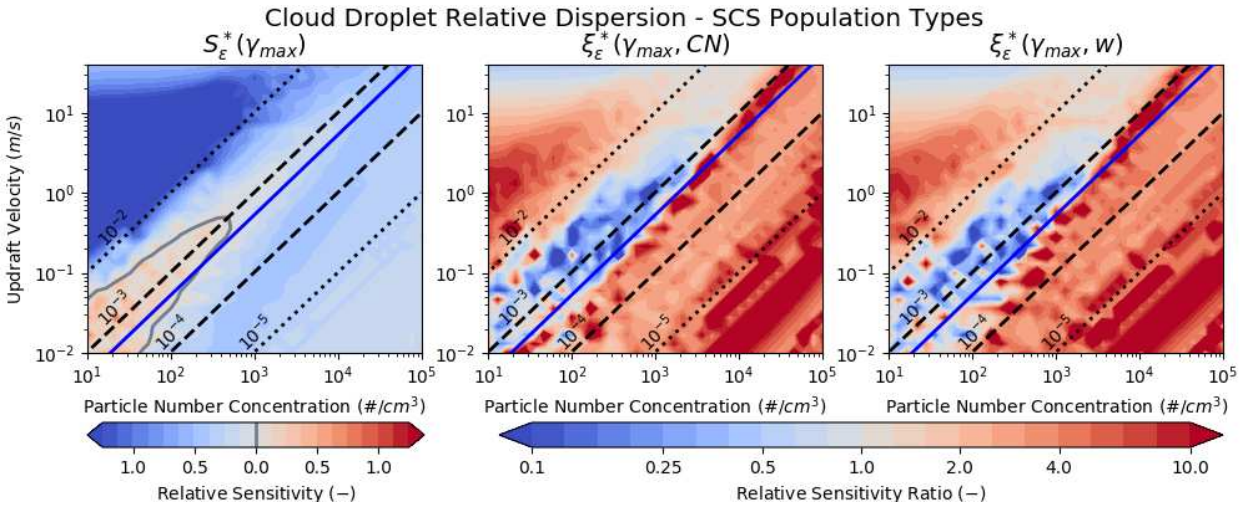

Figure 4.7 Relative sensitivity of cloud droplet relative dispersion to aerosol population type in the SCS dataset. Blue [red] shades indicate larger values of ε were associated with the SCS precipitation [smoke] type. Relative sensitivity ratios for population type against particle number concentration and updraft velocity. The C16 parametrized regime separation equation is included (blue line).

expected to be sensitive to multiple parameters, including population type, throughout much of the CN-*w* parameter-space.

Overall, CDNC had generally higher sensitivity to population type than did ε. There were also regions of the CN-*w* parameter-space where initial cloud droplet properties showed relative sensitivity to the largest change in population type model that was at least as high as to changes in either particle number concentration or updraft velocity. This included conditions in the range of CN concentrations where more than one aerosol population type was observed in the SCS dataset—between roughly 200 cm^{-3} to 2000 cm^{-3}. Within this range of conditions, the initial microphysical properties of developing clouds in the SCS would therefore be expected to be sensitive to changes in population type, number concentration, and updraft velocity. Similar sensitivities have been reported in other studies of aerosol-cloud-climate interaction in marine regions (e.g. Lu et al., 2007; Khain et al., 2008; Xue et al., 2008; van den Heever et al., 2010; Storer and van den Heever, 2012; Li et al., 2013; Sheffield et al., 2015). Among these, Sheffield et al., (2015) found sensitivity of modeled tropical marine cumulus congestus clouds to increasing concentration of particles activating as CCN. Increased latent heat release from more numerous and smaller droplets led to convective invigoration and was further associated with aerosol concentration feedbacks on cold pool development, condensate loading, and the fraction of congestus clouds reaching the freezing level (potentially allowing deep convection to occur). Included in these results were indications that congestus clouds with updraft velocities near 1 m s^{-1} were common, and that cloud aerosol sensitivity (modeled changes from 100 to 1600 cm^{-3} particles activated) was closely related to changes in both CDNC and mean droplet diameter near cloud base. In the SCS results this general regime ($w \approx 1$ m s^{-1}; CN $\approx 10^3$ cm^{-3}) was associated with roughly equal sensitivities to both aerosol number concentration and population type for

both CDNC and ε, suggesting that changes to the type of aerosol could potentially be as important as changes to the total concentration in some tropical congestus clouds. Consequently, in the SCS dataset the choice of aerosol population model may indeed be expected to have some microphysical relevance for initial cloud properties in certain atmospherically relevant scenarios.

4.2.2. *Droplet Activation and Model Stopping Conditions*

The above results assessed the sensitivity of several initial cloud properties to number concentration, updraft velocity, and population type intensive aerosol properties as $\phi(CN, w, \boldsymbol{\gamma}_{max})$. However, several additional parameters of the parcel model were explored for their potential to affect the results in regard to these three primary parameters. As these additional parameters have been investigated extensively elsewhere, they are treated and discussed here and in the following two sections only in terms of their potential to impact these results.

Aerosol particles in a parcel model change size in time due to changes in their water contents arising from condensation or evaporation, with some fraction growing to sizes sufficient to be considered activated as cloud droplets. Estimates of activated fraction from κ-Köhler theory rely on equilibrium at the droplet interface, but kinetic limitations on mass transfer and growth in many circumstances cause CDNC to deviate from equilibrium estimates (Chuang et al., 1997; Nenes et al., 2001). Analysis of parcel model output therefore requires criteria to differentiate between droplets that continue to grow by condensation past the point of parcel peak supersaturation, and smaller hydrated particles with stable sizes or negative growth rates past this point. These smaller particles may still be relevant from a radiative or microphysical perspective but are nevertheless not included in reported droplet number concentration and distribution in the parcel model. In most parcel models this delineation is treated using either a fixed diameter

wherein any droplet larger than some fixed size is considered a droplet, or a variable diameter that is calculated for each bin and time step based on comparison of droplet critical supersaturation to the current cloud supersaturation.

SC04 used a fixed cutoff diameter of 2 μm to count droplets in their parcel model results, in order to create parameterized CDNC lookup tables for the Regional Atmospheric Modeling System (RAMS) microphysics module. Other studies also used a 2 μm fixed cutoff diameter (e.g. Cubison et al., 2008; Ward et al., 2010; Ching et al., 2012), as this choice produces a consistent reference point that is above nearly all equilibrium particle critical activation diameters. However, in conditions of low updraft velocities and high number concentrations (i.e., the updraft-limited regime) this choice can lead to errors in estimates of both CDNC and cloud albedo (Nenes et al., 2001). In these situations, errors arise due to inclusion of particles with zero or negative growth rates but sizes just above the fixed cutoff diameter in the "droplet" category rather than the hydrated but unactivated particle category within the model. Separately in the case of high values for both CN and *w*, kinetic limitations on droplet growth rates can limit some still growing bins to sizes below the fixed cutoff diameter at the model step where properties such as CDNC or ε as assessed (at either the end of the model run or at the level of peak supersaturation where ε is calculated).

Alternatively, studies that utilized variable cutoff diameters, including R09 and C16, compared droplet diameter in each bin to the critical activation diameter for model supersaturation at each model step to calculate the activated fraction. R09 estimated the critical droplet diameter as $D_{wet,c} = \frac{2A}{3 \ln s_c}$, where $A = \frac{4\sigma_w M_w}{RT\rho_w}$, s_c is the critical water vapor supersaturation ratio, σ_w is the surface tension at the droplet interface, M_w and ρ_w are the molar mass and density of water,

respectively, R is the ideal gas constant, and T is the parcel temperature. In cases where supersaturation drops below the critical level for a bin, droplets will begin to evaporate—these bins will be deactivated and no longer counted as droplets under this method. Similarly, in cases of high supersaturation but slower growth rates such as high CN and w, the variable cutoff diameter will potentially be lower than an arbitrary 2 μm size, thereby counting more of the smaller bins as droplets as compared to the fixed cutoff diameter approach.

As droplet size is changing with time, realistic estimates of cloud properties in the model output therefore also require allowing a sufficient number of model steps to ensure that particle activation and deactivation are accounted for in a physically-defensible way before stopping the run. Model stopping conditions can be based on a number of criteria, but the models referenced above generally utilized one of two methods. First, models may track a parcel up to a set height or for a fixed number of steps past the level of maximum supersaturation. SC04 followed the parcel for 50 m past the model step where maximum supersaturation was reached, at which point CDNC (based on bins with droplet diameters above 2 μm) was calculated and written to the output. In a second method, the model run was continued until sufficient water condensed to reach a preset liquid water content (LWC). For example, R09 stopped each parcel run upon reaching an LWC of 0.8 g kg^{-1}. In most atmospherically relevant scenarios, this criterion follows the parcel past the level of peak supersaturation and allows for some particle bins to deactivate. This has been justified as a means of avoiding overestimates of expected CDNC, while still remaining below LWCs reached by more developed clouds where processes other than the initial droplet activation and condensational growth become increasingly important.

Sensitivity tests for droplet activation and stopping conditions were therefore conducted using both of the above prior-implemented criteria. First, runs were conducted using the stopping

condition of 50 m past maximum supersaturation, with all bins with diameters greater than 2 μm contributing to droplet concentration totals and measures of relative dispersion. The resulting CDNC values are shown as the dashed lines in Figure 4.8. The second series of runs, which used the stopping condition of 0.8 g kg^{-1} and counted all bins with diameters greater than the R09 variable cutoff diameter as droplets, are shown as the solid lines. Differences between the methods occurred predominately at higher CN concentrations, with SC04 methods producing higher estimates for CDNC at lower updraft velocities and R09 methods yielding higher CDNC at high updraft velocities. The differences were primarily due each method's estimate of droplet cutoff diameter resulting in different sets of bins used to calculate droplet totals as noted above.

Sensitivity to differences between the two activation and stopping condition methods is shown in Figure 4.9 using the same methodology as population type sensitivity tests. The $S^*_{CDNC}(AS)$ plots for the average of the SCS types showed that CDNC sensitivity was greater at low w and was generally confined to the R09 updraft-limited regime (with a small additional region of

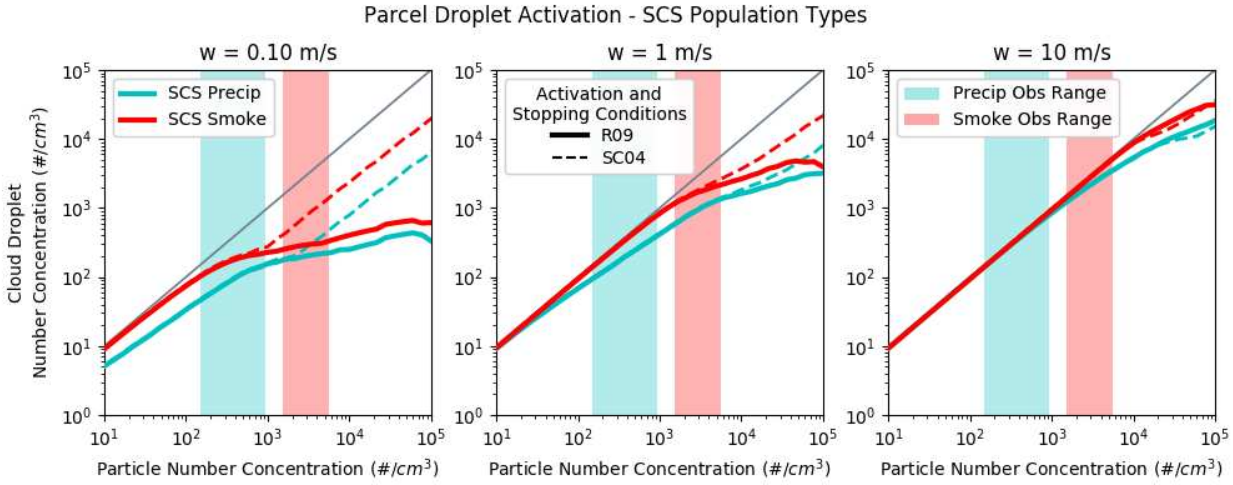

Figure 4.8 Cloud droplet activation for the SCS population types at various updraft velocities. Droplet activation and model stopping conditions associated with the R09 (solid lines) and SC04 (dashed lines) model setups are shown. A grey line at activated fractions of 1.0 is included for reference, with the observed range of CN concentrations for each population type highlighted in the background.

sensitivity at high *w* and high CN). The impact of these changes on CDNC sensitivity to population type (as in the previous section) was similarly confined to this region of the parameter space where $S^*_{CDNC}(\boldsymbol{\gamma}_{max}|AS_{SC04})$ showed differences from the R09 methodology (hatched region). Given the SCS population types, the method selection would therefore only be expected to substantially affect CDNC estimates in conditions of generally high CN concentration (e.g. intrusions of particles above typical background conditions such as in smoke or pollution plumes) and low updraft velocities as might be expected in fog or stratocumulus conditions.

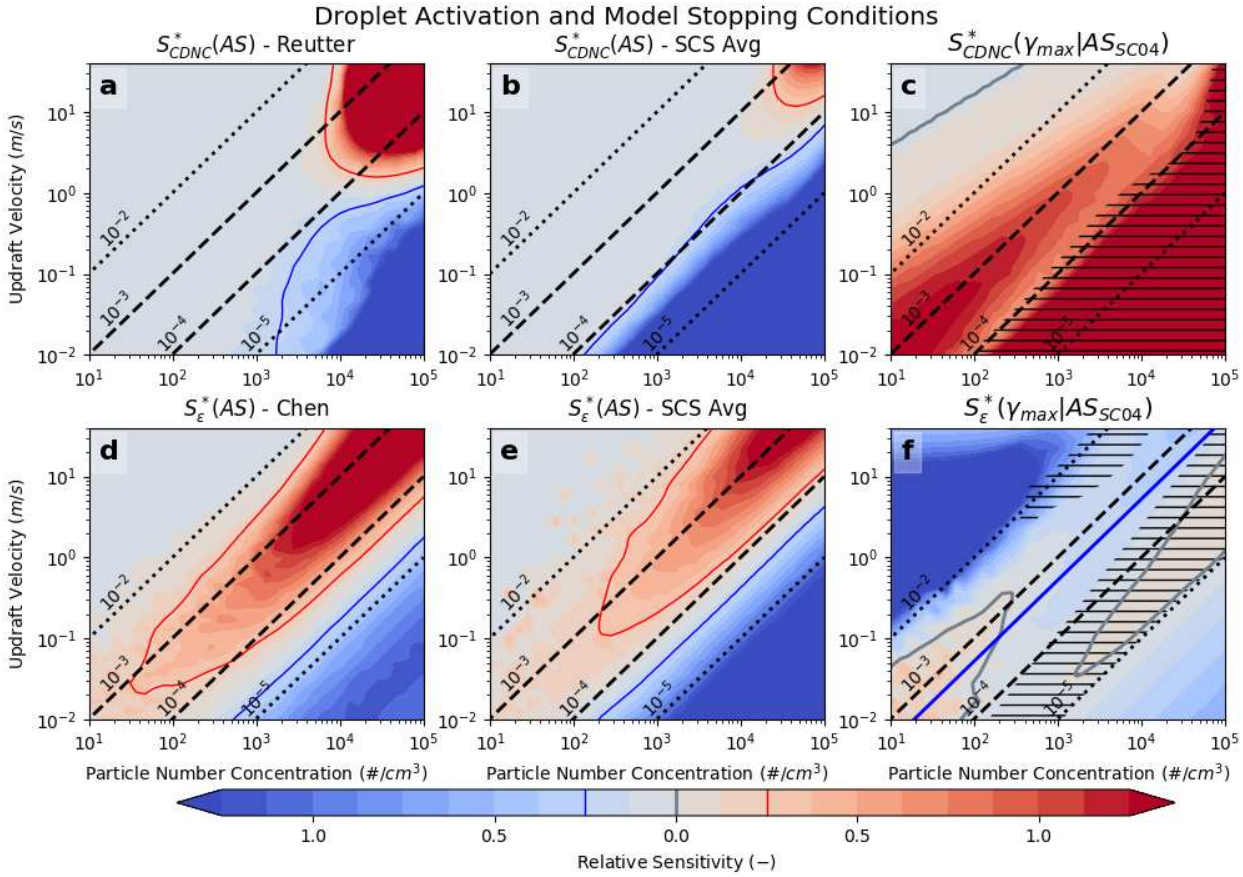

Figure 4.9 Relative sensitivity of cloud droplet number concentration and relative dispersion to differences in droplet activation and model stopping conditions associated with the R09 and SC04 values; shown for the for Reutter and Chen (left column) types, and the average of the SCS population types (center column). Blue shades indicate larger values associated with the SC04 model runs. The updated population type relative sensitivity of these parameters given the SC04 activation and stopping conditions is shown in the right column. Regions where population type relative sensitivity differences between the R09 and SC04 methods were greater than 0.25 are hatched.

Relative dispersion in both cases was calculated at the level of maximum supersaturation, meaning only differences associated with the choice of cutoff diameter affected ε. As with CDNC this led to considerable differences between methods. In conditions of low *w* and high CN the model bins had generally segregated into hydrated particles (near-zero growth rates) and droplets (positive growth rates) by the point of peak parcel supersaturation. However, fixed cutoff diameters at 2 μm tended to include the upper edge of the hydrated particle mode into the droplet classification, increasing relative dispersion considerably as compared to the variable cutoff diameters which did not include these bins. This behavior can be seen in the blue contours of Figure 4.9d&e where SC04 produced larger relative dispersions. Similarly, in the red regions of these figures, the SC04 fixed cutoff diameters did not capture some of the still growing bins that had not reached 2 μm by the level of maximum supersaturation, leading to higher estimates associated with the R09 & C16 methods.

Some impact on population type results were noted, as seen for the hatched regions of the $S_{\varepsilon}^{*}(\boldsymbol{\gamma}_{max}|AS_{SC04})$ plots for relative dispersion. However, as this comparison for both CDNC and ε pointed toward primary sensitivity in choice of droplet cutoff diameter method—and given that variable cutoff diameters tended to capture the growing droplet mode better than the fixed cutoff diameter in some edge cases—further consideration of fixed cutoff diameter results was considered unnecessary. The AS_{R09} activation and stopping condition were therefore considered suitable for assessing the impact of population type in the SCS dataset. Nevertheless, small hydrated particles that can vary between population types could still be relevant from an optical or radiative perspective.

4.2.3. *Accommodation Coefficients*

The thermal and condensational mass accommodation coefficients, α_T and α_c, respectively, describe heat and mass transfer across the liquid-vapor barrier of a droplet and are important for calculation of condensation rates in parcel models (Eqns A1–A3 in Appendix A). However, laboratory experiments and observational attempts to quantify these coefficients have not fully resolved what their values should be in the atmosphere. Experimental measurements of α_c in particular vary over many orders of magnitude, with estimates generally falling into two general categories. Lower values are often reported between roughly 0.04–0.1 (e.g. Shaw and Lamb, 1999), though the effects of organic films have led to reported values as low as 10^{-5} (Feingold and Chuang, 2002; Chuang, 2003). Higher values are typically above 0.1 and often reported as near unity (e.g. Davidovits et al., 2004; Winkler et al., 2004). Laaksonen et al. (2005) contend that for the purposes of cloud modeling where capturing droplet growth rate is of primary concern, values closer to unity may be more consistent with experimental results—though whether this reflects actual values for α_c or merely accounts for additional unresolved kinetic effects is still uncertain (McFiggans et al., 2006).

Values for α_c used in parcel models typically range between 0.04 and 1.0, and may in fact constitute the single largest source of uncertainty in model predicted CDNC values (Kreidenweis et al., 2003). Various parameterizations of CDNC are similarly sensitive to the assumed accommodation coefficients in the simulations used as parameterization inputs (e.g. Fountoukis and Nenes, 2005; Ming et al., 2006). The parcel models used by R09 and C16 for studies of the regime dependence of CDNC and ε used accommodation coefficients of 1 for both α_c and α_T. Other parcel models, including those used for generation of parameterizations and model lookup

tables have utilized values below unity (e.g. Saleeby and Cotton, 2004; Ward et al., 2010), with values of $\alpha_c = 0.042$ and $\alpha_T = 0.96$ used in SC04.

Sensitivity tests varying accommodation coefficients were conducted with values used in each of the two general classes of model setups. As expected, using the SC04 assumptions increased model supersaturations and produced higher CDNC when compared to the R09 assumptions (Figure 4.10a). Relative sensitivity to accommodation coefficients (Figure 4.10b) was generally low, though a region spanning higher values for CN $\gtrsim 10^3$ cm^{-3} and w $\gtrsim 0.2$ m s^{-1}, had CDNC sensitivities to accommodation coefficient greater than 0.25 (blue line). The resulting impact on $S^*_{CDNC}(\boldsymbol{\gamma}_{max}|AC_{SC04})$ was similarly minimal (Figure 4.10c; compare to Figure 4.6a that used values of unity to maintain consistency with R09 and C16 regimes)—differences in CDNC sensitivity to population type between the methods was greater than 0.25 only in a narrow region along the 10^{-3} *w*/CN ratio for concentrations above ~10^2 cm^{-3} (hatched region).

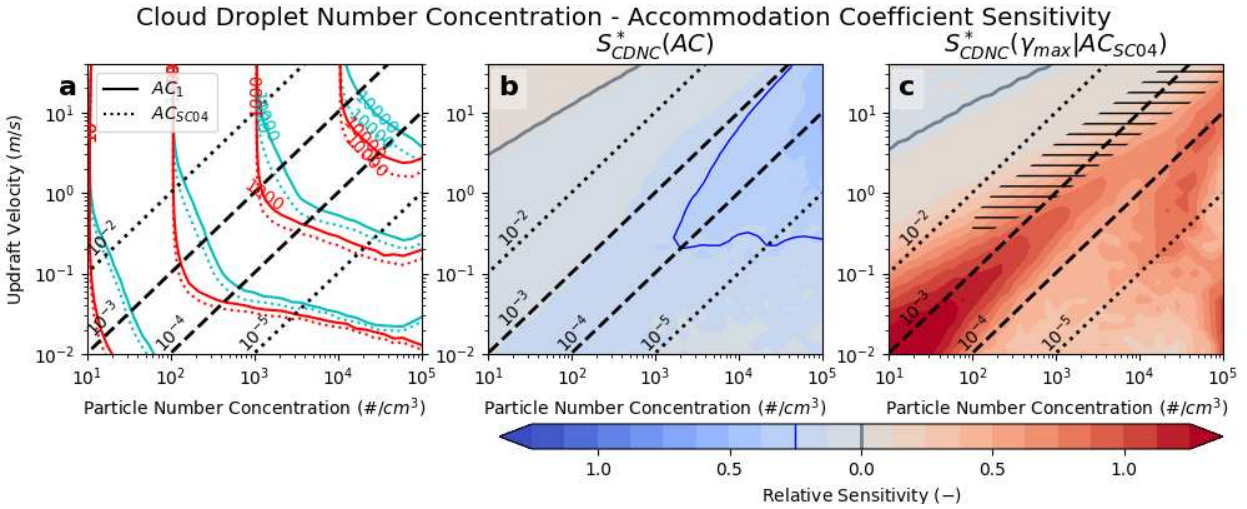

Figure 4.10 (a) Cloud droplet number concentrations for SCS population types using accommodation coefficients of 1 (solid; as in R09) and less than 1 (dotted; as in SC04). (b) Relative sensitivity to differences in accommodation coefficients between R09 and SC04. (c) Relative sensitivity of CDNC to population type given the accommodation coefficients of SC04. Regions where population type relative sensitivity differences between the R09 and SC04 accommodation coefficients were greater than 0.25 are hatched.

In the SCS dataset, accommodation coefficient selection would therefore be expected to impact the magnitude of CDNC across much of the CN-w parameter-space, but with the largest impacts in conditions of generally high CN concentration associated with intrusions of particles above typical background conditions. This region spanned updraft velocities above roughly 0.2 m s^{-1}, and was therefore applicable to stratocumulus clouds, but with higher expected impact on deeper convective systems. The region of the parameter-space where accommodation coefficients impacted the population type sensitivity results again spanned multiple cloud regimes, but was best characterized by the 10^{-3} *w*/CN ratio line across all observed CN concentrations in the SCS.

The SC04 accommodation coefficients increased relative dispersion across most of the CN-*w* parameter space for all population types (Figure 4.11a–c). The largest relative sensitivity to accommodation coefficient selection tended to occur in parts of the C16 aerosol-limited regime and at high CN concentrations near the Chen regime separation line (d). These results were expected as lower accommodation coefficients reduce the droplet growth rate and increase peak supersaturation, thus eventually activating more of the particle bins and generally causing both a wider distribution and lower mean droplet diameter as compared to lower activated fractions. The impact on $S_{\varepsilon}^{*}(\boldsymbol{\gamma}_{max})$ was again fairly minimal (Figure 4.11e; compare to Figure 4.7a) with the hatched region of differences greater than 0.25 occurring in the same region where population type had the least importance for the C16 setup. However, the direction of this change did serve to increase the importance of population type within the aerosol-limited regime. Overall, while the choice of accommodation coefficients was important to the magnitude of both CDNC and ε, the impact on population type sensitivity in the SCS dataset was minimal.

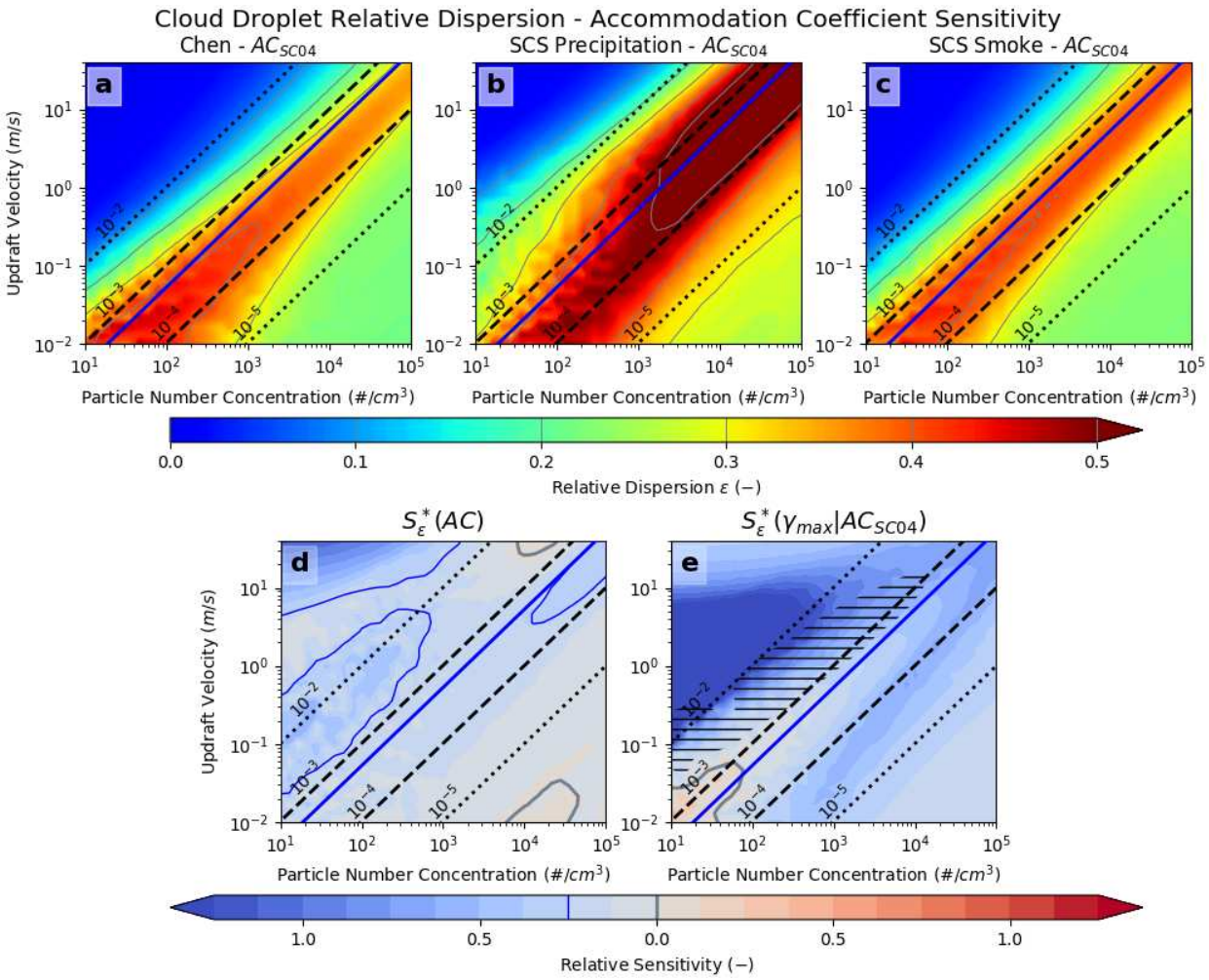

Figure 4.11 (a-c) Cloud droplet relative dispersion for the Chen and SCS population types for accommodation coefficients from SC04. (d-e) As in Figure 4.10 for cloud droplet relative dispersion. The C16 parametrized regime separation equation is included (thick blue line).

4.2.4. *Mixing State*

In simplified aerosol population models, particles are often considered to be internally mixed with one value for hygroscopicity applied to all particles. Actual populations, however, are often externally mixed with different hygroscopicity values across different particles, sizes, or modes. The impact of mixing state representations in parcel models has been investigated in a variety of circumstances (e.g. Anttila, 2010; Ching et al., 2012) and can have considerable impact on the cumulative CCN spectrum and associated estimations of particle activation, but may not necessarily have as large an impact on subsequent activation into cloud droplets (Cubison et al.,

2008). Generally, CDNC has been found to be most sensitive to mixing state when small diameter, low hygroscopicity species (e.g. $\kappa \lesssim 0.1$) with little time to age are present, often from fresh emission sources (Cubison et al., 2008; Anttila, 2010; Wang et al., 2010; Ching et al., 2012). Anttila (2010) found CDNC relative sensitivities to mixing state of less than 0.12 for marine and continental background populations that increased to values up to 0.35 in an urban plume with fresh emissions and high degrees of external mixing. Ching et al. (2012) utilized a more rigorous representation of individual particle activation in a parcel model for an idealized urban plume population, and found relative sensitivities of less than ~0.25 for CDNC and less than ~0.45 for ε. However, they also noted that much of this sensitivity was due to the impact of fresh black carbon containing particles with low hygroscopicity.

In the SCS dataset, external mixing was included on a modal basis, with one hygroscopicity value assigned to each mode based on best-fit observations. However, few of the fresh or low-hygroscopicity particles that would be likely to impact the parcel model results were observed or included in the population type parameterizations. The impact of mixing state representation was therefore expected to be less than in more terrestrially impacted regions. CCN spectra associated with each mixing state and population type are shown in Figure 4.12. Little difference in spectra between internal (dashed lines) and external (solid lines) mixing occurred for the precipitation type, while for the smoke type internal mixing served to decrease the slope and therefore extend the range of supersaturations across which particles activate. As an example, an additional population type (orange lines) with a low hygroscopicity Aitken mode (κ=0.05; μ=50 nm) and higher hygroscopicity accumulation mode (κ=0.6; μ=200 nm) was included to show the larger difference in CCN spectra associated with populations types reported to have more substantial

sensitivity to mixing state. In this case, the spectra for the internally mixed mode deviated more considerably from the external mixing representation than in either of the SCS types.

Mixing state sensitivity tests were conducted by comparing runs that used internal mixing based on κ volume averaging of both population modes for each size bin, against external mixing by mode where each mode and associated modal κ value was included for each bin size (thereby doubling the number of model bins). The results were as expected given the relatively small differences in SCS CCN spectra between mixing state representations, with minimal sensitivity to mixing state found. The largest relative sensitivity for either of the SCS population types was 0.09, with mean values across the CN-*w* parameter space near zero. As a result, in order to more efficiently run the parcel model, internal mixing was assumed in all of the calculations presented here.

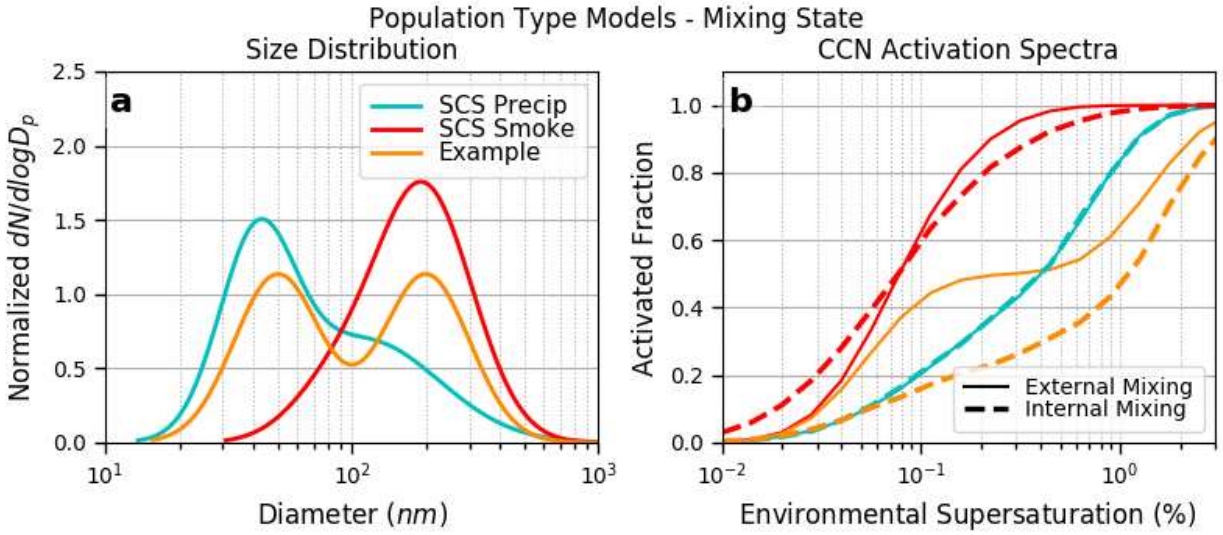

Figure 4.12 (a) Size distributions for SCS Types and an example type, (b) CCN activation spectra for each of the types using both internally mixed (dashed lines) and externally mixed size bins (solid).

4.3. CLOUD PROPERTY SENSITIVITY TO AEROSOL POPULATION TYPE

Extending analysis of initial cloud property sensitivity in remote marine regions to include a generalized aerosol type parameter produced results that fit in well with regime classification methods that map sensitivity within a CN-*w* parameter space. Sensitivity of initial cloud droplet number concentration, $CDNC(CN, w, \boldsymbol{\gamma}_{max})$, for the remote marine SCS dataset showed three distinct regimes based on the highest sensitivity to each of these parameters (Figure 4.13a). Similar to the findings of R09, an aerosol-limited regime characterized by primary sensitivity to CN concentration was observed at high *w*/CN ratios (blue contours), with an updraft-limited regime characterized by primary sensitivity to updraft velocity at low *w*/CN ratios (red contours). Between these two regimes, in the region characterized as a transitional regime by R09, CDNC was in fact most sensitive to the maximum potential difference in aerosol population type observed in the SCS dataset (green contours). Additionally, throughout much of this region CDNC had varying degrees of sensitivity to more than one parameter. As a result, this region

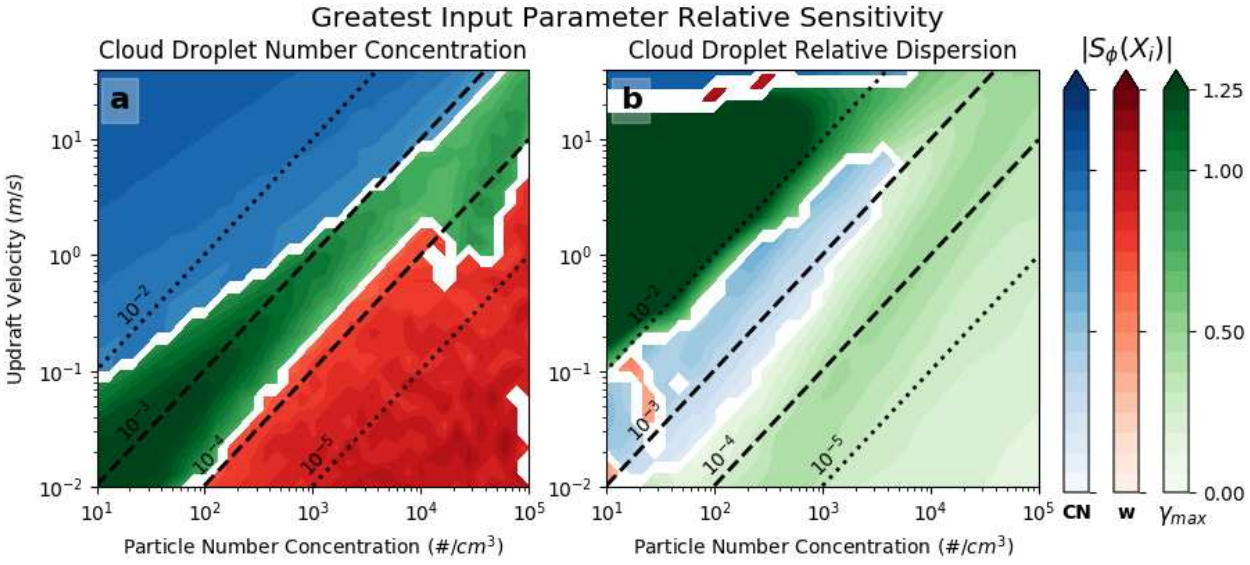

Figure 4.13 Regions of highest cloud property relative sensitivity to total particle number concentration (blue), updraft velocity (red), and maximum observed difference in aerosol population type (green) for the remote marine SCS dataset; (a) initial cloud droplet number concentration; (b) cloud droplet relative dispersion at maximum supersaturation.

could be characterized as a population-type sensitive regime where sensitivity is highest to aerosol population type, but which is also dependent on both CN and *w*.

In addition to identifying a new population-type sensitivity regime, the inclusion of more realistic multi-modal aerosol populations also served to reduce the size of the R09 aerosol-limited regime where CDNC could be confidently said to depend on CN alone. Ratios of *w*/CN greater than 10^{-2} m s^{-1} cm^3 were more indicative of such a regime, rather than the 10^{-3} value given in R09, particularly at lower CN concentrations. The inclusion of multi-modal populations also increased sensitivity to both population type and CN throughout much of the updraft-limited regime—a further complication on top of the somewhat simplistic R09 regimes.

Similar analysis applied to the relative dispersion of cloud droplets at peak parcel supersaturation showed generally lower sensitivity of ε to all three parameters as compared to the sensitivities found for CDNC (Figure 4.13b). The exception in the aerosol-limited regime, associated with higher sensitivity to all parameters, was due to low values for ε and higher median droplet diameters, conditions that limit the utility of the relative dispersion concept. Throughout much of the remainder of the parameter space, ε had slightly higher relative sensitivity to population type than to other parameters. Interestingly, the lowest values of ε sensitivity to population type coincided with the region where CDNC sensitivity to population type was highest. In addition, the multi-modal SCS types resulted in generally similar regimes of behavior in ε as was noted for a simpler mono-modal aerosol population by C16, with maxima falling roughly along a line of constant *w*/CN ratio. Differences associated with varying population type were therefore primarily related to the magnitude of the relative dispersion.

While the population type sensitivity results were specific to observations from the SCS dataset, the more complex aerosol populations may still provide better representations of extremes in many remote marine environments that are periodically impacted by aerosol intrusions such as transported smoke than simpler mono-modal population types. This focus on extremes in population type allowed for estimates of bounds on the impact of aerosol intensive parameters on initial cloud properties in such environments. However, such bounds, discussed further below, still captured large parts of the CN-*w* parameter space and resulted in a somewhat more complex picture of parameter sensitivity than the simpler regime classifications proposed by R09 and C16. Given the multi-modal populations and additional sensitivity to population type, most of the parameter space was associated with sensitivity to more than one parameter. In fact, only in the aerosol-limited regime where nearly all particles activated did sensitivity to only one parameter exist in these results.

Furthermore, in the SCS dataset the range of observed CN concentrations associated with more than one aerosol population type spanned roughly 200 cm^{-3} to 2000 cm^{-3}—a portion of the parameter space that included some degree of sensitivity to each of the parameters. Therefore, in the SCS observations, such particle concentrations also represent bounds on a more atmospherically relevant region of the CN-*w* parameter space where impacts from various population types may exist. As expected, this implied initial cloud properties in the remote marine SCS were sensitive to CN concentration, updraft velocity, and population type, but it also clarified the relative importance of these relative sensitives throughout the regimes in this parameter space. Other studies have similarly highlighted the importance of aerosol concentration under such conditions for cloud development, precipitation, and aerosol indirect effects on climate (Lu et al., 2007; Khain et al., 2008; Xue et al., 2008; van den Heever et al.,

2010; Storer and van den Heever, 2012; Li et al., 2013; Andersen and Cermak, 2015; Sheffield et al., 2015). These results, however, suggest that for marine clouds ranging from fogs and stratocumulus layers to deeper convective clouds, additional sensitivity to aerosol population type may be important as well.

5. SENSITIVITY OF ATMOSPHERIC OPTICAL PROPERTIES TO OBSERVED MARINE AEROSOL POPULATION TYPES

Assessing the effect of changing aerosol populations on atmospheric optical properties in marine regions depends on the underlying microphysical properties of the aerosol population. Changes to the aerosol size distribution, concentration, complex index of refraction, shape, and ambient RH dependent hygroscopic growth can alter optical characteristics of the atmosphere in complex and non-linear ways. In the reverse of this situation, attempts to retrieve properties of the aerosol based on observations of optical properties result in an under-constrained inverse problem, wherein a priori constraints and assumptions on the aerosol are required to reach a solution (Dubovik and King, 2000). MODIS and AERONET aerosol optical depth (AOD) retrievals rely on a priori assumptions for the particle size distribution, index of refraction, and shape to infer further information about the aerosol population from a column extinction or top-of-atmosphere radiance measurement. Similarly, a nominal point measurement of extinction may be associated with a range of possible RH values or mass concentrations that vary with the underlying aerosol model. Fully relating the dry aerosol population to extinction—either for retrieval of aerosol properties from an optical measurement or estimation of optical properties for a given aerosol—requires accurate assumptions for dry size distributions, hygroscopicity, ambient RH, refractive index, and particle shape. Efforts to improve these underlying assumptions will benefit from assessment of the relative role of each of these properties in modifying extinction, including the typical range of variability that may be expected in marine scenarios.

In marine regions the MODIS Collection 5 ocean algorithm selects a combination of one fine and one coarse mode aerosol model for each retrieval (Remer et al., 2006; Levy et al., 2009). Various updates to the ocean algorithm were made for MODIS Collection 6, but the same

underlying ocean aerosol models were preserved (Levy et al., 2013). Of the four fine mode and five coarse mode options from which the retrieval selects a best fit, only the fine modes are relevant to the particle sizes represented by the parameterizations presented in previous chapters. While important to both optical properties and MODIS retrievals, coarse mode particles are likely to be sea-salt dominated marine aerosol with their abundance largely related to surface wind speeds (Zhang and Reid, 2006; O'Dowd and Leeuw, 2007) or transported dust that is not fully measured or accounted for in the parameterizations for the SCS. Therefore, this discussion focuses on the potential impact of fine mode aerosol on optical properties in remote marine regions.

A number of studies have used a variety of methods to examine fine mode optical properties of aerosol as a function of RH in marine regions, and reported on their variability (Carrico et al., 1998, 2000, 2003; Quinn et al., 1998, 2004, 2005, 2006; Gassó et al., 2000; Kleefeld et al., 2002; Quinn and Bates, 2005; Bates et al., 2005, 2006; Wang et al., 2007; Massoli et al., 2009; Zieger et al., 2010; DeWitt et al., 2013; Zhang et al., 2014). Reported values in these studies, discussed further below, include both extensive aerosol optical properties that vary depending on overall aerosol concentration (e.g. extinction or scattering coefficient, or AOD), and intensive properties independent of total concentration (e.g. mass extinction efficiency, single scatter albedo, or scattering enhancement factor as a function of RH), some of which are relevant only at specific RH values. In addition to mean values typically provided for these properties, Clarke et al. (2002) and Doherty et al. (2005) provided detailed treatments of variability and uncertainty in optical properties in marine datasets as part of multi-platform inter-comparison studies of optical property measurements during field campaigns in the Indian Ocean (INDOEX) and the western Pacific (ACE-Asia), respectively. They compared average values and ranges of variability for

both extensive and intensive aerosol optical properties from land, ship, and aircraft platforms, and discussed likely sources of discrepancies in the comparisons. In addition to their campaign wide analyses that included the effect of changing aerosol and environmental conditions on variability, they discussed the nature of relative variability or dispersion in reporting of their results. Among their relevant conclusions, Clarke et al. (2002) found that measurement uncertainties were unlikely to fully explain either observed variability in optical properties or differences in the results between various instrument platforms. They concluded that the various instrumentation systems were therefore likely to be sampling different ambient aerosol populations, even for nominally co-located and/or co-temporal observations. The implication from these studies, along with others listed above, is that natural variability in nominally consistent aerosol populations contributes to some fraction of the variability in observed optical properties (i.e. in addition to measurement error).

As variability in optical properties can be related to changes in intensive and extensive properties of the aerosol, aerosol population type, and environmental conditions such as RH—and variability in some of these relevant properties were quantified as part of the SCS parameterizations—this dataset was used to drive optical reconstruction modeling with a particular focus on the role and range of variability in these properties. It was expected that mass concentration would have the largest impact on extinction and other extensive optical properties at visible wavelengths, consistent with previous findings. However, intensive aerosol parameters, aerosol population type, and environmental relative humidity drive variability of intensive optical properties, while also contributing to some of the variability in the extensive optical properties. Identifying the relative importance of each of these factors of the aerosol in the resulting optical property variability would allow optical modeling, retrieval, and data

assimilation efforts to better constrain expected impacts due to changes in specific factors of the marine aerosol or environment.

5.1. OPTICAL PROPERTY RECONSTRUCTION METHODOLOGY

The relationship between the various relevant aerosol and environmental parameters that impact optical properties of the ambient atmosphere is complex and non-linear. As observations cover situations in which multiple parameters vary, the optical impact of a change to one of these parameters is difficult to quantify in the observational datasets. However, the physics of such changes are well understood, subject to certain general assumptions, allowing physical reconstruction models to probe these impacts in greater depth.

A model for reconstructing optical properties associated with various aerosol and environmental conditions was generated using the algorithm shown in the flow chart in Figure 5.1. First, the underlying dry aerosol population is defined in terms of normalized size distribution, hygroscopicity, index of refraction at a given wavelength, particle density, and number or mass concentration. As the SCS aerosol dataset was described by two nominally independent modes for each aerosol type, the optical model similarly defines independent modes which are calculated separately and then combined as part of the reconstruction. One hundred logarithmically spaced size bins are then created with limits set to capture 99.9% of both the number and mass distributions. Each size bin for each mode is then independently grown to reach thermodynamic equilibrium with a given environmental relative humidity (RH) based on the modal κ value. The complex index of refraction at equilibrium is estimated based on a volume mixing rule between the dry particle index of refraction and that of water ($n = 1.33 + 0.0i$

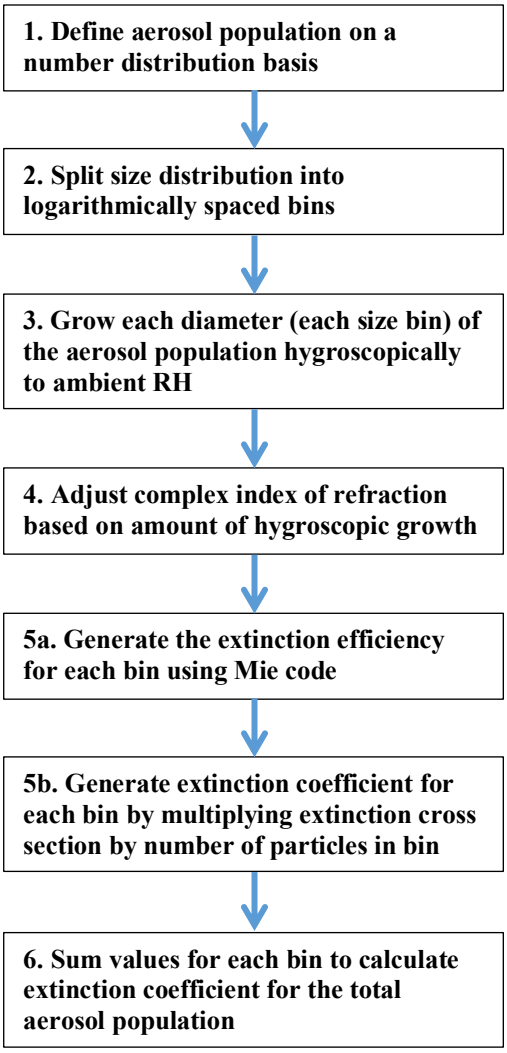

Figure 5.1 Optical reconstruction algorithm flow chart for extinction.

at 550 nm), with the assumption of spherical particles (Tang, 1996, 1997; Randles et al., 2004; Kreidenweis and Asa-Awuku, 2014).

Mie theory is used to estimate reconstructed aerosol optical properties for wavelengths in the visible range relevant to this study (Bohren and Huffman, 1983). The dimensionless extinction efficiency per particle, Q_{ext}, is calculated for each size bin in each mode. Using the particle area, A, the particle extinction cross section, C_{ext} *(m^2)*, is calculated as $C_{ext} = Q_{ext} * A$. For each bin in each mode the number of particles in each bin is then multiplied

by the extinction cross section to generate an extinction coefficient, b_{ext} *(cm^{-1})*. The extinction coefficient for the total population is calculated by summing the calculated extinction coefficient for all bins and modes. This value is normalized against particle number concentration (yielding the population average optical cross section; *(Mm^{-1} / [particles/cm^3] = μm^2)*) or dry mass concentration (yielding the population average dry mass extinction efficiency; *(m^2 g^{-1})*) to generate a value representative of the full population.

This algorithm relies on a set of assumptions in order to remain generally representative of the system it models. Spherical particles are assumed for the purposes of aerosol size and mass distributions and the Mie theory optical model, an assumption that should generally be valid for aged particles and particles that have undergone some degree of hygroscopic growth. Individual particles were also assumed to be internally mixed, with no core-shell modifications to Mie theory utilized here. Each aerosol mode is further assumed to be internally well-mixed, with consistent composition dependent hygroscopicity, density, and refractive indices.

5.1.1. *Optical Property Parameters*

Intensive and extensive optical parameters were used to quantify expected variability in aerosol populations as well as to compare the reconstructions against relevant reported values observed in marine regions. Extensive optical parameters are directly impacted by changes in the amount of aerosol present and are therefore representative of changes to actual environmental conditions. Aerosol total extinction and scattering coefficients, b_{ext} and b_{sca}, respectively, were estimated by the reconstruction algorithm and are commonly reported measures of aerosol optical properties for nominal point observations (Seinfeld and Pandis, 2012). Such values are particularly useful for calculation of extinction through a path in the atmosphere, such as AOD (calculated by integrating b_{ext} through the atmospheric column). Importantly, extinction

coefficients are sensitive to all relevant input parameters to the optical reconstruction model—aerosol intensive parameters, total dry aerosol mass concentration, and environmental relative humidity—and are therefore used as the predominant property for optical comparisons and analysis in the following sections.

However, an important goal of this work is to establish under what conditions the type of aerosol present (i.e. the intensive parameters or population type) may be optically relevant rather than simply the total amount or mass of aerosol. To address this question, an intensive optical parameter that is sensitive to both aerosol intensive parameters and RH is desirable. The mass extinction efficiency (MEE) represents expected extinction at a given wavelength normalized against the aerosol mass, and is often reported for aerosol under nominally dry conditions. Many authors also report the extinction enhancement factor, typically denoted as f(RH), which addresses the impact of changing humidity by measuring the ratio of extinction at two different RH values for a given aerosol population (Kreidenweis and Asa-Awuku, 2014). Here this value is indicated as $f_{ext}(RH, RH_{ref})$ and defined in Eqn 5.1, where the humidified extinction at a given RH is compared against extinction at a reference RH_{ref} value.

$$f\left(RH, RH_{ref}\right) = \frac{b_{ext,RH}}{b_{ext,RH_{ref}}} \tag{5.1}$$

$$f\left(RH, RH_{ref}\right) = \left(\frac{100 - RH_{ref}}{100 - RH}\right)^{\gamma} \tag{5.2}$$

$$\gamma_{RH_{ref}-RH} = \frac{\ln\left(b_{ext,RH_{ref}} / b_{ext,RH}\right)}{\ln\left(100 - RH / 100 - RH_{ref}\right)} \tag{5.3}$$

where $b_{ext,RH}$ is the extinction coefficient at a given RH and equation 5.2 has been commonly applied to parameterize the impacts of RH through the coefficient γ, described further below.

The equivalent scattering enhancement factor is therefore $f_{sca}(RH, RH_{ref})$ in the case where only the ratio of scattering coefficients is used. As environmental humidity increases, the extinction can often be estimated to increase at a roughly exponential rate with respect to RH (Kasten, 1969; Kreidenweis and Asa-Awuku, 2014). The $f(RH)$ function for a given aerosol is therefore often estimated by Eqn 5.2 with the relationship of scattering or extinction enhancement as a function of RH defined by the γ parameter (Carrico et al., 2003; Massoli et al., 2009; Zhang et al., 2014). In the case of two extinction measurements at different RH values, the $\gamma_{RH_{ref}-RH}$ parameter can be estimated by Eqn 5.3. In some cases, scattering or extinction enhancements are measured across a range of RH values (e.g. Carrico et al., 2003). Plots of such measurements are known as humidograms, and the γ parameter for such plots can be estimated by minimizing chi-squared error of the data points to Eqn 5.2.

As hygroscopic growth changes particle size, density, index of refraction, and humidified mass, the MEE parameter is extended here to explicitly include RH. The dry mass extinction efficiency, $MEE_d(RH)$, normalizes extinction by the dry aerosol mass to indicate the extinction expected for a given dry aerosol mass concentration at a given RH (Eqn 5.4).

$$MEE_d(RH) = \frac{b_{ext,RH}}{m_d} \tag{5.4}$$

where m_d is the dry aerosol mass, effectively combining the utility of $f(RH)$ and MEE at dry conditions into a combined statistic.

However, some aerosol models treat the aerosol as a static humidified population with no adjustments for changing RH (e.g. the MODIS over ocean retrieval algorithm). In this case a humidified mass extinction efficiency, $MEE_h(RH)$, that explicitly addresses the effect of RH is used in order to compare the reconstruction results against such models (Eqn 5.5).

$$MEE_h(RH) = \frac{b_{ext,RH}}{m_{h,RH}} \tag{5.5}$$

where $m_{h,RH}$ is the humidified aerosol mass. This representation has the added benefit of determining at which RH (if any) a reconstructed aerosol population type would be optically equivalent to the various humidified, static models used by MODIS or similar retrievals.

In most cases, authors who report observed values of these parameters in remote marine environments do so for RH values that were specific to the study and/or instrument of note. As such, comparisons based on reconstructions were matched to fit conditions reported in the study. All reconstructions in this analysis were conducted at 550 nm, a wavelength commonly reported in field studies of aerosol optical properties in marine regions, to allow for a common point of comparison.

5.1.2. *Measures of Variability in Optical Properties*

Investigation of the range of variability in optical properties expected as a result of natural variability in relevant aerosol and environmental parameters was conducted using a Monte Carlo (MC) methodology. A similar MC method was applied by Clarke el al., (2002), who used a simpler version of such a model with fewer input parameters to successfully reconstruct perturbations to observed scattering coefficients at 55% RH based on measurements of variability in humidified aerosol volume distributions.

Input parameters for the reconstruction model were repeatedly sampled, yielding a distribution of optical properties associated with typical changes to one or more of the inputs. In the case of the extinction, scattering, and mass extinction efficiency optical properties, all are non-negative and can be quantified on a ratio scale, allowing estimates of their relative dispersion in various scenarios to be made using the coefficient of variation (CV)—the ratio of the standard deviation to the mean of the population (Eqn 5.6).

$$CV = \sigma/\mu \tag{5.6}$$

$$\widehat{CV}_a = s/\bar{x} \tag{5.7}$$

where μ and σ are the mean and standard deviation, respectively, describing variability of the optical property in a given scenario.

Comparisons of the relative impacts of various input parameters on optical properties were therefore conducted by comparing the CV statistic between different cases or scenarios. Straightforward estimates of the CV for MC cases can be made using $\bar{x}$ and s, the sample mean and standard deviation for the reconstructed parameter distributions (Eqn 5.7). Reported values for observations of optical properties are typically given via a mean and standard deviation, thereby allowing for CV statistics to be calculated for reported observed optical parameters as well. However, as the observed values included other sources of uncertainty beyond those attributable to natural variability in aerosol and environmental parameters, observed and MC reconstruction CV statistics are not directly comparable. Nevertheless, general comparisons of the relative dispersion in both sources can be informative.

While the arithmetic $\widehat{CV_a}$ estimator in Eqn 5.7 provides a simple and straightforward calculation, in practice it is susceptible to large values or outliers skewing the sample standard deviation estimate. In some of the MC reconstruction scenarios this led to anomalously high estimates for CV. Furthermore, observations of aerosol scattering and extinction coefficients, as well as the associated aerosol optical depths, have often been found to follow lognormal frequency distributions (O'Neill et al., 2000). In at least some cases, frequency distributions for intensive scattering or extinction efficiency variables have also been noted to have positive skewness or lognormal variability as a consequence of the non-linear relationship between aerosol particle size and scattering (Clarke et al., 2002). Moreover, aerosol inversion and retrieval algorithms that utilize observations of non-negative aerosol optical properties have been noted to benefit by treating variability as lognormally distributed (Dubovik and King 2000).

The MC reconstructions in this analysis often showed some degree of positive skew, even if large value outliers were removed. Chi-squared goodness of fit tests of the MC distributions rejected both normal and lognormal distributions at the 1% significance level for nearly all scenarios, owing to the non-linear nature of the optical and thermodynamic processes involved. However, the chi-squared value was lower in the case of the lognormal distribution for all scenarios varying mass and RH, while variable intensive parameters slightly favored normal distributions—though lognormally distributed variables with geometric standard deviations less than ~1.2 (as was the case for most of these distributions) may be difficult to distinguish from a normally distributed ones (Limpert et al., 2001). To account for the effect of such positive skew on the CV estimate, an alternate set of geometric maximum likelihood estimators were used to generate estimates of the geometric mean, $\bar{x}_g$ (Eqn 5.8), and geometric standard deviation factor, s_g (Eqn 5.9), based on the assumption that the optical parameters were better described by a

lognormal distribution (Limpert et al., 2001). The geometric $\widehat{CV_g}$ estimator based on these statistics (Eqn 5.10) was therefore used for relative dispersion estimates for all MC analyses.

$$\bar{x}_g = exp\left(\frac{1}{n}\sum_{i=1}^{n}\ln(x_i)\right) \tag{5.8}$$

$$s_g = exp\left(\sqrt{\frac{1}{n-1}\sum_{i=1}^{n}\left(\ln\left(\frac{x_i}{\bar{x}_g}\right)\right)^2}\right) \tag{5.9}$$

$$\widehat{CV_g} = \left(exp\left(\left(\ln s_g\right)^2\right) - 1\right)^{\frac{1}{2}} \tag{5.10}$$

5.1.3. *Reconstruction Input Parameters*

Relevant aerosol and environmental parameters measured as part of the SCS dataset were organized into four general categories to investigate their relative impact on optical properties in a remote marine region: (A) intensive parameters within a given aerosol population type (specifically: the eight size and hygroscopicity parameters for two modes described in Chapter 2), (B) environmental relative humidity, (C) mass concentration, and (D) population type. Each case was investigated using an MC analysis to generate a range of extinction values associated with natural variability in one or more of these input parameter categories, while all other parameters were held constant at the study average value.

In cases that varied category A, multiple input parameters were selected with each being drawn independently of the others using the mean and standard deviation for the parameter, with the exception of the modal fraction that was only selected for one mode with the other constrained such that the sum of all modes was one. Two hundred such samples were generated for each

remote marine population type on a dry volume normalized basis. Optical reconstructions of extinction (effectively MEE_d after accounting for dry particle density as discussed further below) at 550 nm were then generated for 20 inverse-logarithmically distributed RH values between 0% and 99% (with more values concentrated at higher values of RH where sensitivity is highest). Extinction coefficient for that MC sample could then be calculated by multiplying a given dry aerosol mass by the MEE_d interpolated to any RH between 0 and 99%.

In cases that varied category B the mean and standard deviation of the observed RH values were sampled and applied to a similar MEE_d curve for average population intensive parameters and median dry mass concentration. Given the observed RH values in the SCS dataset between approximately 60% and 95%, aerosol was assumed to have deliquesced in all circumstances, consistent with typical non-dust aerosol behavior in marine regions (e.g. Carrico et al., 2003). For category C cases the dry mass concentration was inferred from the measured integrated volume concentrations and assumed densities for each population type (discussed further below). As these variations were not explicitly presented in Chapter 2, Figure 5.2 shows the frequency distribution of observed volume concentrations for each SCS population type, with a lognormal fit from which the MC scheme sampled.

All cases were run for each of the seven remote marine population types identified in the SCS, along with a combined remote marine population type. The combined type was generated by first selecting a population type based on the frequency at which the various remote marine types were observed. Analysis for category D was based on the combined type's MC selection of only population type while other parameters were held constant.

Variability in optical properties due to variability in the aerosol dry index of refraction was not included in this analysis, as no reliable observation of this property was available for the SCS dataset. However, the actual range of real refractive indices in visible wavelengths is small for most atmospheric aerosol constituents, and the effect decreases with increasing RH as hygroscopic growth causes the index of refraction to approach that of water. Changes to the dry aerosol density would also increase variability of the MEE parameter, but this would similarly be expected to have minimal differences within a population type for generally well mixed species. We note that the above statements are not true for black carbon, which absorbs in the visible and

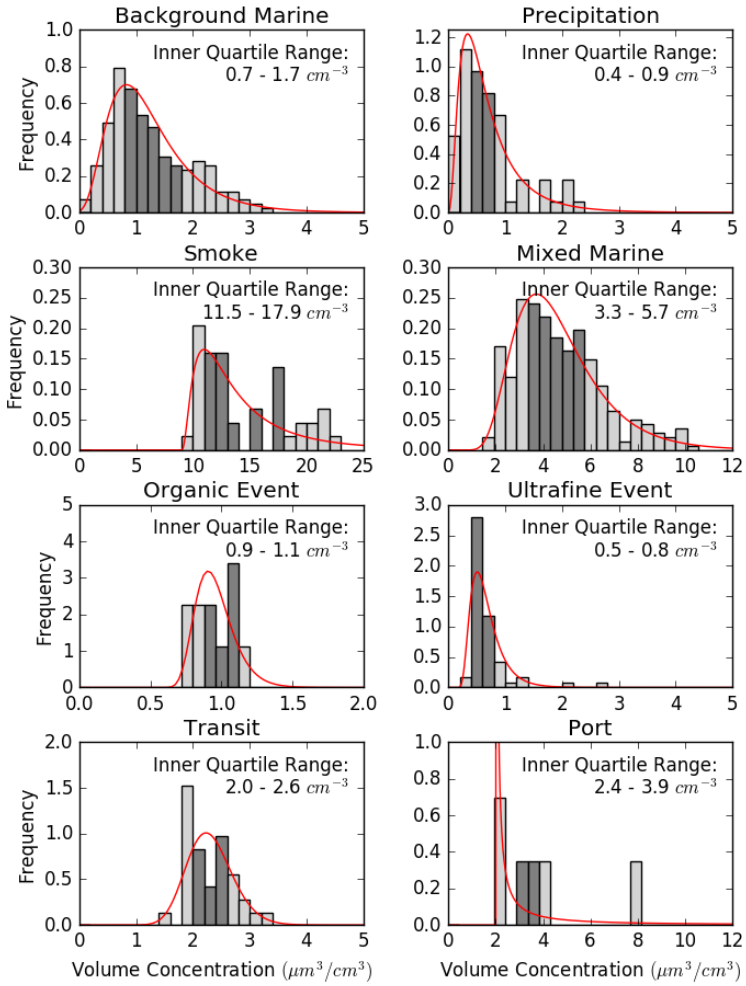

Figure 5.2 Observed volume concentration histograms for each population type in the SCS dataset. The inner quartile range of concentrations for each histogram is listed and shown in dark grey. Best fit lognormal distributions are included for each population type.

also has a significantly different density than other typical aerosol components. However, our dataset did not include measurements to quantify this directly. Some additional consideration of the range of potential errors due to these factors are considered below and in sections 5.2 and 5.4.

In order to compare the reconstructions to observations and generate realistic values for optical parameters, an assumed value for dry index of refraction and dry density was utilized for each population type. As comparisons between observed population types were of interest in this study, the same values were used for most types to minimize introduced sources of variability not based directly on observed values. MODIS retrievals use an assumed density of 1.0 g/cm^3 for mass concentration estimates based on their humidified aerosol models (Remer et al., 2006; Levy et al., 2009), while many measured values are for dry conditions where densities are usually above that of water. Typical dry particle densities range from fresh biomass burning particles that have been reported between approximately 1.2 and 1.9 g/cm^3 (Levin et al., 2010), to sea salt populations that may be closer to 2.2 g/cm^3, and higher for some dust species (e.g. Chin et al., 2002; Clarke et al., 2002). A density of 2.0 g/cm^3 was used for all population types here, though this implied that an additional factor of up to approximately 1.8 could further separate a background marine population above that of smoke for MEE. Such potential discrepancies affect the absolute values (but not CV comparisons) for MEE, and were therefore considered when comparing population types for case D.

The real component of the index of refraction was set to 1.5 for all dry population types based on a best-fit value for reconstructions when compared to scattering observations from the SCS dataset (discussed further in the next section). This value is consistent with typical values assumed for many of the population types used here (e.g. Chin et al., 2002). Further, as only the smoke impacted population types were expected to have substantial absorbing components, the

imaginary component of the refractive index was assumed to be zero for all types except the smoke and mixed marine populations. This component was assumed to be 0.1 for the smoke type, a value generally in the middle of the range reported for biomass burning particles by Levin et al. (2010), but less than some model assumptions (e.g. Chin et al., 2002). A value of 0.07 was used for the mixed marine population type, based on the ratio of modal hygroscopicity parameters for the mixed marine type between those of the smoke and background marine types (i.e. volume mixing of κ was used as a proxy for assumed volume mixing of the imaginary component of the refractive index).

5.2. EVALUATION OF OPTICAL RECONSTRUCTION METHODOLOGY

The optical Mie reconstruction was first validated against dry scattering coefficients measured during the SCS cruise. A TSI 3563 nephelometer was operated in parallel to the size-resolved CCN system described in Chapter 2, and averaged to the same roughly 15-minute periods for each data point. An approximate 1 μm size-cut impactor was used to remove coarse mode sea-salt, yielding an approximate measurement of fine mode scattering coefficient with some influence from submicron coarse mode particles that were observed at sizes as small as 800 nm (Figure 2.2b), followed by drying via passing through a heated copper tube before sampling. All measurements were first corrected for angular non-idealities in the nephelometer following Anderson and Ogren (1998). Further nephelometer results are discussed in Reid et al. (2016).

The measured aerosol size distribution and concentration at each data point were passed to the Mie reconstruction algorithm and the results compared with observed scattering. In order to reconstruct a scattering coefficient comparable to the measured nephelometer data, including contributions to scattering from only those particles with aerodynamic diameters smaller than

approximately 1 µm would be appropriate. As both the PCASP and DMPS instruments spanned this range, four different reconstruction methodologies based on these results were evaluated against the nephelometer, which are shown in each column in Figure 5.3. The reconstructions utilized size distributions for particles spanning the range of (a,e) 17–500 nm as measured by the DMPS instrument in the CCN system; (b,f) 125 nm–2.5 µm from the PCASP; (c,g) 125 nm–1 µm from the PCASP; and (d,h) a combined distribution utilizing DMPS results for the 17–500 nm particles and PCASP particles for those between 500 nm–1µm.

Reconstructed scattering coefficients are shown against the nephelometer measurements for each of the size distribution alternatives in Figure 5.3 using a refractive index with a real component

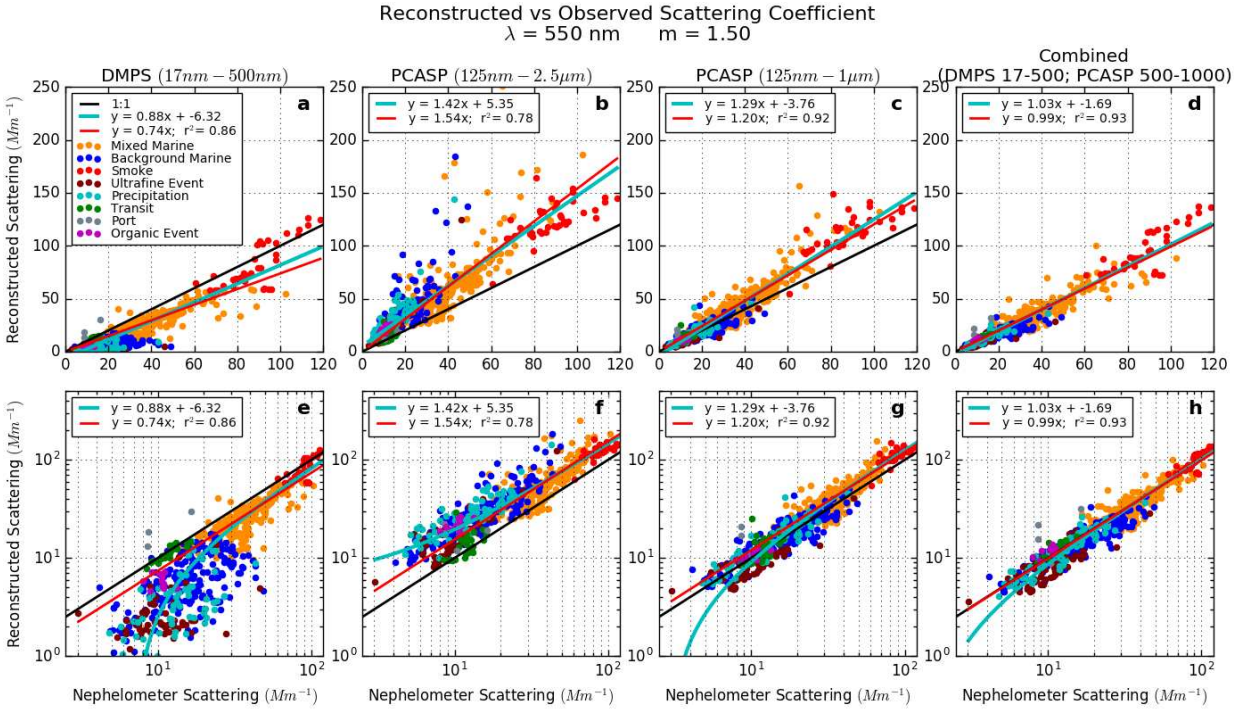

Figure 5.3 Mie reconstruction of aerosol scattering coefficient compared against the equivalent dry scattering coefficient measured by nephelometer, both at 550 nm wavelength. Linear and logarithmic scale plots are shown for reconstruction aerosol size distributions generated from (a,e) DMPS only (17 – 500 nm), (b,f) PCASP only (125 nm – 2.5 µm), (c,g) PCASP only (125 nm – 1 µm), and (d,h) a combined distribution with DMPS (17 – 500 nm) and PCASP (500 nm – 1 µm). A scattering coefficient of m = 1.50 was utilized for all data points. Data points are colored according to population type classification based on results from chapter 2. An OLS regression line (light blue) and OLS line constrained through the origin (red) are shown along with r^2 coefficient of determination.

of 1.50. Each data point was colored according to the population type to which it was classified, while an ordinary least squares (OLS) regression line (light blue), OLS line constrained through the origin (red), and r^2 coefficient of determination were calculated for each reconstruction type. Linear and log scales are shown in the top and bottom rows to highlight the behavior of the reconstruction at both the upper and lower ends of the scattering range, respectively.

The reconstruction utilizing only the DMPS for particles below 500 nm (Figure 5.3a,e) yielded a substantial number of reconstructed data points below the 1:1 line. Interestingly, reconstructions were generally more accurate for higher scattering coefficients that were associated with smoke dominated conditions. As the majority of the smoke population particles were less than 500 nm in size, their total mass was well represented by the DMPS size distribution, with larger particles that had not been included in this parameterization contributing to a smaller fraction of total scattering. In the second reconstruction case, such larger particles were included via the PCASP size distributions (b,f). As expected, reconstructions with size distributions up to 2.5 μm over-predicted scattering due to the measured range including only submicron particles. When the PCASP distribution was constrained to the 125 nm – 1 μm range (c,g) reconstructions were closer to observations with a higher r^2 value (0.92), but still over-predicted when substantial accumulation mode smoke impacts were occurring. Finally, the combined distribution (d,h) yielded a reconstruction most consistent with the observations. Best fit regression lines were closest to the 1:1 line among the alternatives, while r^2 was similar to the constrained PCASP distribution with a value of 0.93. The difference between the last two alternatives was necessarily due to discrepancies in the representation of particles below 500 nm, and would be consistent with slight sizing problems in the optical PCASP measurements, particularly in smoke impacted periods when more particles in this range were present (e.g. Reid et al., 2003, 2006).

In addition, a range of refractive index real components between 1.47 and 1.6 was tested to identify the appropriate value to use in the optical model. The overall best-fit index of refraction was found to be 1.50, as shown in Figure 5.3d&h, consistent with expected values for dry aerosol in marine regions (Tang et al., 1997; Hess et al., 1998; Dubovik et al., 2002; Chin et al., 2002, 2009). This best-fit approach was similarly applied to only the data points from each population type, which yielded a slight improvement in some cases, but unreasonable refractive indices for others. As both the reconstruction and optical measurements were sensitive to other factors beyond just dry refractive index, it was judged that any further inferences about the real component of refractive index specific to each population type were not warranted based on these data, and the overall best-fit value was used for all types.

Further reconstructions were included for RH values up to 60% to test for the possibility that observations were not completely dry. These reconstructions led to markedly increased reconstructed scattering well above the equivalent nephelometer results (not shown), indicating hygroscopic growth beyond that associated with measured DMPS size distributions (RH < 30%) in these observations was likely minimal.

5.2.1. *Variability of Reconstructions*

In order to evaluate the ability of the MC model to represent the expected variability of optical properties, MC results were first compared against variability in observations. The SCS population types and their associated MC reconstructions were representative of Aitken and accumulation aerosol modes, whereas the scattering observations included some coarse mode impacts, making direct comparison of variability between the two inappropriate. Instead, as the optical reconstructions of actual measurements (observed reconstructions) had been validated

against dry scattering observations, the variability in these data points were used to compare against dry MC reconstructions based on resampling of all input parameter categories except RH.

Sets of 100,000 MC reconstructions of the dry extinction coefficient were generated for each population type and the combined remote marine type (blue), which were then compared against the observation reconstructed values (red) and shown as box and whisker plots in Figure 5.4. The CV statistic was calculated for each of the distributions and shown as circles in the figure.

As the reconstructions were non-normally distributed, the non-parametric Wilcoxon-Mann-Whitney rank-sum test (Wilks, 2011) was used to test the null hypothesis that both reconstructions were drawn from the same population. The p-value for the two-sided, Mann-

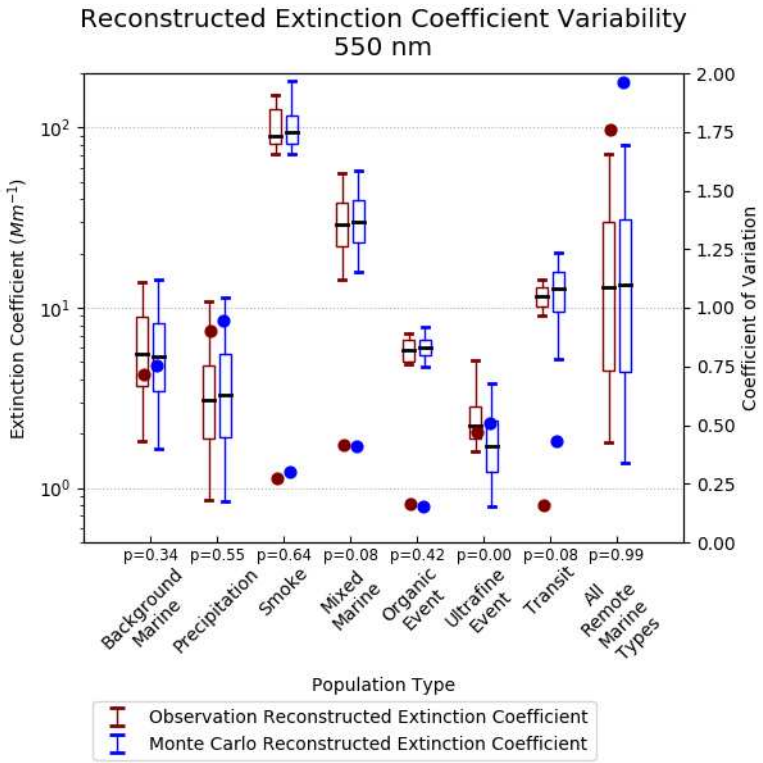

Figure 5.4 Box and whisker plot for reconstructed dry extinction coefficient distributions based on observations (red) and the MC resampling of all input parameter categories (blue) for each remote marine population type and the combined population. Boxes give the inner quartile range with whiskers at the 5th and 95th percentile of the distributions. Geometric means are shown as black lines, with the CV statistic for each distribution shown as circles. Mann-Whitney U-statistic p-values are shown below the x axis.

Whitney U-statistic was calculated for each population type. The null hypothesis would be rejected, indicating that the two reconstructions were from separate underlying populations, if this statistic was below a critical value of 0.05. All but one of the population types had p-values above the critical value, with only the ultrafine event population type rejecting the null hypothesis and suggesting some optically relevant difference between the MC reconstruction and the observations. This ultrafine event type had 59 observations with several outliers towards the higher end, and generally the lowest observed scattering values of all types. The result indicated there was some bias in the MC reconstruction to lower extinction values, however, the CV statistics were generally close for both distributions of this type.

In all but one type the CV statistic was similar between both reconstructions. The transit type had a wider distribution and higher resulting CV for the MC reconstruction when compared to the observed reconstruction, though geometric means were similar, and the U-statistic did not indicate they were likely to be drawn from separate populations. The reason for this difference was not obvious, but may have been due to the relatively larger standard deviations for the transit population intensive parameters as a result of the few data points classified as this type (n=36) and slight differences in the fitting of several data points (Figure 2.3). The combined remote marine type was generally similar between reconstructions as well, with only a small increase in expected variability indicated by the MC analysis as compared to observations.

Finally, values for distribution CV were generally similar between both reconstruction types, and showed distinct differences between population types, improving confidence in the ability of this statistic to quantify variability in optical properties. Given the high correlation and good fit of the reconstructions to comparable observed scattering, and the generally consistent test statistics between the observation and MC based reconstructions, the Mie optical reconstruction model

and use of the Monte Carlo analyses to estimate variability was found to be generally appropriate.

5.3. OPTICAL PROPERTY SENSITIVITY IN A MARINE REGION

Assessment of the sensitivity of optical properties to changes in the four input parameter categories was conducted through use of the MC reconstruction model. In these analyses, each category was allowed to vary (MC resampling) while all other categories were held at their population average value. In several cases as noted below, several or all of the parameter categories were allowed to vary to estimate variability associated with multiple parameters. The range of extinction coefficients and dry mass extinction efficiencies for each of these variability cases are shown in Figure 5.5a&b, respectively. Summary results for each population type and the combined remote marine type are given in Table 5.1, along with the CV statistics for each case. Geometric means for MC distributions (black lines) were typically close to the value for the average population type (colored arrows), indicating the various reconstruction cases influenced variability (CV values) without substantially changing the expected value for extinction or MEE.

Table 5.1 Extinction coefficient and dry mass extinction efficiencies for each average population type and the combined remote marine population type, along with the CV statistic for MC reconstructions of each of the various cases. The weighted mean provides the mean value for all population types weighted by their observed relative frequency.

	Average Population*		CV of MC Reconstruction								
SCS	Ext Coeff	MEE_d	Case A	Case B	Case C	Case D	Case D	Case A&B	Case A&C	Case A&C	Case ABC
Population Type	(Mm^{-1})	(m^2/g)	Aerosol	RH	Mass	Intensive	Extensive			(Dry***)	
1: Back. Marine	18.1	8.5	0.21	0.27	0.68			0.35	0.73	0.75	0.80
2: Precipitation	8.3	7.3	0.27	0.21	0.87			0.35	0.93	0.94	0.98
3: Smoke	191.4	7.5	0.04	0.19	0.30			0.20	0.30	0.30	0.37
4: Mixed Marine	69.6	8.0	0.13	0.21	0.40			0.24	0.43	0.41	0.48
5: Organic Event	9.6	5.3	0.08	0.16	0.14			0.18	0.16	0.16	0.23
6: Ultrafine Event	6.5	5.9	0.26	0.32	0.40			0.42	0.49	0.51	0.60
7: Transit	36.0	7.9	0.25	0.26	0.18			0.36	0.31	0.43	0.41
Weighted Mean	48.4	7.8	0.18	0.24	0.51			0.30	0.55	0.56	0.62
Combined Type**	35.1 (52.7)	7.5	0.22	0.24	1.42	0.12	1.25	0.33	1.58	1.96	1.65
*Calculated using median mass concentration at the average observed RH of 79%											
**Using median and (mean) mass concentration for the combined remote marine population type											
***An RH of 0% was used for all reconstructions in this reconstruction; Results from Figure 6.4											

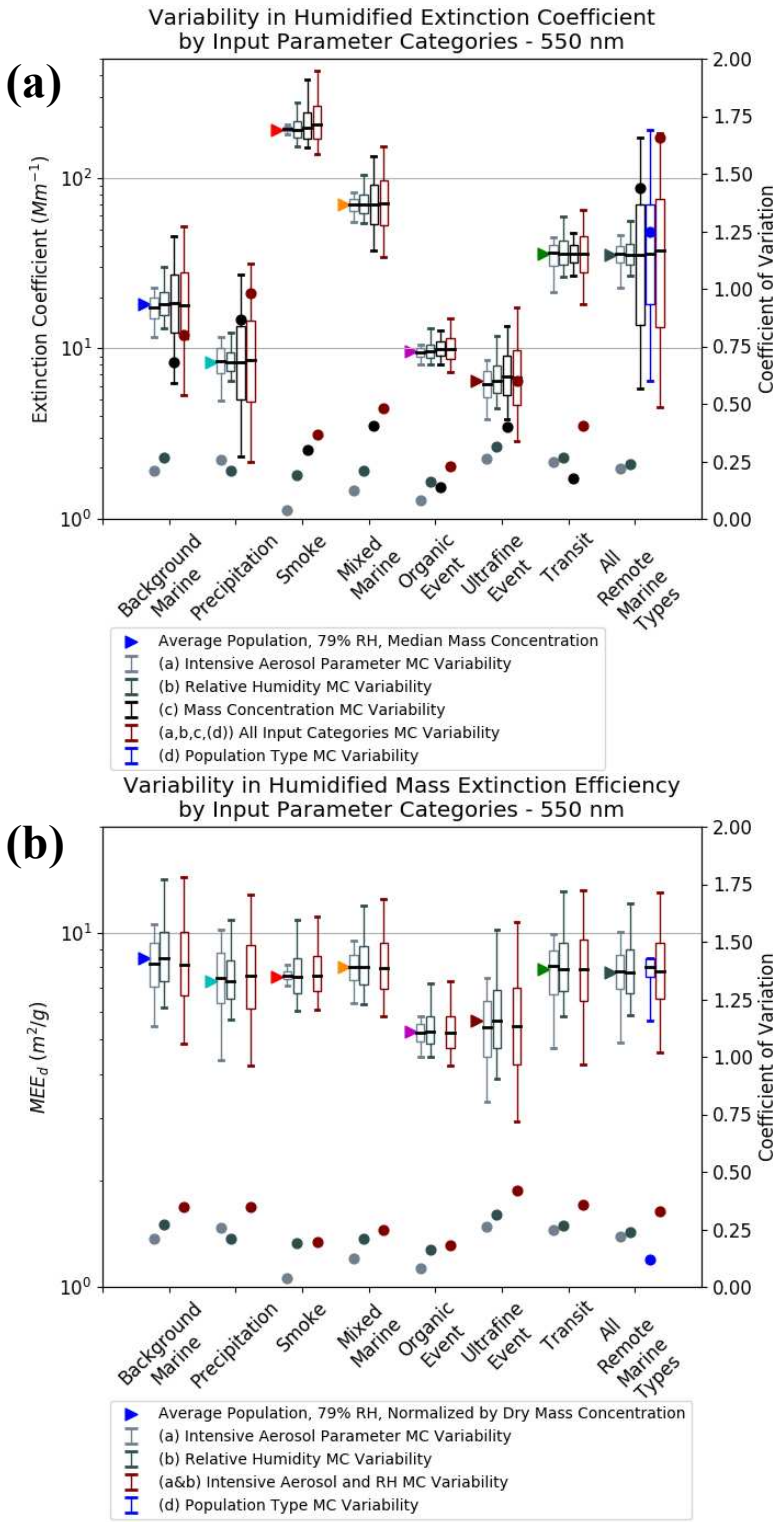

Figure 5.5 SCS population type variability in (a) humidified extinction coefficient and (b) mass extinction efficiency on a dry aerosol mass basis. Extinction for the average population type are shown as colored arrows for median observed mass concentration and average observed RH (79%). Box and whisker plots give the range of variability due to changes in various input categories for the optical model, with associated geometric means (black line). Coefficients of variation for each case are shown as circles.

A weighted mean of all individual remote marine population types was also calculated for these statistics based on the relative frequency at which each type was observed, providing an indication of typical values for statistics when constrained to only one aerosol population type.

Initial interpretation of these results was begun by examining the combined remote marine type, which provides a reconstruction of an "average" aerosol population observed during the SCS study at the mean RH and independent of any specific aerosol type. As input parameters were resampled for each case, the CVs for aerosol intensive parameters (case A) and RH (case B) were 0.22 and 0.24, respectively, while the mass concentration variability (case C; CV=1.42) yielded more than five times the expected relative variability in extinction. When all factors were resampled by the MC model (red box and whisker plots) the CV was only slightly higher at 1.65, indicating that mass concentration was indeed the primary factor influencing extinction in this combined population, consistent with initial hypotheses.

However, when the MC model was constrained to a single population type (part of the case D analysis), expected variability due to mass concentration dropped markedly, while relatively little change in CV due to aerosol parameters and RH occurred. The weighted mean of variability in individual population types for mass concentration (CV=0.51) was a factor of 2.8 lower than the combined type, owing to the strong observed relationship between population type and mass concentration in the SCS dataset. Mass concentration was generally still the most important individual factor within most population types, with more than twice the weighted mean CV of the RH (CV=0.24) and intensive aerosol (CV=0.18) parameters. However, this was in large part due to the much higher sensitivity to mass concentration found in the background marine and precipitation types. In the case of the other observed population types, which were generally associated with aerosol advected into the remote marine region from terrestrial or anthropogenic

sources, there was less variability in mass concentration and therefore less extinction sensitivity to this factor.

Examination of the intensive optical MEE_d statistics in Figure 5.5b showed the reduced variability expected when the effect of mass concentration was removed. The combined impact of aerosol parameters and RH was still generally less than that of mass concentration, even within a given population type. Variability for the combined intensive parameter effect (case A&B) was on average roughly 60% of the mass concentration (case C) impact within a given population type (weighted mean CV of 0.30 vs 0.51, respectively), and about 20% of the impact when population type is not known (combined type CV of 0.33 vs 1.42). Though as with extinction coefficient, this general finding was less applicable to the specific event types where variability in mass concentration dropped.

Interestingly, the CV values for aerosol intensive parameters and RH were relatively consistent across virtually all cases that were run. Weighted mean and combined type CVs were similar for cases A (0.18 vs 0.22), B (0.24 vs 0.24), and A&B (0.30 vs 0.33) where mass concentration was held constant. In case A the CV was in fact between 0.04 and 0.4 across the full range of RH values from 0% to 99%, with many atmospherically relevant values around 0.2.

Lastly, population type (case D) had the smallest effect on intensive optical properties of any of the cases (case D intensive CV=0.12). This was notably different from its larger impact on extensive optical properties where mass concentration was considered (case D extensive CV=1.25), which once again was due to the strong relationship between population type and mass concentration in the SCS dataset.

A general finding of this analysis was therefore that aerosol intensive parameters and RH were each found to have individual CVs on the order of 0.2, and a combined CV on the order of 0.3—values which were relatively independent of other parameters including aerosol population type, mass concentration, and/or magnitude of RH. Conversely, the extinction sensitivity to changes in mass concentration, while higher than aerosol intensive parameters and RH, was also much more dependent on population type—on the order of 0.5 within a given population type, and 1.4 when no information about population type was known. Lastly, CVs due to all sources of natural variability were found to be on the order of 0.6 within a given population type, and 1.7 across the SCS study as a whole. Such information may be of use to models, retrievals, or data assimilation efforts where estimations of the relative impact of these unknown parameters in remote marine regions is desired.

A final important conclusion of the optical reconstruction analysis is therefore that on an intensive property basis the different population types impacting the SCS remote marine location produced variability in optical properties that was generally less that that due to natural variability within a given population type. Only when the extensive dry mass concentration was included did information about population type explain more of the expected variability than did variability in intensive aerosol parameters or RH. Such a result validates the use of relatively simplistic, population type independent aerosol models along with mass concentration, as is the case in MODIS retrievals and many atmospheric models applied to remote marine regions.

5.3.1. *Estimates of Optical Property Uncertainty*

The previous section evaluated sensitivity of atmospheric extinction to various controlling factors, however, CV estimates could similarly be used to constrain expected extinction or estimate its uncertainty due to natural variability in various scenarios. As an example,

background marine ambient extinction during the SCS study could be estimated by the mean and standard deviation of the case ABC reconstruction distribution, at $\bar{x} = 22.4\ Mm^{-1}$ ($s = 17.4\ Mm^{-1}$), or in geometric terms by the geometric mean and standard deviation at $\bar{x}_g = 18.2\ Mm^{-1}$ $\left(s_g = 2.01\right)$. Such values could be used as an estimate of the uncertainty in a background marine extinction measurement due to natural variability.

As was noted previously, in the SCS results the extinction and MEE_d for the average population type models (colored arrows in various figures) were roughly equivalent to the geometric mean values for most MC reconstructions—owing to the tendency for positive skew in the optical parameters in scenarios with all aerosol and environmental parameters varying. As such, using only the parameters for these average population types given in Table 5.1 and Eqn (5.10, similar estimates for background marine ambient extinction would be $\bar{x}_g = 18\ Mm^{-1}$ $\left(s_g = 2.0\right)$, or in arithmetic terms after conversion assuming a lognormal distribution (following Limpert et al., 2001) for a more direct comparison with typical reported values as $\bar{x} = 23\ Mm^{-1}$ ($s = 18\ Mm^{-1}$).

Uncertainty estimates in other scenarios of interest could similarly be estimated. For example, background marine ambient extinction uncertainty due to only natural variability in intensive properties would be estimated using the case A&B CV at $\bar{x}_g = 18\ Mm^{-1}$ $\left(s_g = 1.4\right)$ or $\bar{x} = 19\ Mm^{-1}$ ($s = 6.3\ Mm^{-1}$), demonstrating the lower expected extinction uncertainty in such a scenario. Similar to the last section, models, retrievals, or data assimilation efforts based on the SCS dataset could potentially benefit from treatment of these results as estimates of uncertainty rather than sensitivity.

5.4. COMPARISON WITH MODIS AEROSOL MODELS

As the MODIS fine mode marine aerosol models are generally applied across the range of conditions and aerosol population types found in marine regions, they can be compared with the SCS aerosol types to determine under what conditions they would be optically equivalent. The humidified mass extinction efficiency was calculated for the SCS types and compared against the fixed MODIS MEE values at 550 nm in Figure 5.6. Observed RH varied between roughly 60% and 95% during the SCS cruise. Most average population $MEE_h(RH)$ curves at these RH values were within the range of MODIS values, with the exception of the ultrafine event that had lower extinction efficiency.

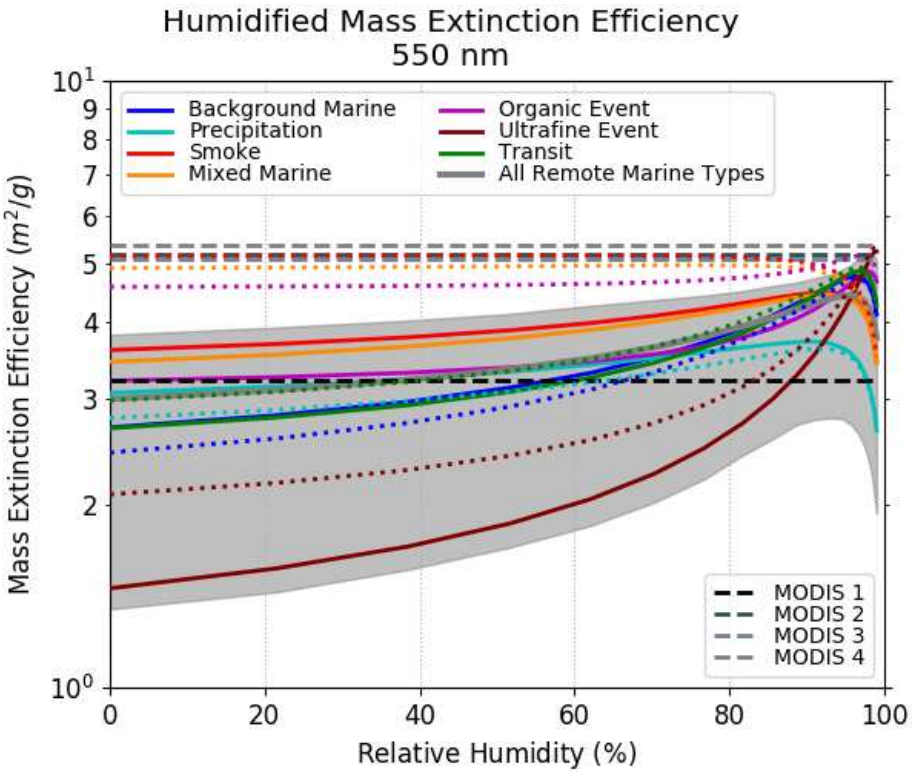

Figure 5.6 Humidified mass extinction efficiency for the SCS remote marine average population types across the range of RH values at the standard assumed density of 2.0 g/cm^3 (solid lines). Alternate densities for each population type are shown as dotted lines. Equivalent values for MODIS marine fine mode aerosol models without additional hygroscopic growth are shown as dashed lines. The 5th and 95th percentile bounds of the Monte Carlo runs for all SCS remote marine types (density of 2.0 g/cm^3) are shown as the grey region.

$MEE_h(RH)$ curves were also generated for all MC reconstructions (based on the ABCD case of variability in all input parameters), with the 5th and 95th percentile of results shown as the grey region. Reconstructed variability in mass extinction efficiency extended to values somewhat lower than the MODIS types, primarily from the ultrafine event and some distributions from the marine background and precipitation types.

The impact of different dry particle densities was also examined and is shown as dotted lines in Figure 5.6. A value of 2.2 g/cm^3 was used for the background marine and precipitation types, consistent with sea salt dominated particles, which resulted in values still within the range of MODIS types for relative humidities above roughly 60%. The transit type was given an alternate density of 1.8 g/cm^3, more consistent with inorganic pollution, and similarly showed general consistency with the MODIS range. Other population types were examined at 1.4 g/cm^3, a density more characteristic of organic influence. The smoke, mixed marine, and organic event types were very similar to the higher of the MODIS MEE values, while the ultrafine event MEE increased and reached equivalence to the MODIS 1 type at just above 80% RH for the average population. In all cases, the impact of different dry densities decreased at higher RH as the total density approached that of water.

The mass extinction efficiencies for average population types in the SCS were therefore generally consistent with MODIS, and further indicate why such models are generally suitable for visible retrievals in marine regions. Reconstructed MEE values outside of the MODIS range were associated with generally smaller particles, as were found in the ultrafine event and with some size distributions in the background marine and precipitation types arising due to natural variability in these types.

5.5. COMPARISON WITH OTHER MARINE REGIONS

The representativeness of the SCS optical reconstruction results to other marine regions was assessed through comparison of both the magnitude and variability of these properties to reported values in other remote marine observations. Scattering coefficient observations and MC reconstructions cases for the SCS dataset were utilized for comparison against reported properties in roughly equivalent contexts.

5.5.1. *Extensive Optical Property Observations*

Extensive optical properties are typically measured as separate scattering and absorption components of extinction. A survey of observations for submicron aerosol in marine regions is given in Table 5.2, along with general classifications of the measured aerosol type as reported in various studies. While nominally intended to be representative of fine mode particles, measurements of submicron scattering may contain some influence from coarse mode particles with distribution tails that extend into submicron sizes and therefore influence measurements. In the SCS coarse mode sea-salt particles often extended down to approximately 800 nm and had a distinct influence on scattering observations. Similar statistics for scattering and absorption coefficients reconstructed using only Aitken and accumulation mode aerosol are given in Table 5.3. Based on these values, as well as the reconstructions in Figure 5.3, in some of the SCS observations more than half of observed submicron scattering may have been a result of coarse mode influences, particularly during periods of lower fine mode mass concentrations.

In the SCS precipitation and background marine types, mean scattering was 14 and 17 Mm^{-1}, respectively, for observations, while the MC reconstructions for types without coarse mode influence were 4.8 and 7.3 Mm^{-1}. Reported values for clean or background marine aerosol were often in the range of 3 and 10 Mm^{-1} in the most pristine regions, consistent with the fine mode

Table 5.2 Observed submicron scattering and absorption coefficients in reported marine datasets.

Experiment	Location / Platform	Aerosol Type	Coefficient (RH) Mm^{-1} (%)	Range	mean	std dev	CV	Source
ACE-1	Southern Ocean	Clean Marine	σ_{sp} (22%)		3.6	(2.0)	0.56	Carrico et al., (1998)
	Ship	Non-Clean Marine	σ_{sp} (22%)		5.4	(3.0)	0.56	
ACE-1		Unperturbed Marine	σ_{sp} (30%-45%)	0.66 - 38	4.4	(3.0)	0.68	Quinn et al., (1998)
ACE-2	Sagres, Portugal	Clean Littoral	σ_{sp} (27%)		6.5	(4.8)	0.74	Carrico et al., (2000)
	Littoral	Polluted Littoral	σ_{sp} (27%)		42.8	(19.1)	0.45	
ACE-Asia	NW Pacific	Marine	σ_{sp} (19%)		7.1	(2.8)	0.39	Carrico et al., (2003)
	Ship	Polluted Marine	σ_{sp} (19%)		41	(24)	0.59	
		Marine	**σ_{ap} (50%)**		0.5	(0.3)	0.60	
		Polluted Marine	**σ_{ap} (50%)**		5.9	(3.6)	0.61	
--	E Atlantic / Ship	Marine	σ_{sp} (41%)	2.8 - 82.9	20.8	(11.5)	0.55	Kleefeld et al., (2002)
INODEX	Indian Ocean	Low scattering period ($\leq$ 25 Mm^{-1})	σ_{sp} (55%)		12	(5.6)	0.47	Clarke et al., (2002)
	Ship	Medium sca. (25 $\leq$ sca $\leq$ 55 Mm^{-1})	σ_{sp} (55%)		40.3	(14.0)	0.35	
		High scattering period ($\geq$ 55 Mm^{-1})	σ_{sp} (55%)		77.8	(8.2)	0.11	
ACE-Asia	NW Pacific / Ship	Ship, all data	σ_{sp} (30%)		74.9	(52.2)	0.70	Doherty et al., (2005)
		Coarse Mode Dominated	σ_{sp} (30%)		78.0	(29.9)	0.38	
		Coarse/Fine Mix	σ_{sp} (30%)		57.5	(34.9)	0.61	
		Fine Mode Dominated	σ_{sp} (30%)		122.1	(68.4)	0.56	
		Ship, all data	**σ_{ap} (55%)**		7.8	(3.8)	0.49	
		Coarse Mode Dominated	**σ_{ap} (55%)**		10.1	(5.0)	0.50	
		Coarse/Fine Mix	**σ_{ap} (55%)**		6.8	(3.3)	0.49	
		Fine Mode Dominated	**σ_{ap} (55%)**		9.7	(3.5)	0.36	
	Gosan, Korea	Littoral, all data	σ_{sp} (30%)		64.6	(34.2)	0.53	
		Coarse Mode Dominated	σ_{sp} (30%)		131.9	(83.4)	0.63	
		Coarse/Fine Mix	σ_{sp} (30%)		75.6	(43.2)	0.57	
		Fine Mode Dominated	σ_{sp} (30%)		87.5	(49.0)	0.56	
		Ship, all data	**σ_{ap} (34%)**		9.8	(6.0)	0.61	
		Coarse Mode Dominated	**σ_{ap} (34%)**		18.4	(10.3)	0.56	
		Coarse/Fine Mix	**σ_{ap} (34%)**		9.7	(5.0)	0.52	
		Fine Mode Dominated	**σ_{ap} (34%)**		9.4	(5.7)	0.61	
	Aircract	All data	σ_{sp} (30%)		53.7	(26.3)	0.49	
		Dust Impacted	σ_{sp} (30%)		49.2	(26.9)	0.55	
		Non-Dust Impacted	σ_{sp} (30%)		62.4	(22.6)	0.36	
		All data	**σ_{ap} (30%)**		14.2	(9.7)	0.68	
		Dust Impacted	**σ_{ap} (30%)**		9.7	(5.5)	0.57	
		Non-Dust Impacted	**σ_{ap} (30%)**		22.1	(10.4)	0.47	
NEAQS-ITCT	NW Atlantic	Local Marine	σ_{sp} (26%)		36.2	(25.7)	0.71	Wang et al., (2007)
	Ship	Regional Cont. Influence	σ_{sp} (26%)		55.0	(37.5)	0.68	
		Distant Continental Infl.	σ_{sp} (26%)		29.0	(18.8)	0.65	
		Forest Fire Case Study	σ_{sp} (26%)		32.6	(30.1)	0.92	
		Local Harbor Case Study	σ_{sp} (26%)		13.9	(2.3)	0.17	
		Regional Plume 1	σ_{sp} (26%)		86.9	(13.5)	0.16	
		Regional Plume 2	σ_{sp} (26%)		65.0	(16.7)	0.26	
		Distant Plume 1	σ_{sp} (26%)		18.0	(11.4)	0.63	
		Distant Plume 2	σ_{sp} (26%)		10.6	(10.9)	1.03	
7SEAS 2012	South China Sea	1: Back. Marine	σ_{sp} (50%)*	4.1 - 49.0	17.2	(8.2)	0.48	This Study
	Ship	2: Precipitation	σ_{sp} (50%)*	4.8 - 42.9	14.1	(6.6)	0.47	
		3: Smoke	σ_{sp} (50%)*	60.7 - 118	87.5	(13.4)	0.15	
		4: Mixed Marine	σ_{sp} (50%)*	14.0 - 103	38.0	(14.3)	0.38	
		5: Organic Event	σ_{sp} (50%)*	8.0 - 13.3	10.4	(1.3)	0.13	
		6: Ultrafine Event	σ_{sp} (50%)*	3.0 - 46.1	11.3	(6.2)	0.55	
		7: Transit	σ_{sp} (50%)*	8.5 - 16.2	12.0	(1.7)	0.14	
		All Remote Marine	σ_{sp} (50%)*	3.0 - 118	28.6	(21.7)	0.76	

*SCS Nephelometer from this study; Nominal 50% RH after heating to dry aerosol

Table 5.3 SCS reconstructed MC scattering and absorption coefficients

SCS Population Type	Coefficient (RH) Mm^{-1} (%)	Range[1]	mean	std dev	CV	median	geo std dev	CV
1: Back. Marine	σ_{sp} (22%)	1.9 - 16.4	7.3	(4.7)	0.64	6.2	(1.94)	0.74
2: Precipitation	σ_{sp} (22%)	0.94 - 12.7	4.8	(4.2)	0.88	3.7	(2.20)	0.93
3: Smoke	σ_{sp} (22%)	48.9 - 124	73	(28.7)	0.39	64.5	(1.34)	0.30
	σ_{ap} (22%)	28.7 - 71.5	42.3	(16.7)	0.39	37.5	(1.34)	0.30
4: Mixed Marine	σ_{sp} (22%)	12.2 - 45.0	25.4	(10.5)	0.41	23.3	(1.48)	0.41
	σ_{ap} (22%)	5.2 - 18.5	10.5	(4.3)	0.41	9.7	(1.48)	0.41
5: Organic Event	σ_{sp} (22%)	5.0 - 8.2	6.4	(1.0)	0.16	6.3	(1.17)	0.16
6: Ultrafine Event	σ_{sp} (22%)	0.93 - 4.5	2.3	(1.2)	0.52	2.0	(1.61)	0.50
7: Transit	σ_{sp} (22%)	6.1 - 22.4	14.2	(4.9)	0.35	14.3	(1.49)	0.41
All Remote Marine	σ_{sp} (22%)	**1.6 - 56.6**	**18.3**	**(19.6)**	1.07	**13.2**	**(2.99)**	**1.52**

[1] Range calculated at 5th and 95th percentile values of MC sets

reconstructions, though some higher values were still associated with general marine aerosol influence. The somewhat higher observations during the SCS cruise may therefore have been in part due to different amounts of coarse mode influence in different experimental setups. Alternatively, this may be in part due to the more permissive classification of background marine aerosol populations afforded by this classification algorithm, whereas some studies with more simplistic classification schemes may be incorrectly removing higher observations that occur in background marine populations due to natural variability.

In marine boundary layer air masses that were impacted by terrestrial or anthropogenic sources, reported means for scattering spanned values from around 10 to over 100 Mm^{-1}, consistent with values of the other SCS population types. Reported variability in measurements for all types spanned CVs between 0.1 and 1.0, though with most between approximately 0.3 and 0.7 for distinct aerosol types. This range of values is similarly consistent with both observations and reconstructions of the SCS when the CV was calculated using the equivalent sample mean and standard deviation estimator.

As a result, despite some uncertainty over influence from coarse mode particles, extensive optical properties of the MC reconstructions for SCS population types were nevertheless

generally consistent with other studies of remote marine boundary layer air masses, both in terms of magnitude and variability.

5.5.2. *Extinction Efficiency Observations*

Dry mass extinction efficiency curves for each of the SCS population types are shown along with the range of MC results in Figure 5.7. The standard assumed density of 2.0 g/cm^3 was used for all population types, though offsets to this curve similar to those for the humidified mass extinction efficiency in Figure 5.6 would occur for different dry particle densities. Similar to extensive observations, intensive mass extinction efficiency is more often reported in terms of separate scattering and absorption components. Mass scattering efficiencies reported for other remote marine regions are presented along with the reconstructed MSE estimates from the SCS MC analysis in Table 5.4.

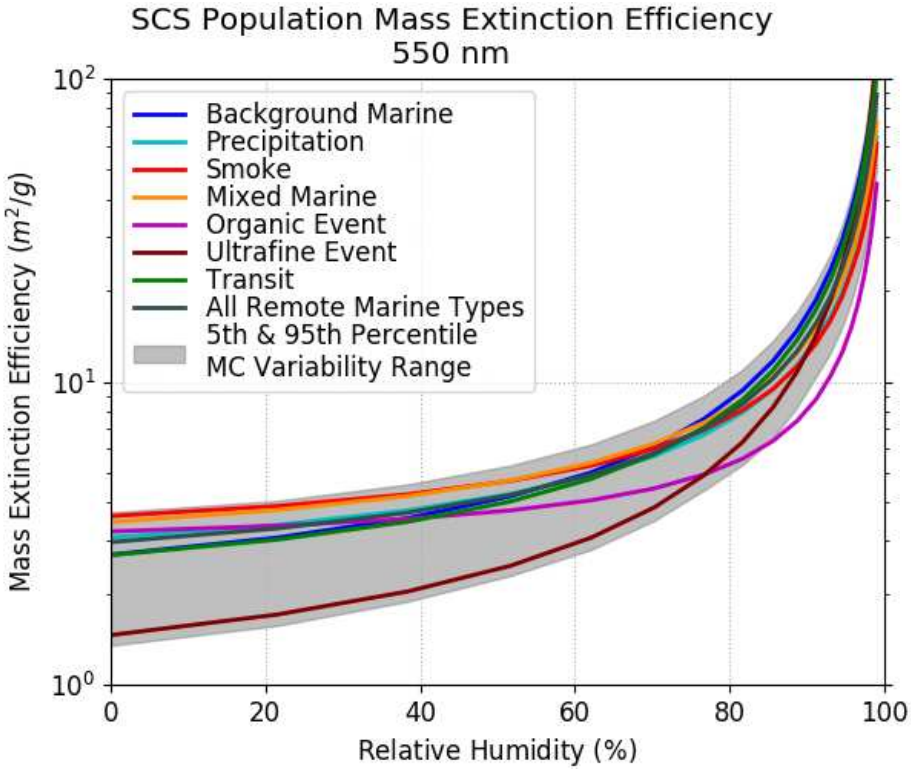

Figure 5.7 Submicron dry mass extinction efficiency for the SCS remote marine average population types across the range of RH values at the standard assumed density of 2.0 g/cm^3. The 5th and 95th percentile bounds of the Monte Carlo runs for all SCS remote marine types are shown as the grey region.

Table 5.4 Observed submicron mass scattering efficiencies (m^2/g) in reported marine datasets. Reconstructed values from MC analysis are given for SCS remote marine population types.

Experiment	Location / Platform	Aerosol Type	Measurement	mean	std dev	CV_a	median	geo std dev	CV_g	reference
ACE-1	Southern Ocean	Short MBL residence time	MSE - 30% to 45% RH	3.4	(0.58)	0.17				Quinn et al., (1998)
	Ship	Long MBL residence time	MSE - 30% to 45% RH	2.9	(0.95)	0.33				
		Perturbed marine	MSE - 30% to 45% RH	3.2	(0.61)	0.19				
INODEX	Indian Ocean	Low scattering period (≤ 25 Mm^{-1})	MSE - 33% RH	4.1	(1.2)	0.29				Clarke et al., (2002)
	Ship	Medium sca. (25 ≤ sca ≤ 55 Mm^{-1})	MSE - 33% RH	3.9	(0.51)	0.13				
		High scattering period (≥ 55 Mm^{-1})	MSE - 33% RH	4.1	(0.23)	0.06				
Various	NW Atlantic	Long-Term measurements	MSE < 40% RH	3.2	(1.1)	0.34	3.0			Bates et al., (2006)
	NW Atlantic	Intensive Campaigns	MSE < 40% RH	3.4	(1.1)	0.32	3.3			
	NW Pacific	Long-Term measurements	MSE < 40% RH	2.4	(1.2)	0.50	2.4			
ACE-Asia[1]	NW Pacific	Polluted - Korea/Japan	MSE - 55% RH - Mie Recon.	4.3	(0.17)	0.04				Quinn et al., (2004)
		Polluted - Japan	MSE - 55% RH - Mie Recon.	4.1	(0.09)	0.02				
Various	Ship cruises	All measured regions - Low range	MSE - 55% RH	3.2						Quinn and Bates (2005)
		All measured regions - high range	MSE - 55% RH	4.1						
7SEAS 2012	South China Sea	1: Back. Marine	MSE - 33% RH - Mie Recon.	3.2	(0.71)	0.22	3.3	(1.28)	0.25	
	Ship	2: Precipitation	MSE - 33% RH - Mie Recon.	3.6	(0.79)	0.22	3.8	(1.29)	0.26	
		3: Smoke	MSE - 33% RH - Mie Recon.	4.2	(0.10)	0.02	4.2	(1.02)	0.02	
		4: Mixed Marine	MSE - 33% RH - Mie Recon.	4.1	(0.26)	0.06	4.1	(1.07)	0.07	
		5: Organic Event	MSE - 33% RH - Mie Recon.	3.4	(0.27)	0.08	3.5	(1.07)	0.07	
		6: Ultrafine Event	MSE - 33% RH - Mie Recon.	1.9	(0.50)	0.26	1.8	(1.31)	0.28	
		7: Transit	MSE - 33% RH - Mie Recon.	3.4	(0.96)	0.28	3.5	(1.41)	0.35	
		All Remote Marine	MSE - 33% RH - Mie Recon.	3.6	(0.83)	0.23	3.9	(1.34)	0.30	

[1] Based on Mie Reconstruction from observed size and composition data, some what similar to this analysis

Reported MSE values for relatively dry observations below about 55% RH in marine regions were generally between roughly 3.2 and 4.1 m^2/g for aerosol classified as a background or clean marine type aerosol population. SCS MSE for the background marine and precipitation types (calculated here at 33% RH) had mean values of 3.2 and 3.6 m^2/g, respectively, and were well within the reported range of observed values. Observed relative dispersion of MSE was often between CV values of 0.1 and 0.4, with the variability decreasing as total submicron scattering (and associated submicron aerosol mass concentration) increased. Clarke et al., (2002) found generally constant mean MSE values around 4.0 m^2/g during a cruise in the Indian Ocean, but with CVs that decreased from 0.29 to 0.06 as total scattering increased from less than 25 Mm^{-1} to greater than 55 Mm^{-1} for measurements made at 33% RH. Similar behavior was noted in the SCS reconstructions, with most population types with mean scattering coefficients below 25 Mm^{-1} having CV values for MSE above 0.2, which dropped to below 0.06 for the smoke and mixed marine types that had higher mean scattering coefficients. The exception to this was the short duration organic event that had very similar aerosol populations throughout the event and

correspondingly low CV. Additionally, the ultrafine event had lower dry MSE values than reported observations and the organic event had lower values at higher RH, distinguishing it from both other SCS types and reported values. However, as these were both short term events associated with likely organic influence (and lower dry particle densities), their actual MSE curves would be higher and more in line with values for other population types.

Overall, only limited conclusions can be formed from direct comparison of reconstructed SCS values against observations, as actual dry particle density may change the magnitude of MSE to some degree. Nevertheless, based on the density estimates that were made, both the magnitude and variability of SCS MSE values were consistent with reported observations of marine aerosol populations.

5.5.3. *Scattering Enhancement Factor Observations*

A final set of comparisons were made against measurements of scattering enhancement factors in remote marine regions. Reconstructed f(RH) curves up to 99% RH are shown as lines in Figure 5.8 for each SCS average population type, with the range of variability associated with changes to aerosol intensive parameters indicated by the 5^{th} and 95^{th} percentile error bars. Studies that reported γ parameters for best-fit f(RH) curves are shown for roughly analogous aerosol types in the figure for comparison.

Several studies reported γ parameters for clean marine boundary layer airmasses in remote ocean environments (Gassó et al., 2000; Carrico et al., 2003). Interestingly, the f(RH) curves from these studies were both within the MC range of the SCS background marine and precipitation types, but were also between the average population curves of these two SCS types. Such results indicate the SCS humidograms were consistent with those reported for other marine regions, but

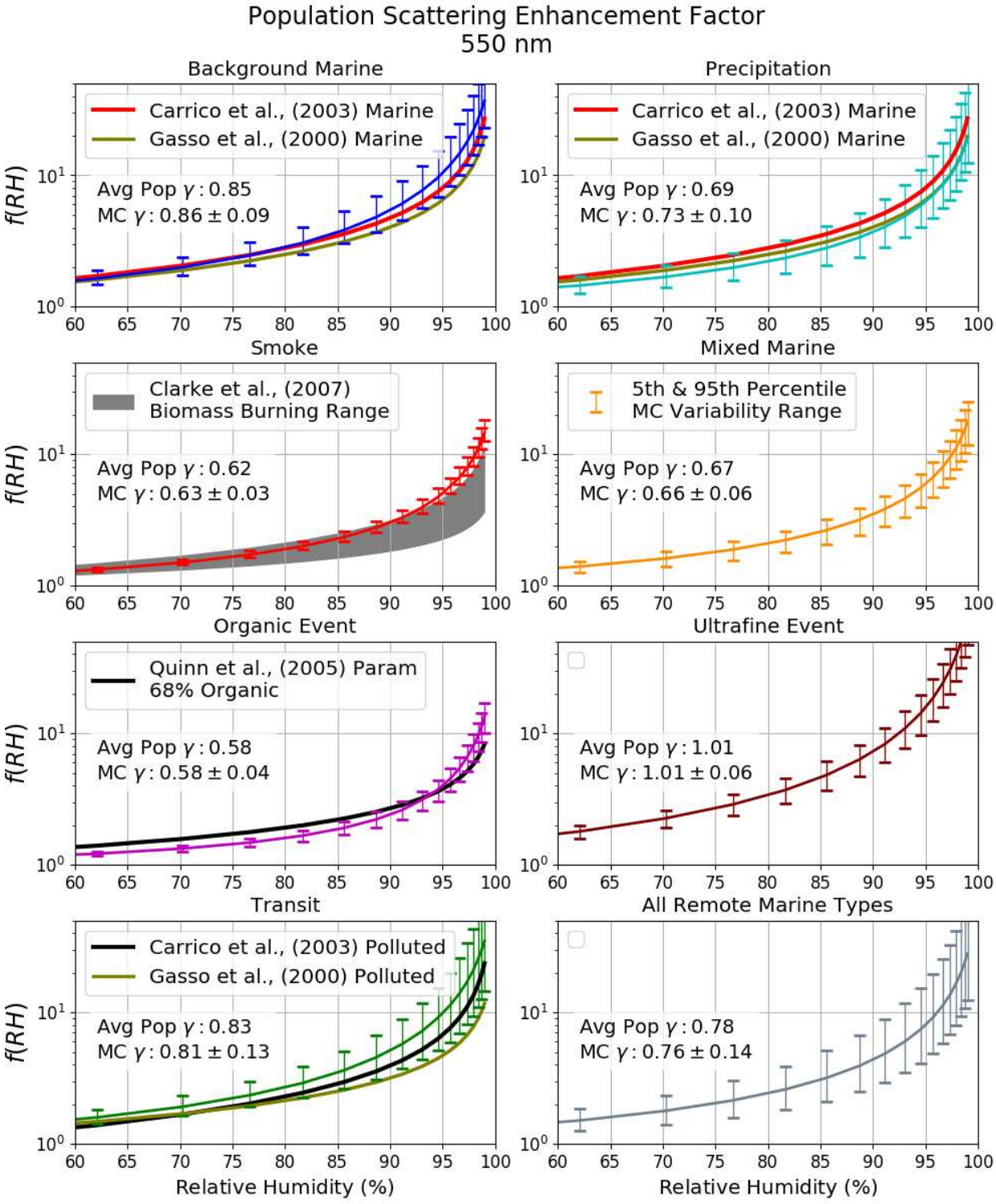

Figure 5.8 Humidograms of the scattering enhancement factor using a reference RH of 22% for average SCS remote marine population types. Error bars give the 5th and 95th percentile of the MC reconstruction based on intensive aerosol parameter variability. Best-fit γ parameters are shown for the average population, along with mean and standard deviation of best-fit γ for each of the MC runs. Enhancement factor curves for reported γ values from other studies are shown with most similar SCS population type.

may also be highlighting different components of what other studies classify as combined clean marine airmass types.

In both of these studies the polluted airmasses had lower scattering enhancement. Similarly, in the SCS, only the ultrafine event had higher scattering enhancement than the background marine curve. The γ parameter associated with inorganic pollution in the average population transit type was only slightly lower than for the average background marine type, though the transit MC range was somewhat lower than the background marine MC range. Other SCS types were also generally lower and would be consistent with lower scattering enhancement for most non-marine influences.

Clarke et al., (2007) reported a range of best-fit scattering γ parameters associated with biomass burning observations, shown as the grey range for the SCS Smoke population in Figure 5.8. The scattering enhancement for the SCS MC smoke range was generally consistent with Clarke et al. range at relevant RH values between 60% and 95%. The higher values for the SCS smoke at higher RH was due to higher hygroscopicity of smoke from sulfur-rich peat fires in Borneo and Sumatra during the SCS study.

The impact of organic matter on scattering enhancement in marine aerosol was parameterized by Quinn et al., (2005) using adjustments to the γ parameter based on the mass fraction of organics (F_o) in the aerosol, as $\gamma_{sca} = 0.9 - 0.6F_o$. Zhang et al., (2014) later validated that this effect was largely due to reduced hygroscopic growth of the aerosol in the generally lower hygroscopic organic aerosol. As the SCS organic event type was thought to possibly be a scenario of growth of background aerosol by condensation of organics, the difference in size parameters between the two types for populations of the same number concentration was used to estimate mass

concentration of organic matter in this aerosol population. Based on this calculation, organic matter was estimated to be 68% of the mass of the aerosol in this scenario, with an associated estimated γ_{sca} of 0.49. The resulting parameterized estimate was plotted in Figure 5.8 for the organic event population type and was somewhat lower than the best fit γ_{sca} of 0.58, though that may be in part due to the reconstruction not following the exponential model as well as some of the other types. Such small deviations from the simple exponential relationship of Eqn 5.2, have been noted in a number of studies and are consistent with observations (Kotchenruther and Hobbs, 1998; Carrico et al., 2003; Zhang et al., 2014).

Overall, organic and smoke impacted population types had generally lower scattering enhancement curves, consistent with reported findings. The noted organic enrichment and lower hygroscopicity of the precipitation type (as compared to the background marine type) appeared to have a similar effect, resulting in lower enhancement factors.

Reported variability in the best-fit γ parameter was limited. Gassó et al., (2000) reported γ variability of 0.69 ± 0.06 for clean marine aerosol and 0.57 ± 0.06 for polluted marine conditions in the Atlantic. Massoli et al., (2009) reported mean γ values of between 0.39 and 0.73 with standard deviations between 0.04 and 0.14 for a variety of polluted air mass types in the Gulf of Mexico. Standard deviations of the SCS MC runs varied between 0.03 and 0.13 for individual population types, and 0.14 for the combined remote marine type, which were consistent with these reports.

Scattering and extinction enhancement factors based on observed scattering at two RH values were more commonly reported in observational studies. Equivalent calculations for roughly analogous aerosol types from the SCS study were calculated where appropriate using the MC

reconstruction sets and are shown in Table 5.5. Study average factors for three cruises (at nearly equivalent 532 nm wavelength) reported by Zhang et al., (2014) had mean values for extinction enhancement between 2.91 and 3.22 with CVs between 0.13 and 0.27. These compared well with the equivalent reconstructed SCS mean of 3.12 and CV of 0.26. Specific aerosol type averages had a larger range of mean values reported in various studies. As humidograms found the SCS background marine and precipitation types spanned typical reported clean marine values, these two were combined for comparisons in Table 5.5. This combined SCS marine type showed general agreement with several cruises in more pristine regions (Carrico et al., 1998, 2003). Factors were generally lower in littoral regions or in studies with a larger amount of terrestrial influence. SCS types showed generally similar behavior with lower factors for many terrestrial influenced types.

Reported variability tended to range between CV values of approximately 0.05 and 0.20 for many distinct types. A similar range applied to SCS types, once again indicating generally consistent behavior. Overall, RH-dependent enhancement factors described in this study for various aerosol types were consistent with observations reported in the literature. In addition, the variability in these factors associated with changes to intensive aerosol parameters appeared to be reconstructed by the MC model in a way that was consistent with reported variability in observations.

Table 5.5 Submicron scattering and extinction enhancement factors reported for various studies. Equivalent factors for roughly equivalent population types from the SCS dataset are reported where appropriate. Coefficients of variation calculated from sample mean and standard deviation are listed.

Experiment	Location / Platform	Aerosol Type	$f(RH,Rh_{ref})$	mean	std dev	CV	SCS Equivalent Population Type	mean	std dev	CV	reference
ACE-1	Southern Ocean	Clean Marine	f_{sca}(82%,40%)	2.46	(0.20)	0.08	Back. Marine & Precip.	2.46	(0.40)	0.16	Carrico et al., (1998)
	Ship	Non-Clean Marine	f_{sca}(82%,40%)	2.36	(0.40)	0.17	Mixed Marine	2.01	(0.20)	0.10	
ACE-2	Sagres, Portugal	Clean Littoral	f_{sca}(82%,27%)	1.86	(0.24)	0.13	Back. Marine & Precip.	2.75	(0.52)	0.19	Carrico et al., (2000)
	Littoral	Polluted Littoral	f_{sca}(82%,27%)	1.48	(0.10)	0.07	Transit	2.80	(0.50)	0.18	
ACE-Asia	NW Pacific	Marine	f_{sca}(82%,19%)	2.95	(0.39)	0.13	Back. Marine & Precip.	2.92	(0.59)	0.20	Carrico et al., (2003)
	Ship	Polluted Marine	f_{sca}(82%,19%)	2.52	(0.27)	0.11	Transit	2.98	(0.57)	0.19	
		Marine	f_{sca}(Ambient,19%)	2.39	(0.93)	0.39	Back. Marine	2.60	(1.17)	0.45	
		Polluted Marine	f_{sca}(Ambient,19%)	1.98	(0.81)	0.41	Transit	2.86	(1.32)	0.46	
ACE-Asia	NW Pacific / Ship	Ship, all data	f_{sca}(85%,40%)	2.68	(0.25)	0.09	All Remote Marine[2]	2.73	(0.64)	0.23	Doherty et al., (2005)
		Coarse Mode Dominated	f_{sca}(85%,40%)	2.26	(0.40)	0.18	Back. Marine[2]	3.21	(0.45)	0.14	
		Coarse/Fine Mix	f_{sca}(85%,40%)	2.71	(0.21)	0.08	Precipitation[2]	2.59	(0.43)	0.17	
		Fine Mode Dominated	f_{sca}(85%,40%)	2.74	(0.19)	0.07	Smoke[2]	2.11	(0.09)	0.04	
	Gosan, Korea	Littoral, all data	f_{sca}(85%,40%)	2.36	(0.50)	0.21	Mixed Marine[2]	2.29	(0.25)	0.11	
		Coarse Mode Dominated	f_{sca}(85%,40%)	2.18	(0.23)	0.11	Organic Event[2]	1.75	(0.11)	0.06	
		Coarse/Fine Mix	f_{sca}(85%,40%)	2.30	(0.40)	0.17	Ultrafine Event[2]	3.80	(0.43)	0.11	
		Fine Mode Dominated	f_{sca}(85%,40%)	2.77	(0.76)	0.27	Transit[2]	2.96	(0.54)	0.18	
	Aircract	All data	f_{sca}(85%,40%)	1.97	(0.23)	0.12	Back. Marine & Precip.[2]	2.90	(0.54)	0.19	
		Dust Impacted	f_{sca}(85%,40%)	2.00	(0.23)	0.12					
		Non-Dust Impacted	f_{sca}(85%,40%)	1.89	(0.21)	0.11					
NEAQS-ITCT	NW Atlantic	Local Marine	f_{sca}(82%,26%)	2.06	(0.19)	0.09	Back. Marine & Precip.	2.77	(0.53)	0.19	Wang et al., (2007)
	Ship	Regional Cont. Influence	f_{sca}(82%,26%)	1.84	(0.11)	0.06	Transit	2.83	(0.50)	0.18	
		Distant Continental Infl.	f_{sca}(82%,26%)	1.53	(0.31)	0.20					
		Forest Fire Case Study	f_{sca}(82%,26%)	1.40	(0.13)	0.09	Smoke	2.00	(0.08)	0.04	
		Local Harbor Case Study	f_{sca}(82%,26%)	1.52	(0.14)	0.09					
		Regional Plume 1	f_{sca}(82%,26%)	1.83	(0.08)	0.04	Organic Event	1.65	(0.09)	0.05	
		Regional Plume 2	f_{sca}(82%,26%)	2.12	(0.18)	0.08	Ultrafine Event	3.61	(0.43)	0.12	
		Distant Plume 1	f_{sca}(82%,26%)	1.92	(0.39)	0.20					
		Distant Plume 2	f_{sca}(82%,26%)	1.75	(0.21)	0.12					
TexAQS[1]	Texas Gulf Coast	Study Average	f_{ext}(85%,25%)	3.22	(0.88)	0.27	All Remote Marine	3.12	(0.81)	0.26	Zhang et al., (2014)
ICEALOT[1]	Remote Artic	Study Average	f_{ext}(85%,25%)	3.00	(0.38)	0.13					
CalNex[1]	California Coast	Study Average	f_{ext}(85%,25%)	2.91	(0.66)	0.23					

[1] Extinction Enhancement factor at 532 nm via three ship based studies

[2] No direct SCS equivalent determined; Equivalent f(RH) shown for all SCS population types

5.5.4. *Bodega Bay Optical Properties*

In addition to reported values of optical properties, the SCS reconstructions were compared against marine populations identified using a similar clustering methodology from the Bodega Bay (BB) dataset of Chapter 3. While this dataset was not a remote marine location, it did experience several periods of impacts from marine aerosol, allowing for comparison of remote marine aerosol against marine types observed in a littoral location and classified using a similar methodology. Dry mass extinction efficiencies are shown in Figure 5.9 for population types from both datasets that were predominately associated with aerosol from marine sources (left) and for all other types identified by the clustering methodology (right). The 5th and 95th percentile range of dry MEE values associated with all SCS remote marine types is also shown in both figures for comparison.

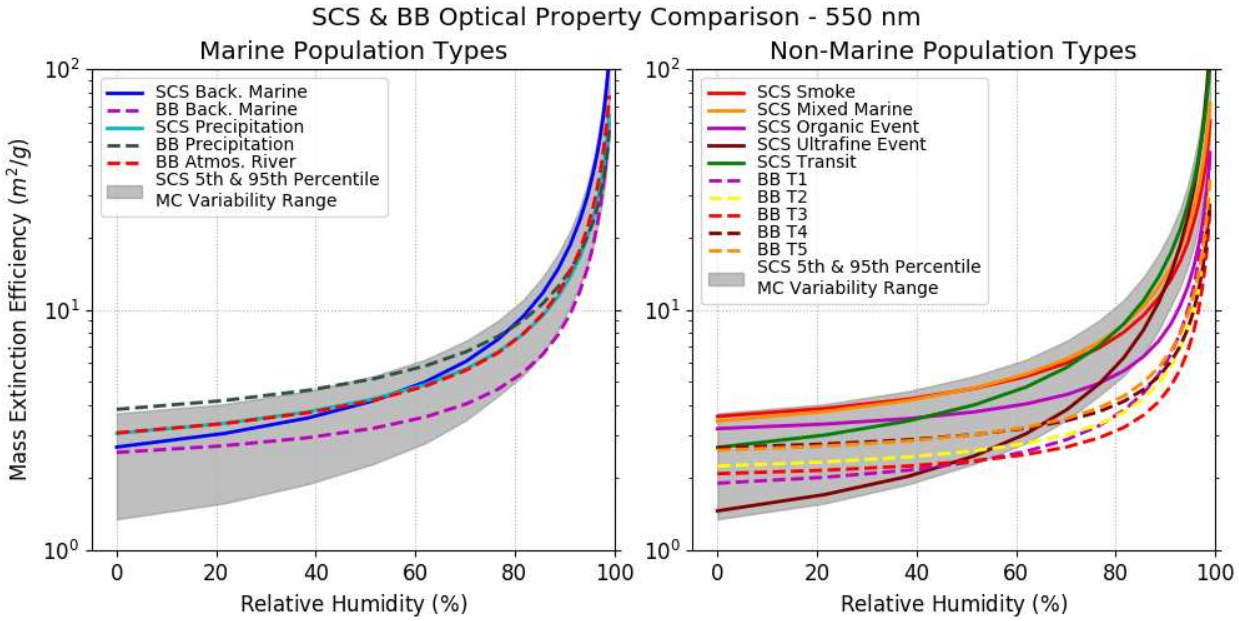

Figure 5.9 Dry mass extinction efficiency comparison for the SCS (solid lines) and Bodega Bay (dashed lines) datasets. Marine population types (left) and non-marine population types (right) are shown for average populations as classified by the clustering methodology. The SCS range of MC results for all population types are shown in grey in both figures.

Marine population types were generally consistent between both datasets, with the background populations having somewhat lower MEE at dry RH values as compared to types with more recent precipitation impacts. In the BB background marine type, hygroscopicities were generally lower, leading to less hygroscopic growth and lower associated extinction at higher relative humidities. This type was thought to be a largely marine sourced aerosol with some small amount of mixing with organic aerosol, potentially through sea-breeze resampling of terrestrial airmasses. The SCS organic event was similarly thought to be a marine aerosol with some organic mixing leading to decreased hygroscopicities. This resulted in similar $MEE_d(RH)$ curves for these two cases, with lower scattering enhancement at higher RH values as compared to the marine types with higher hygroscopicities. Similarly, higher hygroscopicities in the nominally non-marine types in the SCS lead to higher mass extinction efficiencies, with values near those of the marine types from both datasets.

Conversely, the relatively fresh, terrestrial organic aerosol types with low hygroscopicities in the BB dataset had lower hygroscopic growth and associated extinction efficiency with increasing RH. At the range of RH values relevant to marine regions this difference between low-hygroscopicity, organic terrestrial types, and other types (both marine and SCS non-marine) was in fact the largest difference in intensive optical properties between any of the population types.

At 80% RH, marine types from both datasets as well as SCS non-marine types in a remote marine location had $MEE_d(80\%)$ values between approximately 5 and 10 m^2/g. This was contrasted with the BB terrestrial types that had values between approximately 3 and 4.5 m^2/g, roughly a factor of two difference. This difference served to highlight the importance of hygroscopicity in fine mode aerosol types for intensive optical sensitivity in high RH environments typical of marine regions. However, in order to estimate the actual intensive

optical sensitivity to population type an MC analysis similar to the SCS case D was conducted for the BB dataset. The resulting CV was 0.29 for the sensitivity of $MEE_d(80\%)$ to changes in population types based on observed frequencies. While this was approximately 2.5 times higher than the equivalent SCS CV of 0.12, it was nevertheless still on the same order as natural variability due to intensive aerosol parameters and RH in the SCS.

Overall, in the Bodega Bay dataset a general distinction was noted between higher hygroscopic marine population types and organic dominated terrestrial population types with lower hygroscopicities. These intensive differences between aerosol population types were associated with considerably higher optical sensitivity than in the SCS remote marine location but were nevertheless on the same order as natural variability in the SCS. As a result, the general conclusion that information about aerosol type in remote marine regions was relatively unimportant for intensive optical sensitivity appeared to be robust even when tested in this littoral environment.

5.6. OPTICAL PROPERTY SENSITIVITY TO AEROSOL PARAMETERS

Assessment of the sensitivity of optical properties to changes in four controlling categories of environmental and fine mode aerosol parameters yielded several noteworthy conclusions. As expected, extensive optical parameters—including extinction coefficient and by extension related column integrated values such as AOD—showed the highest sensitivity to total dry aerosol mass concentration at visible wavelengths. This extensive parameter of the aerosol is commonly used in models and retrievals to relate aerosol to optical properties. However, the question remains as to what utility, if any, improved representation of intensive properties of the aerosol would yield to such use cases.

Optical reconstruction modeling using the SCS dataset provided a mechanism to test optical sensitivity based on quantifiable observed variability of these controlling factors. The results indicated that natural variability in a nominally consistent aerosol population would lead to changes in optical properties on the same order or greater than would be expected due to differences between aerosol models associated with different population types or sources. This natural variability was due to fluctuations in aerosol size distribution and hygroscopicity, dry aerosol mass concentration, and environmental relative humidity. Distinct aerosol population type models may therefore be of limited use for improving optical models of remote marine regions.

Additionally, while optical sensitivity fluctuated considerably with changes to total fine mode dry aerosol mass concentration, sensitivity due to the intensive component of natural variability from aerosol parameters and RH was relatively consistent. The combined effect of these parameters on optical property sensitivity or uncertainty could be quantified with coefficients of variation on the order of 0.3—a value that was relatively constant and independent of total mass concentration, aerosol population type, or magnitude of RH.

6. CONCLUSIONS

In this dissertation, I presented the results of aerosol and environmental measurements from several field campaigns designed to study various aspects of marine aerosol relevant to microphysical interactions with cloud and climate systems. The analyses focused on classification of measurements into population type models associated with various aerosol sources, and quantification of the observed variability in aerosol and environmental properties associated with these types. The observationally driven results were then used in several modeling studies to investigate circumstances where complex aerosol models that include detailed information about particle intensive properties and internal variability were useful for exploring aerosol-cloud-climate interactions, and where simpler models based primarily on extensive total particle number concentration or mass were sufficient.

Key findings of this work are addressed here in relation to the scientific questions and goals stated in the introduction.

1. *Unsupervised classification methods to quantify internal and external variability among aerosol population types*

An unsupervised K-Means classification methodology was applied to in situ measurements of aerosol properties during the 7SEAS experiment through the remote marine SCS. The result was a set of time periods associated with impacts from specific aerosol types or sources that did not require supervised or subjective classifications of the observations into time periods associated with specific types. A similar methodology was utilized during the littoral CalWater-2015 study that included several meteorological parameters in addition to measurements of relevant aerosol

properties for the classification of aerosol population type. The additional variables allowed for further refinements in the classification methodology that included transport pathway to help differentiate between sources from terrestrial and marine regions.

In both cases classified population types included background marine and precipitation impacted aerosol along with periodic impacts by terrestrial emissions. Identified shifts between population types occurred at time-scales ranging from multiple-day events to short-term changes on the order of minutes. Physical processes including wind-shifts, gust front passage, or changing emissions from source areas could often be associated with such shifts between types, confirming the methodology is able to successfully classify air masses associated with impacts from distinct aerosol types and sources.

Based on these classifications, variability in aerosol and environmental properties was quantified both in terms of external variability (e.g. differences between average values for population types) and internal variability (e.g. standard deviation of properties within time periods associated with a single type). This distinction in variability was later used to drive an optical reconstruction model that differentiated between internal variability in various aerosol optical parameters and external variability between the various population types. The results were compared against reported values of optical properties in various other studies of marine aerosol. Internal variability within the reconstructed SCS aerosol models was consistent with the range of reported values, as were population averages for both intensive and extensive optical properties reported for impacts from similar sources as those identified in the SCS dataset. Additionally, reconstructed aerosol optical properties were consistent with coincident direct measurements of optical properties. As a result, the quantified variability for the aerosol population models was

consistent with expectations and other reported values for similar circumstances, and was therefore considered sufficient for use in assessing aerosol variability impacts.

2. Consistency in marine aerosol models between various observational datasets

Given that the unsupervised classifications for both observed datasets reported in this work identified distinct population types associated with marine and precipitation impacted air masses, these aerosol models were compared against each other to determine how consistent they were with each other as well as other reported marine aerosol models. A total of five aerosol models generated for the SCS and BB datasets were associated with either marine background or precipitation impacted marine aerosol air masses, with the rest of the models associated with impacts from terrestrial outflow or organic aerosol. Size distribution and hygroscopicity results for the marine types were consistent with typical reports of marine aerosol consisting of a mixture of sea salt and organic components (e.g. Clarke et al., 2006; Keene et al., 2007; O'Dowd and Leeuw, 2007; Prather et al., 2013; Quinn et al., 2014), including bimodal size distributions and κ values in the ~0.3–0.65 range across the various modes.

Microphysical implications of variability between the models was more directly comparable using the CCN activated fraction spectra across the range of environmentally relevant supersaturations. In this case, the background marine population types identified had somewhat higher activated fractions than the precipitation impacted types in both datasets. Variability as compared by inner quartile ranges was generally comparable between datasets and was consistent with typical reports of variability in other studies. In addition, there was some indication that aerosol properties reported in other studies of marine regions for generally clean marine air masses were somewhat between the values for the background marine and

precipitation type models generated from the unsupervised clustering methodology. The methods used in this work may therefore be identifying an additional distinction in population type between background marine conditions and precipitation scrubbing in the SCS and BB datasets that has otherwise not been made in some other studies of marine aerosol. Finally, the results of the two marine datasets presented here indicated a general consistency in identified CCN spectra associated with marine aerosol models not impacted by terrestrial outflow or impacts from other sources.

3. *The effectiveness of population type models in restricting the parameter-space of microphysical aerosol impacts to atmospherically relevant values*

Studies of microphysical sensitivity to aerosol intensive properties including size distribution, hygroscopicity, and mixing state, among others, often investigate wider ranges in these properties than would be expected to occur in actual remote marine aerosol populations. In addition, many of the intensive parameters of an aerosol population would not be expected to vary completely independently of one another. The aerosol population models generated from the observationally based studies included values for relevant aerosol intensive parameters associated with identified aerosol types. As such, they allowed us to constrain some of the parameter-space associated with variability in aerosol intensive properties to more atmospherically relevant conditions.

Microphysical impacts of the aerosol were then investigated in terms of their influences on several key initial cloud properties through use of a cloud parcel model. Relative sensitivities of initial cloud droplet number concentration and cloud droplet relative dispersion at peak parcel supersaturation were estimated as a function of updraft velocity, total aerosol number

concentration, and aerosol population type. The maximum observed difference in aerosol intensive properties in the dataset (from a microphysical perspective using the population type CCN spectra) was then able to be more directly compared against extensive properties of the aerosol and environment. This representation of microphysical sensitivity to population type rather than individual aerosol properties may also be more relevant to certain types of modeling studies that track and select from specific aerosol types when representing aerosol impacts in the model.

Previous work by Reutter et al., (2009) on initial cloud droplet number concentration sensitivity to aerosol properties had identified two distinct regimes: an aerosol-limited regime encountered in conditions of generally low particle number concentrations and high updraft velocities where changes in number count directly related to changes in CDNC, and an updraft-limited regime at high particle number concentrations and low updraft velocities where updraft velocity was the primary factor affecting CDNC. Between these regimes was a transitional regime dependent on both parameters. As a result of this representation of aerosol population type as a distinct sensitivity parameter, along with the inclusion of multi-modal aerosol models that are more representative of a marine environment, a modification to this generally simplistic regime categorization was identified. The aerosol-limited regime, wherein sensitivity to total aerosol number concentration was the only factor affecting CDNC, was encountered only in conditions where nearly all particles activated. The updraft-limited regime was characterized by additional sensitivity to both population type and number concentration, with updraft velocity emerging as the parameter with highest relative sensitivity, but not the only significant factor. In between these two regimes a new population-type sensitivity regime was identified that included sensitivity to all three parameters.

The cloud droplet relative dispersion parameter has been categorized into similar regime dependent behaviors by Chen et al., (2016). At maximum parcel supersaturation a change to either particle number count or updraft velocity was found to flip the direction of change in the droplet relative dispersion between the aerosol- and updraft-limited regimes. In this study a change in population type did not change this behavior. However, changing population type did affect the overall magnitude of droplet relative dispersion, with somewhat more relative sensitivity to the largest change in population type in the SCS dataset than either total number concentration or updraft velocity throughout much of the CN-*w* parameter-space.

4. The role of intensive and extensive properties of the aerosol in atmospheric optical properties and the relationship to aerosol population type

Optical properties in remote marine environments change as various aerosol plumes, associated with both marine generated aerosol and long-range transport, advect through these regions. However, some of the variability in optical properties in the atmosphere is associated with impacts from within nominally consistent aerosol population types. Difficulties in describing "typical" optical conditions in marine regions are therefore not just a function of changing aerosol type but from internal variability in aerosol and environmental conditions.

Using the SCS aerosol models, Monte Carlo reconstructions of optical properties were generated using observed variability in the aerosol properties and RH associated with each population type. Various combinations of properties were varied within these reconstructions to estimate internal variability associated with intensive aerosol properties, extensive aerosol properties, and extensive environmental RH for each population type. These were then compared against external optical variability associated with changes to aerosol population type. Importantly, when

intensive properties of the aerosol were allowed to vary within the reconstructions, estimates of internal variability within the various population types were generally of the same order as external variability between different population types. As a result, information regarding the specific type of aerosol impacting the SCS observations would not be expected to lead to considerable improvements in estimates of intensive optical properties, as natural variability in observations would limit the range of any such improvements. Instead, knowledge of the total aerosol mass, independent of type, provided the most utility for prediction of extensive optical properties in the SCS. This was consistent with expectations for a marine region, but also serves to explain why detailed information on aerosol intensive properties or type has proven somewhat unnecessary in some remote sensing efforts such as those from MODIS aerosol retrievals (Remer et al., 2006; Levy et al., 2013).

5. The utility of quantifying variability in aerosol models of remote marine regions

A final set of scientific questions to address was the hypothesis that quantifying observed variability in studies of remote marine aerosol population types would allow for improved understanding of the role of various key aerosol and environmental parameters on subsequent impacts on cloud microphysics and radiative transfer in the atmosphere. The full spectrum of aerosol impacts on these processes is highly complex and the subject of numerous lines of study. Here, we addressed the role of observed aerosol variability in the remote marine SCS on optical properties and initial cloud properties.

The optical reconstructions indicated that while variations in dry aerosol mass concentrations resulted in considerable variability in optical properties, the impact of both intensive aerosol properties and environmental RH was relatively consistent across a variety of conditions in the

SCS dataset. Optical property sensitivity to observed variability in each of these parameter categories resulted in coefficients of variation on the order of 0.2, and a combined value of 0.3 when both categories were allowed to vary. Microphysical implications of the largest differences in aerosol intensive properties observed in the SCS dataset on cloud development pointed towards a regime of population type sensitivity for initial cloud droplet number concentrations. This regime included conditions spanning particle number concentrations associated with various population types in the SCS, and updraft velocities relevant to formation of fogs and stratocumulus cloud layers as well as deeper convective regimes such as those associated with tropical cumulus congestus clouds. The use of unsupervised classification methods to create SCS aerosol models that included quantification of observed variability therefore did provide useful information on aerosol-cloud-climate interactions in remote marine regions.

6.1. FUTURE WORK

As the aerosol-cloud-climate relationships discussed in this work are highly complex, future work using the representations of internal and external variability in these aerosol models may provide additional insights. Several specific areas of potential future work are addressed here.

1. Giant CCN impacts on microphysical development

Giant CCN larger than several microns in diameter, such as those generated by sea spray in higher wind conditions, have been found to impact cloud development, initial droplet size distributions, and potentially parcel model results in some circumstances (e.g. Feingold et al., 1999). An additional mode could be added to the models used in the cloud parcel studies to incorporate giant CCN. The sensitivity of both initial cloud droplet number concentration and relative dispersion at peak supersaturation, and the resulting shape and magnitude of the

sensitivity regimes, could be examined for the impact of giant CCN in marine regions for the different underlying aerosol population types. This would provide further information about the impact of aerosol on initial cloud properties and could potentially improve efforts to incorporate additional meteorological parameters such as wind speed (and the resulting estimates of coarse mode or giant CCN) into predictions or estimates of cloud properties in marine regions.

2. Observed aerosol models for use in cloud dynamics models

In tropical marine clouds, sensitivity to aerosol concentration has been identified as an important factor affecting various processes including convective invigoration, precipitation, and indirect effects on climate (e.g. Khain et al., 2008; Xue et al., 2008; Storer and van den Heever, 2012; Andersen and Cermak, 2015; Sheffield et al., 2015). As this work identified initial cloud property sensitivity to population type to be of the same magnitude as number concentration in some conditions, testing the impact of different aerosol models (i.e. different aerosol intensive parameters) based on these observed types might provide additional insight into cloud development in marine environments.

3. CCN closure in precipitation and background marine population types

In both the SCS and BB datasets CCN closure efforts found greater overprediction for precipitation impacted aerosol types than for some of the other types. Overprediction (relative to direct measurements) of reconstructed CCN using aerosol size and hygroscopicity parameters has been reported in a number of other CCN closure studies (e.g. McFiggans et al., 2006; Kammermann et al., 2010). Various factors have been suggested as the cause of such discrepancies, but the errors (most often overprediction) are most often seen for smaller particle sizes. The precipitation impacted population types in this work typically had larger Aitken modes

as compared to the background marine types. Organic enrichment of smaller marine generated sea salt particles has been shown in many marine environments (Quinn et al., 2014), which would suggest lower hygroscopicity values in the smallest particles in these population types. Measurements of κ by size-resolved CCN systems are most indicative of hygroscopicity for the particles around the D_{50} activation diameter for the supersaturation at which it is set. For modal or population average hygroscopicity values, the effect of decreasing κ values at smaller sizes may therefore be missed. In the precipitation types with a higher fraction of smaller particles this effect could become magnified. Future measurements of marine CCN could examine the distribution of hygroscopicity values further, especially at the smallest sizes. Closure models could also add additional complexity to their representations of particle hygroscopicity. Decreasing κ values with size to match expected organic enrichment may change closure estimates and could explain some of the noted overprediction in the precipitation types as compared to other population types in the SCS and BB results. However, in the case that resolved discrepancies between predicted and observed values result in relatively small changes to CCN spectra, this work may indicate that such CCN closure issues may not be especially important.

REFERENCES

Ackerman, A. S., Toon, O. B. and Hobbs, P. V.: Dissipation of Marine Stratiform Clouds and Collapse of the Marine Boundary Layer Due to the Depletion of Cloud Condensation Nuclei by Clouds, Science, 262(5131), 226–229, doi:10.1126/science.262.5131.226, 1993.

Akagi, S. K., Yokelson, R. J., Wiedinmyer, C., Alvarado, M. J., Reid, J. S., Karl, T., Crounse, J. D. and Wennberg, P. O.: Emission factors for open and domestic biomass burning for use in atmospheric models, Atmos Chem Phys, 11(9), 4039–4072, doi:10.5194/acp-11-4039-2011, 2011.

Albrecht, B. A.: Aerosols, Cloud Microphysics, and Fractional Cloudiness, Science, 245(4923), 1227–1230, doi:10.1126/science.245.4923.1227, 1989.

Allan, J. D., Topping, D. O., Good, N., Irwin, M., Flynn, M., Williams, P. I., Coe, H., Baker, A. R., Martino, M., Niedermeier, N., Wiedensohler, A., Lehmann, S., Müller, K., Herrmann, H. and McFiggans, G.: Composition and properties of atmospheric particles in the eastern Atlantic and impacts on gas phase uptake rates, Atmos Chem Phys, 9(23), 9299–9314, doi:10.5194/acp-9-9299-2009, 2009.

Andersen, H. and Cermak, J.: How thermodynamic environments control stratocumulus microphysics and interactions with aerosols, Environ. Res. Lett., 10(2), 024004, doi:10.1088/1748-9326/10/2/024004, 2015.

Anderson, T. L. and Ogren, J. A.: Determining Aerosol Radiative Properties Using the TSI 3563 Integrating Nephelometer, Aerosol Sci. Technol., 29(1), 57–69, doi:10.1080/02786829808965551, 1998.

Andreae, M. O. and Rosenfeld, D.: Aerosol–cloud–precipitation interactions. Part 1. The nature and sources of cloud-active aerosols, Earth-Sci. Rev., 89(1–2), 13–41, doi:10.1016/j.earscirev.2008.03.001, 2008.

Andreae, M. O., Rosenfeld, D., Artaxo, P., Costa, A. A., Frank, G. P., Longo, K. M. and Silva-Dias, M. a. F.: Smoking Rain Clouds over the Amazon, Science, 303(5662), 1337–1342, doi:10.1126/science.1092779, 2004.

Anttila, T.: Sensitivity of cloud droplet formation to the numerical treatment of the particle mixing state, J. Geophys. Res. Atmospheres, 115(D21), doi:10.1029/2010JD013995, 2010.

Atwood, S. A., Reid, J. S., Kreidenweis, S. M., Yu, L. E., Salinas, S. V., Chew, B. N. and Balasubramanian, R.: Analysis of source regions for smoke events in Singapore for the 2009 El Nino burning season, Atmos. Environ., 78, 219–230, doi:10.1016/j.atmosenv.2013.04.047, 2013.

Atwood, S. A., Reid, J. S., Kreidenweis, S. M., Blake, D. R., Jonsson, H. H., Lagrosas, N. D., Xian, P., Reid, E. A., Sessions, W. R. and Simpas, J. B.: Size-resolved aerosol and cloud condensation nuclei (CCN) properties in the remote marine South China Sea – Part 1:

Observations and source classification, Atmos Chem Phys, 17(2), 1105–1123, doi:10.5194/acp-17-1105-2017, 2017.

Atwood, S. A., Kreidenweis, S. M., DeMott, P. J., Petters, M. D., Cornwell, G. C., Martin, A. C. and Moore, K. A.: Classification of aerosol population type and cloud condensation nuclei properties in a coastal California littoral environment using an unsupervised cluster model, Atmospheric Chem. Phys., 19(10), 6931–6947, doi:https://doi.org/10.5194/acp-19-6931-2019, 2019.

Baarsch, J. and Celebi, M. E.: Investigation of internal validity measures for K-means clustering, in Proceedings of the International MultiConference of Engineers and Computer Scientists, vol. 1, pp. 14–16. [online] Available from: http://www.iaeng.org/publication/IMECS2012/IMECS2012_pp471-476.pdf (Accessed 19 November 2015), 2012.

Balasubramanian, R., Qian, W.-B., Decesari, S., Facchini, M. C. and Fuzzi, S.: Comprehensive characterization of PM2.5 aerosols in Singapore, J. Geophys. Res. Atmospheres, 108(D16), 4523, doi:10.1029/2002JD002517, 2003.

Bates, T. S., Quinn, P. K., Covert, D. S., Coffman, D. J., Johnson, J. E. and Wiedensohler, A.: Aerosol physical properties and processes in the lower marine boundary layer: a comparison of shipboard sub-micron data from ACE-1 and ACE-2, Tellus B, 52(2), 258–272, doi:10.1034/j.1600-0889.2000.00021.x, 2000.

Bates, T. S., Quinn, P. K., Coffman, D. J., Johnson, J. E. and Middlebrook, A. M.: Dominance of organic aerosols in the marine boundary layer over the Gulf of Maine during NEAQS 2002 and their role in aerosol light scattering, J. Geophys. Res. Atmospheres, 110(D18), D18202, doi:10.1029/2005JD005797, 2005.

Bates, T. S., Anderson, T. L., Baynard, T., Bond, T., Boucher, O., Carmichael, G., Clarke, A., Erlick, C., Guo, H., Horowitz, L., Howell, S., Kulkarni, S., Maring, H., McComiskey, A., Middlebrook, A., Noone, K., O'Dowd, C. D., Ogren, J., Penner, J., Quinn, P. K., Ravishankara, A. R., Savoie, D. L., Schwartz, S. E., Shinozuka, Y., Tang, Y., Weber, R. J. and Wu, Y.: Aerosol direct radiative effects over the northwest Atlantic, northwest Pacific, and North Indian Oceans: estimates based on in-situ chemical and optical measurements and chemical transport modeling, Atmos Chem Phys, 6(6), 1657–1732, doi:10.5194/acp-6-1657-2006, 2006.

Bates, T. S., Quinn, P. K., Frossard, A. A., Russell, L. M., Hakala, J., Petäjä, T., Kulmala, M., Covert, D. S., Cappa, C. D., Li, S.-M., Hayden, K. L., Nuaaman, I., McLaren, R., Massoli, P., Canagaratna, M. R., Onasch, T. B., Sueper, D., Worsnop, D. R. and Keene, W. C.: Measurements of ocean derived aerosol off the coast of California, J. Geophys. Res. Atmospheres, 117(D21), D00V15, doi:10.1029/2012JD017588, 2012.

Beddows, D. C. S., Dall'Osto, M. and Harrison, R. M.: Cluster Analysis of Rural, Urban, and Curbside Atmospheric Particle Size Data, Environ. Sci. Technol., 43(13), 4694–4700, doi:10.1021/es803121t, 2009.

Berg, L. K., Berkowitz, C. M., Barnard, J. C., Senum, G. and Springston, S. R.: Observations of the first aerosol indirect effect in shallow cumuli, Geophys. Res. Lett., 38(3), doi:10.1029/2010GL046047, 2011.

Bohren, C. F. and Huffman, D. R.: Absorption and scattering by a sphere, Absorpt. Scatt. Light Small Part., 82–129, 1983.

Bougiatioti, A., Fountoukis, C., Kalivitis, N., Pandis, S. N., Nenes, A. and Mihalopoulos, N.: Cloud condensation nuclei measurements in the marine boundary layer of the Eastern Mediterranean: CCN closure and droplet growth kinetics, Atmos Chem Phys, 9(18), 7053–7066, doi:10.5194/acp-9-7053-2009, 2009.

Brechtel, F. J., Kreidenweis, S. M. and Swan, H. B.: Air mass characteristics, aerosol particle number concentrations, and number size distributions at Macquarie Island during the First Aerosol Characterization Experiment (ACE 1), J. Geophys. Res. Atmospheres, 103(D13), 16351–16367, doi:10.1029/97JD03014, 1998.

Brown, P. N., Byrne, G. D. and Hindmarsh, A. C.: VODE: A variable-coefficient ODE solver, SIAM J. Sci. Stat. Comput., 10(5), 1038–1051, 1989.

Campbell, J. R., Reid, J. S., Westphal, D. L., Zhang, J., Tackett, J. L., Chew, B. N., Welton, E. J., Shimizu, A., Sugimoto, N., Aoki, K. and Winker, D. M.: Characterizing the vertical profile of aerosol particle extinction and linear depolarization over Southeast Asia and the Maritime Continent: The 2007–2009 view from CALIOP, Atmospheric Res., 122, 520–543, doi:10.1016/j.atmosres.2012.05.007, 2013.

Carrico, C. M., Rood, M. J. and Ogren, J. A.: Aerosol light scattering properties at Cape Grim, Tasmania, during the First Aerosol Characterization Experiment (ACE 1), J. Geophys. Res. Atmospheres, 103(D13), 16565–16574, doi:10.1029/98JD00685, 1998.

Carrico, C. M., Rood, M. J., Ogren, J. A., Neusüß, C., Wiedensohler, A. and Heintzenberg, J.: Aerosol Optical properties at Sagres, Portugal during ACE-2, Tellus B, 52(2), 694–715, doi:10.1034/j.1600-0889.2000.00049.x, 2000.

Carrico, C. M., Kus, P., Rood, M. J., Quinn, P. K. and Bates, T. S.: Mixtures of pollution, dust, sea salt, and volcanic aerosol during ACE-Asia: Radiative properties as a function of relative humidity, J. Geophys. Res. Atmospheres, 108(D23), 8650, doi:10.1029/2003JD003405, 2003.

Cavalli, F., Facchini, M. C., Decesari, S., Mircea, M., Emblico, L., Fuzzi, S., Ceburnis, D., Yoon, Y. J., O'Dowd, C. D., Putaud, J.-P. and Dell'Acqua, A.: Advances in characterization of size-resolved organic matter in marine aerosol over the North Atlantic, J. Geophys. Res. Atmospheres, 109(D24), D24215, doi:10.1029/2004JD005137, 2004.

Charlson, R. J., Schwartz, S. E., Hales, J. M., Cess, R. D., Coakley, J. A., Hansen, J. E. and Hofmann, D. J.: Climate Forcing by Anthropogenic Aerosols, Science, 255(5043), 423–430, doi:10.1126/science.255.5043.423, 1992.

Charron, A., Birmili, W. and Harrison, R. M.: Fingerprinting particle origins according to their size distribution at a UK rural site, J. Geophys. Res. Atmospheres, 113(D7), D07202, doi:10.1029/2007JD008562, 2008.

Chen, J.: Investigation and Parameterization of Aerosol-Cloud Interactions Using Cloud Parcel Model and Observations, Doctoral Dissertation, State University of New York at Stony Brook., 2018.

Chen, J., Liu, Y., Zhang, M. and Peng, Y.: New understanding and quantification of the regime dependence of aerosol-cloud interaction for studying aerosol indirect effects, Geophys. Res. Lett., 43(4), 2016GL067683, doi:10.1002/2016GL067683, 2016.

Chin, M., Ginoux, P., Kinne, S., Torres, O., Holben, B. N., Duncan, B. N., Martin, R. V., Logan, J. A., Higurashi, A. and Nakajima, T.: Tropospheric Aerosol Optical Thickness from the GOCART Model and Comparisons with Satellite and Sun Photometer Measurements, J. Atmospheric Sci., 59(3), 461–483, doi:10.1175/1520-0469(2002)059<0461:TAOTFT>2.0.CO;2, 2002.

Chin, M., Diehl, T., Dubovik, O., Eck, T. F., Holben, B. N., Sinyuk, A. and Streets, D. G.: Light absorption by pollution, dust, and biomass burning aerosols: a global model study and evaluation with AERONET measurements, Ann Geophys, 27(9), 3439–3464, doi:10.5194/angeo-27-3439-2009, 2009.

Ching, J., Riemer, N. and West, M.: Impacts of black carbon mixing state on black carbon nucleation scavenging: Insights from a particle-resolved model, J. Geophys. Res. Atmospheres, 117(D23), doi:10.1029/2012JD018269, 2012.

Chuang, P. Y.: Measurement of the timescale of hygroscopic growth for atmospheric aerosols, J. Geophys. Res. Atmospheres, 108(D9), doi:10.1029/2002JD002757, 2003.

Chuang, P. Y., Charlson, R. J. and Seinfeld, J. H.: Kinetic limitations on droplet formation in clouds, Nature, 390(6660), 594, doi:10.1038/37576, 1997.

Clarke, A., McNaughton, C., Kapustin, V., Shinozuka, Y., Howell, S., Dibb, J., Zhou, J., Anderson, B., Brekhovskikh, V., Turner, H. and Pinkerton, M.: Biomass burning and pollution aerosol over North America: Organic components and their influence on spectral optical properties and humidification response, J. Geophys. Res. Atmospheres, 112(D12), D12S18, doi:10.1029/2006JD007777, 2007.

Clarke, A. D., Howell, S., Quinn, P. K., Bates, T. S., Ogren, J. A., Andrews, E., Jefferson, A., Massling, A., Mayol-Bracero, O., Maring, H., Savoie, D. and Cass, G.: INDOEX aerosol: A comparison and summary of chemical, microphysical, and optical properties observed from land, ship, and aircraft, J. Geophys. Res. Atmospheres, 107(D19), 8033, doi:10.1029/2001JD000572, 2002.

Clarke, A. D., Owens, S. R. and Zhou, J.: An ultrafine sea-salt flux from breaking waves: Implications for cloud condensation nuclei in the remote marine atmosphere, J. Geophys. Res. Atmospheres, 111(D6), D06202, doi:10.1029/2005JD006565, 2006.

Clarke, A. D., Freitag, S., Simpson, R. M. C., Hudson, J. G., Howell, S. G., Brekhovskikh, V. L., Campos, T., Kapustin, V. N. and Zhou, J.: Free troposphere as a major source of CCN for the equatorial pacific boundary layer: long-range transport and teleconnections, Atmos Chem Phys, 13(15), 7511–7529, doi:10.5194/acp-13-7511-2013, 2013.

Cubison, M. J., Ervens, B., Feingold, G., Docherty, K. S., Ulbrich, I. M., Shields, L., Prather, K., Hering, S. and Jimenez, J. L.: The influence of chemical composition and mixing state of Los Angeles urban aerosol on CCN number and cloud properties, Atmospheric Chem. Phys., 8(18), 5649–5667, doi:https://doi.org/10.5194/acp-8-5649-2008, 2008.

Davidovits, P., Worsnop, D. R., Jayne, J. T., Kolb, C. E., Winkler, P., Vrtala, A., Wagner, P. E., Kulmala, M., Lehtinen, K. E. J., Vesala, T. and Mozurkewich, M.: Mass accommodation coefficient of water vapor on liquid water, Geophys. Res. Lett., 31(22), doi:10.1029/2004GL020835, 2004.

Dettinger, M. D., Ralph, F. M., Das, T., Neiman, P. J., Cayan, D. R., Dettinger, M. D., Ralph, F. M., Das, T., Neiman, P. J. and Cayan, D. R.: Atmospheric Rivers, Floods and the Water Resources of California, Water, 3(2), 445–478, doi:10.3390/w3020445, 2011.

DeWitt, L. H., Coffman, D. J., Schulz, K. J., Alan Brewer, W., Bates, T. S. and Quinn, P. K.: Atmospheric aerosol properties over the equatorial Indian Ocean and the impact of the Madden-Julian Oscillation, J. Geophys. Res. Atmospheres, 118(11), 5736–5749, doi:10.1002/jgrd.50419, 2013.

Doherty, S. J., Quinn, P. K., Jefferson, A., Carrico, C. M., Anderson, T. L. and Hegg, D.: A comparison and summary of aerosol optical properties as observed in situ from aircraft, ship, and land during ACE-Asia, J. Geophys. Res. Atmospheres, 110(D4), D04201, doi:10.1029/2004JD004964, 2005.

Draxler, R. R. and Hess, G. D.: Description of the HYSPLIT4 modeling system, [online] Available from: http://warn.arl.noaa.gov/documents/reports/arl-224.pdf (Accessed 14 April 2015), 1997.

Draxler, R. R. and Hess, G. D.: An overview of the HYSPLIT_4 modelling system for trajectories, Aust. Meteorol. Mag., 47(4), 295–308, 1998.

Draxler, R. R., Stunder, B., Rolph, G. and Taylor, A.: HYSPLIT4 user's guide, NOAA Tech. Memo. ERL ARL, 230, 35, 1999.

Dubovik, O. and King, M. D.: A flexible inversion algorithm for retrieval of aerosol optical properties from Sun and sky radiance measurements, J. Geophys. Res. Atmospheres, 105(D16), 20673–20696, doi:10.1029/2000JD900282, 2000.

Dubovik, O., Holben, B., Eck, T. F., Smirnov, A., Kaufman, Y. J., King, M. D., Tanré, D. and Slutsker, I.: Variability of Absorption and Optical Properties of Key Aerosol Types Observed in Worldwide Locations, J. Atmospheric Sci., 59(3), 590–608, doi:10.1175/1520-0469(2002)059<0590:VOAAOP>2.0.CO;2, 2002.

Dusek, U., Frank, G. P., Hildebrandt, L., Curtius, J., Schneider, J., Walter, S., Chand, D., Drewnick, F., Hings, S., Jung, D., Borrmann, S. and Andreae, M. O.: Size Matters More Than Chemistry for Cloud-Nucleating Ability of Aerosol Particles, Science, 312(5778), 1375–1378, doi:10.1126/science.1125261, 2006.

Eidhammer, T., DeMott, P. J. and Kreidenweis, S. M.: A comparison of heterogeneous ice nucleation parameterizations using a parcel model framework, J. Geophys. Res. Atmospheres, 114(D6), doi:10.1029/2008JD011095, 2009.

Engelhart, G. J., Hennigan, C. J., Miracolo, M. A., Robinson, A. L. and Pandis, S. N.: Cloud condensation nuclei activity of fresh primary and aged biomass burning aerosol, Atmos Chem Phys, 12(15), 7285–7293, doi:10.5194/acp-12-7285-2012, 2012.

Ervens, B., Feingold, G. and Kreidenweis, S. M.: Influence of water-soluble organic carbon on cloud drop number concentration, J. Geophys. Res. Atmospheres, 110(D18), doi:10.1029/2004JD005634, 2005.

Fan, J., Wang, Y., Rosenfeld, D. and Liu, X.: Review of Aerosol–Cloud Interactions: Mechanisms, Significance, and Challenges, J. Atmospheric Sci., 73(11), 4221–4252, doi:10.1175/JAS-D-16-0037.1, 2016.

Feingold, G.: Modeling of the first indirect effect: Analysis of measurement requirements, Geophys. Res. Lett., 30(19), 1997, doi:10.1029/2003GL017967, 2003.

Feingold, G. and Chuang, P. Y.: Analysis of the Influence of Film-Forming Compounds on Droplet Growth: Implications for Cloud Microphysical Processes and Climate, J. Atmospheric Sci., 59(12), 2006–2018, doi:10.1175/1520-0469(2002)059<2006:AOTIOF>2.0.CO;2, 2002.

Feingold, G. and Heymsfield, A. J.: Parameterizations of Condensational Growth of Droplets for Use in General Circulation Models, J. Atmospheric Sci., 49(23), 2325–2342, doi:10.1175/1520-0469(1992)049<2325:POCGOD>2.0.CO;2, 1992.

Feingold, G., Cotton, W. R., Kreidenweis, S. M. and Davis, J. T.: The Impact of Giant Cloud Condensation Nuclei on Drizzle Formation in Stratocumulus: Implications for Cloud Radiative Properties, J. Atmospheric Sci., 56(24), 4100–4117, doi:10.1175/1520-0469(1999)056<4100:TIOGCC>2.0.CO;2, 1999.

Feingold, G., Eberhard, W. L., Veron, D. E. and Previdi, M.: First measurements of the Twomey indirect effect using ground-based remote sensors, Geophys. Res. Lett., 30(6), doi:10.1029/2002GL016633, 2003.

Feng, N. and Christopher, S. A.: Satellite and surface-based remote sensing of Southeast Asian aerosols and their radiative effects, Atmospheric Res., 122, 544–554, doi:10.1016/j.atmosres.2012.02.018, 2013.

Finlayson-Pitts, B. J. and Pitts, J. N.: Chemistry of the Upper and Lower Atmosphere: Theory, Experiments, and Applications, Elsevier., 1999.

Forestieri, S. D., Cornwell, G. C., Helgestad, T. M., Moore, K. A., Lee, C., Novak, G. A., Sultana, C. M., Wang, X., Bertram, T. H., Prather, K. A. and Cappa, C. D.: Linking variations in sea spray aerosol particle hygroscopicity to composition during two microcosm experiments, Atmos Chem Phys, 16(14), 9003–9018, doi:10.5194/acp-16-9003-2016, 2016.

Fountoukis, C. and Nenes, A.: Continued development of a cloud droplet formation parameterization for global climate models, J. Geophys. Res. Atmospheres, 110(D11), doi:10.1029/2004JD005591, 2005.

Freud, E. and Rosenfeld, D.: Linear relation between convective cloud drop number concentration and depth for rain initiation, J. Geophys. Res. Atmospheres, 117(D2), doi:10.1029/2011JD016457, 2012.

Freud, E., Rosenfeld, D. and Kulkarni, J. R.: Resolving both entrainment-mixing and number of activated CCN in deep convective clouds, Atmospheric Chem. Phys., 11(24), 12887–12900, doi:https://doi.org/10.5194/acp-11-12887-2011, 2011.

Frossard, A. A., Russell, L. M., Burrows, S. M., Elliott, S. M., Bates, T. S. and Quinn, P. K.: Sources and composition of submicron organic mass in marine aerosol particles, J. Geophys. Res. Atmospheres, 119(22), 2014JD021913, doi:10.1002/2014JD021913, 2014.

Gassó, S., Hegg, D. A., Covert, D. S., Collins, D., Noone, K. J., Öström, E., Schmid, B., Russell, P. B., Livingston, J. M., Durkee, P. A. and Jonsson, H.: Influence of humidity on the aerosol scattering coefficient and its effect on the upwelling radiance during ACE-2, Tellus B, 52(2), 546–567, doi:10.1034/j.1600-0889.2000.00055.x, 2000.

Ghan, S. J., Abdul-Razzak, H., Nenes, A., Ming, Y., Liu, X., Ovchinnikov, M., Shipway, B., Meskhidze, N., Xu, J. and Shi, X.: Droplet nucleation: Physically-based parameterizations and comparative evaluation, J. Adv. Model. Earth Syst., 3(4), doi:10.1029/2011MS000074, 2011.

Ghan, S. J., Liu, X., Easter, R. C., Zaveri, R., Rasch, P. J., Yoon, J.-H. and Eaton, B.: Toward a Minimal Representation of Aerosols in Climate Models: Comparative Decomposition of Aerosol Direct, Semidirect, and Indirect Radiative Forcing, J. Clim., 25(19), 6461–6476, doi:10.1175/JCLI-D-11-00650.1, 2012.

Giglio, L., Descloitres, J., Justice, C. O. and Kaufman, Y. J.: An Enhanced Contextual Fire Detection Algorithm for MODIS, Remote Sens. Environ., 87(2–3), 273–282, doi:10.1016/S0034-4257(03)00184-6, 2003.

Good, N., Topping, D. O., Allan, J. D., Flynn, M., Fuentes, E., Irwin, M., Williams, P. I., Coe, H. and McFiggans, G.: Consistency between parameterisations of aerosol hygroscopicity and CCN activity during the RHaMBLe discovery cruise, Atmos Chem Phys, 10(7), 3189–3203, doi:10.5194/acp-10-3189-2010, 2010.

van den Heever, S. C., Stephens, G. L. and Wood, N. B.: Aerosol Indirect Effects on Tropical Convection Characteristics under Conditions of Radiative–Convective Equilibrium, J. Atmospheric Sci., 68(4), 699–718, doi:10.1175/2010JAS3603.1, 2010.

Heintzenberg, J., Birmili, W., Wiedensohler, A., Nowak, A. and Tuch, T.: Structure, variability and persistence of the submicrometre marine aerosol, Tellus B, 56(4), 357–367, doi:10.1111/j.1600-0889.2004.00115.x, 2004.

Hess, M., Koepke, P. and Schult, I.: Optical Properties of Aerosols and Clouds: The Software Package OPAC, Bull. Am. Meteorol. Soc., 79(5), 831–844, doi:10.1175/1520-0477(1998)079<0831:OPOAAC>2.0.CO;2, 1998.

Hewitt, C. N., Lee, J. D., MacKenzie, A. R., Barkley, M. P., Carslaw, N., Carver, G. D., Chappell, N. A., Coe, H., Collier, C., Commane, R., Davies, F., Davison, B., DiCarlo, P., Di Marco, C. F., Dorsey, J. R., Edwards, P. M., Evans, M. J., Fowler, D., Furneaux, K. L., Gallagher, M., Guenther, A., Heard, D. E., Helfter, C., Hopkins, J., Ingham, T., Irwin, M., Jones, C., Karunaharan, A., Langford, B., Lewis, A. C., Lim, S. F., MacDonald, S. M., Mahajan, A. S., Malpass, S., McFiggans, G., Mills, G., Misztal, P., Moller, S., Monks, P. S., Nemitz, E., Nicolas-Perea, V., Oetjen, H., Oram, D. E., Palmer, P. I., Phillips, G. J., Pike, R., Plane, J. M. C., Pugh, T., Pyle, J. A., Reeves, C. E., Robinson, N. H., Stewart, D., Stone, D., Whalley, L. K. and Yin, X.: Overview: oxidant and particle photochemical processes above a south-east Asian tropical rainforest (the OP3 project): introduction, rationale, location characteristics and tools, Atmos Chem Phys, 10(1), 169–199, doi:10.5194/acp-10-169-2010, 2010.

Heymsfield, A. J. and Sabin, R. M.: Cirrus Crystal Nucleation by Homogeneous Freezing of Solution Droplets, J. Atmospheric Sci., 46(14), 2252–2264, doi:10.1175/1520-0469(1989)046<2252:CCNBHF>2.0.CO;2, 1989.

Hogan, T. F. and Rosmond, T. E.: The Description of the Navy Operational Global Atmospheric Prediction System's Spectral Forecast Model, Mon. Weather Rev., 119(8), 1786–1815, doi:10.1175/1520-0493(1991)119<1786:TDOTNO>2.0.CO;2, 1991.

Hoppel, W. A., Frick, G. M. and Larson, R. E.: Effect of nonprecipitating clouds on the aerosol size distribution in the marine boundary layer, Geophys. Res. Lett., 13(2), 125–128, doi:10.1029/GL013i002p00125, 1986.

Hoppel, W. A., Frick, G. M., Fitzgerald, J. W. and Larson, R. E.: Marine boundary layer measurements of new particle formation and the effects nonprecipitating clouds have on aerosol size distribution, J. Geophys. Res. Atmospheres, 99(D7), 14443–14459, doi:10.1029/94JD00797, 1994.

Hudson, J. G. and Noble, S.: Reply to comment by Yangang Liu et al. on "Cloud droplet spectral width relationship to CCN spectra and vertical velocity," J. Geophys. Res. Atmospheres, 119(4), 1878–1882, doi:10.1002/2013JD020559, 2014.

Hudson, J. G., Noble, S. and Jha, V.: Cloud droplet spectral width relationship to CCN spectra and vertical velocity, J. Geophys. Res. Atmospheres, 117(D11), doi:10.1029/2012JD017546, 2012.

Hudson, J. G., Noble, S. and Tabor, S.: Cloud supersaturations from CCN spectra Hoppel minima, J. Geophys. Res. Atmospheres, 120(8), 2014JD022669, doi:10.1002/2014JD022669, 2015.

Hussein, T., Dal Maso, M., Petäjä, T., Koponen, I. K., Paatero, P., Aalto, P. P., Hämeri, K. and Kulmala, M.: Evaluation of an automatic algorithm for fitting the particle number size distributions, Boreal Environ. Res., 10(5), 337–355, 2005.

Hyer, E. J., Reid, J. S., Prins, E. M., Hoffman, J. P., Schmidt, C. C., Miettinen, J. I. and Giglio, L.: Patterns of fire activity over Indonesia and Malaysia from polar and geostationary satellite observations, Atmospheric Res., 122, 504–519, doi:10.1016/j.atmosres.2012.06.011, 2013.

IPCC: Climate Change 2013: The Physical Science Basis. Contribution of Working Group I to the Fifth Assessment Report of the Intergovernmental Panel on Climate Change, Cambridge University Press, Cambridge/New York., 2013.

Irwin, M., Good, N., Crosier, J., Choularton, T. W. and McFiggans, G.: Reconciliation of measurements of hygroscopic growth and critical supersaturation of aerosol particles in central Germany, Atmospheric Chem. Phys., 10(23), 11737–11752, doi:https://doi.org/10.5194/acp-10-11737-2010, 2010.

Irwin, M., Robinson, N., Allan, J. D., Coe, H. and McFiggans, G.: Size-resolved aerosol water uptake and cloud condensation nuclei measurements as measured above a Southeast Asian rainforest during OP3, Atmos Chem Phys, 11(21), 11157–11174, doi:10.5194/acp-11-11157-2011, 2011.

Jensen, T. L., Kreidenweis, S. M., Kim, Y., Sievering, H. and Pszenny, A.: Aerosol distributions in the North Atlantic marine boundary layer during Atlantic Stratocumulus Transition Experiment/Marine Aerosol and Gas Exchange, J. Geophys. Res. Atmospheres, 101(D2), 4455–4467, doi:10.1029/95JD00506, 1996.

Kammermann, L., Gysel, M., Weingartner, E., Herich, H., Cziczo, D. J., Holst, T., Svenningsson, B., Arneth, A. and Baltensperger, U.: Subarctic atmospheric aerosol composition: 3. Measured and modeled properties of cloud condensation nuclei, J. Geophys. Res. Atmospheres, 115(D4), doi:10.1029/2009JD012447, 2010.

Kasten, F.: Visibility forecast in the phase of pre-condensation, Tellus, 21(5), 631–635, doi:10.1111/j.2153-3490.1969.tb00469.x, 1969.

Keene, W. C., Maring, H., Maben, J. R., Kieber, D. J., Pszenny, A. A. P., Dahl, E. E., Izaguirre, M. A., Davis, A. J., Long, M. S., Zhou, X., Smoydzin, L. and Sander, R.: Chemical and physical characteristics of nascent aerosols produced by bursting bubbles at a model air-sea interface, J. Geophys. Res. Atmospheres, 112(D21), D21202, doi:10.1029/2007JD008464, 2007.

Khain, A. P., BenMoshe, N. and Pokrovsky, A.: Factors Determining the Impact of Aerosols on Surface Precipitation from Clouds: An Attempt at Classification, J. Atmospheric Sci., 65(6), 1721–1748, doi:10.1175/2007JAS2515.1, 2008.

Khain, A. P., Beheng, K. D., Heymsfield, A., Korolev, A., Krichak, S. O., Levin, Z., Pinsky, M., Phillips, V., Prabhakaran, T., Teller, A., Heever, S. C. van den and Yano, J.-I.: Representation of microphysical processes in cloud-resolving models: Spectral (bin) microphysics versus bulk parameterization, Rev. Geophys., 53(2), 247–322, doi:10.1002/2014RG000468, 2015.

Kinne, S., Schulz, M., Textor, C., Guibert, S., Balkanski, Y., Bauer, S. E., Berntsen, T., Berglen, T. F., Boucher, O., Chin, M., Collins, W., Dentener, F., Diehl, T., Easter, R., Feichter, J., Fillmore, D., Ghan, S., Ginoux, P., Gong, S., Grini, A., Hendricks, J., Herzog, M., Horowitz, L., Isaksen, I., Iversen, T., Kirkevåg, A., Kloster, S., Koch, D., Kristjansson, J. E., Krol, M., Lauer, A., Lamarque, J. F., Lesins, G., Liu, X., Lohmann, U., Montanaro, V., Myhre, G., Penner, J., Pitari, G., Reddy, S., Seland, O., Stier, P., Takemura, T. and Tie, X.: An AeroCom initial assessment – optical properties in aerosol component modules of global models, Atmospheric Chem. Phys., 6(7), 1815–1834, doi:https://doi.org/10.5194/acp-6-1815-2006, 2006.

Kleefeld, C., O'Dowd, C. D., O'Reilly, S., Jennings, S. G., Aalto, P., Becker, E., Kunz, G. and de Leeuw, G.: Relative contribution of submicron and supermicron particles to aerosol light scattering in the marine boundary layer, J. Geophys. Res. Atmospheres, 107(D19), 8103, doi:10.1029/2000JD000262, 2002.

Klein, S. A. and Hartmann, D. L.: The Seasonal Cycle of Low Stratiform Clouds, J. Clim., 6(8), 1587–1606, doi:10.1175/1520-0442(1993)006<1587:TSCOLS>2.0.CO;2, 1993.

Koren, I., Dagan, G. and Altaratz, O.: From aerosol-limited to invigoration of warm convective clouds, Science, 344(6188), 1143–1146, doi:10.1126/science.1252595, 2014.

Kotchenruther, R. A. and Hobbs, P. V.: Humidification factors of aerosols from biomass burning in Brazil, J. Geophys. Res. Atmospheres, 103(D24), 32081–32089, doi:10.1029/98JD00340, 1998.

Kreidenweis, S. M. and Asa-Awuku, A.: Aerosol Hygroscopicity: Particle water content and its role in atmospheric processes, in Treatise on Geochemistry, vol. 5, pp. 331–361, Elsevier, Oxford., 2014.

Kreidenweis, S. M., Walcek, C. J., Feingold, G., Gong, W., Jacobson, M. Z., Kim, C.-H., Liu, X., Penner, J. E., Nenes, A. and Seinfeld, J. H.: Modification of aerosol mass and size distribution due to aqueous-phase SO2 oxidation in clouds: Comparisons of several models, J. Geophys. Res. Atmospheres, 108(D7), doi:10.1029/2002JD002697, 2003.

Laaksonen, A., Vesala, T., Kulmala, M., Winkler, P. M. and Wagner, P. E.: Commentary on cloud modelling and the mass accommodation coefficient of water, Atmospheric Chem. Phys., 5(2), 461–464, doi:https://doi.org/10.5194/acp-5-461-2005, 2005.

de Leeuw, G., Andreas, E. L., Anguelova, M. D., Fairall, C. W., Lewis, E. R., O'Dowd, C., Schulz, M. and Schwartz, S. E.: Production flux of sea spray aerosol, Rev. Geophys., 49(2), RG2001, doi:10.1029/2010RG000349, 2011.

Leung, L. R.: ARM Cloud-Aerosol-Precipitation Experiment (ACAPEX) Field Campaign Report, DOE ARM Climate Research Facility, Pacific Northwest National Laboratory, Richland, WA. [online] Available from: https://www.osti.gov/biblio/1251152 (Accessed 15 October 2018), 2016.

Levin, E. J. T., McMeeking, G. R., Carrico, C. M., Mack, L. E., Kreidenweis, S. M., Wold, C. E., Moosmüller, H., Arnott, W. P., Hao, W. M., Collett, J. L. and Malm, W. C.: Biomass burning

smoke aerosol properties measured during Fire Laboratory at Missoula Experiments (FLAME), J. Geophys. Res. Atmospheres, 115(D18), D18210, doi:10.1029/2009JD013601, 2010.

Levy, R. C., Remer, L. A., Tanré, D., Mattoo, S. and Kaufman, Y. J.: Algorithm for remote sensing of tropospheric aerosol over dark targets from MODIS: Collections 005 and 051: Revision 2; Feb 2009, MODIS Algorithm Theor. Basis Doc., 2009.

Levy, R. C., Mattoo, S., Munchak, L. A., Remer, L. A., Sayer, A. M., Patadia, F. and Hsu, N. C.: The Collection 6 MODIS aerosol products over land and ocean, Atmospheric Meas. Tech., 6(11), 2989–3034, doi:https://doi.org/10.5194/amt-6-2989-2013, 2013.

Li, X., Tao, W.-K., Masunaga, H., Gu, G. and Zeng, X.: Aerosol Effects on Cumulus Congestus Population over the Tropical Pacific: A Cloud-Resolving Modeling Study, J. Meteorol. Soc. Jpn. Ser II, 91(6), 817–833, doi:10.2151/jmsj.2013-607, 2013.

Limpert, E., Stahel, W. A. and Abbt, M.: Log-normal Distributions across the Sciences: Keys and Clues On the charms of statistics, and how mechanical models resembling gambling machines offer a link to a handy way to characterize log-normal distributions, which can provide deeper insight into variability and probability—normal or log-normal: That is the question, BioScience, 51(5), 341–352, doi:10.1641/0006-3568(2001)051[0341:LNDATS]2.0.CO;2, 2001.

Lin, N.-H., Sayer, A. M., Wang, S.-H., Loftus, A. M., Hsiao, T.-C., Sheu, G.-R., Hsu, N. C., Tsay, S.-C. and Chantara, S.: Interactions between biomass-burning aerosols and clouds over Southeast Asia: Current status, challenges, and perspectives, Environ. Pollut., 195, 292–307, doi:10.1016/j.envpol.2014.06.036, 2014.

Liu, Y. and Daum, P. H.: Indirect warming effect from dispersion forcing, Nature, 419(6907), 580, doi:10.1038/419580a, 2002.

Liu, Y., Daum, P. H. and Yum, S. S.: Analytical expression for the relative dispersion of the cloud droplet size distribution, Geophys. Res. Lett., 33(2), doi:10.1029/2005GL024052, 2006.

Liu, Y., Daum, P. H. and Lu, C.: Comment on “Cloud droplet spectral width relationship to CCN spectra and vertical velocity” by Hudson et al., J. Geophys. Res. Atmospheres, 119(4), 1874–1877, doi:10.1002/2012JD019207, 2014.

Lu, M.-L. and Seinfeld, J. H.: Effect of aerosol number concentration on cloud droplet dispersion: A large-eddy simulation study and implications for aerosol indirect forcing, J. Geophys. Res. Atmospheres, 111(D2), doi:10.1029/2005JD006419, 2006.

Lu, M.-L., Conant, W. C., Jonsson, H. H., Varutbangkul, V., Flagan, R. C. and Seinfeld, J. H.: The Marine Stratus/Stratocumulus Experiment (MASE): Aerosol-cloud relationships in marine stratocumulus, J. Geophys. Res. Atmospheres, 112(D10), doi:10.1029/2006JD007985, 2007.

Lynch, P., Reid, J. S., Westphal, D. L., Zhang, J., Hogan, T. F., Hyer, E. J., Curtis, C. A., Hegg, D. A., Shi, Y., Campbell, J. R., Rubin, J. I., Sessions, W. R., Turk, F. J. and Walker, A. L.: An 11-year global gridded aerosol optical thickness reanalysis (v1.0) for atmospheric and climate sciences, Geosci Model Dev, 9(4), 1489–1522, doi:10.5194/gmd-9-1489-2016, 2016.

Ma, J., Chen, Y., Wang, W., Yan, P., Liu, H., Yang, S., Hu, Z. and Lelieveld, J.: Strong air pollution causes widespread haze-clouds over China, J. Geophys. Res. Atmospheres, 115(D18), doi:10.1029/2009JD013065, 2010.

Martin, A. C., Cornwell, G. C., Atwood, S. A., Moore, K. A., Rothfuss, N. E., Taylor, H., DeMott, P. J., Kreidenweis, S. M., Petters, M. D. and Prather, K. A.: Transport of pollution to a remote coastal site during gap flow from California's interior: impacts on aerosol composition, clouds, and radiative balance, Atmos Chem Phys, 17(2), 1491–1509, doi:10.5194/acp-17-1491-2017, 2017.

Martins, J. A. and Dias, M. A. F. S.: The impact of smoke from forest fires on the spectral dispersion of cloud droplet size distributions in the Amazonian region, Environ. Res. Lett., 4(1), 015002, doi:10.1088/1748-9326/4/1/015002, 2009.

Massoli, P., Bates, T. S., Quinn, P. K., Lack, D. A., Baynard, T., Lerner, B. M., Tucker, S. C., Brioude, J., Stohl, A. and Williams, E. J.: Aerosol optical and hygroscopic properties during TexAQS-GoMACCS 2006 and their impact on aerosol direct radiative forcing, J. Geophys. Res. Atmospheres, 114(D7), D00F07, doi:10.1029/2008JD011604, 2009.

McFiggans, G., Artaxo, P., Baltensperger, U., Coe, H., Facchini, M. C., Feingold, G., Fuzzi, S., Gysel, M., Laaksonen, A., Lohmann, U., Mentel, T. F., Murphy, D. M., O'Dowd, C. D., Snider, J. R. and Weingartner, E.: The effect of physical and chemical aerosol properties on warm cloud droplet activation, Atmos Chem Phys, 6(9), 2593–2649, doi:10.5194/acp-6-2593-2006, 2006.

Ming, Y., Ramaswamy, V., Donner, L. J. and Phillips, V. T. J.: A New Parameterization of Cloud Droplet Activation Applicable to General Circulation Models, J. Atmospheric Sci., 63(4), 1348–1356, doi:10.1175/JAS3686.1, 2006.

Modini, R. L., Frossard, A. A., Ahlm, L., Russell, L. M., Corrigan, C. E., Roberts, G. C., Hawkins, L. N., Schroder, J. C., Bertram, A. K., Zhao, R., Lee, A. K. Y., Abbatt, J. P. D., Lin, J., Nenes, A., Wang, Z., Wonaschütz, A., Sorooshian, A., Noone, K. J., Jonsson, H., Seinfeld, J. H., Toom-Sauntry, D., Macdonald, A. M. and Leaitch, W. R.: Primary marine aerosol-cloud interactions off the coast of California, J. Geophys. Res. Atmospheres, 120(9), 2014JD022963, doi:10.1002/2014JD022963, 2015.

Moore, R. H. and Nenes, A.: Scanning Flow CCN Analysis—A Method for Fast Measurements of CCN Spectra, Aerosol Sci. Technol., 43(12), 1192–1207, doi:10.1080/02786820903289780, 2009.

Murphy, D. M., Anderson, J. R., Quinn, P. K., McInnes, L. M., Brechtel, F. J., Kreidenweis, S. M., Middlebrook, A. M., Pósfai, M., Thomson, D. S. and Buseck, P. R.: Influence of sea-salt on aerosol radiative properties in the Southern Ocean marine boundary layer, Nature, 392(6671), 62–65, doi:10.1038/32138, 1998.

Nair, V. S., Moorthy, K. K. and Babu, S. S.: Influence of continental outflow and ocean biogeochemistry on the distribution of fine and ultrafine particles in the marine atmospheric boundary layer over Arabian Sea and Bay of Bengal, J. Geophys. Res. Atmospheres, 118(13), 7321–7331, doi:10.1002/jgrd.50541, 2013.

Neiman, P. J., Hughes, M., Moore, B. J., Ralph, F. M. and Sukovich, E. M.: Sierra Barrier Jets, Atmospheric Rivers, and Precipitation Characteristics in Northern California: A Composite Perspective Based on a Network of Wind Profilers, Mon. Weather Rev., 141(12), 4211–4233, doi:10.1175/MWR-D-13-00112.1, 2013.

Nenes, A., Ghan, S., Abdul-Razzak, H., Chuang, P. Y. and Seinfeld, J. H.: Kinetic limitations on cloud droplet formation and impact on cloud albedo, Tellus B Chem. Phys. Meteorol., 53(2), 133–149, doi:10.3402/tellusb.v53i2.16569, 2001.

O'Dowd, C. D. and Leeuw, G. de: Marine aerosol production: a review of the current knowledge, Philos. Trans. R. Soc. Math. Phys. Eng. Sci., 365(1856), 1753–1774, doi:10.1098/rsta.2007.2043, 2007.

O'Dowd, C. D., Smith, M. H., Consterdine, I. E. and Lowe, J. A.: Marine aerosol, sea-salt, and the marine sulphur cycle: a short review, Atmos. Environ., 31(1), 73–80, doi:10.1016/S1352-2310(96)00106-9, 1997.

O'Neill, N. T., Ignatov, A., Holben, B. N. and Eck, T. F.: The lognormal distribution as a reference for reporting aerosol optical depth statistics; Empirical tests using multi-year, multi-site AERONET Sunphotometer data, Geophys. Res. Lett., 27(20), 3333–3336, doi:10.1029/2000GL011581, 2000.

Pandithurai, G., Dipu, S., Prabha, T. V., Maheskumar, R. S., Kulkarni, J. R. and Goswami, B. N.: Aerosol effect on droplet spectral dispersion in warm continental cumuli, J. Geophys. Res. Atmospheres, 117(D16), doi:10.1029/2011JD016532, 2012.

Paramonov, M., Kerminen, V.-M., Gysel, M., Aalto, P. P., Andreae, M. O., Asmi, E., Baltensperger, U., Bougiatioti, A., Brus, D., Frank, G. P., Good, N., Gunthe, S. S., Hao, L., Irwin, M., Jaatinen, A., Jurányi, Z., King, S. M., Kortelainen, A., Kristensson, A., Lihavainen, H., Kulmala, M., Lohmann, U., Martin, S. T., McFiggans, G., Mihalopoulos, N., Nenes, A., O'Dowd, C. D., Ovadnevaite, J., Petäjä, T., Pöschl, U., Roberts, G. C., Rose, D., Svenningsson, B., Swietlicki, E., Weingartner, E., Whitehead, J., Wiedensohler, A., Wittbom, C. and Sierau, B.: A synthesis of cloud condensation nuclei counter (CCNC) measurements within the EUCAARI network, Atmos Chem Phys, 15(21), 12211–12229, doi:10.5194/acp-15-12211-2015, 2015.

Partridge, D. G., Vrugt, J. A., Tunved, P., Ekman, A. M. L., Gorea, D. and Sorooshian, A.: Inverse modeling of cloud-aerosol interactions – Part 1: Detailed response surface analysis, Atmospheric Chem. Phys., 11(14), 7269–7287, doi:https://doi.org/10.5194/acp-11-7269-2011, 2011.

Pedregosa, F., Varoquaux, G., Gramfort, A., Michel, V., Thirion, B., Grisel, O., Blondel, M., Prettenhofer, P., Weiss, R., Dubourg, V., Vanderplas, J., Passos, A., Cournapeau, D., Brucher, M., Perrot, M. and Duchesnay, É.: Scikit-learn: Machine Learning in Python, J Mach Learn Res, 12, 2825–2830, 2011.

Peng, Y. and Lohmann, U.: Sensitivity study of the spectral dispersion of the cloud droplet size distribution on the indirect aerosol effect, Geophys. Res. Lett., 30(10), doi:10.1029/2003GL017192, 2003.

Peng, Y., Lohmann, U., Leaitch, R. and Kulmala, M.: An investigation into the aerosol dispersion effect through the activation process in marine stratus clouds, J. Geophys. Res. Atmospheres, 112(D11), doi:10.1029/2006JD007401, 2007.

Petters, M. D. and Kreidenweis, S. M.: A single parameter representation of hygroscopic growth and cloud condensation nucleus activity, Atmos Chem Phys, 7(8), 1961–1971, doi:10.5194/acp-7-1961-2007, 2007.

Petters, M. D., Snider, J. R., Stevens, B., Vali, G., Faloona, I. and Russell, L. M.: Accumulation mode aerosol, pockets of open cells, and particle nucleation in the remote subtropical Pacific marine boundary layer, J. Geophys. Res. Atmospheres, 111(D2), D02206, doi:10.1029/2004JD005694, 2006.

Petters, M. D., Carrico, C. M., Kreidenweis, S. M., Prenni, A. J., DeMott, P. J., Collett, J. L. and Moosmüller, H.: Cloud condensation nucleation activity of biomass burning aerosol, J. Geophys. Res. Atmospheres, 114(D22), D22205, doi:10.1029/2009JD012353, 2009.

Petters, M. D., Rothfuss, N. E., Taylor, H., Kreidenweis, S. M., DeMott, P. J. and Atwood, S. A.: Size-resolved cloud condensation nuclei data collected during the CalWater 2015 field campaign, , doi:10.5281/zenodo.2605668, 2019.

Petters, S. S. and Petters, M. D.: Surfactant effect on cloud condensation nuclei for two-component internally mixed aerosols, J. Geophys. Res. Atmospheres, 121(4), 1878–1895, doi:10.1002/2015JD024090, 2016.

Phillips, B. N., Royalty, T. M., Dawson, K. W., Reed, R., Petters, M. D. and Meskhidze, N.: Hygroscopicity- and Size-Resolved Measurements of Submicron Aerosol on the East Coast of the United States, J. Geophys. Res. Atmospheres, 123(3), 1826–1839, doi:10.1002/2017JD027702, 2018.

Prather, K. A., Bertram, T. H., Grassian, V. H., Deane, G. B., Stokes, M. D., DeMott, P. J., Aluwihare, L. I., Palenik, B. P., Azam, F., Seinfeld, J. H., Moffet, R. C., Molina, M. J., Cappa, C. D., Geiger, F. M., Roberts, G. C., Russell, L. M., Ault, A. P., Baltrusaitis, J., Collins, D. B., Corrigan, C. E., Cuadra-Rodriguez, L. A., Ebben, C. J., Forestieri, S. D., Guasco, T. L., Hersey, S. P., Kim, M. J., Lambert, W. F., Modini, R. L., Mui, W., Pedler, B. E., Ruppel, M. J., Ryder, O. S., Schoepp, N. G., Sullivan, R. C. and Zhao, D.: Bringing the ocean into the laboratory to probe the chemical complexity of sea spray aerosol, Proc. Natl. Acad. Sci., 110(19), 7550–7555, doi:10.1073/pnas.1300262110, 2013.

Pruppacher, H. R. and Klett, J. D.: Microstructure of Atmospheric Clouds and Precipitation, in Microphysics of Clouds and Precipitation, edited by H. R. Pruppacher and J. D. Klett, pp. 10–73, Springer Netherlands, Dordrecht., 2010.

Quinn, P. K. and Bates, T. S.: Regional aerosol properties: Comparisons of boundary layer measurements from ACE 1, ACE 2, Aerosols99, INDOEX, ACE Asia, TARFOX, and NEAQS, J. Geophys. Res. Atmospheres, 110(D14), D14202, doi:10.1029/2004JD004755, 2005.

Quinn, P. K., Coffman, D. J., Kapustin, V. N., Bates, T. S. and Covert, D. S.: Aerosol optical properties in the marine boundary layer during the First Aerosol Characterization Experiment (ACE 1) and the underlying chemical and physical aerosol properties, J. Geophys. Res. Atmospheres, 103(D13), 16547–16563, doi:10.1029/97JD02345, 1998.

Quinn, P. K., Coffman, D. J., Bates, T. S., Welton, E. J., Covert, D. S., Miller, T. L., Johnson, J. E., Maria, S., Russell, L., Arimoto, R., Carrico, C. M., Rood, M. J. and Anderson, J.: Aerosol optical properties measured on board the Ronald H. Brown during ACE-Asia as a function of aerosol chemical composition and source region, J. Geophys. Res. Atmospheres, 109(D19), D19S01, doi:10.1029/2003JD004010, 2004.

Quinn, P. K., Bates, T. S., Baynard, T., Clarke, A. D., Onasch, T. B., Wang, W., Rood, M. J., Andrews, E., Allan, J., Carrico, C. M., Coffman, D. and Worsnop, D.: Impact of particulate organic matter on the relative humidity dependence of light scattering: A simplified parameterization, Geophys. Res. Lett., 32(22), L22809, doi:10.1029/2005GL024322, 2005.

Quinn, P. K., Bates, T. S., Coffman, D., Onasch, T. B., Worsnop, D., Baynard, T., de Gouw, J. A., Goldan, P. D., Kuster, W. C., Williams, E., Roberts, J. M., Lerner, B., Stohl, A., Pettersson, A. and Lovejoy, E. R.: Impacts of sources and aging on submicrometer aerosol properties in the marine boundary layer across the Gulf of Maine, J. Geophys. Res. Atmospheres, 111(D23), D23S36, doi:10.1029/2006JD007582, 2006.

Quinn, P. K., Bates, T. S., Coffman, D. J. and Covert, D. S.: Influence of particle size and chemistry on the cloud nucleating properties of aerosols, Atmos Chem Phys, 8(4), 1029–1042, doi:10.5194/acp-8-1029-2008, 2008.

Quinn, P. K., Bates, T. S., Schulz, K. S., Coffman, D. J., Frossard, A. A., Russell, L. M., Keene, W. C. and Kieber, D. J.: Contribution of sea surface carbon pool to organic matter enrichment in sea spray aerosol, Nat. Geosci., 7(3), 228–232, doi:10.1038/ngeo2092, 2014.

Ralph, F. M., Neiman, P. J. and Wick, G. A.: Satellite and CALJET Aircraft Observations of Atmospheric Rivers over the Eastern North Pacific Ocean during the Winter of 1997/98, Mon. Weather Rev., 132(7), 1721–1745, doi:10.1175/1520-0493(2004)132<1721:SACAOO>2.0.CO;2, 2004.

Ralph, F. M., Prather, K. A., Cayan, D., Spackman, J. R., DeMott, P., Dettinger, M., Fairall, C., Leung, R., Rosenfeld, D., Rutledge, S., Waliser, D., White, A. B., Cordeira, J., Martin, A., Helly, J. and Intrieri, J.: CalWater Field Studies Designed to Quantify the Roles of Atmospheric Rivers and Aerosols in Modulating U.S. West Coast Precipitation in a Changing Climate, Bull. Am. Meteorol. Soc., 97(7), 1209–1228, doi:10.1175/BAMS-D-14-00043.1, 2015.

Ramanathan, V., Crutzen, P. J., Kiehl, J. T. and Rosenfeld, D.: Aerosols, Climate, and the Hydrological Cycle, Science, 294(5549), 2119–2124, doi:10.1126/science.1064034, 2001.

Randles, C. A., Russell, L. M. and Ramaswamy, V.: Hygroscopic and optical properties of organic sea salt aerosol and consequences for climate forcing, Geophys. Res. Lett., 31(16), L16108, doi:10.1029/2004GL020628, 2004.

Reid, J. S., Jonsson, H. H., Maring, H. B., Smirnov, A., Savoie, D. L., Cliff, S. S., Reid, E. A., Livingston, J. M., Meier, M. M., Dubovik, O. and Tsay, S.-C.: Comparison of size and morphological measurements of coarse mode dust particles from Africa, J. Geophys. Res. Atmospheres, 108(D19), doi:10.1029/2002JD002485, 2003.

Reid, J. S., Brooks, B., Crahan, K. K., Hegg, D. A., Eck, T. F., O'Neill, N., de Leeuw, G., Reid, E. A. and Anderson, K. D.: Reconciliation of coarse mode sea-salt aerosol particle size measurements and parameterizations at a subtropical ocean receptor site, J. Geophys. Res. Atmospheres, 111(D2), D02202, doi:10.1029/2005JD006200, 2006.

Reid, J. S., Hyer, E. J., Prins, E. M., Westphal, D. L., Zhang, J., Wang, J., Christopher, S. A., Curtis, C. A., Schmidt, C. C., Eleuterio, D. P., Richardson, K. A. and Hoffman, J. P.: Global Monitoring and Forecasting of Biomass-Burning Smoke: Description of and Lessons From the Fire Locating and Modeling of Burning Emissions (FLAMBE) Program, IEEE J. Sel. Top. Appl. Earth Obs. Remote Sens., 2(3), 144–162, doi:10.1109/JSTARS.2009.2027443, 2009.

Reid, J. S., Xian, P., Hyer, E. J., Flatau, M. K., Ramirez, E. M., Turk, F. J., Sampson, C. R., Zhang, C., Fukada, E. M. and Maloney, E. D.: Multi-scale meteorological conceptual analysis of observed active fire hotspot activity and smoke optical depth in the Maritime Continent, Atmos Chem Phys, 12(4), 2117–2147, doi:10.5194/acp-12-2117-2012, 2012.

Reid, J. S., Hyer, E. J., Johnson, R. S., Holben, B. N., Yokelson, R. J., Zhang, J., Campbell, J. R., Christopher, S. A., Di Girolamo, L., Giglio, L., Holz, R. E., Kearney, C., Miettinen, J., Reid, E. A., Turk, F. J., Wang, J., Xian, P., Zhao, G., Balasubramanian, R., Chew, B. N., Janjai, S., Lagrosas, N., Lestari, P., Lin, N.-H., Mahmud, M., Nguyen, A. X., Norris, B., Oanh, N. T. K., Oo, M., Salinas, S. V., Welton, E. J. and Liew, S. C.: Observing and understanding the Southeast Asian aerosol system by remote sensing: An initial review and analysis for the Seven Southeast Asian Studies (7SEAS) program, Atmospheric Res., 122, 403–468, doi:10.1016/j.atmosres.2012.06.005, 2013.

Reid, J. S., Lagrosas, N. D., Jonsson, H. H., Reid, E. A., Sessions, W. R., Simpas, J. B., Uy, S. N., Boyd, T. J., Atwood, S. A., Blake, D. R., Campbell, J. R., Cliff, S. S., Holben, B. N., Holz, R. E., Hyer, E. J., Lynch, P., Meinardi, S., Posselt, D. J., Richardson, K. A., Salinas, S. V., Smirnov, A., Wang, Q., Yu, L. and Zhang, J.: Observations of the temporal variability in aerosol properties and their relationships to meteorology in the summer monsoonal South China Sea/East Sea: the scale-dependent role of monsoonal flows, the Madden–Julian Oscillation, tropical cyclones, squall lines and cold pools, Atmos Chem Phys, 15(4), 1745–1768, doi:10.5194/acp-15-1745-2015, 2015.

Reid, J. S., Lagrosas, N. D., Jonsson, H. H., Reid, E. A., Atwood, S. A., Boyd, T. J., Ghate, V. P., Lynch, P., Posselt, D. J., Simpas, J. B., Uy, S. N., Zaiger, K., Blake, D. R., Bucholtz, A., Campbell, J. R., Chew, B. N., Cliff, S. S., Holben, B. N., Holz, R. E., Hyer, E. J., Kreidenweis, S. M., Kuciaskas, A. P., Lolli, S., Oo, M., Perry, K. D., Salinas, S. V., Sessions, W. R., Smirnov, A., Walker, A. L., Wang, Q., Yu, L., Zhang, J. and Zhao, Y.: Aerosol meteorology and Philippine receptor observations of Maritime Continent aerosol emissions for the 2012 7SEAS southwest monsoon intensive study, Atmospheric Chem. Phys. Discuss., 1–61, doi:10.5194/acp-2016-214, 2016.

Remer, L. A.: Just add aerosols, Science, 344(6188), 1089–1089, doi:10.1126/science.1255398, 2014.

Remer, L. A., Tanre, D., Kaufman, Y. J., Levy, R. and Mattoo, S.: Algorithm for remote sensing of tropospheric aerosol from MODIS: Collection 005, Natl. Aeronaut. Space Adm., 1490 [online] Available from: http://citeseerx.ist.psu.edu/viewdoc/download?doi=10.1.1.385.6530&rep=rep1&type=pdf (Accessed 8 January 2017), 2006.

Reutter, P., Su, H., Trentmann, J., Simmel, M., Rose, D., Gunthe, S. S., Wernli, H., Andreae, M. O. and Pöschl, U.: Aerosol- and updraft-limited regimes of cloud droplet formation: influence of particle number, size and hygroscopicity on the activation of cloud condensation nuclei (CCN), Atmos Chem Phys, 9(18), 7067–7080, doi:10.5194/acp-9-7067-2009, 2009.

Robinson, N. H., Newton, H. M., Allan, J. D., Irwin, M., Hamilton, J. F., Flynn, M., Bower, K. N., Williams, P. I., Mills, G., Reeves, C. E., McFiggans, G. and Coe, H.: Source attribution of Bornean air masses by back trajectory analysis during the OP3 project, Atmos Chem Phys, 11(18), 9605–9630, doi:10.5194/acp-11-9605-2011, 2011.

Robinson, N. H., Allan, J. D., Trembath, J. A., Rosenberg, P. D., Allen, G. and Coe, H.: The lofting of Western Pacific regional aerosol by island thermodynamics as observed around Borneo, Atmos Chem Phys, 12(13), 5963–5983, doi:10.5194/acp-12-5963-2012, 2012.

Rose, D., Nowak, A., Achtert, P., Wiedensohler, A., Hu, M., Shao, M., Zhang, Y., Andreae, M. O. and Pöschl, U.: Cloud condensation nuclei in polluted air and biomass burning smoke near the mega-city Guangzhou, China – Part 1: Size-resolved measurements and implications for the modeling of aerosol particle hygroscopicity and CCN activity, Atmos Chem Phys, 10(7), 3365–3383, doi:10.5194/acp-10-3365-2010, 2010.

Rosenfeld, D.: TRMM observed first direct evidence of smoke from forest fires inhibiting rainfall, Geophys. Res. Lett., 26(20), 3105–3108, doi:10.1029/1999GL006066, 1999.

Rosenfeld, D., Kaufman, Y. J. and Koren, I.: Switching cloud cover and dynamical regimes from open to closed Benard cells in response to the suppression of precipitation by aerosols, Atmospheric Chem. Phys., 6(9), 2503–2511, doi:https://doi.org/10.5194/acp-6-2503-2006, 2006.

Rosenfeld, D., Lohmann, U., Raga, G. B., O'Dowd, C. D., Kulmala, M., Fuzzi, S., Reissell, A. and Andreae, M. O.: Flood or Drought: How Do Aerosols Affect Precipitation?, Science, 321(5894), 1309–1313, doi:10.1126/science.1160606, 2008.

Rosenfeld, D., Sherwood, S., Wood, R. and Donner, L.: Climate Effects of Aerosol-Cloud Interactions, Science, 343(6169), 379–380, doi:10.1126/science.1247490, 2014a.

Rosenfeld, D., Andreae, M. O., Asmi, A., Chin, M., de Leeuw, G., Donovan, D. P., Kahn, R., Kinne, S., Kivekäs, N., Kulmala, M., Lau, W., Schmidt, K. S., Suni, T., Wagner, T., Wild, M. and Quaas, J.: Global observations of aerosol-cloud-precipitation-climate interactions, Rev. Geophys., 52(4), 2013RG000441, doi:10.1002/2013RG000441, 2014b.

Rotstayn, L. D. and Liu, Y.: Sensitivity of the First Indirect Aerosol Effect to an Increase of Cloud Droplet Spectral Dispersion with Droplet Number Concentration, J. Clim., 16(21), 3476–3481, doi:10.1175/1520-0442(2003)016<3476:SOTFIA>2.0.CO;2, 2003.

Royalty, T. M., Phillips, B. N., Dawson, K. W., Reed, R., Meskhidze, N. and Petters, M. D.: Aerosol Properties Observed in the Subtropical North Pacific Boundary Layer, J. Geophys. Res. Atmospheres, 122(18), 9990–10,012, doi:10.1002/2017JD026897, 2017.

Russell, L. M., Pandis, S. N. and Seinfeld, J. H.: Aerosol production and growth in the marine boundary layer, J. Geophys. Res. Atmospheres, 99(D10), 20989–21003, doi:10.1029/94JD01932, 1994.

Russell, L. M., Hawkins, L. N., Frossard, A. A., Quinn, P. K. and Bates, T. S.: Carbohydrate-like composition of submicron atmospheric particles and their production from ocean bubble bursting, Proc. Natl. Acad. Sci., 107(15), 6652–6657, doi:10.1073/pnas.0908905107, 2010.

Sakamoto, K. M., Allan, J. D., Coe, H., Taylor, J. W., Duck, T. J. and Pierce, J. R.: Aged boreal biomass-burning aerosol size distributions from BORTAS 2011, Atmos Chem Phys, 15(4), 1633–1646, doi:10.5194/acp-15-1633-2015, 2015.

Saleeby, S. M. and Cotton, W. R.: A Large-Droplet Mode and Prognostic Number Concentration of Cloud Droplets in the Colorado State University Regional Atmospheric Modeling System (RAMS). Part I: Module Descriptions and Supercell Test Simulations, J. Appl. Meteorol., 43(1), 182–195, doi:10.1175/1520-0450(2004)043<0182:ALMAPN>2.0.CO;2, 2004.

Saleeby, S. M. and van den Heever, S. C.: Developments in the CSU-RAMS Aerosol Model: Emissions, Nucleation, Regeneration, Deposition, and Radiation, J. Appl. Meteorol. Climatol., 52(12), 2601–2622, doi:10.1175/JAMC-D-12-0312.1, 2013.

Salimi, F., Ristovski, Z., Mazaheri, M., Laiman, R., Crilley, L. R., He, C., Clifford, S. and Morawska, L.: Assessment and application of clustering techniques to atmospheric particle number size distribution for the purpose of source apportionment, Atmos Chem Phys, 14(21), 11883–11892, doi:10.5194/acp-14-11883-2014, 2014.

Sanchez, K. J., Russell, L. M., Modini, R. L., Frossard, A. A., Ahlm, L., Corrigan, C. E., Roberts, G. C., Hawkins, L. N., Schroder, J. C., Bertram, A. K., Zhao, R., Lee, A. K. Y., Lin, J. J., Nenes, A., Wang, Z., Wonaschütz, A., Sorooshian, A., Noone, K. J., Jonsson, H., Toom, D., Macdonald, A. M., Leaitch, W. R. and Seinfeld, J. H.: Meteorological and aerosol effects on marine cloud microphysical properties, J. Geophys. Res. Atmospheres, 121(8), 2015JD024595, doi:10.1002/2015JD024595, 2016.

Sayer, A. M., Smirnov, A., Hsu, N. C. and Holben, B. N.: A pure marine aerosol model, for use in remote sensing applications, J. Geophys. Res. Atmospheres, 117(D5), D05213, doi:10.1029/2011JD016689, 2012a.

Sayer, A. M., Smirnov, A., Hsu, N. C., Munchak, L. A. and Holben, B. N.: Estimating marine aerosol particle volume and number from Maritime Aerosol Network data, Atmospheric Chem. Phys., 12(18), 8889–8909, doi:10.5194/acp-12-8889-2012, 2012b.

Sayer, A. M., Hsu, N. C., Bettenhausen, C., Ahmad, Z., Holben, B. N., Smirnov, A., Thomas, G. E. and Zhang, J.: SeaWiFS Ocean Aerosol Retrieval (SOAR): Algorithm, validation, and comparison with other data sets, J. Geophys. Res. Atmospheres, 117(D3), D03206, doi:10.1029/2011JD016599, 2012c.

Seinfeld, J. H. and Pandis, S. N.: Atmospheric Chemistry and Physics: From Air Pollution to Climate Change, John Wiley & Sons., 2012.

Shank, L. M., Howell, S., Clarke, A. D., Freitag, S., Brekhovskikh, V., Kapustin, V., McNaughton, C., Campos, T. and Wood, R.: Organic matter and non-refractory aerosol over the remote Southeast Pacific: oceanic and combustion sources, Atmos Chem Phys, 12(1), 557–576, doi:10.5194/acp-12-557-2012, 2012.

Shaw, R. A. and Lamb, D.: Experimental determination of the thermal accommodation and condensation coefficients of water, J. Chem. Phys., 111(23), 10659–10663, doi:10.1063/1.480419, 1999.

Sheffield, A. M., Saleeby, S. M. and Heever, S. C. van den: Aerosol-induced mechanisms for cumulus congestus growth, J. Geophys. Res. Atmospheres, 120(17), 8941–8952, doi:10.1002/2015JD023743, 2015.

Song, C. H. and Carmichael, G. R.: The aging process of naturally emitted aerosol (sea-salt and mineral aerosol) during long range transport, Atmos. Environ., 33(14), 2203–2218, doi:10.1016/S1352-2310(98)00301-X, 1999.

Spracklen, D. V., Pringle, K. J., Carslaw, K. S., Mann, G. W., Manktelow, P. and Heintzenberg, J.: Evaluation of a global aerosol microphysics model against size-resolved particle statistics in the marine atmosphere, Atmos Chem Phys, 7(8), 2073–2090, doi:10.5194/acp-7-2073-2007, 2007.

Stein, A. F., Draxler, R. R., Rolph, G. D., Stunder, B. J. B., Cohen, M. D. and Ngan, F.: NOAA's HYSPLIT Atmospheric Transport and Dispersion Modeling System, Bull. Am. Meteorol. Soc., 96(12), 2059–2077, doi:10.1175/BAMS-D-14-00110.1, 2015.

Storer, R. L. and van den Heever, S. C.: Microphysical Processes Evident in Aerosol Forcing of Tropical Deep Convective Clouds, J. Atmospheric Sci., 70(2), 430–446, doi:10.1175/JAS-D-12-076.1, 2012.

Suda, S. R., Petters, M. D., Matsunaga, A., Sullivan, R. C., Ziemann, P. J. and Kreidenweis, S. M.: Hygroscopicity frequency distributions of secondary organic aerosols, J. Geophys. Res. Atmospheres, 117(D4), D04207, doi:10.1029/2011JD016823, 2012.

Suda, S. R., Petters, M. D., Yeh, G. K., Strollo, C., Matsunaga, A., Faulhaber, A., Ziemann, P. J., Prenni, A. J., Carrico, C. M., Sullivan, R. C. and Kreidenweis, S. M.: Influence of Functional Groups on Organic Aerosol Cloud Condensation Nucleus Activity, Environ. Sci. Technol., 48(17), 10182–10190, doi:10.1021/es502147y, 2014.

Tang, I. N.: Chemical and size effects of hygroscopic aerosols on light scattering coefficients, J. Geophys. Res. Atmospheres, 101(D14), 19245–19250, doi:10.1029/96JD03003, 1996.

Tang, I. N.: Thermodynamic and optical properties of mixed-salt aerosols of atmospheric importance, J. Geophys. Res. Atmospheres, 102(D2), 1883–1893, doi:10.1029/96JD03085, 1997.

Tang, I. N., Tridico, A. C. and Fung, K. H.: Thermodynamic and optical properties of sea salt aerosols, J. Geophys. Res. Atmospheres, 102(D19), 23269–23275, doi:10.1029/97JD01806, 1997.

Tao, W.-K., Chen, J.-P., Li, Z., Wang, C. and Zhang, C.: Impact of aerosols on convective clouds and precipitation, Rev. Geophys., 50(2), RG2001, doi:10.1029/2011RG000369, 2012.

Tosca, M. G., Randerson, J. T., Zender, C. S., Nelson, D. L., Diner, D. J. and Logan, J. A.: Dynamics of fire plumes and smoke clouds associated with peat and deforestation fires in Indonesia, J. Geophys. Res. Atmospheres, 116(D8), D08207, doi:10.1029/2010JD015148, 2011.

Tunved, P., Ström, J. and Hansson, H.-C.: An investigation of processes controlling the evolution of the boundary layer aerosol size distribution properties at the Swedish background station Aspvreten, Atmos Chem Phys, 4(11/12), 2581–2592, doi:10.5194/acp-4-2581-2004, 2004.

Twomey, S.: Pollution and the planetary albedo, Atmospheric Environ. 1967, 8(12), 1251–1256, doi:10.1016/0004-6981(74)90004-3, 1974.

Twomey, S.: The Influence of Pollution on the Shortwave Albedo of Clouds, J. Atmospheric Sci., 34(7), 1149–1152, doi:10.1175/1520-0469(1977)034<1149:TIOPOT>2.0.CO;2, 1977.

Wang, J., Cubison, M. J., Aiken, A. C., Jimenez, J. L. and Collins, D. R.: The importance of aerosol mixing state and size-resolved composition on CCN concentration and the variation of the importance with atmospheric aging of aerosols, Atmospheric Chem. Phys., 10(15), 7267–7283, doi:https://doi.org/10.5194/acp-10-7267-2010, 2010.

Wang, J., Ge, C., Yang, Z., Hyer, E. J., Reid, J. S., Chew, B.-N., Mahmud, M., Zhang, Y. and Zhang, M.: Mesoscale modeling of smoke transport over the Southeast Asian Maritime Continent: Interplay of sea breeze, trade wind, typhoon, and topography, Atmospheric Res., 122, 486–503, doi:10.1016/j.atmosres.2012.05.009, 2013.

Wang, W., Rood, M. J., Carrico, C. M., Covert, D. S., Quinn, P. K. and Bates, T. S.: Aerosol optical properties along the northeast coast of North America during the New England Air Quality Study–Intercontinental Transport and Chemical Transformation 2004 campaign and the influence of aerosol composition, J. Geophys. Res. Atmospheres, 112(D10), D10S23, doi:10.1029/2006JD007579, 2007.

Ward, D. S., Eidhammer, T., Cotton, W. R. and Kreidenweis, S. M.: The role of the particle size distribution in assessing aerosol composition effects on simulated droplet activation, Atmos Chem Phys, 10(12), 5435–5447, doi:10.5194/acp-10-5435-2010, 2010.

Wegner, T., Hussein, T., Hämeri, K., Vesala, T., Kulmala, M. and Weber, S.: Properties of aerosol signature size distributions in the urban environment as derived by cluster analysis, Atmos. Environ., 61, 350–360, doi:10.1016/j.atmosenv.2012.07.048, 2012.

West, R. E. L., Stier, P., Jones, A., Johnson, C. E., Mann, G. W., Bellouin, N., Partridge, D. G. and Kipling, Z.: The importance of vertical velocity variability for estimates of the indirect aerosol effects, Atmospheric Chem. Phys., 14(12), 6369–6393, doi:https://doi.org/10.5194/acp-14-6369-2014, 2014.

Wex, H., Dieckmann, K., Roberts, G. C., Conrath, T., Izaguirre, M. A., Hartmann, S., Herenz, P., Schäfer, M., Ditas, F., Schmeissner, T., Henning, S., Wehner, B., Siebert, H. and Stratmann, F.: Aerosol arriving on the Caribbean island of Barbados: physical properties and origin, Atmos Chem Phys, 16(22), 14107–14130, doi:10.5194/acp-16-14107-2016, 2016.

White, A. B., Anderson, M. L., Dettinger, M. D., Ralph, F. M., Hinojosa, A., Cayan, D. R., Hartman, R. K., Reynolds, D. W., Johnson, L. E., Schneider, T. L., Cifelli, R., Toth, Z., Gutman, S. I., King, C. W., Gehrke, F., Johnston, P. E., Walls, C., Mann, D., Gottas, D. J. and Coleman, T.: A Twenty-First-Century California Observing Network for Monitoring Extreme Weather Events, J. Atmospheric Ocean. Technol., 30(8), 1585–1603, doi:10.1175/JTECH-D-12-00217.1, 2013.

Whitehead, J. D., Irwin, M., Allan, J. D., Good, N. and McFiggans, G.: A meta-analysis of particle water uptake reconciliation studies, Atmospheric Chem. Phys., 14(21), 11833–11841, doi:https://doi.org/10.5194/acp-14-11833-2014, 2014.

Wilks, D. S.: Statistical Methods in the Atmospheric Sciences, Academic Press., 2011.

Winkler, P. M., Vrtala, A., Wagner, P. E., Kulmala, M., Lehtinen, K. E. J. and Vesala, T.: Mass and Thermal Accommodation during Gas-Liquid Condensation of Water, Phys. Rev. Lett., 93(7), 075701, doi:10.1103/PhysRevLett.93.075701, 2004.

Wood, R.: Stratocumulus Clouds, Mon. Weather Rev., 140(8), 2373–2423, doi:10.1175/MWR-D-11-00121.1, 2012.

Xian, P., Reid, J. S., Atwood, S. A., Johnson, R. S., Hyer, E. J., Westphal, D. L. and Sessions, W.: Smoke aerosol transport patterns over the Maritime Continent, Atmospheric Res., 122, 469–485, doi:10.1016/j.atmosres.2012.05.006, 2013.

Xue, H., Feingold, G. and Stevens, B.: Aerosol Effects on Clouds, Precipitation, and the Organization of Shallow Cumulus Convection, J. Atmospheric Sci., 65(2), 392–406, doi:10.1175/2007JAS2428.1, 2008.

Yokelson, R. J., Christian, T. J., Karl, T. G. and Guenther, A.: The tropical forest and fire emissions experiment: laboratory fire measurements and synthesis of campaign data, Atmos Chem Phys, 8(13), 3509–3527, doi:10.5194/acp-8-3509-2008, 2008.

Yu, F., Wang, Z., Luo, G. and Turco, R.: Ion-mediated nucleation as an important global source of tropospheric aerosols, Atmos Chem Phys, 8(9), 2537–2554, doi:10.5194/acp-8-2537-2008, 2008.

Yuan, T., Remer, L. A., Pickering, K. E. and Yu, H.: Observational evidence of aerosol enhancement of lightning activity and convective invigoration, Geophys. Res. Lett., 38(4), L04701, doi:10.1029/2010GL046052, 2011.

Yum, S. S. and Hudson, J. G.: Adiabatic predictions and observations of cloud droplet spectral broadness, Atmospheric Res., 73(3), 203–223, doi:10.1016/j.atmosres.2004.10.006, 2005.

Zender, C. S., Krolewski, A. G., Tosca, M. G. and Randerson, J. T.: Tropical biomass burning smoke plume size, shape, reflectance, and age based on 2001–2009 MISR imagery of Borneo, Atmos Chem Phys, 12(7), 3437–3454, doi:10.5194/acp-12-3437-2012, 2012.

Zhang, J. and Reid, J. S.: MODIS aerosol product analysis for data assimilation: Assessment of over-ocean level 2 aerosol optical thickness retrievals, J. Geophys. Res. Atmospheres, 111(D22), doi:10.1029/2005JD006898, 2006.

Zhang, X., Massoli, P., Quinn, P. K., Bates, T. S. and Cappa, C. D.: Hygroscopic growth of submicron and supermicron aerosols in the marine boundary layer, J. Geophys. Res. Atmospheres, 119(13), 2013JD021213, doi:10.1002/2013JD021213, 2014.

Zhao, Y., Zhang, Y., Fu, P., Ho, S. S. H., Ho, K. F., Liu, F., Zou, S., Wang, S. and Lai, S.: Non-polar organic compounds in marine aerosols over the northern South China Sea: Influence of continental outflow, Chemosphere, 153, 332–339, doi:10.1016/j.chemosphere.2016.03.069, 2016.

Zieger, P., Fierz-Schmidhauser, R., Gysel, M., Ström, J., Henne, S., Yttri, K. E., Baltensperger, U. and Weingartner, E.: Effects of relative humidity on aerosol light scattering in the Arctic, Atmos Chem Phys, 10(8), 3875–3890, doi:10.5194/acp-10-3875-2010, 2010.

APPENDIX A: PARCEL MODEL DROPLET GROWTH RATE GOVERNING EQUATIONS

The Lagrangian cloud parcel model (Heymsfield and Sabin, 1989; Feingold and Heymsfield, 1992; Saleeby and Cotton, 2004) used in Chapter 4 relies on a cloud droplet growth formulation from Pruppacher and Klett (2010) modified by κ-Köhler theory (Petters and Kreidenweis, 2007) to utilize the κ hygroscopicity parameter for computing droplet interface supersaturation. An initial population of aerosol particles are defined and distributed across a range of size bins. The mid-point radius for each bin is adjusted as particles grow or shrink by condensation and evaporation of water vapor. Each bin is initialized to a size based on equilibrium with the environment at some relative humidity. With each model time step the parcel is raised and the change in size for each bin with mid-point radius, r, is calculated by means of the governing droplet growth equation as:

$$r\frac{dr}{dt} = \frac{s_{v,w} - y}{\frac{\rho_w RT}{e_{sat,w} D_v^* M_w} + \frac{L_v \rho_w}{k_a^* T}\left(\frac{L_v M_w}{RT} - 1\right)} \tag{A1}$$

where $s_{v,w}$ is the parcel saturation ratio, y is the saturation ratio at the droplet interface given curvature and solute effects from κ-Köhler theory and using the κ value for the particles in the bin, ρ_w is the density of water, R is the universal gas constant, T is the ambient temperature, $e_{sat,w}$ is the saturation vapor pressure over water at ambient temperature, M_w is the molecular weight of water, and L_v is latent heat of vaporization. The modified diffusivity, D_v^*, and modified thermal conductivity, k_a^*, terms account for heat and mass transfer across the liquid-vapor barrier at the droplet interface. These terms modify the diffusivity of water vapor in air, D_v, and the

thermal conductivity of air, k_a, through the thermal and condensational mass accommodation coefficients, α_T and α_c, respectively as:

$$D_v^* = \frac{D_v}{\frac{r}{r+\Delta_v} + \frac{D_v}{r\alpha_c}\left(\frac{2\pi M_w}{R_v T_r}\right)^{1/2}} \tag{A2}$$

$$k_a^* = \frac{k_a}{\frac{r}{r+\Delta_T} + \frac{k_a}{r\alpha_T \rho c_p}\left(\frac{2\pi M_a}{R_v T_r}\right)^{1/2}} \tag{A3}$$

where Δ_v and Δ_T are the temperature and pressure dependent vapor and thermal jump lengths, respectively, ρ is the moist air density, c_p is the specific heat of air at constant pressure, and M_a is the molecular weight of air. Further detail is provided in Pruppacher and Klett (2010).